Celso de Mello Donegá *Editor*

Nanoparticles

Workhorses of Nanoscience

Springer

Nanoparticles

Celso de Mello Donegá
Editor

Nanoparticles

Workhorses of Nanoscience

Springer

Editor
Celso de Mello Donegá
Debye Institute for Nanomaterials Science
Utrecht University
Utrecht
The Netherlands

ISBN 978-3-662-44822-9 ISBN 978-3-662-44823-6 (eBook)
DOI 10.1007/978-3-662-44823-6

Library of Congress Control Number: 2014952448

Springer Heidelberg New York Dordrecht London

Printed on acid-free paper

Springer is part of Springer Science+Business Media (www.springer.com)

To Lourdes and Vanessa

Preface

The investigation of nanoscale phenomena and nanomaterials (i.e., Nanoscience) has become one of the most dynamic and interdisciplinary fields in contemporary science, and continues to develop at an astounding rate and in many different directions. Nanoscience is also attracting a growing interest from the general public, as Nanotechnology has been hailed one of the key technologies of the twenty-first century. This intense activity produces vast amounts of new knowledge on a daily basis, which are periodically condensed in authoritative and up-to-date reviews and books covering selected topics within Nanoscience. Nevertheless, the field progresses so fast that topic reviews are needed at increasingly shorter time intervals! Nanoscience is also a dynamic cross-road of many disciplines, and, as a result, its topics do not have sharp boundaries and are continuously evolving and changing. Although this is exactly what makes Nanoscience a very fertile cradle for groundbreaking ideas, it may be overwhelming and bewildering for students and beginner researchers trying to grasp the essence of the field. For those, an *introductory teaching textbook* would be a great asset. However, introductory books to Nanoscience, which are both general and sufficiently deep to be used as textbooks, are scarce, albeit highly needed.

This book aims to address this need by using one particular class of nanomaterials (viz., Nanoparticles) as an exemplary case from which all the fundamental principles of Nanoscience can be derived. The essential feature of nanomaterials is that their physical and chemical properties are size-dependent. Nanoparticles are perfectly suited to illustrate and explain this principle, since they can be made in a variety of sizes and shapes, and from a myriad of different materials ranging from metals to insulators through semiconductors. Further, colloidal nanoparticles beautifully demonstrate the multi- and cross-disciplinary character of Nanoscience, as they integrate concepts from several disciplines within chemistry, physics, and biology (e.g., colloidal science, coordination chemistry, organic chemistry, solid state physics, photophysics, quantum mechanics, magnetism, and interfacial chemistry). We will loosely interchange the terms “nanocrystal” (NC) and “nanoparticle” (NP) throughout the book, even though they are not rigorously synonyms, as nanoparticles also include amorphous materials such as silica.

This work is intended as a basic textbook for graduate students beginning in this field and advanced undergraduate students in Chemistry, Physics, and Materials Science. The overall structure of the book and the treatment of some of the topics reflect my classroom experience teaching a course on Nanomaterials to senior undergraduate students. This course has been taught for several years at Utrecht University, together with some of the contributing authors of this book (de Jongh and Vanmaekelbergh). The chapters are not intended as reviews of the recent scientific literature, but instead convey a comprehensible coverage of the fundamental principles of the subject matter. They also provide a flavor of the state-of-the-art and an outlook on potential developments. Our approach is to emphasize the essential concepts with the objective of developing student understanding. The topics are addressed with conciseness, but without compromising effectiveness and depth. Mathematics are kept to the minimum necessary to ensure proper understanding. For more detailed or rigorous treatments the reader is referred to the literature. To facilitate understanding and highlight the essential concepts, each chapter contains a set of exercises. The student who masters this book will know what Nanoscience is and why it is important, and will also understand its fundamental principles and be able to integrate and combine concepts from different disciplines to address research questions within Nanoscience.

The book can be roughly divided into three parts: fundamental physico-chemical and physical principles of Nanoscience, chemistry and synthesis of nanoparticles, and techniques to study nanoparticles. These parts are however strongly interconnected and intermingled, with the fundamental principles forming a framework that permeates through the whole book.

The first chapter is concerned with the origin of the size dependence of the properties of nanomaterials, explaining it in terms of two fundamental nanoscale effects. This chapter also serves as a general introduction to the book, briefly addressing the definition and classification of nanomaterials and the techniques used to fabricate and study them. Chapter 2 lays out the theoretical framework within which to understand size effects on the properties of semiconductor nanocrystals, with particular emphasis on the quantum confinement effect. The optical properties of metal nanoparticles and metal nanostructures (periodic lattices) are discussed in Chap. 3.

Chapter 4 is devoted to nanoporous materials, treating in detail their synthesis, structure and functional properties, as well as the physical properties of liquids confined in nanopores. The preparation methods, characterization techniques, and applications of supported nanoparticles are covered in Chap. 5. Chapter 6 presents the essential physical-chemical concepts needed to understand the preparation of colloidal inorganic nanoparticles, and the remarkable degree of control that has been achieved over their composition, size, shape and surface.

The last four chapters are dedicated to a few selected characterization techniques that are very valuable tools to study nanoparticles. Chapter 7 concentrates on electron microscopy techniques, while Chap. 8 focuses on scanning probe microscopy and spectroscopy. Electron paramagnetic resonance (EPR) based spectroscopic techniques and their application to nanoparticles are explored in

Chap. 9. Finally, Chap. 10 shows how solution Nuclear Magnetic Resonance (NMR) spectroscopic techniques can be used to unravel the surface chemistry of colloidal nanoparticles.

We have attempted to cover as much as possible of the broad field of Nanoparticles, but had no intention of producing a comprehensive and exhaustive treatise. To keep the length of the book manageable, some topics are not addressed in detail. The most noticeable examples are no doubt superlattices and nanomagnetism, which are briefly mentioned, but not treated in any detail. Further, very actual issues, such as charge transport and multiexciton generation (MEG), are also not discussed. This should not be seen as deliberate omissions from our part, but rather as necessary compromises for the sake of conciseness. These topics are still contained in the book, but the reader is referred to recent literature for a comprehensive treatment.

Most of the excitement about Nanoscience originates from the potential of nanomaterials to lead to a dazzling multitude of applications (e.g., solar energy conversion, optoelectronics, nanophotonics, spintronics, smart catalysts, biomedical applications, etc.). Therefore, it is perhaps surprising that the potential and current applications of nanoparticles are only briefly addressed in this book. This choice was motivated both by our desire to keep the book concise and by the fact that the field is developing so rapidly that the applications section of the book would soon be outdated. In contrast, the fundamental concepts will remain valid, despite the further growth of the field. Our treatment of the applications of nanoparticles should thus be regarded as a blurred snapshot of a fast-moving object. We have made no attempt to sharpen the image, but instead tried to describe it in general terms, highlighting the essential concepts behind the scene. We have left it up to the reader to follow the references provided and fill in the fine details, which are bound to change as progress is made.

In conclusion, it is my pleasant duty to thank all contributors for investing their valuable time into writing exciting and instructive chapters for this book. Thanks are also due to many generations of students for their valuable assistance in the form of questions and remarks that have stimulated me (and certainly also the contributing authors) to seek better ways to present the topics discussed here. I would also like to express my gratitude to Mayra Castro at Springer for inviting me to put together a textbook on Nanomaterials. At the time, it sounded like a very challenging project, and I am glad I took up the challenge. Let us hope this book fulfills its purpose of inspiring many new generations of students and guiding them into the ever changing realms of Nanoscience.

Utrecht, July 2014 Celso de Mello Donegá

Contents

Chapter 1
The Nanoscience Paradigm: "Size Matters!"

Celso de Mello Donegá

Abstract The essential feature of nanomaterials is that their physical and chemical properties are size dependent, making it possible to engineer the material properties not only by defining its chemical composition, but also by tailoring the size and shape of the nanostructures, and the way in which individual building blocks are assembled. This chapter addresses the origin of the size dependence of the properties of nanomaterials, which can be traced to two fundamental nanoscale effects: (a) the increase in the surface/volume ratio with decreasing size, and (b) spatial confinement effects. Furthermore, the definition and classification of nanomaterials is introduced, and the techniques used to fabricate and study them are briefly discussed, with emphasis on nanoparticles of inorganic materials.

1.1 What Is Different About the Nanoscale?

Most of the excitement about Nanoscience and Nanotechnology originates from the potential of nanomaterials to lead to a dazzling multitude of applications (e.g., solar energy conversion, optoelectronics, nanophotonics, spintronics, smart coatings, smart catalysts, biomedical applications, etc.). The essential feature of nanomaterials is that their physical and chemical properties are size dependent, making it possible to engineer the material properties not only by defining its chemical composition, but also by tailoring the size and shape of the nanostructures and the way in which individual building blocks (atoms or smaller nanoparticles) are assembled [1–3].

This may seem strange, as in our daily lives we experience the properties of materials as being completely independent from the dimensions of the objects they make. For example, the colour of a sheet of paper does not change if one cuts it into increasingly smaller pieces. However, when the dimensions of materials reach the nanoscale regime (≤100 nm), their intrinsic properties become size-dependent and

C. de Mello Donegá (✉)
Debye Institute for Nanomaterials Science, Utrecht University, Utrecht, Netherlands
e-mail: c.demello-donega@uu.nl

C. de Mello Donegá (ed.), *Nanoparticles*,
DOI 10.1007/978-3-662-44823-6_1

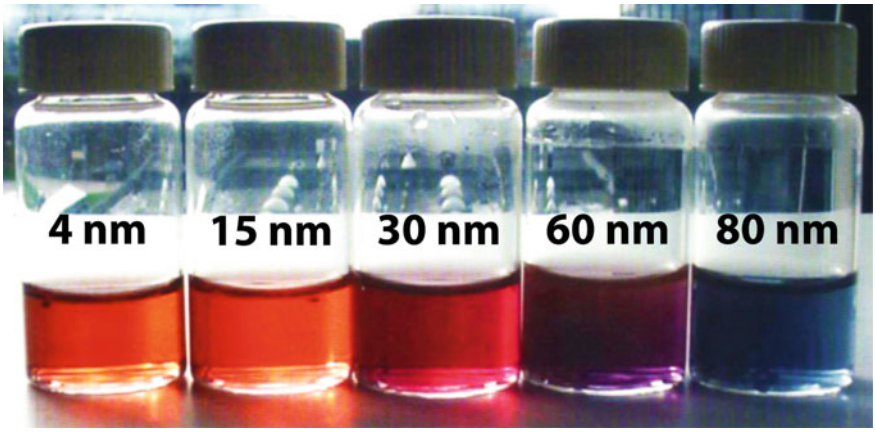

Fig. 1.1 Colloidal suspensions of gold nanoparticles in water. The nanoparticle diameters are indicated on the flasks (*courtesy* F.H. Reincke, Utrecht University)

may be strikingly different from those of their macroscopic (bulk) counterparts. This is clearly illustrated in Figs. 1.1 and 1.2 for two different materials: Gold (a noble metal) and CdSe (a semiconductor with a band-gap of 1.74 eV).

Let us consider the familiar metal Gold in more detail. If we would browse an encyclopaedia (or the internet) for the properties of Gold, we would probably find: "soft and ductile metal with a bright yellow color and luster, melting point 1,337 K, chemically inert…". Strictly speaking, this definition is correct only in first approximation, since those are the properties of bulk Gold. As Fig. 1.1 eloquently demonstrates, Gold nanoparticles (NPs) are actually soluble (or, to be precise, easily form colloidal dispersions in solvents) and, when dispersed into transparent media (like water or glass), give rise to intense colours (orange, red, violet, blue, depending on the NP size). Moreover, gold NPs are chemically active, being very efficient catalysts [4], and melt at progressively lower temperatures as their size decreases below $\sim$50 nm, reaching values as low as 600 K for 3 nm diameter NPs [5].

The origin of the size dependence of the properties of nanomaterials can be traced to two fundamental nanoscale effects [1–3, 5]: (a) the fraction of surface atoms (i.e., the surface/volume ratio) increases with decreasing size and becomes significantly large in NPs; and (b) the limited dimensions of the NP lead to spatial confinement effects that may affect a variety of different properties. These finite size effects will be discussed in detail in the following two subsections.

1.1.1 Finite Size Effects I: Spatial Confinement

Spatial confinement effects are a consequence of the quantum mechanical nature of matter, which is not immediately obvious for macroscopic objects since they consist of a very large number of atoms (for example, a Gold particle as small as 1 μm

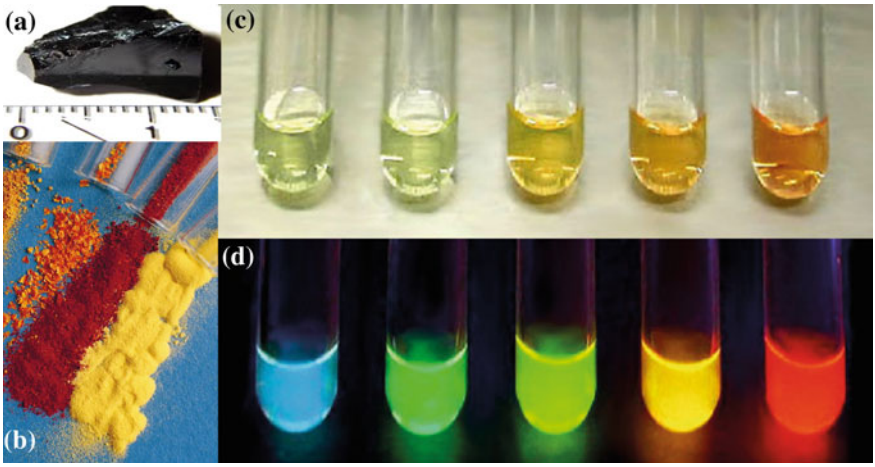

Fig. 1.2 **a** Fragment of a bulk CdSe single crystal (scale bar: 1 cm). **b** CdSe nanocrystals with diameters ranging from 2 nm (*yellow powder*) to 5 nm (*red powder*). Reprinted with permission from Ref. [31]. Copyright (1992) Scientific American, Inc. **c** Colloidal suspensions of CdSe nanocrystals with diameters ranging from 2 nm (*extreme left*) to 5 nm (*extreme right*) under ambient light illumination. Reprinted with permission from Ref. [32]. Copyright (2005) The Chemical Society of Japan. **d** The same suspensions shown in **c**, but under UV excitation. Reprinted with permission from Ref. [32]. Copyright (2005) The Chemical Society of Japan

already contains $\sim 10^{11}$ atoms). However, quantum effects become increasingly important as the size, and consequently the number of atoms, decreases below a certain critical limit. Interestingly, this critical length scale is not the same for different physical properties and different materials, as it depends both on the property under consideration and the exact nature of the chemical bonds in the material. The impact of spatial confinement is thus not the same for different materials and/or different properties. For example, confinement effects on the magnetic properties of NPs will only occur if the NP dimensions are comparable to or smaller than the critical magnetic single domain size of that particular material (20–100 nm, depending on the material) [6, 7].

The dramatic impact of spatial confinement on the optical properties of NPs is quite evident in Figs. 1.1 and 1.2 above. In the case of NPs of semiconductors, such as CdSe, the relevant length scale is the exciton Bohr radius (a_0), a dimension describing the spatial extension of excitons (i.e., electron-hole pairs) in solids, which ranges from ~ 2 to ~ 50 nm depending on the material [2]. As the size of the semiconductor NP approaches a_0, confinement begins to affect the exciton wave function, inducing changes in the electronic states that are manifested in an increase of the band-gap energy with decreasing NP size. As a result, the optoelectronic properties of semiconductor NPs become strongly size- and shape-dependent, making it possible to tune the photoluminescence (PL) of semiconductor NPs through a wide spectral window by choosing the composition, size and shape of the NP. This effect is known as **quantum confinement**, and will be discussed in detail in Chap. 2.

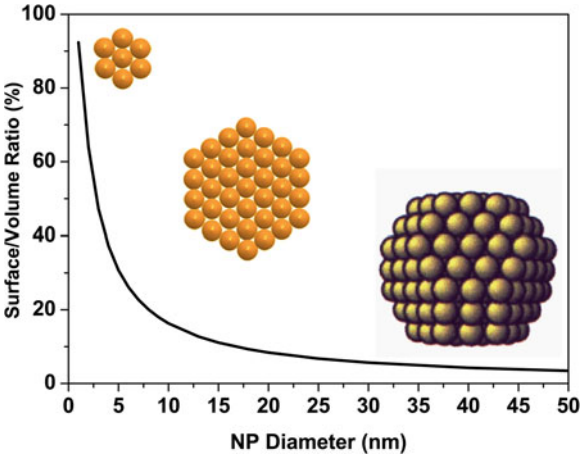

Fig. 1.3 Size dependence of the surface to volume ratio for spherical gold nanoparticles. For clarity, the evolution of the surface/volume ratio for diameters larger than 50 nm is not shown, since it decreases very slowly, reaching 2 % for 100 nm NPs and 0.8 % for 200 nm NPs. The calculations are based on the assumption that the nanoparticles are perfect spheres, regardless of the size. However, one should keep in mind that real nanoparticles are facetted and therefore can only in first approximation be described as spherical. A model for a 2 nm diameter gold NP (surface/volume ratio = 60 %) is shown at the extreme right of the figure. The cartoons at the centre and upper left show two-dimensional representations of NPs with surface/volume ratios equal to 50 and 86 %, respectively

In contrast, optical excitations in metals do not create excitons, but instead induce collective oscillations of the free electrons, which are known as plasmon resonances. Therefore, in the case of a metal the relevant length scale to observe spatial confinement effects on optical properties is the free electron mean free path, which in gold is $\sim$50 nm [5]. Size effects on the plasmon resonance of metals will be addressed in Chap. 3.

1.1.2 Finite Size Effects II: Scaling

As the NP size decreases, the number of atoms is gradually reduced (e.g., 1×10^7, 1×10^4, and 100, for NP diameters of 100, 10, and 2 nm, respectively), while the fraction of atoms located at the surface increases (Fig. 1.3) [1–3]. This is essentially a scaling effect, since the surface to volume ratio of any object increases as its size decreases. For example, the surface of a sphere scales with the square of its radius r, while its volume scales with r^3. Since the total number of atoms in the NP scales linearly with the volume, the fraction of atoms located at the surface of a spherical NP scales with the inverse of its radius.

The increase in the surface to volume ratio has a dramatic impact on several properties, since surface atoms are significantly different from those in the interior of the particle, as they have fewer neighbours and thus possess unsatisfied chemical bonds (i.e., dangling bonds). As a result, surface atoms have a higher free energy, higher reactivity, and increased mobility. Consequently, as the NP size gradually decreases, the contribution of the surface atoms to the total free energy and the properties of the NP progressively increases, causing a number of properties to change: melting and evaporation temperature decrease, and the reactivity, elasticity and plasticity increase. Moreover, this also increases the ability of the NPs to form stable colloidal dispersions, either by charge or steric stabilization. This has important consequences, one of them being that the NP becomes easily dispersible in solvents (Figs. 1.1 and 1.2 above), making fabrication and processing in solution possible.

The larger surface contribution may also lead to changes in interatomic spacings (either contraction or expansion) and bond angles, which may eventually stabilize crystal structures that are metastable for the bulk counterparts, or even lead to global structural reconstruction. It should also be noted that the dangling orbitals at the surface of a semiconductor NP give rise to energy levels within the band-gap [1]. As will be discussed in Chap. 2, this is detrimental to the photoluminescence quantum yield of the NP, because it favours non-radiative recombination of the exciton. For these reasons, it is essential to eliminate dangling bonds from the surface of semiconductor NPs, a process known as **surface passivation**. This can be achieved either by overgrowing a shell of a wider band gap semiconductor or by coating the surface with suitable organic ligands (see Chap. 6 for details).

1.2 Nanomaterials: Definition and Classification

1.2.1 What Are Nanomaterials?

The answer to this seemingly trivial question has been elusive for years, and it is only recently that scientists and other stakeholders (policy makers, funding agencies, etc.) reached a consensus on a general definition. The US National Nanotechnology Initiative (NNI) proposed in 2004 the following definition of Nanomaterials: "materials with dimensions of roughly 1–100 nm, where unique phenomena enable novel applications" [8]. A more specific definition was drafted by the European Commission (EC) in 2011: "Nanomaterial" means a natural, incidental or manufactured material containing particles, in an unbound state or as an aggregate or as an agglomerate and where, for 50 % or more of the particles in the number size distribution, one or more external dimensions is in the size range 1–100 nm"; and/or "has internal or surface structures in one or more dimensions in the size range 1–100 nm"; and/or "has a specific surface area by volume greater than 60 m^2 cm^{-3}, excluding materials consisting of particles with a size smaller than

1 nm" [9]. The EC definition may sound too elaborated and finicky, while the one proposed by the US-NNI is somewhat vague, but they both highlight an essential aspect of nanomaterials: "Size does matter, but only if it changes an intrinsic material property". In other words, nanoscale size is a necessary but not sufficient condition. Basically, as clearly demonstrated in Sect. 1.1. above, the critical length scale defining the boundary between the "mesoscale" (i.e., the size range between macro- and nanoscale) and the "nanoscale" domains is not the same for different materials and/or different properties. Consequently, a meaningful and precise definition of "Nanomaterials" must take both aspects into account: "Nanomaterials are materials having at least one characteristic length scale in the range 1–100 nm, and with at least one property being considerably different from that of the bulk counterpart as a result of the nanoscale dimensions".

1.2.2 Types of Nanomaterials

The definition above (Sect. 1.2.1) implies that Nanomaterials encompass a wide variety of different compounds and comprise many different categories. For instance, proteins, enzymes and DNA also fulfil the requirements mentioned above, and are therefore often referred to as **bionanomaterials**. This chapter (and the remainder of this book) deals only with inorganic nanomaterials, including carbon nanomaterials (viz., carbon nanotubes and nanostructured carbon materials, Chap. 4). Nanomaterials can also be larger objects that contain nanoscale structures, either internally or on their surfaces. These materials are typically referred to as **nanostructured materials**. An interesting example of nanostructured materials is provided by **nanoporous materials** [10]. In this case, the dimensions of the material body itself are much larger than 100 nm, but its pores are on the nanoscale. Nanoporous materials are addressed in detail in Chap. 4.

The concept of **dimensionality** is very useful in the classification of nanomaterials: **zero-dimensional** (**0-D**) nanomaterials are smaller than 100 nm in all directions (e.g., **nanoparticles, nanopores**), while **one-dimensional** (**1-D**) nanomaterials are smaller than 100 nm in 2 directions only (e.g., **nanorods**, **nanowires**, **nanotubes**), and **two-dimensional** (**2-D**) nanomaterials are smaller than 100 nm only in the thickness direction (e.g., **thin films**, **nanoplates**). However, one should keep in mind that, as discussed above (Sect. 1.1), the critical length scale is not necessarily 100 nm, as it depends on the material and property under consideration. For example, a CdSe nanoparticle of 50 nm in diameter will nevertheless be bulk-like (i.e., three-dimensional) from the point of view of the exciton, since the exciton Bohr radius of CdSe is only 3.5 nm (see Chap. 2 for details).

This book deals primarily with **nanoparticles**. Nanoparticles may be free-standing (both in colloidal suspension or as dry powders), supported on substrates, or embedded within a macroscopic matrix of a different material. **Colloidal nanoparticles** are addressed in detail in Chap. 6. It should be noted that not all colloidal particles are nanomaterials, since colloids span the size range from 1 nm

to 1 μm [11]. Therefore, colloidal nanoparticles are often referred to as "**nanocolloids**". **Supported nanoparticles** are discussed in Chap. 5. Optical applications often require that the nanoparticle be embedded into a transparent matrix (e.g., polymer or glass), forming a **nanocomposite** [12]. Colloidal nanoparticles can also be used as building blocks for **nanoparticle solids or superlattices** [13–15], which are very promising for applications requiring thin-films [16].

1.3 The Nanoscale Tool Box

1.3.1 Techniques to Make Nanoparticles

Nanomaterials can be made using a wide variety of methods, which can be classified in two broad categories [17]:

(a) **Top-down processes**, in which material is removed from a larger scale object to create nanostructures (e.g., lithography, either using electron beams, ion beams or X-rays). Lithography is heavily used in the semiconductor processing industry to fabricate integrated circuits and optoelectronic components. Alternatively, the material can broken down into subsequently smaller particles, until the nanoscale is reached (high-energy ball milling). This process is widely used to fabricate nanomaterials in the form of powders.

(b) **Bottom-up processes**, in which building blocks (atoms, molecules) are assembled together into progressively larger structures until the nanoscale is reached. Bottom-up processes can be carried out in numerous ways, yielding a wealth of different nanomaterials [17, 18]. A brief overview of some of the more common methods is presented below. For details the reader will be referred to the literature or subsequent chapters.

1.3.1.1 Bottom-up Approaches to Nanomaterials

Vapour phase deposition methods can be classified as physical vapor deposition (PVD) or chemical vapor deposition (CVD), and are widely used to fabricate thin-films, multilayers, nanotubes, or nanoparticles (either freestanding as powders or embedded into films of another material) [17]. CVD involves the reaction or thermal decomposition of gas phase species (precursors) at high temperatures (500–1,000 °C) followed by deposition on a substrate. A very important variation of this technique is the so-called Molecular Beam Epitaxy (MBE), in which the precursors are deposited directly on the substrate, allowing epitaxial, single atomic layers to be grown. Atomic layers can be sequentially grown on top of each other yielding thin-films with thicknesses that can be controlled with atomic precision. Depending on the nature of the precursor, this technique can also be termed

Chemical Beam Epitaxy (CBE), Metallorganic MBE (MOMBE) or Metallorganic CVD (MOCVD). MOCVD is used extensively to fabricate thin-films of compound semiconductors (e.g., AlGaAs). The chemical composition of subsequent layers can be changed, enabling the fabrication of complex multicomponent nanostructured thin-films, in which a smaller band-gap semiconductor is sandwiched between wider band-gap semiconductors, yielding a 2D-confined system (i.e., a quantum well) (see Chap. 2 for details), that can be readily integrated into devices (e.g., a quantum well laser). The technique can also be used to grow 0D-confined semiconductor nanoparticles (i.e., quantum dots, see Chap. 2 for details) embedded in a matrix of a wider band gap semiconductor, by using conditions that promote the Stranski-Krastanow growth mode [19].

The **Vapor-Liquid-Solid (VLS) method** is widely used to grow semiconductor (e.g., Si, GaAs, etc.) nanowires on substrates [20]. In this process, metal (e.g., Au) nanoparticles are deposited on a substrate and heated above the eutectic temperature for the metal-semiconductor system of choice, in the presence of a vapor-phase source of the semiconductor, resulting in a liquid droplet of the metal-semiconductor alloy. The continued feeding of the semiconductor into the liquid droplet supersaturates the eutectic, leading to the nucleation and growth of the solid semiconductor at the solid-liquid interface. This results in the growth of a nanowire with the alloy droplet on its top.

Liquid-phase methods make use of chemical precipitation reactions in solution [17, 18], and can be divided in:

(a) **Colloidal Methods**. These methods rely on chemical reactions that lead to the nucleation and growth of nanoparticles (NPs) within a solvent, forming a colloidal sol. This process will be discussed in detail in Chap. 6. Colloidal methods are relatively inexpensive, facile and scalable. They are also highly versatile, and can be used to make nanoparticles of a plethora of different compositions: single compounds (metals, e.g. Au, semiconductors, e.g. CdSe, or insulators, e.g. SiO_2) [1, 5], alloys (e.g., FePt, $Cd_{1-x}Zn_xS$) [1], doped materials (e.g., ZnSe:Mn, $NaYF_4$:Yb,Er) [21–24], or combinations of two (or more) different materials joined by one or more interfaces in the same nanoparticle (i.e., heteronanocrystals, e.g., a CdSe core surrounded by a ZnS shell) [1] (see Chap. 6 for details).
It should be noted that the size and shape control offered by colloidal techniques are unmatched by epitaxial techniques (such as MBE and MOCVD), which typically yield nanostructures in the weak quantum confinement regime, owing to their relatively large lateral dimensions (> 10 nm). Moreover, colloidal NPs can easily be subjected to post-synthesis procedures, such as size-selection and surface functionalization (see Chap. 6 for details). They can also be solution-processed into **nanocomposites** with polymers [12], either by dissolving the NPs and polymers in a common solvent and subsequently drying out the mixture (ex situ method), or by carrying out the polymerization reaction in the presence of the NPs (in situ method). These nanocomposites are promising materials for devices that require optically active waveguides, such

as luminescent solar concentrators [25, 26], or optical switches [27]. Another attractive feature of colloidal NPs is that they can be used as building blocks for NP thin-films, either by directly depositing the colloidal NPs onto a substrate and evaporating the solvent, or by allowing the NPs to self-assemble into long-range ordered **superlattices** at air-liquid interfaces and subsequently transferring the superstructure to a suitable substrate [13–15, 28]. These superstructures are also referred to as NP arrays, NP solids, artificial solids or metametarials [13–15]. Under certain conditions the NPs may also self-assemble into ordered three-dimensional superstructures known as supercrystals. NP thin-films hold imense promise for a variety of optoelectronic devices, such as light emitting devices, solar cells, photodiodes, photoconductors and field-effect transistors [16].

(b) **Sol-gel methods** [17, 18]. In this case the metal precursors undergo hydrolysis and condensation reactions, forming colloidal sols that subsequently aggregate into a wet porous network (gel). Upon aging the gel undergoes a process of densification (syneresis) through which the pores contract and expel the solvent. The gels can then be dried yielding a nanoporous structure (xerogel or aerogel). Alternatively the dried gel can be thermally treated to yield a glass monolith. Sol-gel methods are also widely used to fabricate nanopowders, thin (50–500 nm) films, fibers, and also nanocomposites, if NPs are dispersed in the reaction medium prior to the onset of the hydrolisis reaction.

(c) **Templated growth.** Liquid-phase growth can also be carried out inside templating or confining structures, which yield supported NPs. These methods will be discussed in detail in Chap. 5.

1.3.2 Techniques to Study Nanoparticles

The multi- and cross-disciplinary character of Nanoscience is also reflected in the multitude of techniques that are required to unravel and understand the properties of nanomaterials [1]. Given the extent of the subject, we will provide below only a brief overview of the essential techniques to study nanoparticles (NPs). For a more comprehensive treatment the interested reader will be referred to the literature or subsequent chapters.

Size, shape and crystal structure. Transmission Electron Microscopy (TEM) and High-Resolution TEM (HRTEM) are indispensable tools for the characterization of the size and shape of NPs. HRTEM may also yield information about the crystal structure and chemical composition of single NPs when associated to electron diffraction analysis and energy-dispersive X-ray spectroscopy (EDS), respectively. Electron microscopy techniques are addressed in detail in Chap. 7. X-Ray diffraction (XRD) can be used to determine the crystal structure of nanomaterials and may also yield information about the NP size (finite size effects lead to peak broadening in the XRD pattern).

Surface Characterization Techniques. Despite the large surface/volume ratio of nanoparticles, the NP surface has been scarcely investigated. Techniques commonly used for the surface characterization of bulk materials, such as X-Ray photoelectron spectroscopy (XPS) and Rutherford back-scattering spectroscopy (RBS), have penetration depths comparable to the typical dimensions of NPs and therefore yield information about the whole NP [1]. These techniques are thus useful to accurately determine the elemental composition of NPs, but cannot distinguish between surface and interior atoms. The degree of interior strain and disorder of NPs can be directly observed by combined small-angle X-Ray scattering (SAXS) and high-energy wide-angle X-ray scattering (WAXS) measurements, and also by extended X-Ray absorption fine structure (EXAFS) [1]. Solution Nuclear Magnetic Resonance (NMR) spectroscopy has been used to investigate in situ the composition of the surfactant layer of colloidal NPs and is discussed in detail in Chap. 10.

Optical spectroscopy. To unravel the optical properties and electronic structure of NPs a combination of spectroscopic techniques is needed [29, 30]. Absorption, photoluminescence (PL), and PL excitation (PLE) spectroscopy provide information about the energy level structure, and may also be used to identify radiative recombination at dopants or defects (Chap. 2). Time-resolved (TR) PL spectroscopy is well-established as a quantitative tool for the analysis of photoexcitation dynamics in colloidal NPs, yielding information about both radiative and non-radiative exciton recombination channels. TR spectroscopy is also essential to investigate energy transfer processes within or between NPs (Chap. 2). To probe the dynamics of fast processes, such as intraband relaxation, multiexciton generation and decay, and charge injection, a combination of ultrafast TR techniques must be used (viz., transient absorption, THz time-domain spectroscopy). These techniques provide complementary information regarding the fast relaxation of electrons and holes. The insights provided by optical spectroscopy on the photophysical properties of semiconductor and metals NPs are discussed in detail in Chaps. 2 and 3, respectively.

Scanning Tunneling Spectroscopy (STS). STS is a powerful technique to unravel the electronic energy levels of individual NPs and has been applied to both metallic and semiconductor NPs (see Chap. 8 for details).

Magnetic resonance spectroscopic techniques. NMR spectroscopy was already mentioned above, in the context of surface characterization techniques. Electron paramagnetic resonance (EPR) spectroscopy has been mostly applied to characterize paramagnetic ions (e.g., Mn^{2+}) in NPs, as it allows dopants at surface to be distinguished from those in the interior of the NP [1]. The technique can also be applied after photoexcitation of the sample, allowing the interaction between the exciton and paramagnetic impurities to be observed, as well as photoexcited carriers bound to impurities (i.e., donor and acceptor centres). These techniques will be addressed in Chap. 9.

1.4 Exercises

1. Why are nanomaterials different from macroscopic materials?
2. What is the dimensionality of a:
   (a) spherical 200 nm Pd particle?
   (b) spherical 2 nm Pd particle?
   (c) 400 nm long Pd wire with a 4 nm diameter?
   (d) 2 nm thick film of Pd on a flat substrate?
3. Assume you are heating 2 g of each of the materials mentioned in exercise 2. Which one would be the first to melt? Justify your answer.
4. (a) Explain the difference between the "top-down" and "bottom-up" methods of fabrication of nanomaterials. Provide one example of each.
5. The surface/volume ratio of a nanoparticle increases as its size decreases. This has both beneficial and deleterious consequences. Give one example of each, and comment on possible preparation strategies to minimize the negative consequences and take advantage of the beneficial ones.

References

1. Donega, C.D.M.: Synthesis and properties of colloidal heteronanocrystals. Chem. Soc. Rev. **40**, 1512–1546 (2011)
2. Alivisatos, A.P.: Perspectives on the physical chemistry of semiconductor nanocrystals. J. Phys. Chem. **100**, 13226–13239 (1996)
3. Roduner, E.: Size matters: why nanomaterials are different. Chem. Soc. Rev. **35**, 583–592 (2006)
4. Haruta, M.: Chance and necessity: my encounter with gold catalysts. Angew. Chem. Int. Ed. **53**, 52–56 (2014)
5. Burda, C., Chen, X., Narayanan, R., El-Sayed, M.A.: Chemistry and properties of nanocrystals of different shapes. Chem. Rev. **105**, 1025–1102 (2005)
6. Frey, N.A., Peng, S., Cheng, K., Sun, S.: Magnetic nanoparticles: synthesis, functionalization, and applications in bioimaging and magnetic energy storage. Chem. Soc. Rev. **38**, 2532–2542 (2009)
7. Law, M., Goldberger, J., Yang, P.: Semiconductor nanowires and nanotubes. Ann. Rev. Mater. Res. **34**, 83–122 (2004)
8. The National Nanotechnology Initiative—Strategic Plan (2004)
9. European Commission: Recommendation on the definition of nanomaterial, Official Journal of the European Union L275/38-40 (2011)
10. de Jongh, P.E., Eggenhuisen, T.M.: Nanoporous materials and confined liquids. In: Donega C. D.M. (ed.) Nanoparticles: Workhorses of Nanoscience. Springer, Heidelberg (2015) (Chapter 4)
11. Lekkerkerker, H.N.W., Tuinier, R.: Colloids and the Depletion Interaction. Springer, Heidelberg (2011)
12. Holder, E., Tessler, N., Rogach, A.L.: Hybrid nanocomposite materials with organic and inorganic components for opto-electronic devices. J. Mater. Chem. **18**, 1064–1078 (2008)
13. Talapin, D.V., Lee, J., Kovalenko, M.V., Shevchenko, E.V.: Prospects of colloidal nanocrystals for electronic and optoelectronic applications. Chem. Rev. **110**, 389–458 (2010)

14. Quan, Z., Fang, J.: Superlattices with non-spherical building blocks. Nano Today **5**, 390–411 (2010)
15. Vanmaekelbergh, D.: Self-assembly of colloidal nanocrystals as a route to novel classes of nanostructured materials. Nano Today **6**, 419–437 (2011)
16. Shirasaki, Y., Supran, G.J., Bawendi, M.G., Bulovic, V.: Emergence of colloidal quantum-dot light-emitting technologies. Nat. Photon. **7**, 13–23 (2013)
17. Kelsall, R.W., Hamley, I.W., Geoghegan, M. (eds.) Nanoscale Science and Technology, pp. 32–55. Wiley, New Jersey (2005)
18. Manna, L., Kudera, S.: Mechanisms underlying the growth of inorganic nanoparticles in the liquid phase. In: Cozzoli, P.D. (ed.) Advanced Wet-Chemical Synthetic Approaches to Inorganic Nanostructures, pp. 1–53. Transworld Research Network, Kerala (2008)
19. Bhattacharya, P., Ghosh, S., Stiff-Roberts, A.D.: Quantum dot opto-electronic devices. Annu. Rev. Mater. Res. **34**, 1–40 (2004)
20. Lu, W., Lieber, C.M.: Semiconductor nanowires. J. Phys. D Appl. Phys. **39**, R387–R406 (2006)
21. Norris, D.J., Efros, A.L., Erwin, S.C.: Doped nanocrystals. Science **319**, 1776–1779 (2008)
22. Mocatta, D., Cohen, G., Schattner, J., Millo, O., Rabani, E., Banin, U.: Heavily doped semiconductor nanocrystal quantum dots. Science **332**, 77–81 (2011)
23. Buonsanti, R., Milliron, D.J.: Chemistry of doped colloidal nanocrystals. Chem. Mater. **25**, 1305–1317 (2013)
24. Beaulac, R., Ochsenbein, S.T., Gamelin, D.R.: Colloidal Transition-Metal-Doped Quantum Dots. In: Klimov, V.I. (ed.) Nanocrystal Quantum Dots, 2nd edn, pp. 397–453. CRC Press, Boca Raton (2010) (Chapter 7)
25. Meinardi, F., Colombo, A., Velizhanin, K.A., Simonutti, R., Lorenzon, M., Beverina, L., Viswanatha, R., Klimov, V.I., Brovelli, S.: Large-area luminescent solar concentrators based on 'Stokes-shift-engineered' nanocrystals in a mass-polymerized PMMA matrix. Nat. Photon. **8**, 392–399 (2014)
26. Krumer, Z., Pera, S.J., van Dijk-Moes, R.J.A., Zhao, Y., de Brouwer, A.F.P., Groeneveld, E., van Sark, W.G.J.H.M., Schropp, R.E.I., Donega, C.D.M.: Tackling self-absorption in luminescent solar concentrators with type-II colloidal quantum dots. Sol. Energy Mater. Sol. Cells **111**, 57–65 (2013)
27. Petruska, M.A., Malko, A.V., Voyles, P.M., Klimov, V.I.: High-performance, quantum dot nanocomposites for nonlinear optical and optical gain applications. Adv. Mater. **15**, 610–613 (2003)
28. van der Stam, W., Gantapara, A.P., Akkerman, Q.A., Soligno, G., Meeldijk, J.D., van Roij, R., Dijkstra, M., Donega, C.D.M.: Self-assembly of colloidal hexagonal bipyramid- and bifrustum-shaped ZnS nanocrystals into two-dimensional superstructures. Nano Lett. **14**, 1032–1037 (2014)
29. Meijerink, A.: Exciton dynamics and energy transfer processes in semiconductor nanocrystals. In: Rogach, A.L. (ed.) Semiconductor Nanocrystal Quantum Dots: Synthesis, Assembly, Spectroscopy and Applications, pp. 277–310. Springer, Heidelberg (2008)
30. Gaponenko, S.V.: Introduction to Nanophotonics. Cambridge University Press, Cambridge (2010)
31. Reed, M.A.: Quantum dots. Scient. Am. **268**, 118–123 (1993)
32. Teranishi, T., Nishida, M., Kanehara, M.: Size-tuning and optical properties of high-quality CdSe nanoparticles synthesized from Cadmium Stearate. Chem. Lett. **34**, 1004–1005 (2005)

Chapter 2
Size Effects on Semiconductor Nanoparticles

Rolf Koole, Esther Groeneveld, Daniel Vanmaekelbergh, Andries Meijerink and Celso de Mello Donegá

Abstract This chapter addresses the fundamental concepts needed to understand the impact of size reduction on the electronic structure and optoelectronic properties of semiconductor nanostructures, with emphasis on quantum confinement effects. This effect is explained by two different approaches: the "top-down" and the "bottom-up". Subsequently, a brief description of the optical properties of semiconductor nanocrystals is presented. This is followed by sections discussing the essential characteristics of nanocrystals consisting of two (or more) different semiconductors joined together by heterointerfaces (i.e., heteronanocrystals). Moreover, the essential differences between the impact of size reduction on semiconductors in comparison to metals and insulators is discussed. The chapter ends by briefly discussing the potential applications of semiconductor nanoparticles.

2.1 Introduction

There is currently a strong drive among scientists to explore the possibilities of making and characterizing materials of ever smaller dimensions. This effort is motivated by two factors. First of all, there is a great fundamental interest in the novel properties that arise when the dimensions of a material reach the nanoscale (see Chap. 1). Besides the fundamental interest, the wide range of potential applications based on nanomaterials provides an important driving force to push the size of materials to the smallest limits. The most illustrative example is that of the chip-technology, where the continuation of Moore's law has dictated industry to make ever smaller transistors, which recently became only a few tens of nanometers wide [1]. As another example, the large effective surface area that can be achieved using nanomaterials can be very beneficial in catalytic applications. Moreover, the tunable properties of nanomaterials are very attractive for a variety of technologies,

R. Koole · E. Groeneveld · D. Vanmaekelbergh · A. Meijerink · C. de Mello Donegá (✉)
Debye Institute for Nanomaterials Science, Utrecht University, Utrecht, The Netherlands
e-mail: c.demello-donega@uu.nl

C. de Mello Donegá (ed.), *Nanoparticles*,
DOI 10.1007/978-3-662-44823-6_2

Fig. 2.1 Luminescence from suspensions of colloidal CdSe nanocrystals (1.7–4.5 nm diameter, from *left* to *right*) under UV excitation (*courtesy* A. Brinkman and M. Vis, Utrecht University)

ranging from lighting and optoelectronics to biomedical imaging, photovoltaics and thermoelectrics [2].

As discussed in Chap. 1, the impact of spatial confinement is not the same for different materials and/or different properties, as it depends on characteristic length scales of a given property, which are ultimately determined by the material's composition and structure. The profound impact of spatial confinement on the optical properties of semiconductor nanostructures is illustrated in Fig. 2.1. The relevant length scale in this case is the so-calledexciton Bohr radius (a_0), a dimension describing the spatial extension of excitons (i.e., electron-hole pairs) in semiconductors, which ranges from $\sim$2 to $\sim$50 nm depending on the material [3]. The spatial confinement of excitons in semiconductor nanostructures leads to a phenomenon known as quantum confinement [4]. Understanding the origin of quantum confinement and how it influences the electronic structure of semiconductor nanostructures is an essential aspect of Nanoscience. This has stimulated a vast research effort to unravel the fundamental properties of semiconductor nanostructures, leading to great advances in the last few decades [2–9].

This chapter addresses the impact of size reduction on the properties of semiconductor nanostructures, with emphasis on quantum confinement effects. To understand the unique properties that result from quantum confinement, it is instructive to first look at the electronic structure and electronic transitions of bulk semiconductors. Next, the impact of size reduction to the nanoscale on the electronic structure of semiconductors is addressed. Subsequently, a brief description of the optical properties of semiconductor nanocrystals (NCs) is presented. This is followed by sections discussing the essential characteristics of NCs consisting of two (or more) different semiconductors joined together by heterointerfaces. Section 2.8 discusses the essential differences between the impact of size reduction on semiconductors in comparison to metals and insulators. The final section deals with the applications of semiconductor NCs.

2.2 Electronic Structure of Bulk Semiconductors

In contrast to a free electron traveling through vacuum, electrons in a semiconductor experience a periodic potential caused by the atoms in the crystal lattice. To simplify the problem we will start with the description of a hypothetical one dimensional crystal [5], which can be described by the following Hamiltonian:

$$H = H^0 + V(x) = -\frac{\hbar^2}{2m}\frac{\partial^2}{\partial x^2} + V(x) \tag{2.1}$$

where H^0 is the kinetic energy operator, and $V(x)$ describes the periodic potential set by the crystal lattice. The potential is periodic over the lattice constant a, so that $V(x) = V(x + a)$. This means that the Schrödinger equation after translation of the wave function $\psi(x)$ by a distance $a(\psi(x + a))$, can be written as:

$$-\frac{\hbar^2}{2m}\frac{\partial^2}{\partial x^2}\psi(x+a) + V(x)\psi(x+a) = E\psi(x+a) \tag{2.2}$$

After translation over distance a, the wave functions should still have the same eigenvalue E. This implies that the wave functions $\psi(x)$ and $\psi(x + a)$ should only differ by a phase-factor. A wave function that obeys this criterion and that is an eigenfunction of Eq. 2.2 can be written as follows:

$$\psi_{bloch,k}(x) = e^{ikx} \cdot u_k(x) \tag{2.3}$$

where k is defined as the wave vector ($k = 2\pi/\lambda$) and $u_k(x)$ is a function that is periodic with the lattice constant ($u_k(x) = u_k(x + a)$). The resulting wave function is called a Bloch function and is a plane wave (e^{ikx}) that is modulated by a periodic function ($u_k(x)$) [5]. Physically, the plane wave represents the phase (i.e., the sign of the amplitude) of the wave function, whereas $u_k(x)$ describes the response of the valence electrons to the periodic potential of the crystal lattice. Translation of the Bloch function over a distance a gives:

$$\psi_{bloch,k}(x + a) = e^{ika} \cdot \psi_{bloch,k}(x) \tag{2.4}$$

which shows that the wave function indeed only differs by a (phase) constant after translation over a.

Before examining the energy levels of an electron perturbed by the periodic potential of the crystal lattice, we first consider a free electron in vacuum, which is described only by the plane wave $\psi(x) = e^{ikx}$ [5], and has a continuum of energy levels given by the dispersion relation (Fig. 2.2a):

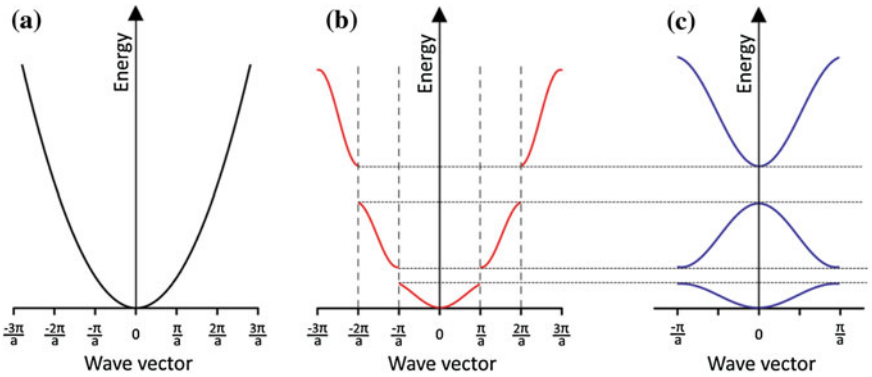

Fig. 2.2 **a** Dispersion relation of a free electron in vacuum. **b** Dispersion relation of an electron in a one dimensional crystal with lattice constant a. **c** Reduced zone representation of the dispersion relation presented in **b**. Reprinted with permission from Ref. [45]

$$E(k) = \frac{\hbar^2 k^2}{2m_0} \tag{2.5}$$

where m_0 is the free electron mass.

The periodic potential in a crystal lattice causes an important change in the dispersion relation for electrons. Electrons that propagate through the lattice with a wavelength that is very different from the lattice spacing a are only slightly disturbed and therefore the energy is similar to that of free electrons. However, when the wavelength of electrons is similar to twice the lattice spacing, or in other words when $k = \pi/a$, the electrons are reflected by the periodic potential of the crystal lattice. These Bragg reflections result in standing waves, described by a linear combination of the plane waves with $k = \pi/a$ and $k = -\pi/a$. The two resulting standing waves ψ^{+}_{bloch} and ψ^{-}_{bloch} are identical, except for a displacement along x by $a/2$. This causes a significant difference in energy between the two standing waves, because the first one concentrates the electron probability at the ions (lowering the potential energy), whereas the second standing wave concentrates the probability exactly in between the ions (increasing the potential energy). Hence, due to the difference in electronic charge distribution, the two standing waves have a different energy at the same k-value, leading to an energy gap in the dispersion relation. The periodicity of the lattice causes Bragg reflections to occur at multiple k-values ($k = n\pi/a$, where n is an integer). This leads to a dispersion relation containing multiple energy gaps, which are referred to as band gaps (Fig. 2.2b).

Another property of the Bloch function is the periodicity in k: wave functions with k-values that differ by $n2\pi/a$ are equivalent, as can be derived from Eq. 2.4. This may be interpreted as follows: the value of the phase (i.e. e^{ikx}) at the ions ($x = qa$, where q is an integer) is exactly the same for k and $k + 2\pi/a$, thus describing the same physical situation. Consequently, the energy dispersion relation may be restricted to k-values between $-\pi/a < k < \pi/a$. Values of larger k can be

folded inside this region by subtracting $2\pi/a$ from the k-value. The resulting interval (in 1 dimension) is called the first Brillouin zone, and the energy dispersion relation can be plotted within this reduced zone (Fig. 2.2c). By reducing the dispersion relation to the interval $-\pi/a < k < \pi/a$, energy bands appear, and one k-value has multiple corresponding energies (which may be regarded as overtones). The band gaps between the different bands occur at $k = \pi/a$ and $k = 0$.

What happens if we consider a semiconductor crystal of more than one dimension? The electronic structure of a three-dimensional (3-D) semiconductor crystal can be explained along the same lines as the 1-D case. However, Bragg reflections in a 3-d crystal lattice are more complex because the periodicity is not the same in different directions. For a simple (primitive) cubic lattice, this means that in the $\langle 110 \rangle$ direction reflection will occur when $k = \sqrt{2}\pi/a$, and in the $\langle 111 \rangle$ direction when $k = \sqrt{3}\pi/a$. This implies that band gaps will arise not only at $k = \pi/a$, but also at $k = \sqrt{2}\pi/a$ (where $k_x = k_y = \pi/a$ and $k_z = 0$) and at $k = \sqrt{3}\pi/a$ (with $k_x = k_y = k_z = \pi/a$). The first Brillouin zone of a simple cubic lattice in 3 dimensions is a plain cube in reciprocal space, and has different band gaps at different points in this Brillouin zone. For the hexagonal close-packed lattice (HCP, e.g., the wurtzite crystal structure of CdSe), the first Brillouin zone is more complicated, as depicted in Fig. 2.3a. The (Greek) letters are the conventional symbols to denote the different points in the Brillouin zone (BZ) of the HCP lattice. For example, the Γ-point is located at $k_{x,y,z} = 0$. It can be seen that there is only one Γ-point in the first BZ of a HCP lattice. In case of a cubic FCC crystal structure (e.g., the rock salt lattice of PbSe, or the zinc blende lattice of CdTe), the first Brillouin Zone has the shape of a truncated octahedron (Fig. 2.3b).

It is difficult to draw the complete dispersion relation as displayed in Fig. 2.2 for a three-dimensional system. The usual way of plotting the energy dependence of electrons in a 3-d semiconductor crystal is shown in Fig. 2.4, which shows the band structure of PbSe as a representative example. The symbols on the x-axis correspond to the symbols in Fig. 2.3b, and the diagram shows the evolution of energy when

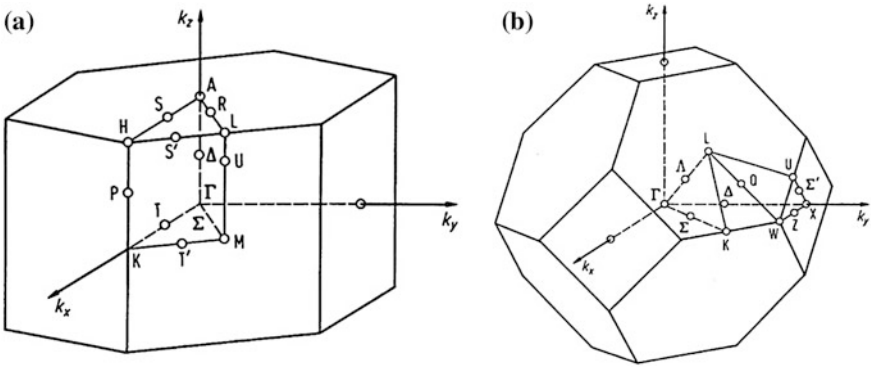

Fig. 2.3 First Brillouin Zone of HCP **a**, and FCC **b** crystal structures. Reprinted with permission from Ref. [19]

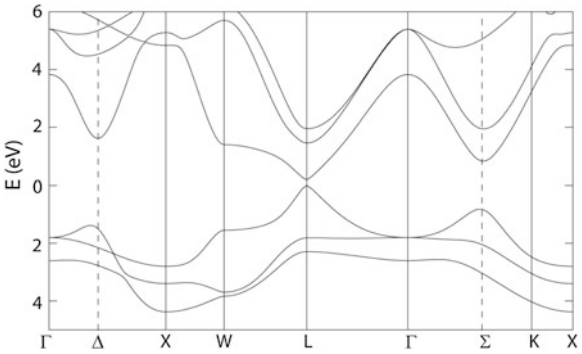

Fig. 2.4 Band structure of bulk PbSe. The zero of energy is at the *top* of the valence band at the L-point, where the fundamental band gap is located. Reprinted with permission from Ref. [46], copyright (2008) Wiley-VCH Verlag GmbH & Co. KGaA, Weinheim

going from one point in the BZ to the other. The highest occupied energy band is called the valence band (VB) and the lowest unoccupied energy band is referred to as conduction band (CB). The energy difference between the VB and CB is referred to as the fundamental band gap. For semiconductors the fundamental energy gap is smaller than 4 eV, which allows electrons to be thermally excited from the VB to the CB at sufficiently high temperatures. The top of the VB and the bottom of the CB for the smallest energy gap can be located at the same *k*-value, yielding a direct band-gap semiconductor (e.g., CdSe), or at different *k*-values, in which case the material is referred to as an indirect band gap semiconductor (e.g., silicon) [5].

It should be noted that band diagrams do *not* show all *k*-values and therefore are only a representation of the dispersion relation for some of the most relevant points in the BZ, in only a few directions in reciprocal space. For example, it is clear from the band structure of PbSe in Fig. 2.4 that the fundamental band gap is located at the L-point in the BZ. In contrast, the fundamental band gap of semiconductors with HCP crystal structure (e.g., wurtzite CdSe) is located at the Γ-point. It is apparent from Fig. 2.3b that there are 8 L-points at the edges of the first BZ of a FCC crystal. Since every L-point is shared by a neighbouring BZ, the fundamental band gap of PbSe is 4-fold degenerate (8-fold including spin). The L-point is in the $\langle 111 \rangle$ direction in reciprocal space, and the four L-states can be seen as states with the same absolute value of *k*, but with a momentum in four different directions ($\langle 111 \rangle$, $\langle 11\text{-}1 \rangle$, $\langle 1\text{-}11 \rangle$, and $\langle \text{-}111 \rangle$).

2.3 Electronic Transitions in Bulk Semiconductors

The valence band (VB) of a semiconductor is completely occupied, while the conduction band (CB) is unoccupied. An electron can be promoted from the VB to the CB as result of an external perturbation, e.g., the absorption of a photon with

energy equal to or higher than the fundamental band gap. The promotion of an electron from the VB to the CB can be described as a system in which the CB contains one particle whereas the VB, consisting of many particles, lacks a particle. This situation is a many-body system. A standard approach to simplify a many-body system is by describing a large number of interacting particles by as little as possible non-interacting particles called '*quasi-particles*' [5]. A first step is the introduction of a *quasi*-particle in the VB, namely 'hole', which is correlated to the ensemble of electrons in the VB from which the electron is removed. The electron in the CB is described by charge (e^-), spin (s = 1/2), and effective mass (m_e^*), whereas the hole in the VB is characterized by a positive charge (e^+), spin (s = 1/2), and effective mass (m_h^*). Due to their charge, electrons and holes are referred to as charge carriers. The concept of effective mass is introduced to account for the interaction of the particle with the periodic crystal lattice. The effective mass thus reflects the increased or decreased mobility of a charge carrier (electron or hole) in the semiconductor with respect to that of an electron in vacuum. An effective mass that is larger than the free electron mass corresponds to an interaction with the crystal lattice that slows down the charge carrier, whereas a higher carrier mobility is reflected in a smaller effective mass. Alternatively, one can take the effective masses as indicators for the spatial extension of the carrier wave function, since the degree of delocalization is inversely proportional to the effective mass of the charge carrier (i.e., lighter carriers are more delocalized).

Since electrons and holes have opposite charges they interact via a Coulomb potential, forming an electron-hole pair that can be described as a *quasi-particle* (the 'exciton'). The formation of an exciton requires a minimum amount of energy given by [5, 10]:

$$E = \hbar\omega = E_g + E_{e,kin} + E_{h,kin} \tag{2.6}$$

in which $E_{e,kin}$ and $E_{h,kin}$ are the kinetic energies of the electron and hole, respectively, and E_g is the semiconductor fundamental band gap. Further, momentum conservation requires that:

$$\hbar k_{cb} = \hbar k_{vb} + \hbar k_{photon} \tag{2.7}$$

where k_{cb} and k_{vb} are the wave vectors of the promoted electron in the CB and the hole in the VB, respectively. Because photons have negligible momentum, the condition $k_{\mathrm{cb}} = k_{\mathrm{vb}}$ must be met. Therefore, without other external perturbations, only transitions within the same k-values (i.e., vertical or direct transitions) can occur [5, 10], as shown in Fig. 2.5.

The energy of an exciton can be expressed by the following dispersion relation:

$$E_n = E_g - \frac{Ry^*}{n^2} + \frac{\hbar^2 k^2}{2(m_e{}^* + m_h{}^*)} \tag{2.8}$$

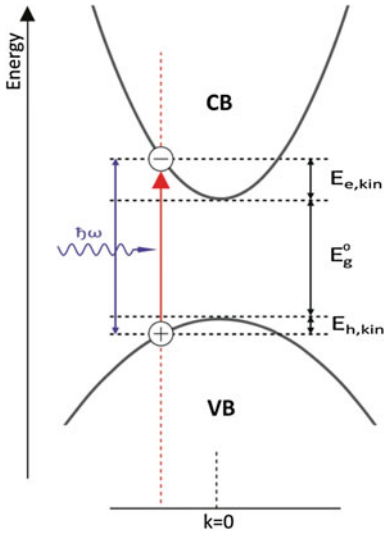

Fig. 2.5 Schematic representation of the promotion of an electron from the valence band to the conduction band in a direct band gap semiconductor as result of the absorption of a photon [5, 10]. Reprinted with permission from Ref. [45]

where the second term contains Hydrogen-like set of energy levels in which Ry^* is the exciton Rydberg energy (corresponds to the ionization energy of the lowest hydrogenic state) [5]. The third term in Eq. 2.8 accounts for the kinetic energy of the exciton centre of mass motion in which k is the exciton wave vector. The kinetic energy term resembles the dispersion curve of a free electron, but with the difference that it is corrected for the effective mass of the exciton. The third term originates from the fact that the interacting holes and electrons can be described as two particles interacting via a Coulomb potential. A Hamiltonian analogous to the hydrogen atom Hamiltonian is used to calculate the energy of the exciton, in which the exciton effective mass replaces the free electron mass m_0. By analogy to the Hydrogen atom the most probable distance between the electron and hole in an exciton is given by the so-called exciton Bohr radius (a_0) [5]

$$a_0 = \frac{\hbar^2 \varepsilon}{e^2}\left(\frac{1}{m_e{}^*} + \frac{1}{m_h{}^*}\right) \tag{2.9}$$

where $m_e{}^*$ and m_h^* are the effective masses of electron and hole, respectively. Further, e is the electron charge and ε is the dielectric constant of the semiconductor. The exciton Bohr radius provides a very useful length scale to describe the spatial extension of excitons in semiconductors, and ranges from $\sim$2 to $\sim$50 nm depending on the semiconductor [3, 5]. It is interesting to note that the exciton Bohr radius a_0 and the band gap of the semiconductor are correlated, so that materials with wider band gaps possess smaller a_0 (e.g., E_g and a_0 are, respectively, 0.26 eV and 46 nm for PbSe, 1.75 eV and 4.9 nm for CdSe, and 3.7 eV and 1.5 nm for ZnS).

2.4 Electronic Structure of Semiconductor Nanocrystals

The description of the band structure of semiconductors presented above was based on an infinite crystal. What happens if the dimensions of the semiconductor crystal are decreased to the nanoscale? As Fig. 2.1 clearly demonstrates, the electronic structure of semiconductor NCs is strongly size dependent. This effect, known as quantum confinement, can be understood via two different approaches. In the first approach ("top-down"), the NC is treated as a small piece of semiconductor material in which the exciton is spatially confined. The second method ("bottom-up") involves a quantum chemical (molecular) approach, in which the NC is build up atom by atom and is treated as an increasingly larger molecular cluster that eventually evolves into a bulk semiconductor crystal. These two approaches will be discussed in the following subsections.

2.4.1 The Top-Down Approach: Nanocrystal as a Small Crystal

In the top-down approach, the Bloch wave functions describing the bulk properties of the semiconductor (including Brillouin zone and band the structure) are maintained, but multiplied by an envelope function to correct for the spatial confinement of the charge carriers (electrons and holes) and the exciton in the small NC [4, 5]:

$$\Psi_{total}(x) = \psi_{bloch}(x) \cdot \varphi_{env}(x) \tag{2.10}$$

The total wave function (Ψ_{tot}) is thus the product of the Bloch function describing the bulk properties of the semiconductor, and the envelope function (φ_{env}) that describes the confinement effects of the charge carriers in the NC. The envelope function is then the solution of the Schrödinger equation for a "particle-in-a-box" problem. For a 3-dimensional box with dimensions L, the wave function would simply be the product of sinusoidal functions in x, y, and z-directions. However, if the confinement is the same in all directions, the NC can better be represented as a spherical potential box (i.e., a quantum dot, QD). The *eigen* functions can then best be described as the product of spherical harmonics ($Y((\theta,\varphi))$) and a radial Bessel function ($R(r)$) [4, 5]:

$$\varphi_{env}(\theta, \phi, r) = Y_l^m(\theta, \phi) \cdot R(r) \tag{2.11}$$

The envelope function has a close resemblance with the wave functions describing the electron of a hydrogen atom. In that case, however, the potential experienced by the electron is determined by the positively charged proton (i.e., V (r) $\sim$ 1/r), while there is no positively charged core in a QD, but instead the electrons experience a spherical potential well of diameter D for which V(r) equals

$-V_0$ (finite) for r < D/2 and zero elsewhere. Inserting Eq. 2.11 in the Schrödinger equation gives the solutions for the discrete energy-levels of a confined electron in a sphere [4, 5]:

$$E_{n,l}^{conf}(D) = \frac{2\hbar^2 \chi_{nl}^2}{m^* D^2} \tag{2.12}$$

where m^* is the effective mass of electrons (or holes), and χ_{nl} are the roots of the Bessel function, which are absolute values depending on (and increasing with) the principal quantum numbers n (1, 2, 3,…) and azimuthal quantum number l (0, 1, 2, 3…, corresponding to s, p, d,…, orbitals) (Fig. 2.6). The lowest energy level ($n = 1$, $l = 0$) has the symmetry of a 1 s orbital in a hydrogen atom (i.e., it is a 1S level). A direct consequence of the difference in the potential function ($V(r)$) between the hydrogen atom and a quantum dot is that the latter system has no restriction of quantum number l with respect to quantum number n, as is the case in the hydrogen atom ($l \leq n - 1$). Therefore the second energy level in a quantum dot has quantum

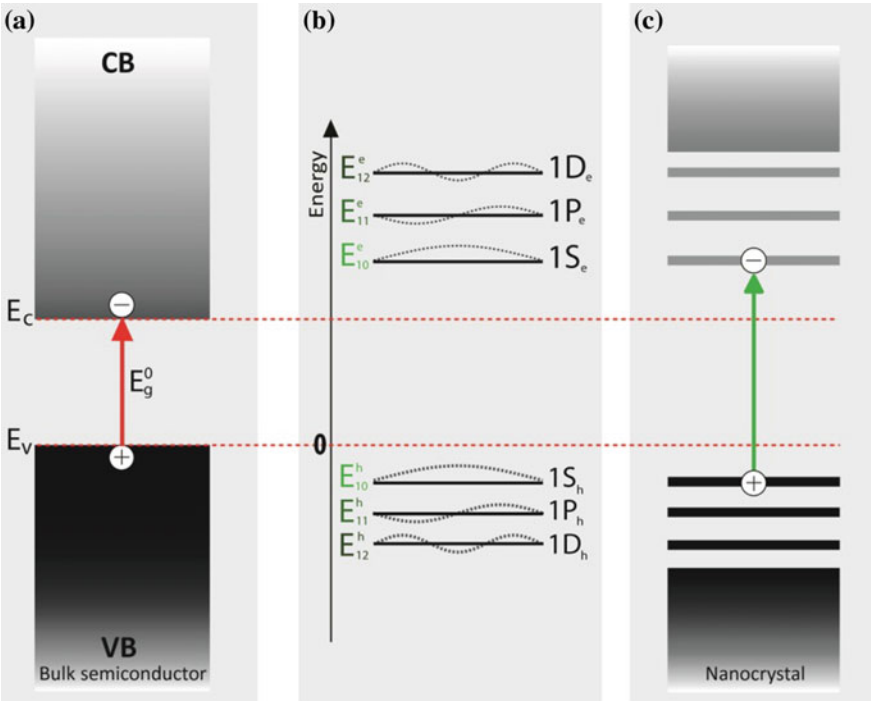

Fig. 2.6 Schematic of the effect of quantum confinement on the electronic structure of a semiconductor. The arrows indicate the lowest energy absorption transition. **a** Bulk semiconductor (CB = conduction band; VB = valence band). **b** Three lowest electron (E_{nl}^e) and hole (E_{nl}^h) energy levels in a quantum dot. The corresponding wave functions are represented by *dashed lines*. **c** Semiconductor nanocrystal (quantum dot). Reprinted with permission from [45]

numbers $n = 1$ and $l = 1$ (i.e., 1P level). The third level is described by $n = 1$, $l = 2$ (1D level), and the fourth level is a 2S level ($n = 2$, $l = 0$). Due to the atomic-like envelope wave functions of the lowest lying energy levels, QDs are often referred to as "artificial atoms".

The band gap of a QD is then the sum of the fundamental bulk band gap (E_g^0) and the confinement energy (E^{conf}) of both electrons and holes:

$$E_g^{tot}(D) = E_g^0 + E_{n,l}^{conf}(D) = E_g^0 + \frac{2\hbar^2\chi_{nl}^2}{m_e^* D^2} + \frac{2\hbar^2\chi_{nl}^2}{m_h^* D^2} \tag{2.13}$$

It should be noted that the electron and hole energy levels are treated independently in the approach above, implying the assumption that the Coulomb interaction between electron and hole is no longer sufficiently strong to form a bound exciton. This approximation is valid only in the so-called strong confinement regime, which holds for NC radius r smaller than the exciton Bohr radius a_0 [4–7]. In this regime the confinement potential becomes larger than the Coulomb interaction. It should be pointed out that the Coulomb interaction is actually much larger than in a bulk crystal, since the charge carriers are confined together in a much smaller volume. However, when $r \ll a_0$ the kinetic energies of the charge carriers are still much larger than the Coulomb interaction between them. Therefore, the electron and hole are no longer correlated and can be treated independently. In first approximation only the change in kinetic energy of the electron and hole are considered, and the Coulomb interaction can be neglected and added later as first order energy corrections.

If the NC radius r is larger than a_0 (viz., weak confinement regime) the increase in exciton energy is due to quantization of the exciton center-of-mass motion [4–7]. The exciton is then described as a particle in a spherical potential, and its discrete energy levels will be given by an expression similar to Eq. (2.12) by replacing the electron (or hole) effective mass by the exciton effective mass. The shift of the energy levels in the weak confinement regime (viz., <100 meV) is much smaller than that in the strong confinement regime. The impact of quantum confinement is usually no longer observable for sizes larger than 2–3 times the exciton Bohr radius.

If the Coulomb interaction is also taken into account the band gap of a QD of radius r can be described as [4–7]

$$E_g(r) = E_g^0 + \frac{\hbar^2\pi^2}{2r^2}\left[\frac{1}{m_e^*} + \frac{1}{m_h^*}\right] - J_{e-h} + E_e^{pol} + E_h^{pol} - 0.248E_{Ry}^* \tag{2.14}$$

where J_{e-h} represents the effective Coulomb interaction between the electron and the hole, which is equal to $1.786e^2/\varepsilon_1 r$ (ε_1 is the dielectric constant of the QD). The terms E_e^{pol} and E_h^{pol} give the self-polarization energies of the electron and hole, respectively, which depend on e^2/r and on the dielectric constants of the QD and the surrounding medium (ε_1 and ε_m, respectively). The exciton Rydberg energy, which accounts for spatial correlation between the electron and the hole, is represented by E_{Ry}^*.

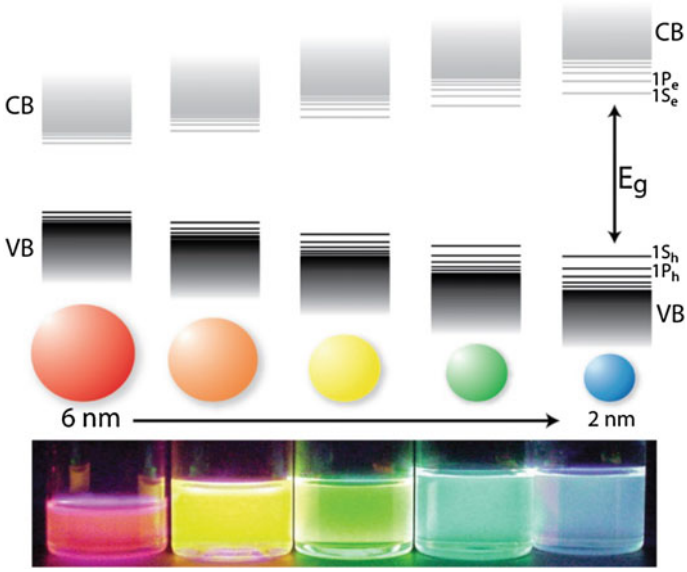

Fig. 2.7 Schematic representation of the quantum confinement effects: the bandgap of the semiconductor material increases with decreasing size, and discrete energy levels arise at the band-edges. Note that the energy difference between the band-edge levels also increases with decreasing size. *Lower panel* shows a photograph of the fluorescence of 5 dispersions of CdSe QDs with different sizes, under excitation with a UV-lamp in the dark. Reproduced by permission of the Royal Society of Chemistry from Ref. [2]

Equations 2.13 and 2.14 clearly describe the two most important consequences of quantum confinement. The first consequence is that the band gap of a semiconductor NC becomes larger with decreasing size, scaling as D^{-2} if the Coulomb interaction is negligible. The second consequence is that discrete energy levels (with different quantum numbers) arise at the band-edges of both the conduction band and valence band. These two size-dependent effects are schematically depicted in Fig. 2.7. In practice, this means that the optical band gap of QDs can be tuned by simply changing their size. For QDs emitting in the visible (e.g.,CdTe or CdSe QDs) this is nicely visualized by their size-dependent luminescence colours (Figs. 2.7 and 2.8).

Quantum confinement effects are also reflected in the optical absorption spectra of QDs. This is illustrated in Fig. 2.8, which shows the absorption spectra of CdTe QDs of different sizes. In the strong quantum confinement regime the energy-spacing between the discrete levels of the envelope functions with different quantum numbers (Eq. 2.12) is in the order of hundreds of meV, and therefore optical transitions between these levels can be clearly resolved in the optical absorption spectrum. Figure 2.8 clearly illustrates that all absorption transitions shift to higher energy as the QD size decreases. The lowest energy optical transition can be assigned to the $1S_h$ to $1S_e$-level (*h* denotes the hole and *e* the electron), the second

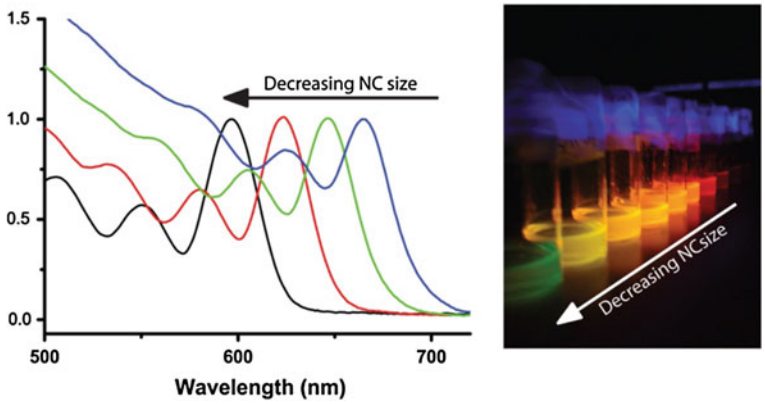

Fig. 2.8 (*Left*) Absorption spectra of colloidal suspensions of CdTe nanocrystal (NC) quantum dots of different sizes. (*Right*) Photograph of vials containing colloidal suspensions of CdTe QDs of different sizes under UV excitation. Reprinted with permission from Ref. [45]

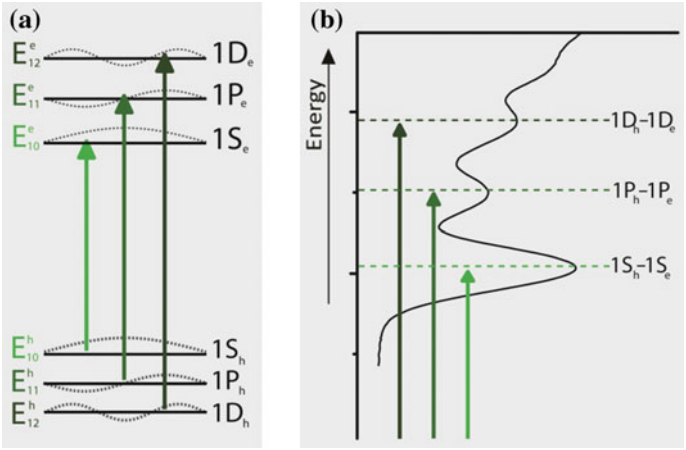

Fig. 2.9 **a** Three lowest electron (E^e_{nl}) and hole (E^h_{nl}) energy levels in a semiconductor nanocrystal quantum dot. The corresponding wavefunctions are represented by the *dashed lines*. Allowed optical transitions are given by the *arrows*. **b** Assignment of the transitions in the absorption spectrum of colloidal CdTe quantum dots. Reprinted with permission from [45]

transition to the $1P_h$ to $1P_e$ level, and so on (Fig. 2.9). The optical selection rules in a QD will be discussed in more detail in Sect. 2.5.

It is interesting to note that the exciton Bohr radius a_0 provides a very convenient length scale to evaluate the impact of quantum confinement on the properties of semiconductor NCs. As discussed above, confinement begins to affect the exciton wave function as the size of the NC approaches a_0. This means that the onset of quantum confinement effects will occur at different NC dimensions for different

semiconductors, since the exciton Bohr radius a_0 varies widely within the semiconductor materials. It is worth noting that a_0 and the band gap E_g are correlated, so that materials with narrower E_g have larger a_0 (e.g., E_g and a_0 are, respectively, 0.26 eV and 46 nm for PbSe, 1.75 eV and 4.9 nm for CdSe, and 3.7 eV and 1.5 nm for ZnS), and will thus experience quantum confinement at larger NC sizes. In contrast, insulators (i.e., materials with $E_g > 4$ eV, e.g., SiO_2, $E_g = 7$ eV) are characterized by strongly localized excitons and hence very small a_0 (typically <1 nm), and are thus affected by quantum confinement only for sizes already in the cluster regime (<20 atoms) [2].

2.4.1.1 Types of Quantum Dots

As discussed above, a semiconductor nanostructure in which the exciton is confined in all three dimensions can be described as a quantum dot, i.e., a structure in which the exciton has no degrees of spatial freedom (zero-dimensional). These so-called quantum confinement effects result in discrete energy levels and larger energy gaps with decreasing sizes. The confinement of electrons and holes in QDs results from the fact that their potential energy is smaller inside the QD than in the surrounding matrix. Such a potential well for charge carriers can be achieved by various architectures, of which three examples are given below (Fig. 2.10).

The first type of QDs is represented by colloidal semiconductor NCs. Colloidal QDs are prepared by wet chemical synthesis, which allow accurate control over the size and shape of the NCs by varying the reaction conditions (see Chap. 6 for details). The potential well for electrons (holes) within the QD is caused by the much higher potential energy of the surrounding medium, which is typically a solvent. The passivating organic ligands that are attached to the surface of the QD

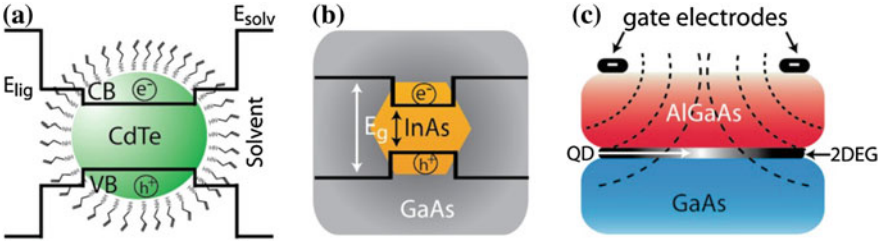

Fig. 2.10 Schematic representation of three types of QD-structures. **a** Colloidal CdTe QD in dispersion. The potential well in the QD is formed by the much higher potential energy for electrons (*holes*) of the surrounding solvent. The organic ligands at the surface of the QD form an intermediate energy barrier. **b** Epitaxially grown InAs QD in a GaAs matrix that has a larger band gap, resulting in a potential well for charge carriers within the InAs QD. **c** Laterally gated QD. A 2-dimensional electron gas (2DEG) is formed at the interface between (n-type) AlGaAs and GaAs and confined in two more dimensions by an electric field generated by gate electrodes on *top* of the device. Reprinted with permission from Ref. [19]

form an intermediate energy barrier between the semiconductor NC and the surrounding medium, as schematically depicted in Fig. 2.10a.

The second example is that of embedded QDs grown by vapour phase epitaxy. These QDs are also known as epitaxial or self-assembled QDs. In this case the potential well for electrons and holes within the semiconductor QD is produced by a surrounding semiconductor material which has a higher conduction band potential and a lower valence band potential (Fig. 2.10b). A typical example of such a system is the combination of small InAs islands embedded in a matrix of GaAs. These structures can be grown with a high degree of control using molecular beam epitaxy (MBE) [11].

The final example concerns a more complicated QD design and is formed in a semiconductor crystal by the field effect of a gate electrode. In such a gated semiconductor QD, one starts with a 2-dimensional electron gas (2DEG) that is formed at the interface between a GaAs and (n-doped) AlGaAs layer. The 2DEG is confined in two more dimensions by applying a negative potential to metal gate electrodes that are deposited on top of the device (Fig. 2.10c). The negative potential causes a depletion of electrons in the 2DEG in the close vicinity of the gate electrodes, which confines the electron to a well-defined spot in between the electrodes. This potential well forms the laterally gated QD [12]. It should be noted that from a fabrication viewpoint this type of QD can also be categorized as epitaxial, since the semiconductor active layers are also deposited by vapour phase epitaxy.

2.4.1.2 Shape Effects

In the discussion above we considered only the case of a spherical quantum dot, in which the exciton is confined in a zero-dimensional spherical potential well. Nevertheless, semiconductor nanostructures can be made with a wide variety of shapes. This is particularly true for colloidal NCs, which can be controllably obtained with a plethora of 0-d (e.g., spheres, cubes, stars, pyramids, and other polyhedra), 1-d (e.g., nanorods, straight or zig-zag wires), and 2-d (e.g., platelets and disks) shapes, as well as with more complex morphologies (e.g., multipods and nanorings) [2] (see Chap. 6 for details). Moreover, vapour phase epitaxial techniques, such as MBE, typically yield non-spherical 0-d (e.g., pyramids) or thin films [11], while a number of techniques is available to grow nanowires [13–15].

It is thus possible to have non-spherical QDs, provided all dimensions are small enough with respect to a_0. In such a case, the electronic structure of the QD will still be characterized by a series of discrete energy levels (Fig. 2.11). The degree of quantum confinement may also vary along different directions depending on the nanostructure shape [3]. If only the diameter of an anisotropic NC is sufficiently small to induce quantum confinement, the exciton will experience a 2-dimensional confinement and the nanocrystal will then be referred to as a Quantum Wire or Quantum Rod, depending on its relative aspect ratio (wires are significantly longer than a_0, while rods have lengths smaller than a few a_0). If the exciton is confined

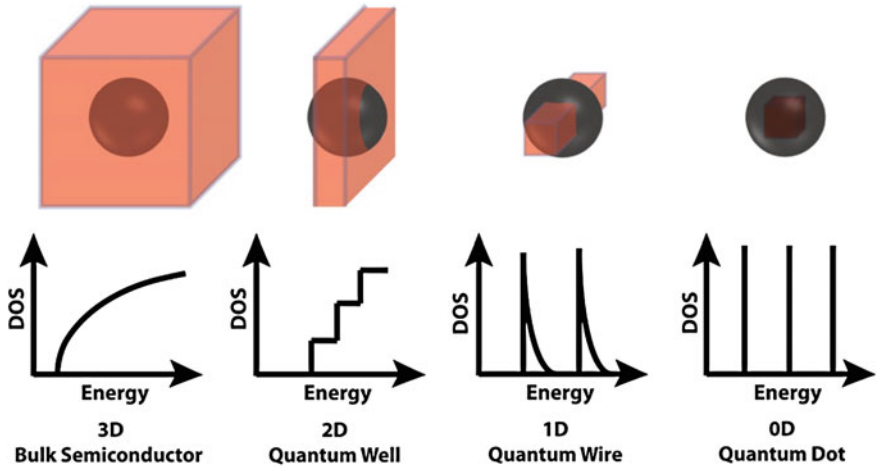

Fig. 2.11 Schematic illustration of the energy level structure of semiconductor nanostructures with reduced dimensionality(2D, 1D and 0D indicate two, one, or zero-dimensional, respectively) [3]. The energy level structure of a bulk semiconductor (3D) is shown for comparison. The exciton Bohr diameter is represented by the sphere. DOS gives the density of states

only in the thickness direction, a Quantum Well is formed (1-dimensional confinement). A schematic overview of the energy level structure of semiconductor nanostructures with reduced dimensionality is given in Fig. 2.11.

2.4.2 Nanocrystal as a Large Molecule: Building Up Atom by Atom

Another method to explain the unique properties of a quantum dot is based on a bottom-up approach [3, 16]. In this approach, the QD is seen as a large molecule or cluster. In analogy with quantum chemical methods for obtaining molecular orbitals (i.e. the Linear Combination of Atomic Orbitals, LCAO), the overall wave functions in a QD can be constructed from the individual atomic orbitals [3].

The simplest example of a multiple electron molecule is that of diatomic hydrogen (H_2). In this molecule, two atomic orbitals (AOs) combine to form two molecular orbitals (MOs) that spread out over both H atoms, namely a bonding and an anti-bonding MO. The bonding MO is lower in energy compared to the individual AOs, whereas the anti-bonding MO is higher in energy than the individual AOs. The MOs are occupied by electrons in such manner that the potential energy of the molecule is minimized. In the H_2 molecule the 2 electrons originally in the 1s AOs of the individual H atoms are accommodated in the bonding MO, thereby leaving the anti-bonding MO unoccupied. The highest occupied molecular orbital is referred to as HOMO and the lowest unoccupied molecular orbital is called LUMO.

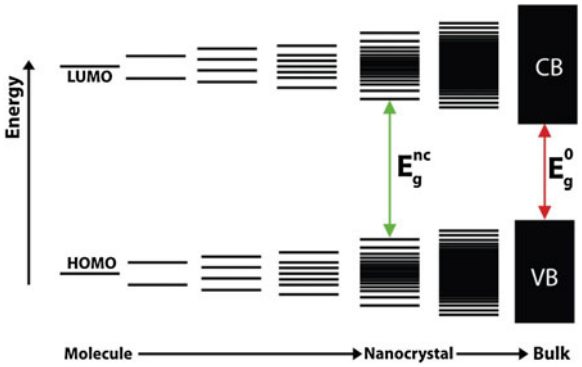

Fig. 2.12 Evolution of the energy level structure from a hypothetical diatomic molecule (*extreme left*) to a bulk semiconductor (*extreme right*). E_g^{nc} and E_g^0 indicate the energy gap between the highest occupied molecular orbital (HOMO) and the lowest unoccupied molecular orbital (LUMO) for a nanocrystal and bulk, respectively (CB = conduction band, VB = valence band). Reprinted with permission from Ref. [45]

The same approach can be extended to larger molecules, clusters and even bulk materials. As the molecule (e.g, a small CdSe cluster) becomes larger, the number of AOs that are combined to form MOs (bonding and anti-bonding) increases, leading to an increasingly larger number of energy levels and decreasing the HOMO-LUMO energy gap (Fig. 2.12). Each MO combination has a well-defined energy value, but MOs with intermediate energy values are more common than those with energies near the minimum or maximum values (i.e., fully bonding or fully anti-bonding). This means that the density of MO states is maximum at intermediate energy values, decreasing to a minimum at both energy extremes (i.e., highest and lowest). For a sufficiently large number of combining atoms (i.e., when the bulk limit is reached) the energy levels become so numerous and so closely spaced that a quasi-continuum (i.e., an energy band) is formed, analogous to the conduction and valence bands described above. The HOMO level is the top of the VB, whereas the LUMO is the bottom of the CB (Fig. 2.12).

A semiconductor NC can be regarded as a very large molecule or cluster consisting of a few tens to a few thousand atomic valence orbitals, forming as many MOs (for example, a 1.5 nm diameter CdSe NC contains about 50 atoms, while a 10 nm NC consists of 10^4 atoms). Therefore, its electronic structure will be characterized by energy bands with a large density of levels at intermediate energy values and discrete energy levels near the band edges, where the density of MO states is small. Moreover, the HOMO-LUMO energy gap will be larger than for bulk and size-dependent, increasing with decreasing size of the NC (Fig. 2.12). This explains both quantum confinement effects discussed in the previous section from a molecular point-of-view.

The MO approach described above provides a simple and general description of the electronic structure of a hypothetical 1-dimensional NC, and clearly illustrates the size dependence of the HOMO-LUMO gap. However, Fig. 2.12 presents the

evolution of the MOs that would be obtained from combining an increasingly larger number of identical AOs (i.e, with the same energy and symmetry). The situation for compound semiconductors (e.g, CdSe, CdTe, PbSe, InP) is more complicated since elements with different electronegativities and different types of AOs are combined. We will use the LCAO-approach in one dimension to describe the properties of a compound QD, using CdTe and CdSe as representative examples. The atomic structure of Cd, Te and Se are $[Kr]4d^{10}5\ s^2$, $[Kr]4d^{10}5\ s^25p^4$, and $[Ar]\ 3d^{10}4s^24p^4$, respectively. The electronic structure of CdTe and CdSe will thus be similar. In both cases the CB is comprised of linear combinations of the (empty) 5s atomic orbitals of Cd^{2+} [3], while the VB can be regarded as a linear combination of the (filled) sp^3 valence orbitals of Te^{2-} or Se^{2-}. For simplicity, we will neglect the sp^3 hybridization and consider that the VB is constructed from the p orbitals of Te or Se. It should be noted that this is an oversimplification, since p orbitals alone would not lead to the formation of a VB under the symmetry constraints imposed by the crystal structure of CdSe and CdTe (zinc blende or wurtzite), in which both the cation and the anion are tetrahedrally coordinated. Under this symmetry, the overlap between the p orbitals of the Se (or Te) anions would be too small. Nevertheless, this oversimplification is useful to illustrate the essential concepts behind the formation of bands from MOs, since in a hypothetical 1-d NC the overlap between the p-orbitals is sufficient to lead to band formation.

For a hypothetical single unit of CdTe the LUMO will be closer in energy to the 5s AOs of Cd, while the HOMO will be closer in energy to the 5p AOs of Te (Fig. 2.13a). As an increasingly larger number of units are combined in a hypothetical 1-dimensional CdTe crystal (constructed along the z-axis), the VB is progressively constructed from the π_y-like MOs resulting from the linear combinations of the $5p_y$ AOs of Te, whereas the CB is constructed from σ-like MOs resulting from the linear combinations of the 5 s AOs of Cd (Fig. 2.13b). Note that the

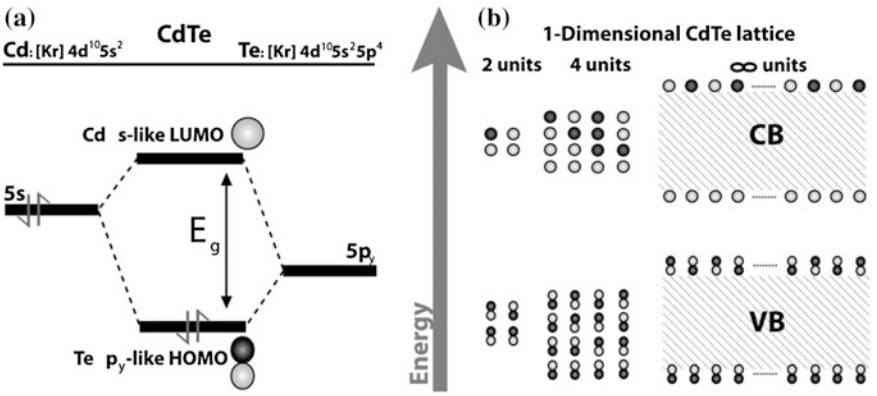

Fig. 2.13 **a** LCAO diagram of a hypothetical CdTe unit. **b** LCAO representation of n-units of CdTe. *Dark gray* and *light gray* indicate different phases of the MOs. Note the π-character of the valence band. Reprinted with permission from Ref. [19]

extremes of the bands consist of the most bonding and the most anti-bonding MOs. It should be pointed out that a similar π-band would emerge from the combination of the $5p_x$ AOs of Te. Since the degeneracy of the p-orbitals would not be lifted in a linear CdTe chain, the two π-bands would also be degenerate, and thus combine in a (hypothetical) π_{xy}-band extending over the whole 1-d CdTe NC. A σ-VB would also be formed from the linear combination of the $5p_z$ orbitals. Figure 2.14 schematically depicts the possible linear combinations of the p_z orbitals, using a hypothetical 1-dimensional CdSe crystal as an example. The MO diagram for a 1-d CdSe crystal is similar to that of CdTe, except that the VB emerges from the linear combinations of the 4p AOs of Se. A sinusoidal function that describes the phase (i.e. the sign of the amplitude) of each (hypothetical) σ-MO is also plotted in Fig. 2.14. The energetically most favourable combination takes place when the phase of each p-orbital changes sign at each selenium site, to form σ-bonding orbitals only. The linear combination of the Se 4p orbitals with the highest energy consists of p-orbitals that are all in phase (all anti-bonding). Similarly, the CB consists of linear combinations of the 5s-orbitals of Cd. The MO with the lowest energy is the linear combination of (bonding) s-orbitals that are all in phase, while the highest energy will be given by all the s orbitals out of phase.

At this point, it is instructive to compare the LCAO-approach with the Bloch-functions described above. The sinusoidal function describing the phase of the p-orbitals may be seen as the plane wave (e^{ikz}) of the Bloch function. As mentioned in Sect. 2.2, the fundamental band gap of CdSe is located at the Γ-point in the Brillouin zone. This means that the top of the valence band and the bottom of the conduction band are both situated at a k-value equal to zero. This is consistent with all the p-orbitals being in phase for the highest lying valence band level (HOMO), described by the sinusoidal function with the longest wavelength (i.e. smallest k). On the other hand, the lowest valence band level has the maximum k-value of π/a, which corresponds to all the p-orbitals changing phase at each selenium site (described by the sinusoidal function with the smallest wavelength). The periodic function ($u_k(z)$) in the Bloch-equation can be seen as the function describing the atomic orbitals; which is periodic over the lattice constant a because at each (selenium) site there is an identical atomic (p) orbital. Only the phase changes, which is described by the plane wave. A similar analysis can be carried out for the conduction band. The MO with the lowest energy is the linear combination of s-orbitals that are all in phase. The number of anti-bonding s-orbitals (and thus the energy) increases with increasing number of phase-flips (increasing k-value), and the conduction band level with the highest energy consists of a MO with only anti-bonding s-orbitals ($k = \pi/a$).

This 1-dimensional analysis is an oversimplification of the QD electronic structure, but it is helpful to understand the QD optical properties, since it shows that the nature of the orbitals constituting the VB and the CB is different. The discrete energy levels of the QDs can be related to different MOs, such as those shown in Fig. 2.14. Naturally, the number of MOs (and therefore of states) is much higher when all three dimensions are taken into account. The atomic-like symmetry of the band-edge levels (1S, 1P, etc.) is not apparent from the sinusoidal functions

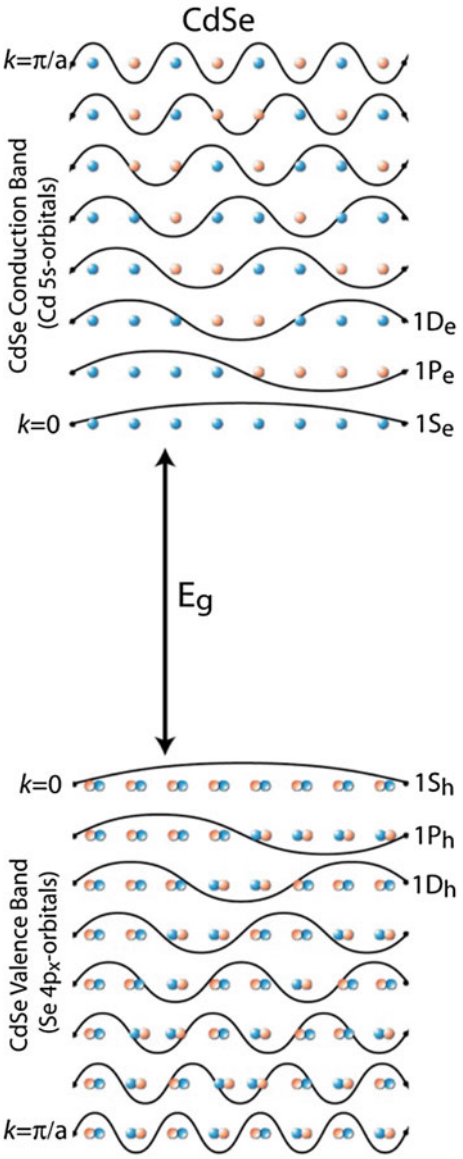

Fig. 2.14 LCAO-representation of the σ-MO levels in a one dimensional CdSe NC. The sinusoidal functions describe the phase of the atomic orbitals, and can be seen as the plane wave-part of the Bloch function. Reprinted with permission from Ref. [19]

(plane waves) in Fig. 2.14. However, it is clear that the probability of finding an electron at the edge of a QD (in real space) cannot be the same as in its centre. In this qualitative description, an envelope function (explained in the previous section) can be inserted to obtain the atomic-like symmetries for the band-edge MOs. When performing tight-binding or pseudo-potential calculations (based on the LCAO-approach), these atomic-like symmetries automatically arise from the boundary conditions that define the quantum dot [17, 18].

2.5 Optical Transitions in a Semiconductor Nanoparticle

As discussed above, the effect of quantum confinement is clearly observed in the optical properties of semiconductor nanostructures, causing a shift of all optical transitions to higher energies as the dimensions of the NC decrease (Figs. 2.1, 2.7, 2.8, 2.9). Moreover, the absorption spectra of QDs consist of a series of discrete peaks corresponding to optical transitions between different electron and hole levels of the QD (Figs. 2.7, 2.8, 2.9). As discussed in the sections above, the discrete energy levels of electrons and holes in semiconductor QDs are sequentially labelled as S, P, D, and so forth (Figs. 2.6, 2.7, 2.9). The optical transitions observed in the absorption spectra of QDs can thus be assigned to $1S_h$-$1S_e$, $1P_h$-$1P_e$, $1D_h$-$1D_e$, (and so forth, the subscripts h and e indicate hole and electron levels, respectively) electronic transitions.

To understand the optical transitions in semiconductor nanostructures (e.g., a quantum dot), we first look at what happens during an optical transition in the simpler case of a two level system [10]. In such an optical transition, an electron is excited from a ground state orbital $|1\rangle$ of the molecule to an excited state orbital $|2\rangle$. The underlying process of the excitation is the mixing of the ground state and excited state orbitals into a combined (mixed) state $(\psi = c_1|1\rangle + c_2|2\rangle)$. This mixing of the two orbitals is induced by the oscillating electric field of an incoming electromagnetic (EM) wave (photon), and can only take place if the mixed state has a dipole moment. The two wave functions are mixed because of a distortion (polarization) caused by the oscillating electric field of a photon, which can only happen if a dipole moment is induced in the mixed state, and if the frequency of the EM field corresponds to the frequency difference between the two states. Figure 2.15 shows what happens when different orbitals (with different phases) are combined. It is clear that two orbitals with the same parity combine into a symmetric mixed wave function, without a dipole moment. Mixing of these orbitals cannot be induced by an oscillating electric field. On the other hand, when two orbitals with a different parity are mixed, the net result is an orbital with a dipole moment [10]. In summary, optical transitions in atoms or molecules can only occur between orbitals with a different parity (e.g., s $\rightarrow$ p, p $\rightarrow$ s, or p $\rightarrow$ d, etc.). This is known as the parity selection rule ($\Delta\ell = \pm 1$). In the treatment below, we focus only on this selection rule. Other selection rules, such as the spin selection rule, are not considered.

Let us now consider the (coherent) excitation of an electron from the 1s to 1p orbitals in a hydrogen atom. During excitation, the combined state of the 1s and 1p orbitals (with a net dipole moment, see Fig. 2.15) [19] starts to oscillate with the frequency of the EM field, and by doing so, the states become more and more mixed. Note that this only happens when the frequency of the incoming wave is resonant with the *eigen*-frequency of the oscillating dipole (in other words, when the energy of the photon matches the energy difference between the ground and excited state). Initially, the mixed state has mainly 1s-character $(\psi = c_1|1\rangle + c_2|2\rangle)$ with $c_1 \gg c_2$). After a certain number of oscillations (typically $\sim 10^8$ for a

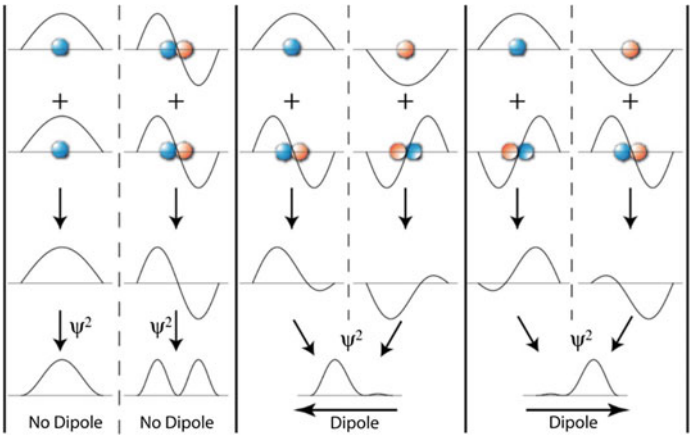

Fig. 2.15 Schematic representation of the linear combination of s and p orbitals. When two s or two p orbitals are mixed (*left*), a symmetric wave function results without a dipole moment. Mixing of an s and p orbital (*middle* and *right*) results in an asymmetric wave function with a dipole moment, the direction of which depends on the phase of the original wave functions. Reprinted with permission from Ref. [19]

molecule, depending on the intensity of the EM field) [20] the s and p orbitals are in the maximally mixed state ($c_1 = c_2$) (Fig. 2.15, middle and right panels). After this, the mixed state becomes more and more p-like, and after again $\sim 10^8$ oscillations the state has purely p-character ($c_1 = 0$ and $c_2 = 1$); i.e., the excitation is complete. However, the oscillations can continue, to go back to the maximally mixed state and finally the pure s-state again (which can be regarded as stimulated emission, see below). The complete cycle from 1S to 1P states and back to the 1S-state is called the Rabi-cycle, and is a fully coherent process. The coherent excitation from the ground state (1S) to the excited state (1P) takes half of the Rabi-cycle, which typically involves $\sim 10^8$ oscillations of the EM field (~ 10 ns). In practice, excitation (using an incoherent light source) in atoms or molecules is incoherent, which means that already after a few oscillations ($\ll$ps), the mixed state collapses (decoheres) to either the ground state or excited state.

What about an optical transition in a quantum dot? We will use the bottom-up (LCAO) approach to analyse the optical transitions and corresponding selection rules in a QD. In contrast to the case of a hydrogen atom, electrons in a QD (e.g. CdSe) occupy molecular orbitals (MOs). Therefore, we have to consider optical transitions between two MOs in a QD. The lowest energy interband transition is between the lowest hole level ($1S_h$) and lowest electron level ($1S_e$) (see Fig. 2.9 above). As illustrated in Fig. 2.16a, this involves a transition from a MO formed by the linear combination of Se 4p-orbitals to an MO formed by the linear combination of Cd 5s orbitals. Within each unit cell, mixing of these states yields a dipole moment (indicated by the small arrows in Fig. 2.16). Because the atomic orbitals are all in phase ($k = 0$), all the dipoles of the individual unit cells point in the same direction. Note that the length scale of the collection of individual dipoles (a few

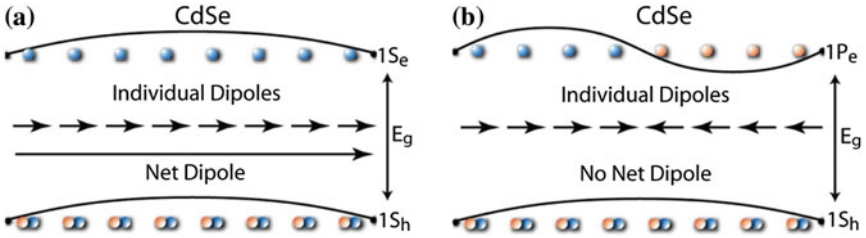

Fig. 2.16 Schematic representations of the individual dipoles and net dipole moments that arise when VB atomic orbitals are mixed with CB orbitals, for three different interband transitions in a CdSe QD. The direction of the individual dipole can be deduced from Fig. 2.15. When the individual dipoles add up to a net dipole, the optical transition is parity-allowed. If they cancel out (B), the transition is parity-forbidden. Reprinted with permission from Ref. [19]

nm) is much smaller than the wavelength of the excitation light (e.g., ~500 nm). Therefore, the individual dipoles all experience the same oscillating field of the incoming EM wave. As a result, the individual dipoles add up to a total net dipole moment of the two mixed MOs, making the $1S_h$-$1S_e$ optical transition parity-allowed. The same reasoning applies to any other interband transition involving electron and hole states of the same parity, such as $1P_h$-$1P_e$ or $1D_h$-$1D_e$, which are all parity-allowed.

The situation is different for interband transitions between electron and hole states of different parity, such as $1S_h$-$1P_e$ or $1S_h$-$1D_e$, which are strongly parity-forbidden and are therefore never observed in the absorption spectrum of QDs. In this case, the direction of the individual dipoles changes half-way of the QD (in real space) because of the phase-shift in the 5s-orbitals in the conduction band (Fig. 2.16b). The individual dipoles now cancel out yielding a net dipole moment of zero (i.e., no dipole). Therefore, the $1S_h$-$1P_e$ interband optical transition is not allowed. From these examples, we see that the selection rule for an optical interband transition in a quantum dot is $\Delta L = 0$ for the envelope-wave functions. The parity-selection rule is still obeyed in e.g. a CdSe QD, because the interband transition involves the transition from (a linear combination of) 4p orbitals to (a linear combination of) 5s orbitals, which have different parities (viz., 1 and 0, respectively, thus $\Delta\ell = 1$).

Optical transitions in semiconductor nanostructures can also take place between different electron levels or different hole levels (e.g., $1S_e$-$1P_e$). These transitions are referred to as intraband transitions. For an intraband transition, a similar treatment can be used to obtain the optical selection rules. These transitions involve MOs consisting of different combinations of the same type of atomic orbitals (e.g., Cd 5s for the electron levels of CdSe QDs). In this case $\Delta\ell = 0$ for the atomic orbitals and no dipoles will arise within the individual unit cells (Fig. 2.15). Therefore, the dipole has to arise from a change in parity of the envelope functions ($\Delta L = \pm 1$), which means that for example the $1S_e$ to $1P_e$ intraband transition is parity-allowed, whereas the $1S_e$-$1D_e$ transition is forbidden. The net dipole arises because half of the 5s-orbitals (that are in phase) add up, whereas the other half of the 5s-orbitals

cancel out because they have a different phase. This causes an asymmetric electron density distribution in the quantum dot when the $1S_e$ and $1P_e$ levels are mixed, giving rise to a net dipole, which makes the transition parity-allowed.

2.6 Exciton Relaxation and Recombination

Exciton Relaxation. After absorption of a photon by a semiconductor NC (e.g., a quantum dot or quantum rod) an exciton is created, with the electron and hole occupying one of the discrete energy levels available within the conduction and valence bands. If the energy of the photon is sufficiently large a hot exciton is formed, in which the electron and hole occupy excited states (i.e., states above the 1S level). In such a case, the electron and hole will quickly (<1 ps) relax to their ground states (the $1S_e1S_h$ exciton) by means of a cascade of intraband non-radiative relaxation steps, through which their excess energy is dissipated as heat [6]. These radiationless intraband transitions are not constrained by the optical selection rules mentioned above, and therefore can take place very fast, either by coupling with phonons (i.e., lattice or ligand vibrations) of suitable energy, or by Auger scattering processes through which the excess energy of one carrier (e.g., the electron) is transferred to the other (e.g., the hole) [6, 9].

Exciton Recombination. Once the exciton has reached its ground state (i.e., the lowest energy $1S_e1S_h$ exciton), further relaxation can only take place by electron-hole recombination, through which the excited electron returns to the valence band and the exciton energy is released either radiatively or non-radiatively (Fig. 2.17) [10].

Radiative recombination results in the emission of a photon. In the emission spectra of QDs (and quantum rods) the direct radiative recombination of the exciton is observed as a well-defined peak with energy close to the lowest energy absorption transition. The emission peak position presents thus the same size

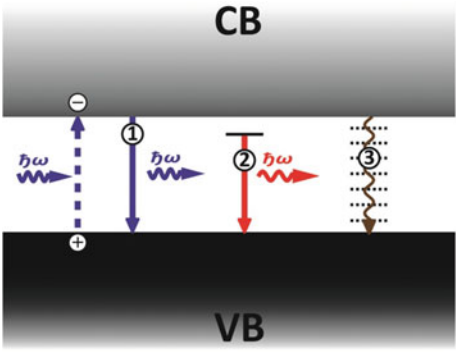

Fig. 2.17 Schematic illustration of exciton recombination pathways in semiconductors. *1* radiative recombination. *2* defect assisted radiative recombination. *3* non-radiative recombination. Reprinted with permission from Ref. [45]

dependence as the absorption transitions. The peak widthsare determined primarily by the size and shape distribution of the ensemble of NCs investigated (inhomogeneous line broadening).

It should be noted that the emission transition is just the reverse of the lowest energy absorption transition. Therefore, the selections rules discussed above for absorption also apply for emission. Emission of a photon results from the mixing of the excited state orbital with the ground state orbital. This mixing also has to be induced by an external oscillating field. Without this external "trigger", an electron can theoretically reside in the excited state for an infinite time. An incoming EM wave that is resonant with the transition can induce the mixing (just as in case of absorption) resulting in radiative recombination. This is called stimulated emission, which is used in lasers.

Usually, the fluorescence of dyes, phosphors, and quantum dots takes place without the stimulus of an external oscillating field. In that case one speaks of spontaneous emission, where mixing of the excited and ground state is induced by so-called vacuum modes (or vacuum fluctuations). The rate of spontaneous emission is not only dependent on the magnitude of the transition dipole moment $\mu_{i,f}$ between initial and final states (proportional to the oscillator strength), but also on the density of optical modes that can couple to the transition. The density of optical modes in vacuum is frequency-dependent and increases with frequency. The radiative decay rate Γ_{rad} for spontaneous emission in an ideal two-level atom system can be deduced from Fermi's Golden Rule [10, 21] and contains both the "atomic" part (transition dipole moment) and "field" part (density of optical modes):

$$\Gamma_{rad}(\omega) = \frac{\omega^3 n \left|\mu_{i,f}\right|^2}{3\pi\varepsilon_0 \hbar c^3} \tag{2.15}$$

where ω is the frequency of light, n is the refractive index, ε_0 is the permittivity of free space, and c is the speed of light. The rate of spontaneous emission can be modified by changing the density of optical modes, which can be achieved in photonic crystals [21].

Non-Radiative Exciton Recombination is usually mediated by defects or impurities, since the dissipation of the exciton energy by coupling to phonons (vibrations) requires the simultaneous creation of a large number of phonons (>50 for CdSe QDs), making it a very unlikely process. On the other hand, trapping (i.e., localization) of one of the charge carriers at a defect or surface state (trap states) is a much faster process, which can efficiently compete with radiative recombination, resulting in quenching of the exciton emission. Trapping leads to strong carrier localization, which decreases the overlap between the electron and hole wave functions, thereby making the radiative recombination less likely and facilitating non-radiative relaxation by coupling to local vibrations. Radiative recombination can still occur if the exciton is trapped in a defect or surface state, but this will lead to a broad emission band at lower energies than the band gap (trap or defect related

luminescence), which is typically very inefficient (photoluminescence quantum yields below 5 %) [2]. The surface is the most important source of trap states in NCs. As discussed in Chap. 1, surface atoms have fewer neighbours than their interior counterparts, and therefore possess unsatisfied chemical bonds (dangling bonds). These unshared atomic orbitals give rise to energy levels within the HOMO-LUMO gap of the semiconductor NC (surface states) [3]. Surface defects (e.g., vacancies) give rise to even more strongly localized energy states, which can very effectively trap the electron or hole. For these reasons, it is essential to control the surface quality of semiconductor NCs and eliminate dangling bonds, a process known as surface passivation. This can be achieved either by overgrowing a shell of a wider band gap semiconductor or by coating the surface with suitable organic ligands (Chap. 6) [2].

Exciton Energy Transfer. Another possible non-radiative recombination pathway is energy transfer between QDs. When two QDs are in close proximity, an exciton in one QD (donor) can be transferred to a neighbouring QD (acceptor) through a dipole-dipole interaction [22]. This process is called resonant exciton energy transfer (ET), and is an alternative pathway for an exciton in the donor QD to recombine. Exciton ET should not be confused with radiative ET, where a QD re-absorbs light that was emitted by another QD. Classically, resonant ET can be seen as an oscillator that induces a neighbouring oscillator (with the same resonance frequency) to oscillate as well. In the case of exciton ET, the oscillating dipole in a donor QD induces the oscillation of a dipole in the acceptor QD. Through this dipole-dipole interaction, the energy of the exciton in the donor QD can be transferred to the acceptor QD. The net result is a physical displacement of the exciton from the donor QD to the neighbouring acceptor QD (Fig. 2.18), which is not mediated by an external EM field. Exciton ET between neighbouring QDs can be studied by using (time-resolved) fluorescence spectroscopy, through which the emission decay functions of the donor and acceptor QDs are followed (see below).

Several conditions must be satisfied for exciton ET to occur [22]. First, the distance between the two QDs must be sufficiently small. Secondly, the (absorp-

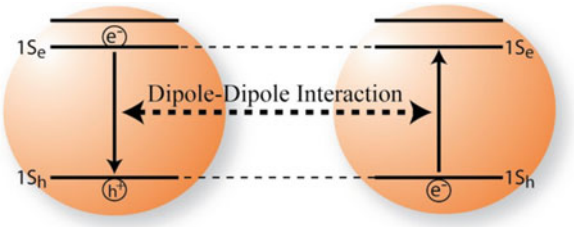

Fig. 2.18 Schematic representation of resonant exciton energy transfer from the donor QD (*left*) to the acceptor QD. The exciton in the donor QD recombines, inducing an exciton in the acceptor QD through a dipole-dipole interaction. Reprinted with permission from Ref. [19]

tion) transition of the acceptor QD must be resonant with the (emission) transition of the donor QD (i.e., there must be spectral overlap). This implies that the band gap of the acceptor QD has to be equal to or smaller than the band gap of the donor QD (ET to higher-lying levels in the acceptor QD is also possible). Finally, the orientation of the oscillating dipoles in both QDs also influences the transfer rate. Based on these conditions, the total energy transfer rate (Γ_{ET}) can be written as:

$$\Gamma_{ET} = \frac{2\pi}{\hbar}\frac{\mu_D^2\mu_A^2\kappa^2}{r^6 n^4}\Theta \tag{2.16}$$

as was first derived by Förster [23], where μ_D and μ_A denote the transition dipole moments of the donor and acceptor quantum dot respectively, r is the distance between the (centre of) the dipoles, and n is the refractive index of the surrounding medium. This r^{-6} distance dependence is only valid when r is larger than l, where l is the length of the dipole ($l = \mu/q$, q is the elemental charge). The orientational average of the dipoles κ in quantum dots is 2/3, assuming that the dipoles are randomly oriented. The spectral overlap is represented by Θ, which is defined as:

$$\Theta = \int E_D(\lambda) \cdot A_A(\lambda) d\lambda \tag{2.17}$$

where $E_D(\lambda)$ is the (normalized) emission spectrum of the donor QD, and $A_A(\lambda)$ represents the (normalized) absorption spectrum of the acceptor QD.

Exciton Lifetime. The lifetime of an exciton in a semiconductor QD can be determined by measuring the photoluminescence (PL) decay times τ, and can be described as

$$\tau = \frac{1}{W_{TOT}} = \frac{1}{W_{Rad}} + \frac{1}{W_{NRad}} + \frac{1}{W_{ET}} \tag{2.18}$$

where W_{TOT} is the total decay rate, W_{Rad} is the radiative decay rate, W_{NRad} the non-radiative decay rate, and W_{ET} the energy transfer rate. The latter can be neglected for a sufficiently diluted solution of QDs. If the excitons in a system decay only radiatively, the PL decay will follow a single exponential behaviour:

$$N(t) = N_0 e^{-t/\tau} \tag{2.19}$$

where t is the elapsed time after the excitation, τ is the exciton radiative lifetime and N_0 is the population of the emitting state at t = 0, which determines the PL intensity at t = 0. When non-radiative recombination and energy transfer contribute to the exciton relaxation, the PL decay will no longer follow a single exponential behaviour. The total decay rate will then contain different contributions and therefore the PL decay curves will show a multiexponential behaviour. The balance between the radiative and non-radiative decay rates will be reflected in the PL quantum yield (PL QY), which is the ratio between the number of emitted (n_{em}) and absorbed (n_{abs}) photons, as given by:

$$QY = \frac{n_{em}}{n_{abs}} = \frac{W_{Rad}}{W_{TOT}} \tag{2.20}$$

2.7 Excitons in Semiconductor Heteronanostructures

The ability to create novel optoelectronic properties can be extended further by using semiconductor heteronanocrystals (HNCs) instead of single composition NCs. HNCs are comprised of two (or more) different materials joined in the same particle by one or more heterointerfaces (see Chap. 6 for details) [2]. The energy level alignment between the materials that are combined at the heterojunction is of paramount importance. Depending on the energy offsets between the HOMO and the LUMO levels of the two adjoining materials, different charge carrier localization regimes will be observed after photoexcitation. Three limiting cases can be identified: type-I, type-$I^{1/2}$ (also referred to as *quasi*-type-II) and type-II (Fig. 2.19) [2]. In the **Type-I regime** the band gap of one semiconductor lies entirely within the gap of the other material. Therefore, after photoexcitation electron (e) and hole (h) are confined primarily in the same part of the HNC (the narrower gap material), resulting in a **direct exciton**. In the **Type-II regime** the staggered energy level alignment results in the spatial separation of the electron and hole on different sides of the heterojunction, leading to the formation of a **spatially indirect exciton**. In the **Type-$I^{1/2}$ regime** one carrier is confined in one of the components, while the other is delocalized over the whole HNC.

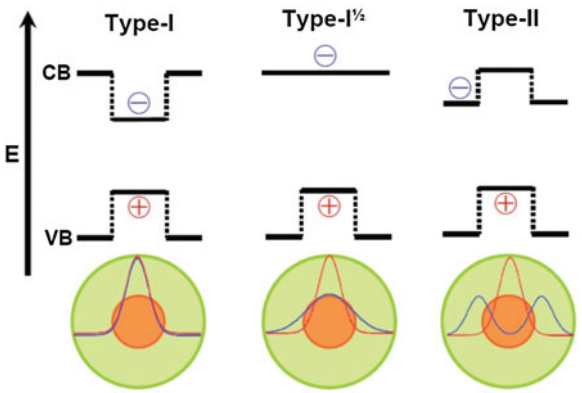

Fig. 2.19 Schematic representation of the three limiting charge carrier localization regimes incore/shell semiconductor HNCs. The conduction and valence band edges (i.e., the LUMO and HOMO energy levels) are indicated by CB and VB, respectively. The *plus* and *minus* signs represent the charge carriers (hole and electron, respectively). The electron and hole ground-state wave functions are schematically depicted in the *lower panel*. Reproduced by permission of the Royal Society of Chemistry from Ref. [2]

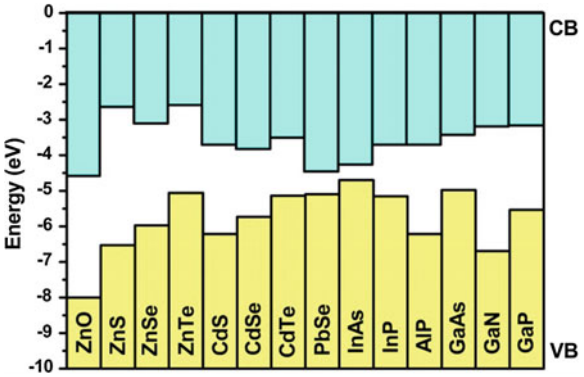

Fig. 2.20 The energy of the electronic band edges relative to the vacuum level of selected semiconductors (VB: valence band, CB: conduction band). The space between the *solid bars* gives the band gap. Bulk values are used, except for PbSe, which have been estimated from NC results. Reproduced by permission of the Royal Society of Chemistry from Ref. [2]

The band offsets in the bulk limit can be obtained from the band positions of the bulk semiconductors, which are known only for a limited number of materials (Fig. 2.20). The nanoscale dimensions of HNCs can be exploited to further expand the gamut of properties originating from a given combination of materials. Since the position and the density of energy states in quantum confined semiconductor nanostructures is governed by size and dimensionality (Sect. 2.4), the energy offsets in semiconductor HNCs can be tuned by a judicious control of the composition, size and shape of each component. This offers the possibility of directly controlling the *e-h* wave function overlap, thereby tailoring the material optoelectronic properties. This flexibility in engineering the properties of colloidal HNCs has important consequences for a number of technologies, and opens up interesting application possibilities: low-threshold lasers, light-emitting diodes, photovoltaic devices, fast optical switches, IR detectors, fast access memories, spintronic devices, and labels for biomedical imaging [2]. An overview of the properties associated with each type of HNC will be given below.

Type-I HNCs. Type-I concentric core/shell QDs (e.g., CdSe/ZnS, CdS/ZnS, InP/ZnS) are the most investigated colloidal semiconductor HNCs [2, 24]. This large interest stems from the fact that the exciton is confined to the core, and therefore is protected from interaction with the surface and the environment. Moreover, the exciton no longer probes dangling orbitals since the interface core atoms are bound to the shell atoms. Consequently, the photoluminescence quantum yields are high (≥50 %) and the stability against photodegradation is enhanced [24]. The properties of a direct exciton in a type-I HNC are dictated primarily by the narrow gap material. This means that upon the shell overgrowth the emission and absorption spectra of the core should remain unaffected, except for the appearance of new high energy absorption peaks associated with the shell material. However, the energy offsets between the two materials are finite and therefore the exciton wave function partially

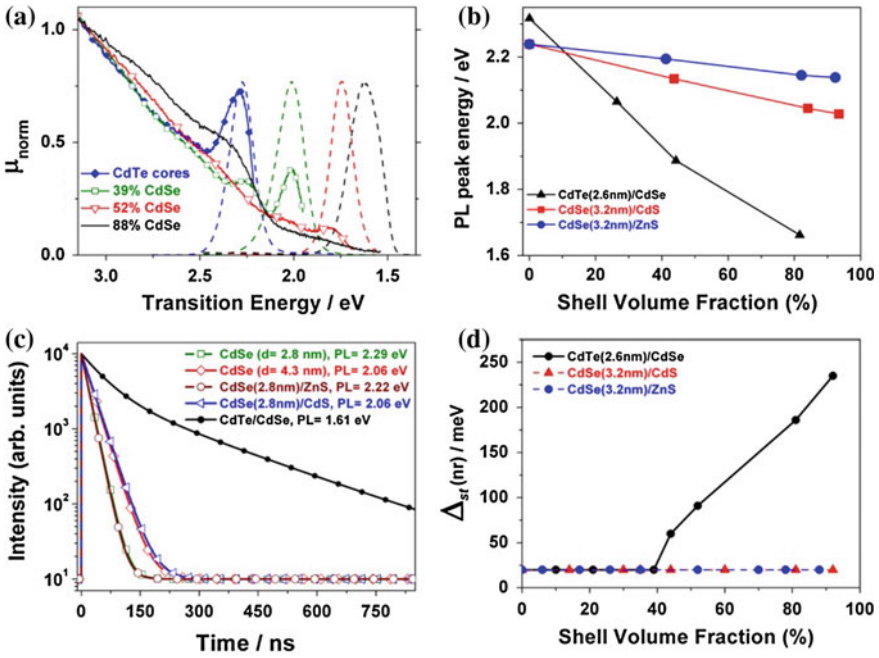

Fig. 2.21 **a** Photoluminescence (PL, *dashed lines*) and PL excitation (PLE, *solid lines*) spectra of colloidal CdTe/CdSe HNCs with a 2.6 nm CdTe core and increasing CdSe volume fraction (39–88 %). PL spectra are normalized at the peak. PLE spectra are normalized to 1 at 3.1 eV. The symbol μ_{norm} gives the normalized absorption cross section per Cd(Te, Se) ion pair unit. The evolution from Type-$I^{1/2}$ (39 % CdSe) to Type-II (88 % CdSe) localization regimes is clearly observed. **b** PL peak position of colloidal core/shell HNCs of different compositions as a function of the shell volume fraction. The diameter of the core NC is indicated between brackets. The compositions were chosen as representative examples of different carrier localization regimes (viz., Type-I: CdSe/ZnS; Type-$I^{1/2}$: CdSe/CdS, CdTe/thin shell CdSe; Type-II: CdTe/thick shell CdSe). **c** PL decay curves of CdSe QDs and three different core/shell HNCs. To facilitate comparison, only the initial 850 ns of the decay curve of CdTe/CdSe HNCs are shown. (d) Non-resonant Stokes shift ($\Delta_{ST}(nr)$) as a function of the shell volume fraction for different core/shell HNCs (viz., Type-I: CdSe/ZnS; Type-$I^{1/2}$: CdSe/CdS, CdTe/thin shell CdSe; Type-II: CdTe/thick shell CdSe). Reproduced by permission of the Royal Society of Chemistry from Ref. [2]

extends into the shell (this is usually referred to as "exciton leakage"). Consequently, a small (i.e., ≤50 meV) redshift is observed for all exciton transitions, both in emission and absorption (see, e.g., CdSe/ZnS) [2] (Fig. 2.21). The redshift is proportional to the reduction in exciton confinement and therefore is larger for smaller offsets. The energy difference between the maxima of the emission band and of the lowest energy absorption band (the so-called "non-resonant Stokes shift") is not affected, and remains ≤20 meV [2] (Fig. 2.21). The exciton radiative lifetime also remains essentially the same (Fig. 2.21), although the observed photoluminescence decay time will typically be longer, due to the reduction of the non-radiative recombination rates, since the exciton no longer probes the surface [2].

In practice, the exciton leakage into the shell implies that thick shells (and larger offsets) are needed to effectively prevent the exciton from probing the surface. However, interfacial strain induced by lattice mismatch between the core and shell materials becomes a serious issue for thick shells, and may severely limit the maximum thickness [2, 24]. For example, from the viewpoint of energy offsets, ZnS is the best shell material for CdSe based core/shell QDs, but the large lattice mismatch (12 %) makes it difficult to grow shells thicker than 2–3 monolayers (MLs). ZnSe and CdS give smaller lattice mismatches (6.3 and 3.9 %, respectively), but also smaller energy offsets. The solution is to grow multiple shells of different compositions around a central core, so that the energy offsets progressively increase towards the surface, but with small lattice mismatches between subsequent shells (e.g., CdSe/CdS/(Cd,Zn)S/ZnS core/multishell QDs [24]). Shell growth strategies are discussed in detail in Chap. 6.

Type-I$^{1/2}$ HNCs. The most investigated Type-I$^{1/2}$ HNC composition is CdSe/CdS, although it is usually referred to as a "Type-I" core/shell QD. However, it is well established that the energy offset for the electron is too small to confine it to the CdSe core, and, consequently, the electron wave function may delocalize over the entire HNC, while the hole remains confined in the CdSe core [25]. Other examples of Type-I$^{1/2}$ HNCs are ZnSe/CdSe core/shell QDs (*e* localized in CdSe shell, *h* delocalized over the HNC) [26], CdTe/CdSe core/thin shell HNCs (*h* is confined to core, *e* is delocalized) [27], and PbSe/CdSe core/thin shell QDs (*h* in core, *e* delocalized) [28]. The redshift observed in the PL and absorption spectra upon shell overgrowth (viz., up to 200–400 meV, depending on the core diameter) is much larger than that observed for Type-I HNCs, due to the loss in confinement energy of the carrier that is delocalized over the entire volume of the HNC [27] (Fig. 2.21). The Stokes shift, however, remains small (≤20 meV) and is comparable to that observed for single component NCs and Type-I HNCs [27] (Fig. 2.21). The absorption peaks remain distinct and well-defined, in contrast to the behaviour observed for Type-II HNCs (see below) [25, 27]. The delocalization of one of the carriers reduces the *e*-*h* overlap, leading to longer exciton radiative lifetimes (Fig. 2.21). The PL QYs can be as high as 80 % [2, 24–27].

Type-II HNCs. The properties of the spatially indirect exciton can be manipulated by choosing suitable combinations of semiconductors [2, 24–27]. It should be noted that complete spatial separation occurs only for the physically unrealistic case of infinite offsets. For finite offsets the wave functions of the carriers partially extend across the heterojunction, leading to non-zero *e*-*h* overlap. The indirect nature of the exciton leads to longer radiative lifetimes [2, 26, 27], increased exciton polarisability [26], and emission at lower energies than those of the band-gaps of both materials [2], thus allowing access to wavelengths that would otherwise not be available. It has also been reported to make single exciton lasing possible [29]. Further, the rates for hot carrier relaxation [30] and spin flip [31] decrease, as a consequence of the (partial) spatial separation of the photoexcited charge carriers. The potential of colloidal type-II HNCs has attracted increasing attention over the last few years, leading to the investigation of HNCs of various compositions (viz.,

CdTe-CdSe, CdSe-ZnTe, ZnTe-ZnSe, and ZnSe-CdS) and shapes (viz., core/shell NCs, rods and multipods, and dumbbells) [2].

The redshift observed in the PL and absorption spectra upon shell overgrowth is very large (e.g., up to 0.5–0.8 eV for CdTe/CdSe HNCs, depending on the CdTe core diameter) [2, 27, 32] (Fig. 2.21), making Type-II HNCs promising near-IR emitters. It should be noted that thick shells (>1 nm) are needed to achieve the Type-II localization regime [2, 26, 27]. Thin shells yield Type-$I^{1/2}$ HNCs. The onset of the Type-II regime is characterized by the loss of structure of the lowest energy absorption band (i.e., a featureless absorption tail develops), accompanied by a simultaneous increase in the Stokes shift (up to 200–300 meV) and bandwidths [2, 27] (Fig. 2.21). Also, the absorption cross section at emission energies decreases dramatically and the exciton radiative lifetime becomes much longer (0.2–2 μs, 1–2 orders of magnitude longer than that of a direct exciton in the same materials) [2, 27] (Fig. 2.21).

2.8 Size Effects on the Electronic Structure of Nanocrystals: Semiconductors in Comparison to Metals

As discussed in Chap. 1, the optical properties ofmetal NCs may also be strongly size dependent. This is particularly evident for gold, as clearly illustrated in Fig. 1.1 (Chap. 1), 2.22, and 3.4 (Chap. 3). Nevertheless, the wide range of colours observed for suspensions of gold NCs cannot be ascribed to quantum confinement effects [3]. Since the highest energy band in metals is partially occupied, the Fermi level lies close to the centre of the band. As shown in Fig. 2.12 above, the density of states (and the energy level spacing) near the centre of the bands is only affected when the

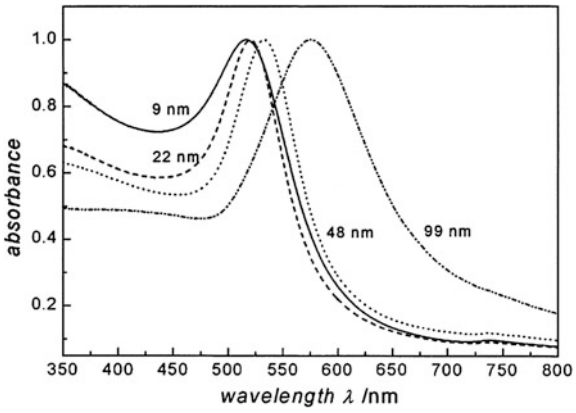

Fig. 2.22 Absorption spectra of colloidal suspensions of gold NCs in water (diameters: 9, 22, 48 and 99 nm). The spectra are normalized at their maxima (517, 521, 533, and 575 nm, respectively). Reprinted with permission from [47], Copyright (1999) American Chemical Society

NC size approaches the cluster size regime. As a result, the electrical and optical properties of metal NCs will be affected by quantum confinement effects only when the dimensions of the NC become comparable to or smaller than the Fermi wavelength in the metal (<2 nm for all metals). To understand the size dependence of the optical properties of metal NCs and nanostructures larger than 2 nm, one has to consider the impact of spatial confinement on the plasmon resonances of metals. This will be addressed in detail in Chap. 3.

2.9 Applications of Semiconductor Nanoparticles

The unique size- and shape-dependent optoelectronic properties of semiconductor nanostructures can be exploited in many different applications. The field is currently developing at an astounding pace, and it is therefore not possible to present here a comprehensive overview of all the current and potential applications of semiconductor NCs. We will instead limit ourselves to sketch the state-of-the-art on a number of applications, highlighting the specific properties of semiconductor nanoparticles that make them attractive for a particular application. This section should be regarded as a blurred snapshot of a fast-moving object and, as such, bound to change soon, as far as the details are concerned.

Epitaxial and colloidal nanostructures. As discussed above (Sect. 2.4.1.1), semiconductor nanostructures (NSs: QDs, Quantum Wells, Quantum Wires) can be classified in "Colloidal" and "Epitaxial" depending on their synthesis method. Epitaxial NSs are prepared by relatively high-energy input vapour phase methods, which require ultrahigh-vacuum environments and extremely high purity chemical precursors. In contrast, colloidal NSs are prepared by solution based approaches ('wet' chemistry) that are relatively inexpensive, facile, scalable, and less sensitive to impurities (see Chap. 6 for details). The size and shape control offered by colloidal techniques are unmatched by epitaxial techniques, which typically yield NSs in the weak quantum confinement regime, owing to their relatively large lateral dimensions (>10 nm) [33]. Moreover, epitaxial NSs are substrate-bound, which makes their integration into electronic devices easier, but severely limits their applicability. In contrast, colloidal NSs can easily be subjected to post-synthesis procedures, such as size-selection and surface functionalization, and can be solution-processed into thin-film assemblies and composites (see Chaps. 1 and 6 for details).

Lasers. The density of states near the band edge increases in NSs as a result of quantum confinement (Fig. 2.11 above). This effect becomes more and more pronounced as the dimensionality of the active layer is further reduced, so that injected charge carriers concentrate in an increasingly narrower energy range near the band edge. As a result, the maximum material gain increases and the temperature dependence of laser parameters is reduced [34]. Moreover, quantum confinement effects considerably extend the wavelength tunability. The superior performance of lasers based on semiconductor nanostructures has led to a number commercial

devices based on dense ensembles (10^{10} cm^{-2}) of epitaxial QDs as the active layer. These lasers show excellent thermal, temporal, and spatial stabilities, and large radiation resistance [34]. Low-threshold lasing has also been observed in colloidal QDs [35], but devices have yet to be demonstrated, although much progress has been made in recent years [36].

Optical amplifiers. Devices based on dense ensembles of epitaxial QDs are also effective as low-cost optical amplifiers and signal regenerators in all-optical networks, and promise superior performance in comparison with devices based on quantum wells and bulk media owing to its inherently faster gain recovery and broader bandwidth [34].

Single-photon source. Single-QD devices are compact and easy to integrate into existing technology, making them attractive for applications in quantum information processing, where they can fulfil the roles of both single-photon emitters and quantum memory by storing the polarization state of a single photon [34].

Light emitting devices. The bright, spectrally narrow, and tunable luminescence of colloidal QDs makes them outstanding sources of saturated emission colours for light emitting devices (LEDs) and displays, since these properties allow for wider colour gamut, larger colour rendering index, and high luminous efficiency [33, 36]. Moreover, colloidal QDs (cQDs) are stable and solution processable, enabling the use of low-cost deposition techniques such as spin-coating, inkjet printing, or microcontact printing [33]. They are therefore promising materials for light-weight flexible displays, offering an alternative for Organic LED's (OLEDs). The performance of electrically driven cQD-LEDs has improved dramatically over the last decade, reaching in 2013 peak external quantum efficiencies (EQE) of 18 % and brightness values of 3×10^4 cd m^{-2} [33]. At the time of writing, these values were still below those of OLEDs (viz., 25 % and 8×10^4 cd m^{-2}), but were increasing steadily, indicating that cQD-LEDs may still become a serious competitor for OLEDs. Nevertheless, there are still many challenges to be addressed before cQD-LEDs become an accepted and viable technology (viz., lifetimes are only 100–1,000 h, operating mechanisms are poorly understood, most efficient devices are based on heavy metal based QDs, such as CdSe) [33, 36].

Biomedical imaging applications. One of the most rapidly developing applications of nanotechnology in biomedical research is the use of colloidal nanoparticles as contrast agents and luminescent labels for (in vivo) biomedical imaging [37]. For example, iron oxide NCs can be used as contrast agents for MRI (Magnetic Resonance Imaging), and gold NCs are suitable contrast agents for Computed Tomography (CT). Colloidal QDs exhibit a number of exceptional optical properties compared to fluorescent dyes, which greatly enhances their potential as labels in fluorescence based bio-imaging. The most significant properties include: (1) broad and strong absorption (2) narrow and symmetric photoluminescence spectra with high quantum yields, and (3) high resistance to photobleaching and chemical degradation. In addition, the surface of colloidal QDs can be functionalized with molecules that improve pharmacokinetics and bio-applicability, or target specific biomolecules. Interestingly, new developments allow the creation of QD-based nanoparticles that can be detected with several imaging techniques, so-called multimodal QDs.

Photovoltaic applications. The high absorption cross-section of colloidal QDs (cQDs) at tunable wavelengths makes them attractive for thin film solar cells, since this characteristic allows for optimal harvesting of the solar spectrum, thereby opening a promising route to high efficiency [36, 38–41]. Moreover, just like for cQD-LEDs, solution processability is a great asset, offering the prospect of low fabrication costs and easy upscaling. The exciton dissociation in cQDs is also relatively easy and can be boosted by using HNC architectures. These properties have led to the utilization of cQDs in a variety of different solar cell concepts [38, 40, 41]. The present record efficiencies, however, are still below 6 %, mostly due to low charge carrier mobility through the cQD-film and contact losses. cQDs have also been used as sensitizers in Gratzel-type solar cells (cQD sensitized solar cell, cQD-SSC), leading to 5–6 % power conversion efficiency [39]. This value is significantly lower than that achieved by dye sensitized solar cells (viz., 12 %). The losses in cQD-SSCs are mostly due to inefficient interfacial electron transfer processes and parasitic processes such as photocorrosion of the cQD [39]. cQDs can also be used as luminophores in luminescent solar concentrators (LSCs). These devices consist of a plastic plate containing a luminophore (QD or dye) that absorbs the sun light and reemits the energy at longer wavelengths. The emitted light is trapped by total internal reflection in the plate and waveguided towards the narrow facets of the LSC plate where a solar cell is mounted. The efficiency of these devices is as yet rather low, due to several loss mechanisms, of which reabsorption of the emitted light by the fluorophore itself is of high importance. The use of Type-II HNCs as luminophores in LSCs has been recently shown to greatly minimize reabsorption losses [42]. At present, there is a worldwide research effort addressing the loss mechanisms in cQD solar cells, cQD-SSCs and cQD-LSCs. It may therefore be expected that in time cQD-based solar cells will fulfil their promise of providing abundant and cheap energy.

Photocatalysis. Solar energy conversion with colloidal NSs can also be achieved through photocatalysis. In this case, the photogenerated charge carriers are used to promote redox chemical reactions, such as Hydrogen generation from water or synthesis of methanol from water and CO_2 [43]. Colloidal anisotropic Type-II heteronanocrystals in which two semiconductors and a metal are combined (e.g., ZnSe/CdS dot core/rod shell heteronanorods coupled to a Pt NC tip) have been shown to be particularly efficient in the photocatalytic generation of Hydrogen, since very fast charge separation occurs in these systems [44]. Nevertheless, the development of these systems into commercially viable photocatalystsis still hampered by an incomplete understanding of the complex chain of coupled processes that takes place between light absorption by the semiconductor and the actual splitting or formation of chemical bonds. Moreover, strategies to hinder parasitic processes (e.g., photocorrosion) must still be developed.

2.10 Outlook

This chapter has summarized the current understanding of quantum confinement effects and nanoscale excitons in semiconductor nanostructures, with particular emphasis on quantum dots. We limited ourselves to the fundamental concepts. For a more detailed and comprehensive analysis, the reader is referred to the literature. There are still some aspects that are currently not fully understood, and are the subject of on-going research. For instance, a comprehensive understanding of the exciton-phonon coupling in semiconductor nanostructures has yet to emerge. The relaxation dynamics of spatially confined excitons is also the subject of extensive investigation. Another interesting aspect that is attracting increasing attention in recent years is the investigation of colloidal semiconductor hetero-nanocrystals, which allow for a remarkable degree of control over the properties of nanoscale excitons. Electronic coupling and transport phenomena in quantum dot superlattices is also currently under intense scrutiny. These worldwide research efforts will undoubtedly deepen our understanding and provide a wealth of new insights that will pave the way to a number of as yet unforeseen applications.

2.11 Exercises

1. The absorption and emission spectra of CdTe nanocrystals ranging in diameter from 2.9 to 14.8 nm are presented in Fig. 2.23. CdTe is a direct band gap semiconductor material with a bulk band gap of 1.56 eV and an exciton Bohr radius of 7.3 nm.
   (a) How do you explain the size dependent spectral shift observed in the optical spectra?
   (b) Explain the spectral changes observed in the absorption spectra of the nanocrystals as their size is reduced.
   (c) What emission wavelength do you expect for CdTe nanocrystals with 3.7 nm in diameter?
   (d) How large is the band gap of a 30 nm diameter CdTe nanocrystal?
   (e) Do you expect that optical spectroscopy would remain an useful technique to follow the growth of CdTe nanocrystals in the 20–40 nm diameter range? Justify your answer.
2. When a quartz (SiO_2) crystal is pulverized to 5 μm particles a white powder is obtained. Do you expect any colour change if the particle size is further decreased to 10 nm? Do you expect any size effect on the properties of 10 nm SiO_2 nanocrystals? (i.e. would they differ in any way from those of the micrometer sized particles shown below?). The band-gap of SiO_2 is 7 eV (exciton Bohr radius 0.5 nm).

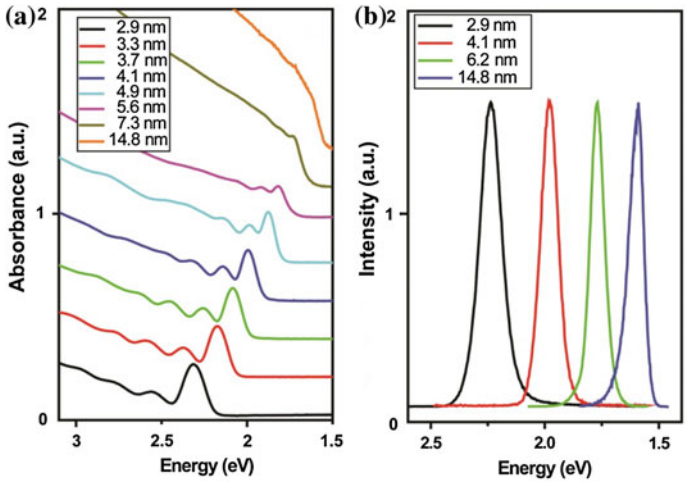

Fig. 2.23 Absorption and photoluminescence spectra of colloidal CdTe nanocrystals

3. The abstract of a paper published in a well-known scientific journal is reproduced below:
   Abstract: *Pronounced structure in X-ray excited luminescence* (*XEL*) *has been observed in dilute Tb-doped* Y_2O_3 (Y_2O_3*:Tb*) *nanocrystals. This effect affords a means to assess different energy transfer mechanisms in the nanocrystals and also an opportunity for novel device applications. Sharp jumps and oscillations are found in the XEL output with the incident X-ray energy around the absorption edges of Y and Tb. When compared with a bulk* Y_2O_3*:Tb sample, these effects are attributed to some unique electronic and optical properties of doped nanocrystals related to quantum confinement of charge carriers, and the main features can be explained by a proposed model of multichannel energy transfer. Extended X-ray absorption fine structure techniques have also been employed to study the effect of size variation and chemical doping on the local structures in* Y_2O_3 *and* Y_2O_3*:Tb nanocrystals. The local environment surrounding Y and Tb in the nanocrystals is compared with that in the respective bulk material. The results indicate that Tb impurity atoms substitute for Y sites in bulk* Y_2O_3*, while doping in the nanocrystals is complicated by the large fraction of surface atoms and local disorder.* (*C*) *1998 American Institute of Physics.*

Basically, the authors state that they observed a new phenomenon in Y_2O_3:Tb nanocrystals (viz. "*pronounced structure in x-ray excited luminescence*") and explain it by quantum confinement effects (see underlined section above).

The nanocrystals investigated range from 2.5 to 5.5 nm in diameter. The bulk band-gap of Y_2O_3 is 5.5 eV (exciton Bohr radius: 0.6 nm). Do you agree or disagree with the authors? Justify your answer.

References

1. Brynjolfsson, E., McAfee, A.: Winning the race with ever-smarter machines. MIT Sloan Manage. Rev. **53**, 53 (2012)
2. Donega, C.D.M.: Synthesis and properties of colloidal heteronanocrystals. Chem. Soc. Rev. **40**, 1512–1546 (2011)
3. Alivisatos, A.P.: Perspectives on the physical chemistry of semiconductor nanocrystals. J. Phys. Chem. **100**, 13226–13239 (1996)
4. Rossetti, R., Brus, L.: Electron-hole recombination emission as a probe of surface-chemistry in aqueous CdS colloids. J. Phys. Chem. **86**, 4470–4472 (1982)
5. Gaponenko, S.V.: Introduction to Nanophotonics. Cambridge University Press, Cambridge (2010)
6. Klimov, V.I.: Spectral and dynamical properties of multiexcitons in semiconductor nanocrystals. Annu. Rev. Phys. Chem. **58**, 635–673 (2007)
7. Efros, A.L., Rosen, M.: The electronic structure of semiconductor nanocrystals. Annu. Rev. Mater. Sci. **30**, 475–521 (2000)
8. Lo, S.S., Mirkovic, T., Chuang, C., Burda, C., Scholes, G.D.: Emergent properties resulting from Type-II band alignment in semiconductor nanoheterostructures. Adv. Mater. **23**, 180–197 (2011)
9. Kambhampati, P.: Hot exciton relaxation dynamics in semiconductor quantum dots: radiationless transitions on the nanoscale. J. Phys. Chem. C **115**, 22089–22109 (2011)
10. Henderson, B., Imbusch, G.F.: Optical Spectroscopy of Inorganic Solids. Clarendon Press, Oxford (1989)
11. Bhattacharya, P., Ghosh, S., Stiff-Roberts, A.D.: Quantum dot opto-electronic devices. Annu. Rev. Mater. Res. **34**, 1–40 (2004)
12. Elzerman, J.M., Hanson, R., van Beveren, L.H.W., Witkamp, B., Vandersypen, L.M.K., Kouwenhoven, L.P.: Single-shot read-out of an individual electron spin in a quantum dot. Nature **430**, 431–435 (2004)
13. Tian, B., Kempa, T.J., Lieber, C.M.: Single nanowire photovoltaics. Chem. Soc. Rev. **38**, 16–24 (2009)
14. Hochbaun, A.I., Yang, P.: Semiconductor nanowires for energy conversion. Chem. Rev. **110**, 527–546 (2010)
15. Hocevar, M., Immink, G., Verheijen, M., Akopian, N., Zwiller, V., Kouwenhoven, L., Bakkers, E.: Growth and optical properties of axial hybrid III-V/silicon nanowires. Nature Commun. **3**, 1266 (2012)
16. Bawendi, M.G., Steigerwald, M.L., Brus, L.E.: The quantum-mechanics of larger semiconductor clusters (quantum dots). Annu. Rev. Phys. Chem. **41**, 477–496 (1990)
17. Delerue, C., Lannoo, M.: Nanostructures: Theory and Modelling. Springer, Berlin (2004)
18. An, J.M., Franceschetti, A., Dudiy, S.V., Zunger, A.: The peculiar electronic structure of PbSe quantum dots. Nano Lett. **6**, 2728–2735 (2006)
19. Koole, R.: Fundamentals and applications of semiconductor nanocrystals Ph.D. Thesis, Utrecht University, Utrecht (2008)
20. Wright, J.C.: Chemistry 623 Notes-Experimental Spectroscopy. Dept. of Chemistry, University of Wisconsin, pp. 47–69 (1990)
21. Lodahl, P., van Driel, A.F., Nikolaev, I.S., Irman, A., Overgaag, K., Vanmaekelbergh, D., Vos, W.L.: Controlling the dynamics of spontaneous emission from quantum dots by photonic crystals. Nature **430**, 654–657 (2004)
22. Rogach, A.L., Klar, T.A., Lupton, J.M., Meijerink, A., Feldmann, J.: Energy transfer with semiconductor nanocrystals. J. Mater. Chem. **19**, 1208–1221 (2009)
23. Förster, T.: Energiewanderung und Fluoreszenz. Naturwissenshaften **33**, 166–175 (1946)
24. Reiss, P., Protière, M., Li, L.: Core/shell semiconductor nanocrystals. Small **5**, 154–168 (2009)
25. Pandey, A., Guyot-Sionnest, P.: Intraband spectroscopy and band offsets of colloidal II-VI core/shell structures. J. Chem. Phys. **127**, 104710 (2007)

26. Ivanov, S.A., Piryatinski, A., Nanda, J., Tretiak, S., Zavadil, K.R., Wallace, W.O., Werder, D., Klimov, V.I.: Type-II core/shell CdS/ZnSe nanocrystals: Synthesis, electronic structures, and spectroscopic properties. J. Am. Chem. Soc. **129**, 11708–11719 (2007)
27. Donegá, C.D.M.: Formation of nanoscale spatially indirect excitons: evolution of the type-II optical character of CdTe/CdSe heteronanocrystals. Phys. Rev. B **81**, 165303 (2010)
28. Grodzińska, D., Evers, W.H., Dorland, R., van Rijssel, J., van Huis, M.A., Meijerink, A., de Mello Donegá, C., Vanmaekelbergh, D.: Two-Fold emission from the S-Shell of PbSe/CdSe core/shell quantum dots. Small **7**, 3493–3501 (2011)
29. Klimov, V.I., Ivanov, S.A., Nanda, J., Achermann, M., Bezel, I., McGuire, J.A., Piryatinski, A.: Single-exciton optical gain in semiconductor nanocrystals. Nature **447**, 441–446 (2007)
30. Pandey, A., Guyot-Sionnest, P.: Slow electron cooling in colloidal quantum dots. Science **322**, 929–932 (2008)
31. He, J., Lo, S.S., Kim, J., Scholes, G.D.: Control of exciton spin relaxation by electron-hole decoupling in type-II nanocrystal heterostructures. Nano Lett. **8**, 4007–4013 (2008)
32. Kim, S., Fisher, B., Eisler, H., Bawendi, M.: Type-II quantum dots: CdTe/CdSe(core/shell) and CdSe/ZnTe(core/shell) heterostructures. J. Am. Chem. Soc. **125**, 11466–11467 (2003)
33. Shirasaki, Y., Supran, G.J., Bawendi, M.G., Bulovic, V.: Emergence of colloidal quantum-dot light-emitting technologies. Nat. Photon. **7**, 13–23 (2013)
34. Bimberg, D., Pohl, U.W.: Quantum dots: promises and accomplishments. Mater. Today **14**, 388–397 (2011)
35. Garcıa-Santamarıa, F., Chen, Y., Vela, J., Schaller, R.D., Hollingsworth, J.A., Klimov, V.I.: Suppressed Auger recombination in "giant" nanocrystals boosts optical gain performance. Nano Lett. **9**, 3482–3488 (2009)
36. Konstantatos, G., Sargent, E.H.: Colloidal quantum dot optoelectronics and photovoltaics. Cambridge University Press, Cambridge (2013)
37. Doane, T.L., Burda, C.: The unique role of nanoparticles in nanomedicine: Imaging, drug delivery and therapy. Chem. Soc. Rev. **41**, 2885–2911 (2012)
38. Lunt, R.R., Osedach, T.P., Brown, P.R., Rowehl, J.A., Bulovic, V.: Practical roadmap and limits to nanostructured photovoltaics. Adv. Mater. **23**, 5712–5727 (2011)
39. Kamat, P.V.: Boosting the efficiency of quantum dot sensitized solar cells through modulation of interfacial charge transfer. Acc. Chem. Res. **45**, 1906–1915 (2012)
40. Kramer, I.J., Sargent, E.H.: Colloidal quantum dot photovoltaics: a path forward. ACS Nano **5**, 8506–8514 (2011)
41. Nozik, A.J., Conibeer, G., Beard, M.C.: Advanced concepts in photovoltaics. Royal Society of Chemistry, Oxford (2014)
42. Krumer, Z., Pera, S.J., van Dijk-Moes, R.J.A., Zhao, Y., de Brouwer, A.F.P., Groeneveld, E., van Sark, W.G.J.H.M., Schropp, R. E.I., Donega, C.D.M.: Tackling self-absorption in luminescent solar concentrators with type-II colloidal quantum dots. Sol. Energy Mater. Sol. Cells **111**, 57–65 (2013)
43. Fan, W., Zhang, Q., Wang, Y.: Semiconductor-based nanocomposites for photocatalytic H_2 production and CO_2 conversion. Phys. Chem. Chem. Phys. **15**, 2632–2649 (2013)
44. O'Connor, T., Panov, M.S., Mereshchenko, A., Tarnovsky, A.N., Lorek, R., Perera, D., Diederich, G., Lambright, S., Moroz, P., Zamkov, M.: The effect of the charge-separating interface on exciton dynamics in photocatalytic colloidal heteronanocrystals. ACS Nano **6**, 8156–8165 (2012)
45. Groeneveld, E.: Synthesis and optical spectroscopy of (hetero)-nanocrystals. Ph.D. Thesis, Utrecht University, Utrecht (2012)
46. Koole, R., Allan, G., Delerue, C., Meijerink, A., Vanmaekelbergh, D., Houtepen, A.J.: Optical Investigation of Quantum Confinement in PbSe Nanocrystals at Different Points in the Brillouin Zone. Small **4**, 127–133 (2008)
47. Link, S., El-Sayed, M.A.: Size and temperature dependence of the plasmon absorption of colloidal gold nanoparticles. J. Phys. Chem. B **103**, 4212–4217 (1999)

Chapter 3
Metal Nanoparticles for Microscopy and Spectroscopy

Peter Zijlstra, Michel Orrit and A. Femius Koenderink

Abstract Metal nanoparticles interact strongly with light due to a resonant response of their free electrons. These 'plasmon' resonances appear as very strong extinction and scattering for particular wavelengths, and result in high enhancements of the local field compared to the incident electric field. In this chapter we introduce the reader to the optical properties of single plasmon particles as well as finite clusters and periodic lattices, and discuss several applications.

3.1 Introduction

In the last two decades, nanostructured metals in the form of structured thin films and nanoparticles (NPs) have attracted attention from physicists and chemists alike as interesting materials for optics and spectroscopy. Metals do not intuitively stand out as particularly interesting materials for optics. Indeed, textbook physics tells that a perfect conductor simply expels any electric field, so that the only function of a metal should be to block light and act as a perfect reflector. Microscopically, this shielding of the bulk from any penetrating field is attributable to free electrons that provide a surface charge density on the metal surface to counteract any incident field.

P. Zijlstra (✉)
Faculty of Applied Physics, Eindhoven University of Technology, Den Dolech 2, 5612 AZ Eindhoven, The Netherlands
e-mail: p.zijlstra@tue.nl

M. Orrit
Leiden Institute of Physics, Huygens-Kamerlingh Onnes Laboratory, Leiden University, Postbus 9504, 2300 RA Leiden, The Netherlands

A. Femius Koenderink
Center for Nanophotonics, FOM Institute AMOLF, Science Park 104, 1098 XG Amsterdam, The Netherlands

C. de Mello Donegá (ed.), *Nanoparticles*,
DOI 10.1007/978-3-662-44823-6_3

This interpretation holds over a wide range of frequencies, from DC to well above the GHz range of current electronics. However, the free electrons intrinsically have a finite response time, above which they will not be fast enough to shield the bulk metal from incident fields. For typical metals the inverse of this response time, which is known as the 'plasma frequency', is around 500–1,000 THz. These frequencies correspond to electromagnetic waves in the visible and UV range.

Above the plasma frequency, a metal is not strongly reflective, but changes into a transparent material because the electrons cannot respond fast enough to screen the field. In most metals, the plasma frequency is in the ultraviolet, making them reflective in the visible range. Some metals, such as copper and gold, have inter-band transitions in the visible range, whereby specific wavelengths are absorbed yielding their distinct color. In the regime around and just below the plasma frequency metals are 'plasmonic'. As a consequence, small metal objects will support resonances of the free electron gas that strongly interact with light. For metal surfaces and metal sheets of submicron thickness, the free electron gas gives rise to resonances referred to as 'surface plasmon polaritons': surface waves at optical frequencies that are part photon (electromagnetic energy stored in electric field just above the surface) and part surface charge density wave. In this chapter we focus on a different type of plasmon resonance, namely localized plasmon resonances in nanoscale metal particles.

Gustav Mie [1] was the first to discuss in detail the peculiar optical properties of solutions of colloidal gold NPs, which have a ruby appearance. This color is tunable by particle size and shape (see Fig. 1.1 in Chap. 1), and is due to the resonant response of the 10^3–10^4 free electrons that a metal NP typically contains. Due to this resonant response, metal NPs are among the most strongly scattering solid state objects (when the scattering strength is normalized to the objects geometric cross section). In this Chapter we explain how this strong scattering comes about through the metal's dielectric function (Sect. 3.2) and how it can be tuned and optimized (Sect. 3.3). Owing to the strong electromagnetic fields that the ultra-tightly confined resonances support, the plasmon response is useful for a variety of spectroscopic applications ranging from sensing and label-free microscopy to enhancement of photophysical processes such as fluorescence and Raman scattering (Sect. 3.4). These properties that occur on the single particle level can be further manipulated and controlled by building small clusters or periodic lattices of plasmon particles using either lithographic methods or colloidal self-assembly techniques. In particular, coherences in scattering by multiple excited plasmon particles in clusters and lattices give further control over field enhancement and resonance linewidths of plasmonic structures, as well as a handle on directionality. This directionality expresses itself in the form of a strong dependence of a structure's local response on the direction from which the structure is illuminated, and conversely a strong anisotropy in light that is scattered or radiated by the structure. We discuss the physics of such plasmonic antennas in Sect. 3.5.

3.2 The Optical Response of Bulk Metals

The optical response of metal nanostructures is primarily determined by the metal's conduction electrons, which react collectively to external perturbations such as the applied electric field of a light wave. In this chapter, we are concerned with small particles and structures that are, however, large enough that the metal's response can be described by its bulk dielectric response. Deviations from the bulk response due to the small size of the nanoparticle are usually not observed above sizes of about 10 nm [2] (see Chap. 2, Sect. 2.4.2.1, for more details). Furthermore, it is assumed that the properties of the material close to the surface are identical to the bulk properties, and the lattice discreteness is disregarded. With these assumptions, and further neglecting quantum mechanical effects such as the spill-out of the electronic wave functions beyond the particle's surfaces, the metal can be represented by a continuous medium in classical electromagnetic theory. The metal is thus fully characterized by its complex dielectric permittivity $\varepsilon(\omega)$. In many cases, in particular for metals with a cubic lattice and for isotropic polycrystals, the permittivity tensor is isotropic and is therefore represented by a single function. It is important to realize that electromagnetism is a nonlocal theory involving long-range Coulomb forces, and that the response of free electrons in a metal particle is collective, i.e., it integrates all perturbations and boundary conditions imposed on the electronic system as a whole. This is in contrast to molecular systems or many semiconductor materials where each electron responds locally, independent from the boundary conditions at large distances.

3.2.1 The Drude Model for a Free Electron Plasma

Let us first consider the ideal case of a plasma of free electrons, i.e., a free electron gas whose electronic neutrality is ensured by a uniform and fixed distribution of positive charges. Those are carried by the heavy counter-ions, which can be taken as immobile in most cases. The free electron gas in a uniform positive charge density is called the jellium model [3]. Coulomb forces arise from the charge imbalance between the electron gas and the fixed jellium. They apply to the free electrons and tend to restore electric neutrality. For small displacements on large scales, the combination of restoring forces with electron inertia gives rise to harmonic oscillations around electric neutrality at the plasma frequency ω_P. As an easy argument to derive this characteristic frequency, consider a rod of metal with an volume electron density N. Suppose we displace all the free electrons by an amount x along the rod normal relative to the ionic backbone. As a consequence, on one end of the rod an excess layer of electrons arises, which represents a surface charge $\sigma = -Nex$, while on the other end of the rod the ionic backbone represents a positive but equally large surface charge. The surface charge sets up a homogeneous electric field $E = \sigma/\varepsilon_0\varepsilon_r$ that tends to pull the electron gas back to zero

displacement. According to Newton's equation, the motion of an electron will be governed by

$$m_e\ddot{x} = -eE = \frac{-Ne^2}{\varepsilon_0\varepsilon_r}x, \tag{3.1}$$

which is an equation of motion for a harmonic oscillator resonant at ω_P, given by

$$\omega_P = \sqrt{\frac{Ne^2}{m_e\varepsilon_0\varepsilon_r}}, \tag{3.2}$$

where e and m_e are the charge and effective mass of conduction electrons, N is their volume density, and $\varepsilon_0\varepsilon_r$ is the permittivity due to all other charges of the medium.

For noble metals such as gold and silver, with one conduction electron per atom, the electronic density is typically around $5 \times 10^{28}\,\mathrm{m}^{-3}$, which leads to a plasma frequency in the UV range. The plasma oscillation is damped by electron scattering off impurities, phonons, and surfaces. It is described phenomenologically by a viscous friction constant γ, whose inverse τ is called the Drude relaxation time and is of the order of some tens of fs in noble metals. This time is related through the Fermi velocity to a mean free path for electrons, which is of the order of a few tens of nanometers at room temperature.

By including only the free electrons' contribution to the polarization of a metal at frequency ω, we can derive the complex electronic permittivity $\varepsilon(\omega)$. To this end, suppose that we have an infinite block of metal and we consider the motion of a free electron when we drive the electrons with an oscillating electric field. The motion is governed by

$$\ddot{x} + \gamma\dot{x} = -\frac{eE}{m_e}e^{-i\omega t}. \tag{3.3}$$

If we solve for the *conductivity* $\sigma(\omega)$ of the metal which is defined through the relation between applied field E and induced volume current density j

$$j = -Ne\dot{x} = \sigma(\omega)E \tag{3.4}$$

we obtain the so-called 'Drude model' for the AC conductivity of a metal

$$\sigma(\omega) = \frac{\sigma_0}{1 - i\omega\tau} \text{ with } \sigma_0 = \frac{Ne^2\tau}{m_e}, \tag{3.5}$$

where τ is the Drude relaxation time. The Drude model describes the conductivity of metals such as gold, copper, and silver well over a very large frequency range, from DC (conductivity σ_0, with units of inverse Ohm-meters) to beyond the range of AC electronics, i.e., to optical frequencies.

In optics, the conductivity is an inconvenient parameter, as one usually deals with the permittivity $\varepsilon_0\varepsilon(\omega)$, and its square root, the refractive index $n = \sqrt{\varepsilon(\omega)}$. Using Maxwell's equation, in particular Ampère's circuit law in its microscopic and its macroscopic form, we can convert conductivity to permittivity, arriving at

$$\varepsilon(\omega) = 1 + \frac{i\sigma(\omega)}{\varepsilon_0\omega} = 1 - \frac{\omega_P^2}{\omega(\omega + i\gamma)}. \tag{3.6}$$

This description for permittivity is known as the 'Drude model'. Solving Maxwell's equations with this permittivity automatically takes all electromagnetic interactions between electrons into account. Therefore, whereas each electron responds individually to the local field it experiences, this field itself is determined by the collective response of all electrons. The Drude model captures the salient optical features of metals. For $\omega \ll \omega_P$ the dielectric constant is strongly negative. The limit of zero frequency and no loss ($\gamma = 0$), in fact corresponds to a 'perfect conductor', i.e., a medium that is completely impenetrable for electric fields. As the frequency approaches ω_P, the free electrons are less able to screen the incident field, and the field penetrates further into the metal. When $\omega > \omega_P$ the dielectric constant becomes positive and the metal becomes transparent.

3.2.2 The Dielectric Function of Ag and Au in Reality

Although the Drude model accounts for the main qualitative features of metal optics, modeling real metals requires including the response of the other, bound electrons. For example, the yellow color of gold in the visible range arises from the so-called interband transitions, which bring electrons from the filled *d*-bands to the open (*sp*) conduction band, above the Fermi level.

As shown in Fig. 3.1 for gold, interband transitions give rise to considerable deviations from the Drude model for wavelengths shorter than 600 nm by introducing strong losses for green and blue light. We must therefore consider the contribution of bound *d*-electrons to the optical properties to properly model the dielectric function of gold. Gold behaves as an excellent metal with very high conductivity only for wavelengths longer than 600 nm. For silver (Fig. 3.1), interband transitions peak for wavelengths around 310 nm and are negligible in the visible range. Silver presents a white shine and a flat and nearly total reflection throughout the visible and is well described by a Drude model. More accurate models of the optical properties of noble metal nanostructures and nanoparticles are often based on the measurements of optical constants by Johnson and Christy [4], for gold and silver, shown as data points in Fig. 3.1. Alternatively, one uses the values listed in the handbook by Palik [5].

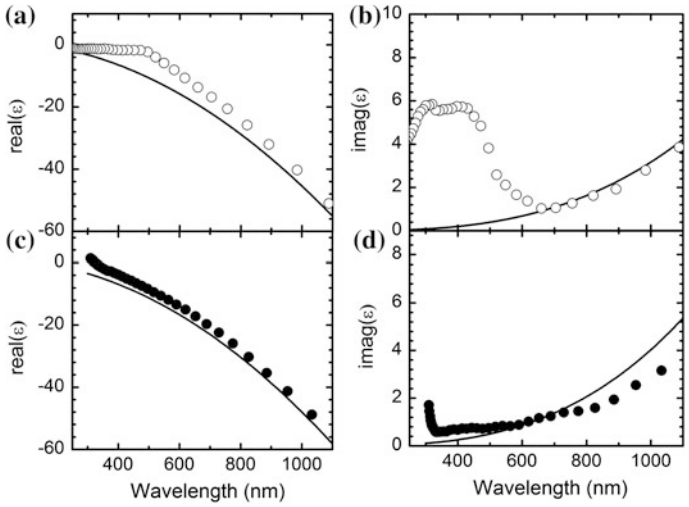

Fig. 3.1 Real and imaginary parts of the dielectric function of **a**, **b** gold, and **c**, **d** silver. *Solid lines* are deduced from the Drude model including only conduction electrons; the *symbols* represent measurements by Johnson and Christy [4] and include interband transitions. Drude parameters *gold* $\omega_p = 1.4 \times 10^{16}$ s^{-1} (or ~9 eV) and $\gamma \sim 0.01\ \omega_p$. *Silver* $\omega_p = 1.4 \times 10^{16}$ s^{-1} (or ~9 eV) and $\gamma \sim 0.003\omega_p$

3.2.3 Comparison of Metals

The interesting optical phenomena that we describe in the remainder of this chapter take place for visible and infrared wavelengths provided two conditions are met. Firstly, the plasma frequency has to be in the blue/UV part of the spectrum, since plasmonic resonances of nanoobjects usually occur just to the red of the plasma frequency. Secondly, damping must be low. The first requirement is met by most metals, including gold, silver, copper and aluminium. The second requirement, i.e., the low-loss requirement is met by only a few metals (see the handbook by Palik [5]). Indeed, DC resistivities of metals already show that damping is high except for the noble metals silver and gold, and possibly a few materials that are very difficult to handle, such as alkali metals. A further promising candidate is aluminium, which is suited for plasmonics in the UV. It has a plasma frequency at about 15 eV with a damping factor $\gamma \sim 0.02\omega_p$. It should be noted that the physics we describe below in principle scales to any frequency range provided one can shift the plasma frequency. For instance, many chemical compounds have a unique fingerprint in the mid IR and at THz frequencies. Since these frequencies are a factor 100 lower than optical frequencies, they require materials with 10,000 lower electron density in order to lower the plasma frequency. Such concentrations are achievable in doped semiconductors such as doped Si or materials such as InSb, which are being investigated for use in THz plasmonics.

3.3 Scattering by Small Particles

Because of the large negative value of the real part of the dielectric constant of noble metals, small particles present a large dielectric contrast with their surroundings, which usually have positive dielectric permittivity. This large contrast leads to strong scattering of light, which is often used for the detection and study of metal NPs. Scattering increases when the particles are dispersed in media with higher refractive indices, a phenomenon known as the immersion effect (pp. 37–40 in [2]). In the following, we discuss the scattering of a small sphere in the electrostatic dipole approximation. Section 3.3.1 deals with the polarizability of nanospheres, while Sect. 3.3.2 describes observables in scattering experiments. Section 3.3.3 discusses non-spherical particles, in particular spheroids.

3.3.1 Polarizability of a Small Sphere

Mie's theory [1] of scattering by a sphere in a homogeneous and isotropic medium with a different dielectric permittivity provides exact solutions for the scattered and transmitted fields [6]. These solutions simplify considerably if the sphere is much smaller than the wavelength of light in the materials involved. In that case, it is possible to neglect the variations of the electromagnetic field over the sphere's dimensions and to replace the exact electric field by a static one, giving rise to an effectively dipolar response. To evidence that this is indeed the case, let us consider the classical problem of a sphere of radius a in a static homogeneous incident electric field of strength E oriented along z. In electrostatics, the field is minus the gradient of a potential Φ that satisfies the Poisson equation. We are looking for solutions of the following equations:

$$\begin{aligned} \Delta\Phi_{\text{in,out}}(r) &= 0 \text{ everywhere with} \\ \Phi_{\text{in}}(r=a) &= \Phi_{\text{out}}(r=a), \text{and} \\ \varepsilon_{\text{in}}\frac{\mathrm{d}\Phi_{\text{in}}(r=a)}{\mathrm{dr}} &= \varepsilon_{\text{out}}\frac{\mathrm{d}\Phi_{\text{out}}(r=a)}{\mathrm{dr}}, \text{while} \\ \lim_{\mathrm{r}\to\infty}\Phi_{\text{out}}(r) &= -Er\cos\,\theta. \end{aligned} \tag{3.7}$$

These equations assume (1) there is no free charge, (2) the potential is continuous across the sphere boundary, but (3) its slope jumps, while finally the potential far away from the sphere is simply that of the incident homogeneous field oriented along $z = r\cos\,\theta$. The jump comes from Maxwell's boundary condition $\nabla\mathbf{D} = -\nabla(\varepsilon\nabla\Phi) = 0$, and has as interpretation that the response of the free electrons in the sphere effectively form a surface charge layer at the sphere boundary. It is easy to check that:

$$\Phi_{\text{in}} = -Er\cos\,\theta + \left(\frac{\varepsilon_{\text{in}} - \varepsilon_{\text{out}}}{\varepsilon_{\text{in}} + 2\varepsilon_{\text{out}}}\right) Er\cos\,\theta = -\left(\frac{-3\varepsilon_{\text{out}}}{\varepsilon_{\text{in}} + 2\varepsilon_{\text{out}}}\right) Er\cos\,\theta \qquad (3.8)$$

and

$$\Phi_{\text{out}} = -Er\cos\,\theta + a^3\left(\frac{\varepsilon_{\text{in}} - \varepsilon_{\text{out}}}{\varepsilon_{\text{in}} + 2\varepsilon_{\text{out}}}\right) E\frac{\cos\,\theta}{r^2} = -Er\cos\,\theta + \frac{p\cos\,\theta}{4\pi\varepsilon_0 r^2} \qquad (3.9)$$

solve the problem exactly. The solution shows two facts. Firstly, *inside* the sphere, the induced field is homogeneous, and exactly along the applied incident field, but with a different strength $3\varepsilon_{\text{in}}/(\varepsilon_{\text{in}} + 2\varepsilon_{\text{out}})$. Secondly, *outside* the sphere the field is the sum of the incident field, plus a term that is exactly equal to the field of a dipole of strength p located at the origin. The electrostatic response of a sphere is hence identified with an induced dipole moment p, the magnitude of which is proportional to the incident field E. The constant of proportionality is termed *polarizability*, defined through $p = \alpha_0 E$.

Returning to Mie's solution for scattering by a sphere, we note that in case of spheres much smaller than the wavelength λ, the electrostatic result essentially carries over. As the scattering object grows in size, the Mie solution deviates from the electrostatic solution. So-called radiative corrections, which are small, can be added to the polarizability of the sphere to simulate scattering, assimilating the sphere to a dipole. For noble metals, the dipole approximation is usually very good for diameters less than 50 nm. For larger sizes, contributions from higher multipoles can be included, but electromagnetic calculations soon become indispensable when the particle or structure sizes become comparable to a quarter-wavelength. Metal NPs that are used in optics experiments typically have diameters smaller than 100 nm, implying that the electrostatic approximation is reasonable for most experiments.

To obtain the scattered fields in the dipole approximation, one can start from Mie's result and expand it for small volumes, neglecting all terms of order 2 or higher in volume. The scattered field is that of a dipole oriented along the polarization of the exciting light. Where the scattered field overlaps with the incident exciting field, it leads to an attenuation of the latter in the transmitted direction, called extinction. Extinction includes losses to the incident wave either because of scattering to other modes or because of true dissipation leading to heat production or to the generation of other wavelengths. The polarizability $\alpha_0(\omega)$ of a small sphere with volume V in the dipole approximation is given by:

$$\alpha_0(\omega) = 3\varepsilon_0 V\left(\frac{\varepsilon(\omega) - \varepsilon_{\text{m}}}{\varepsilon(\omega) + 2\varepsilon_{\text{m}}}\right), \qquad (3.10)$$

in agreement with the electrostatic analysis in Eqs. (3.8) and (3.9). Here we use $\varepsilon(\omega)$ to refer to the dielectric permittivity of the metal that we already discussed, while ε_{m} refers to the dielectric permittivity of the embedding medium.

The polarizability shows a resonance at the surface plasmon resonance (SPR, or hereafter plasmon for short) frequency ω_{SPR}, when the real part of its denominator cancels, i.e., for Re $[\varepsilon(\omega_{SPR})] = -2\varepsilon_m$. If we assume a Drude model for the metal, and assume a particle in air, the polarizability simplifies to a Lorentzian resonance

$$\alpha_0(\omega) = \frac{3\varepsilon_0 V \omega_{SPR}^2}{\omega_{SPR}^2 - \omega^2 - i\omega\gamma}, \tag{3.11}$$

with the resonance frequency at $\omega_{SPR} = \omega_P/\sqrt{3}$, i.e., at frequencies significantly red-shifted from the plasma frequency. For silver and gold, this estimate results in plasmon resonances in the UV/blue part of the spectrum. The relation Re $[\varepsilon(\omega_{SPR})] = -2\varepsilon_m$ further also explains the sensitivity of the plasmon resonance to the surrounding index of refraction. Generally, the resonance red-shifts upon immersion in higher index media.

The electrostatic analysis of the field nearby a small sphere can be used also to estimate how strongly the incident electric field strength E can be enhanced due to the plasmon resonance. If we evaluate the dipole field exactly at the sphere boundary, where it is highest, we find

$$E_{\text{dipole}}(r = a) = \frac{p\cos\theta}{4\pi\varepsilon_0 a^3} = \frac{3\varepsilon_0 V}{4\pi\varepsilon_0 a^3}\left(\frac{\varepsilon(\omega) - \varepsilon_m}{\varepsilon(\omega) + 2\varepsilon_m}\right)E = \left(\frac{\varepsilon(\omega) - \varepsilon_m}{\varepsilon(\omega) + 2\varepsilon_m}\right)E. \tag{3.12}$$

To first order, the field enhancement is hence *independent* of the size of the sphere. On resonance Re $[\varepsilon(\omega_{SPR})] = -2\varepsilon_m$, then the ratio of dipole field to incident field reduces to

$$\left|\frac{E_{\text{dipole}}(r = a)}{E}\right| = \frac{3|\text{Re }[\varepsilon(\omega_{SPR})]|}{\text{Im }[\varepsilon(\omega_{SPR})]}. \tag{3.13}$$

Evidently, the lower the Drude damping rate of the metal, the higher the quality factor of the plasmon resonance as gauged from the resonance width in Eq. (3.11), and consequently, the higher the field enhancement. For a Drude metal, the field at the metal approximately reduces to ω_{SPR}/γ, i.e., to a factor 30 or so. Turning to a real metal, the field enhancement by a silver particle indeed approaches the Drude limit, whereas in gold the additional damping due to the interband transitions limits the enhancement to a factor ~ 5.

3.3.2 Extinction and Scattering Cross Sections

The polarizability that we introduced above in principle describes the response of a metal sphere to incident light. However, in actual experiments, the induced dipole moment, or polarizability, is not usually the actual observable. Instead, in a typical

experiment one would irradiate a particle with a known intensity (units W/m^2), and measure how much power (units W) the object takes out of the incident beam [6]. The ratio between power and intensity has units of area, and is hence coined 'cross-section'. The so-called 'extinction cross-section' quantifies how much light a particle takes out of a beam, while the 'scattering cross-section' quantifies how much light a particle reradiates as scattered light. It should be noted that the units of area for cross-sections lend itself to a very graphical interpretation: if, for instance, the extinction cross-section exceeds the geometrical cross-section, this means that the particle is more efficient at casting a shadow than would be expected from its geometric size. On plasmon resonance, this 'efficiency' (cross-section divided by geometrical area) can reach values up to 10 for spheres and even more for elongated particles. Extinction and scattering cross-sections in the dipole approximation can be expressed in terms of the polarizability by

$$\sigma_{\text{ext}} = \frac{k}{\varepsilon_0} \text{Im}\ \alpha(\omega), \quad \text{and} \tag{3.14}$$

$$\sigma_{\text{scatt}} = \frac{k^4}{6\pi\varepsilon_0} |\alpha(\omega)|^2, \tag{3.15}$$

where $k = 2\pi\sqrt{\varepsilon_m}/\lambda$ is the wavevector of light outside the scattering sphere. Equation (3.15) is essentially the famous Rayleigh scattering law: for a small particle scattering scales inversely with the fourth power of wavelength, and with the square of the volume (sixth power of diameter). On the other hand, the extinction cross-section, which is related to the scattered field by the optical theorem [6], scales with volume only. Since the difference between extinction and scattering must be due to absorption, the scaling implies that for very small particles (i.e., smaller than 1/10 of the wavelength of light), the extinction is mainly determined by absorption, as is well known for colored molecular solutions. Scattering becomes more and more important for larger and larger particles. Therefore, to detect small particles, absorption or extinction is much more interesting than dark-field scattering, which is weak and easily obscured by experimental imperfections. Once particles are above approximately 100 nm in diameter, the extinction of a metal particle is mainly due to scattering instead of absorption.

By way of example, Fig. 3.2 shows absorption, extinction and scattering spectra of a 25 nm gold sphere placed in vacuum, and in water (n = 1.33). All lines show spectra calculated using a full Mie calculation, except for the dashed spectrum in the left panel, which is calculated using Eqs. (3.14) and (3.15). Agreement between the approximate model and the full calculation is good. For both approaches we have taken the measured dielectric constant of gold according to Johnson and Christy [4] instead of the Drude function. The calculated spectra are in good agreement with the experimental ones (see, e.g., Fig. 2.22, Chap. 2). Spheres of diameter between 10 and 50 nm show a resonance at a plasmon frequency of

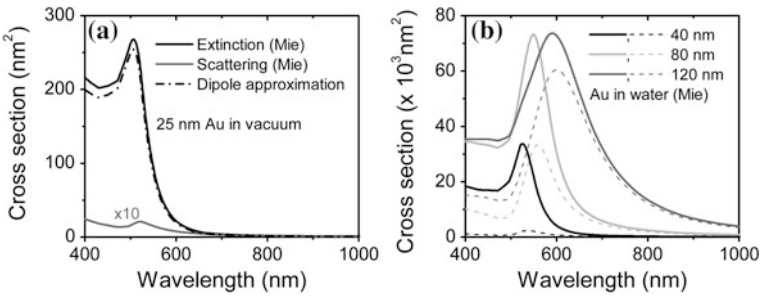

Fig. 3.2 *Left* cross section for extinction (*solid line*) and scattering (*grey line*) for a 25 nm diameter Au NP in vacuum, according to a Mie calculation. The dipole resonance at 507 nm is well captured by the dipole approximation. The on-resonance extinction cross section of $\sim$300 nm^2 is almost entirely due to absorption (the *grey curve* 'Scattering' was multiplied by a factor 10). *Right* Mie cross sections for extinction (*solid lines*) and scattering (*dashed*) for 40, 80, and 120 nm Au NPs in water. The water shifts the plasmon resonance to 520 nm for the smallest particles. The resonance further redshifts with increasing NP size, due to retardation effects not contained in the simple electrostatic model. For larger NPs the extinction is mostly due to scattering (*dashed line* close to *solid line*), and not to absorption (difference between solid and *dashed line*). For silver NPs as much as 95 % of the extinction can be due to scattering

around 520 nm. This resonance is broadened by losses due to the interband transitions. For 25 nm diameter spheres the absorption cross-section at the maximum is about 300 nm^2. We note that this explains the colors observed for colloidal suspensions of spherical gold NPs and their extinction spectra, which are nearly size independent for NPs smaller than 50 nm (Fig. 1.1, Chap. 1, and Fig. 2.22, Chap. 2). The color change between 50 and 20 nm (from red to orange, Fig. 1.1) is caused by a very small shift in the maximum of the extinction peaks (a few nm, see Fig. 2.22). For sizes larger than 50 nm, this spectral shift becomes increasingly larger, since the extinction cross-section grows less than linearly with volume and the absorption maximum shifts to lower frequencies (Fig. 2.22) because of corrections induced by retardation. This red-shift of the extinction peak leads to changes in the perceived color of the transmitted light, which gradually shifts from red to blue (Fig. 1.1).

The polarizability of a small NP can be corrected to include the effects of radiation by introducing an additional radiative damping channel, leading to a new polarizability [7]:

$$\alpha(\omega) = \frac{\alpha_0(\omega)}{1 - i\frac{k^3\alpha_0(\omega)}{6\pi\varepsilon_0}}. \tag{3.16}$$

A convenient shorthand for his relation is $1/\alpha(\omega) = 1/\alpha_0(\omega) - ik^3/6\pi\varepsilon_0$. The expression for the extinction and scattering cross-section in terms of the polarizability retain their validity with this revised polarizability, even for NPs with diameters up to 100–150 nm.

3.3.3 Spheroids

The analysis of spherical scatterers already contains all the generic physics of a plasmon resonance, the associated cross-sections, and the prediction of electric field enhancement. Yet, variations in particle shape offer significant control over these properties. For elongated particles such as nanorods, the particle is often approximated as an ellipsoid because there are analytical solutions for the polarizability of very small ellipsoidal nanoparticles. For ellipsoidal particles the depolarization field in the particle is uniform but not necessarily collinear with the applied field, which can be accounted for by incorporating a geometrical depolarization factor L in the dipole approximation [8]. The polarizability of an ellipsoid with volume V embedded in a homogeneous medium with dielectric constant ε_m can then be expressed as [2, 6]

$$\alpha_p = \varepsilon_0 V \frac{\varepsilon(\omega) - \varepsilon_m}{\varepsilon_m - L_p(\varepsilon(\omega) - \varepsilon_m)}, \tag{3.17}$$

where $p = (1, 2, 3)$ denotes the polarization of the incoming field along one of the principal axes of the particle. The dielectric function of the metal $\varepsilon(\omega)$ is given in Fig. 3.1 for different metals. The depolarization factors L_p depend on the elongation of the particle, and can be expressed as (for prolate spheroids) [2, 6]

$$L_1 = \frac{1 - e^2}{e^2}\left(1 + \frac{1}{2e}\ln\frac{1+e}{1-e}\right), \tag{3.18}$$

and

$$L_{2,3} = \frac{1}{2}(1 - L_1), \tag{3.19}$$

where L_1 ($L_{2,3}$) is the depolarization factor along the long (short) axis, and $e^2 = 1 - b^2/a^2$ is the eccentricity of a prolate (cigar shaped) ellipsoid with semi-major axis length a and semiminor axis length b. For a sphere the depolarization factors are 1/3 and Eq. (3.17) reduces to Eq. (3.10). Typical values for elongated particles are $(L_1, L_{2,3}) = (0.11, 0.45)$ for a prolate spheroid with an aspect ratio of 3. The optical cross sections of the particle are then given by Eqs. (3.14) and (3.15). The above equations give the optical properties of a single particle. For randomly oriented particles in a suspension, the optical cross-sections are simply given by the orientational average of the single-particle cross-sections.

Figure 3.3 shows examples of calculated absorption spectra for gold spheroids with different aspect ratios. An increasing aspect ratio results in a red-shifted longitudinal plasmon resonance due to a reduced restoring force on the oscillating electron cloud. This red-shift is also seen experimentally, as shown in Fig. 3.4. The transmitted light exhibits pronounced color differences due to the red-shift of the

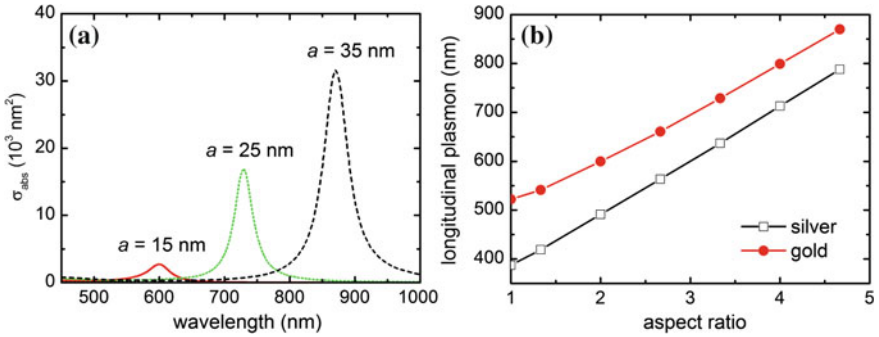

Fig. 3.3 **a** Calculated absorption cross sections of gold spheroidal NPs excited along their long axis. The NPs have a fixed semi-minor axis length (b = 7.5 nm) and varying semi-major axis length a. The dielectric constant of gold $\varepsilon(\omega)$ was taken from Ref. [4]. Note that the absorption cross section increases steeply because the volume of the NPs is different. **b** Longitudinal plasmon wavelength in the absorption spectrum of silver and gold prolate spheroids

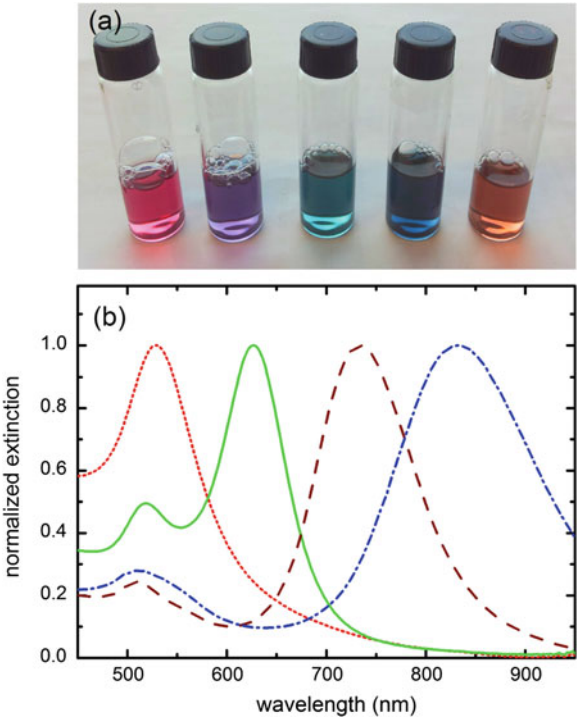

Fig. 3.4 **a** Photographs of colloidal suspensions of gold NPs with an ensemble average aspect ratio ranging from 1 (nanospheres, extreme *left*) to 4.5 (extreme *right*). The average diameter of the particles is ~20 nm and varies between the individual samples. **b** Normalized extinction spectra of colloidal suspensions of gold NPs with an ensemble average aspect ratio of 1 (nanospheres, *red dotted line*), 2.5 (*green solid line*), 3.5 (*brown dashed line*) and 4.5 (*blue dash-dotted line*). A clear red-shift of the absorption band is observed as the aspect ratio increases, which is responsible for the color changes observed in **a**

longitudinal plasmon absorption with increasing aspect ratio. As discussed above, for spherical Au NPs smaller than 50 nm the plasmon absorption occurs in the blue-green, hence the solutions appear red. For increasing aspect ratios the longitudinal plasmon resonance moves through the visible region to near-infrared wavelengths. For the largest aspect ratios the solutions appear brownish due to a featureless absorption profile in the visible with a small peak around the transverse plasmon resonance in the blue. Representative extinction spectra are shown under the photograph and confirm this interpretation (Fig. 3.4). Note that the linewidths in Fig. 3.4 are significantly broader than the calculated ones (Fig. 3.3). This is caused by inhomogeneous broadening due to the size distribution of the Au NPs.

The same effect is seen in silver nanorods (Fig. 3.3b), only here the plasmon occurs at a shorter wavelength due to the higher plasma frequency of silver. The transverse plasmon occurs at 520 nm for gold and at $\sim$400 nm for silver nanorods but is little affected by particle aspect ratio in the range of lengths we consider here. In the dipole approximation, nanospheres with diameters between 10 and 50 nm present a plasmon mode at about 520 nm (2.4 eV) for gold and about 400 nm (3.1 eV) for silver. We see from Fig. 3.1 that dissipation is weak for nanosphere plasmons in silver but not in gold. Gold exhibits intraband absorption at wavelengths between 200 nm and 550 nm, leading to additional losses for the plasmon. For gold nanorods of aspect ratios $a/b > 2$, however, the plasmon is shifted to wavelengths longer than 600 nm (2.08 eV), for which dissipation is weak. The plasmon dephasing time for gold nanorods is therefore longer than for gold nanospheres, resulting in a narrow plasmon linewidth [9]. This narrow plasmon of gold nanorods is useful for many applications that exploit the optical properties of a single particle, as we will discuss in the next section.

3.4 Applications of Single Metal Nanoparticles

Since the first far-field detection of single metal NPs in 1998, different applications have arisen that specifically rely on the optical detection of single particles [10]. Applications range from physical to biochemical and biological contexts. After a short introduction to the optical detection of single metal NPs we will highlight some of these applications, with the intention to give the reader insight into the current state-of-the-art. In Sect. 3.4.1 we firstly describe the basic principles of optically detecting a single metal particle. Then we discuss several applications including optical labeling and tracking (Sect. 3.4.2), optical trapping of single particles (Sect. 3.4.3), biosensing (Sect. 3.4.4) and the use of a single particle as a nano-antenna to enhance fluorescence (Sect. 3.4.5).

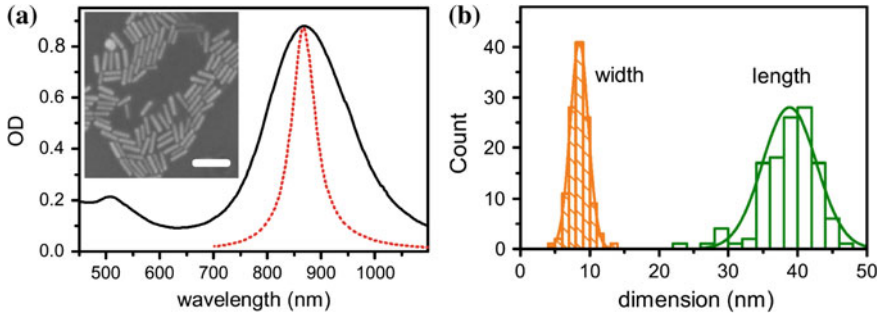

Fig. 3.5 **a** Extinction spectrum of an aqueous solution of as-prepared gold nanorods. The *inset* shows a scanning electron microscope image of a small volume of the sample that was drop cast on a silicon substrate. Scale bar 50 nm. To illustrate the inhomogeneous broadening of the optical spectrum we show the calculated spectrum of a single particle of 9 nm × 40 nm [Eq (3.17) inserted in (3.14)] as a *red dashed curve*. **b** Size distribution of the sample obtained from electron microscopy images as shown in **a**. Reprinted with permission from [10], Copyright (2011) Institute of Physics (IOP)

3.4.1 Optical Detection of a Single Particle

It is important to motivate why single particles bring new information, complementary to the more conventional measurements on ensembles. Although single-particle experiments are more difficult and provide a lower signal-to-noise ratio than ensemble measurements, they have distinct advantages:

(i) Even the best synthesis methods available produce a distribution of sizes and shapes (see Chap. 6 for details). Figure 3.5 shows the inhomogeneity of a colloidal sample of gold nanorods prepared by wet-chemical synthesis observed in an electron microscope and optically on an ensemble. By measuring the properties of individual particles, one recovers the full distribution of a variable in the heterogeneous ensemble.

(ii) The effect of small perturbations or changes in particle size, shape and composition, or in local surroundings can be measured with enhanced sensitivity due to the elimination of inhomogeneous broadening.

(iii) Single-particle experiments enable studies of rare but interesting objects, which would be difficult or impossible to extract or purify from an ensemble. Examples are the small assemblies of particles that are often used as antennas (see Sect. 3.5 below).

The most important component of a setup that is capable of detecting a single metal NP is the microscope objective lens. A high quality objective can focus the light to a diffraction limited spot, which is typically several hundreds of nanometers in diameter for visible light focused with a numerical aperture of about one. When combined with a stable light-source (either a laser source or a non-coherent

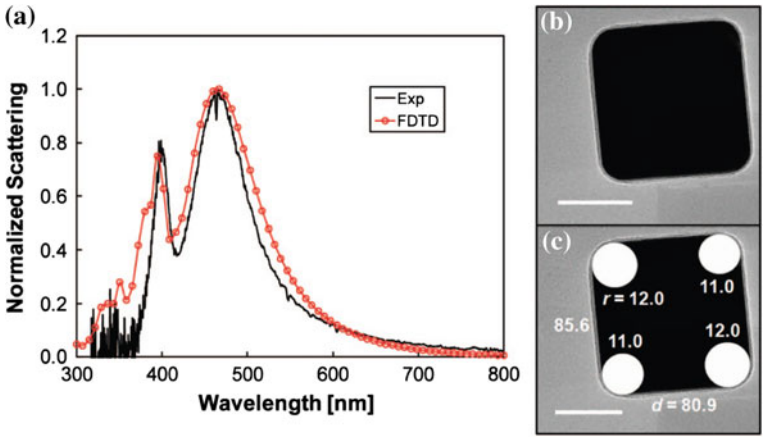

Fig. 3.6 Scattering spectrum and transmission electron microscopy image of the same gold nanocube. The electron microscopy image yields information about the morphology of the particle such as the edge-length and tip curvature, information that cannot be obtained from the spectrum alone. Scale bar 40 nm. Reprinted with permission from [13], Copyright (2009) American Chemical Society

broadband source such as a halogen lamp) and a sensitive detector, single particles can be studied in a variety of configurations, as will be discussed below.

Dark-field scattering: The most commonly employed configuration detects the light scattered by the metal particle on a dark background by using a commercially available dark-field condenser. This approach was first demonstrated in 1998 [11, 12] and has since been used to characterize the spectral and polarization properties of individual NPs. A powerful approach to correlate the morphology of the NP with its optical response is to deposit the particles on a conducting substrate (e.g. indium-tin-oxide coated glass). By imaging the same area on the sample in both an optical and an electron microscope the shape and size of the particle can be correlated to its plasmon spectrum [13] (see Fig. 3.6). This technique yields valuable information on the effects of minute differences in particle morphology (e.g. the endcap shape of a gold nanorod, the truncation of a triangular plate or cube, or the sphericity of a particle) on the plasmon resonance. Moreover, this correlation can definitively separate single particles from small clusters, something that is often difficult from the optical spectrum alone.

Bright-field detection: The scattered intensity scales as the squared volume of the particle (Eq. 3.15), making it difficult to image NPs smaller than 30 nm with dark-field scattering microscopy. In that case the scattered intensity is drowned by the noise level of a typical detector. Spectra of these small NPs are therefore better collected interferometrically in a bright-field setup [14]. Herein the scattered wave is overlapped with a reference wave, causing interference between the two. For convenience the reference wave is most often the reflection off the glass sample substrate, but it can also be a secondary beam. For small NPs the interference between

the reference and scattered wave results in a detected intensity that scales as the NP volume instead of the volume squared. This technique is capable of detecting NPs as small as 5 nm with a reasonable signal-to-noise ratio. Bright-field microscopy detects the NPs against a high background (the reference field) so it is important to use a stable light source to prevent fluctuations in the background intensity.

Photothermal microscopy: A complementary method that detects particles down to 1.4 nm and even single absorbing molecules is photothermal detection [15]. In photothermal microscopy a pump beam is absorbed by the particle, which subsequently heats up due to the efficient non-radiative decay of the excited electron-hole pairs. The thermal energy is dissipated into the environment, which causes a change in the index of refraction around the particle due to thermal expansion of the solvent. This so-called thermal lens is then detected by a secondary probe beam either in transmission or reflection. Because the probe beam wavelength is chosen far away from the plasmon resonance it is not absorbed by the NP, and much higher probe intensity can be used to reduce photon noise. The heating beam is time-modulated at a high frequency in the MHz range, and the resulting variations in the detected probe laser intensity are extracted with a lock-in amplifier. The photothermal signal thus detects a weak effect (the refractive index change) but by accumulating the contribution of many photons it can still achieve an excellent signal-to-noise ratio.

Photoluminescence: Photoluminescence (PL) microscopy is also capable of detecting a single metal NP. Luminescence detection is gaining popularity because the technique is analogous to fluorescence microscopy to image single organic fluorophores, and because highly sensitive setups are already available in many laboratories. The advantage of PL microscopy is that, since the luminescence wavelength is different from the excitation wavelength, it is in principle easy to separate signal from scattered background, simply using optical filters. The first observation of PL of gold dates back to 1969 [16], when Mooradian studied bulk gold and observed a broad PL spectrum with a quantum yield (number of emitted photons per absorbed photon) of about 10^{-10}. PL from bulk gold originates from radiative transitions of conduction electrons toward empty electron states, which can be either holes in the d-band (electron–hole interband recombination), or empty electron states or holes within the sp-conduction band (intraband transitions). Later studies showed that this low quantum yield can be enhanced by several orders of magnitude in the presence of surface roughness (lightning-rod effect) and localized surface plasmons. Recent studies have reported that the photoluminescence quantum yield of a single plasmonic particle only weakly depends on its size and shape and typically lies in the range of 10^{-5}–10^{-6}. Despite this low quantum yield single particles are easily detectable in a standard microscope due to their large absorption cross section. Under single-photon excitation, the luminescence brightness of a single metal NP of several tens of nanometers in diameter is comparable to that of a single fluorophore.

3.4.2 A Metal Particle as an Optical Label

Contrary to single organic fluorophores or semiconductor quantum dots the signal of metal NPs does not blink or bleach due to the large number of conduction electrons per particle (typically 10^3–10^5, compared to a single electron involved in fluorescence for an organic fluorophore). This gives metal NPs a considerable advantage over fluorophores when used as optical labels. The stable signals (scattering, luminescence, harmonic emission, photothermal) of metal NPs are hardly affected by their environment and allow for observation times only limited by diffusion out of the field-of-view of the microscope. Moreover, the high signal-to-noise ratio enables tracking of single metal NPs with microsecond time resolution. By tracking the particle in space and time one gains valuable information about the location and transport of proteins in living cells.

Once a metal NP is taken up by a cell either actively or passively, its strong scattering or luminescence can be used to track biomolecules attached to it. As an example, Fig. 3.7 shows the trajectory of a single 40 nm gold NP attached to a phospholipid [17]. The diffusion of the phospholipid in the plasma membrane of epithelial cells was monitored using differential interference contrast microscopy with a time resolution of 25 μs. Remarkably, the conjugate undergoes hopping diffusion between compartments in the membrane. To resolve the hop movement, the temporal resolution must be considerably better than the average residency time within a compartment (a few ms). The dwell time was thus not observable with the time resolution typical for imaging with organic fluorophores (viz., 33 ms).

In the crowded environment of a cell, the label size should be minimized to prevent effects of viscous drag on the process. Metal NPs of 10 nm and smaller

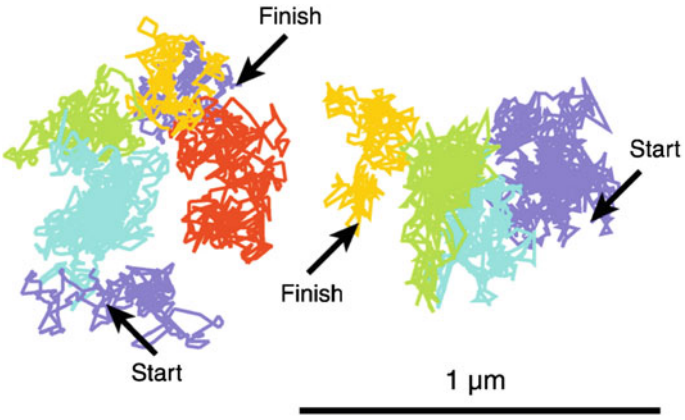

Fig. 3.7 Trajectories of two lipids in the cell membrane of an epithelial cell. The lipid was tracked by imaging a 40 nm gold NP attached to it with a time resolution of 25 μs. The different *colors* indicate the compartments through which the lipid diffused. Copyright 2002 Rockefeller University Press. Originally published in Ref. [17]

(no bigger than a large protein) cannot be detected with a conventional scattering-based setup and require a more selective method, such as photothermal microscopy (see Sect. 3.4.1 for details). In 2006 Lasne et al. [18] used this technique to track single gold NPs as small as 5 nm in a living cell. Even though the metal NP is small it still absorbs significantly more than the cellular background, enabling background-free detection inside the cell. Trajectories of a single particle can be recorded at video rate by employing a triangulation procedure yielding a localization accuracy of ~ 10 nm, comparable to state-of-the art super resolution microscopy techniques. With anisotropic NPs, one may not only track and measure translational motions of biomolecules, but also extract information on their orientation and rotation by exploiting the dipolar character of the plasmon resonance. Gold nanorods are often employed for two-dimensional orientation tracking due to their ease of synthesis and strong and anisotropic optical response. Assemblies of spherical NPs such as dimers also exhibit a dipolar optical response (Sect. 3.5), and have been used to track rotations.

As is evident from the above description, the ability to detect single metal NPs has led to exciting new insights in biophysical questions which are difficult to address with single organic fluorophores or semiconductor NPs. Passive tracking of single Au NPs has already yielded exciting results, but the active manipulation of particles for single-molecule force spectroscopy would immediately open a whole new realm of experimental possibilities. Recent developments in the optical trapping of single metal NPs have brought this prospect closer than ever, as will be described in the next section.

3.4.3 Optical Trapping

Optical trapping of a single metal NP can be accomplished by strongly focusing a near-infrared laser beam using a high numerical-aperture objective lens. The force exerted by the laser beam onto the NP consists of three components: the gradient force, the scattering force and the absorption force. The scattering and absorption forces scale as their respective optical cross-sections and act in the propagation direction of the laser beam. These forces therefore displace the particle along the optical axis and tend to push it out of the laser focus. The gradient force on the other hand stabilizes the position of the NP in the trap and can be expressed as

$$\vec{F}_{grad} = \frac{1}{2}\alpha'(\omega)\nabla\langle\vec{E}^2\rangle, \tag{3.20}$$

with α' the real part of the polarizability of the particle (see Sect. 3.3 for expressions for α in the dipole approximation) and $\vec{E}$ the electric field vector in the focus. Stable trapping can thus only be achieved when the axial gradient force exceeds the sum of the scattering and absorption forces. Maximizing the gradient force is often done by employing microscope objectives with a high numerical aperture. These objectives

focus the trap laser to the smallest possible spot-size (limited by diffraction), thereby maximizing the field gradient $\nabla\langle\vec{E}^2\rangle$ in Eq. (3.20). Note that trapping cannot be achieved with a laser wavelength on the blue side of the plasmon resonance because the polarizability, and thus the gradient force, is negative. The particles will then be propelled out of the laser focus.

It is immediately obvious that metal NPs can be trapped down to smaller sizes than dielectric particles. For example, α (in the dipole approximation, at 1,064 nm) is $\sim$10 times larger for a 40 nm diameter gold bead than for a polystyrene one. For an ellipsoidal particle of 70 nm × 20 nm this difference is as much as $\sim$50 times in the dipole approximation. As a result, single-beam optical tweezers allow for the stable optical trapping of single Au spheres and nanorods, and Ag NPs. For particles >100 nm forces in the pN range can be exerted with a laser power of several tens of milliwatts. This range of forces is promising for applications in single-molecule force spectroscopy, for example to stretch a single DNA molecule or to stall a molecular motor. Non-spherical metal NPs also experience a torque in an optical trap because of the anisotropy of their polarizability tensor. Au and Ag nanorods therefore align with the trapping laser polarization. The optical torque that can be exerted on a single Au nanorod was recently quantified to be $\sim$100 pN nm for 80 mW of trapping laser power [19], enough to twist biomolecules such as DNA. Although the absorption cross-section of the NP at the trap laser wavelength is small, it is non-negligible, and causes the NP to heat and eventually melt if the trapping power is sufficiently high. Typical heating rates of metal NPs in an optical trap are 0.1–1 K/mW, depending on the shape and size of the NP [19–21].

Force spectroscopy has now mainly been performed outside the cell, in a well-controlled environment. The main reason is that the dielectric particles often employed for these studies have diameters in the range of 500 nm–5 μm. These large particles are much bigger than typical organelles in the cell, and significantly distort cell function. Due to their large volume polarizability compared to dielectrics, the trapping of metal NPs seems a promising avenue to take single-molecule force-spectroscopy into the cell.

3.4.4 Biosensing

The frequency of the plasmon resonance is not only sensitive to the morphology and the composition of the particle, but also to the refractive index of its local environment. This sensitivity arises from the electric field associated to the plasmon, which extends beyond the particle's surface. The evanescent near-field penetrates the medium around the particle, making the plasmon resonance frequency sensitive to the refractive index in its immediate vicinity (Eq. 3.10). This index sensitivity opens up possibilities to optically detect molecules without the need to label them by using plasmon shifts as reporters for molecular binding. Remarkable progress has been made in the past two decades in the development of plasmonic biosensors. The commercial sensors do not contain metal NPs, but use thin metal

films that support propagating plasmon polaritons, optical excitations bound as a guided mode to the metal due to the free electron response. Propagating plasmonic biosensors are now commercially available to perform label-free interaction analysis with a high throughput and sub-nM sensitivity. However, large quantities of analyte are required to cover the surface of the sensor (on the order of a mm^2), which is problematic when expensive reagents are to be tested. The detection of only a few or even a single molecule is not possible because the response of the sensor is integrated over a large surface area. Plasmonic sensors based on single metal NPs are promising alternatives that do not suffer from these drawbacks.

Plasmon sensing can refer to one of two variations, namely (bulk) refractive index sensing and the sensing of molecular binding. In the former, only the bulk index sensitivity and linewidth of the plasmon determine the sensitivity. The sensitivity of a single particle sensor is often expressed in terms of its figure-of-merit (FOM), which can be expressed as

$$\mathrm{FOM} = \frac{\Delta\omega_{RIU}}{\Gamma}, \tag{3.21}$$

with $\Delta\omega_{RIU}$ the frequency shift of the plasmon for unit refractive index change, and Γ is the linewidth. The FOM is higher for narrower resonances because it is easier to determine peak-shifts. The FOM of different shapes of NPs has been widely investigated, and varies from $\sim$0.5–1 for a single Au sphere to $\sim$10 for a single Au nanorod. Gold nanorods are therefore widely used for sensing not only because of their high sensitivity but also due to the availability of straightforward protocols to synthesize (single crystalline) particles with a high yield. Bulk index changes of 10^{-2} cause a plasmon shift of several nanometers and are straightforward to detect using a single metal particle.

In the second case, when the binding of a (bio-)molecule is measured, the size of the NP is also of concern because it determines the spatial overlap between the local electric field and the analyte molecule. The local electric field decays approximately exponentially from the particle surface with a characteristic decay length that scales as the particle radius. The optimum NP size therefore depends on the volume of the molecule to detect, and generally smaller molecules require a smaller NP to achieve the highest sensitivity. Recently, such a single-particle plasmon sensor in the form of a single nanorod has allowed for the detection of binding events caused by a single molecule. Plasmon shifts can be monitored in time using for example photothermal microscopy [22] or dark-field scattering spectroscopy [23]. A typical time trace of the plasmon wavelength exhibits step-wise shifts caused by the binding and unbinding of single proteins to receptors on the surface of the NP (Fig. 3.8). Currently, label-free single-molecule detection is limited to proteins with a molecular weight > 50 kDa. These smaller proteins typically induce a plasmon shift of less than a nanometer, which is close to the noise level in a standard optical setup. Smaller molecules can still be detected by enhancing the plasmon shift [24]. The analyte can be coupled to a label with a high refractive index, for example another (small) metal NP (Fig. 3.8). Although the sensing is then not label-free

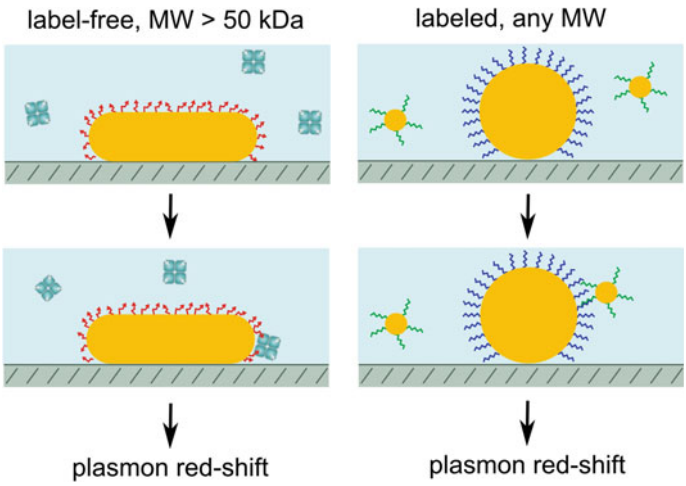

Fig. 3.8 Schematic showing current detection limits of biomolecular detection techniques that exploit the plasmon of a single NP. (*left*) The detection of large proteins (in this case streptavidin) can be accomplished by monitoring the plasmon of single gold nanorod, without the need to label the protein. (*right*) For smaller molecules such as DNA, the analyte (displayed in *green*) is usually labeled with a highly polarizable reporter particle to amplify the red-shift. The reporter particle in this example is a secondary gold nanosphere

anymore, the shift of the plasmon upon binding of the molecule can now be easily determined because coupling between the sensor NP and labeled analyte causes a dramatic plasmon resonance shift due to the hybridization of the plasmons in the NPs (see Sect. 3.5 for details on plasmon hybridization).

The proper functionalization of a metal NP allows for the specific detection of proteins, which is an important aspect of the development of functional biosensors. It is well-known that the highest sensitivity is reached at the edges of NPs (e.g. the tips of a nanorod), where the electric field strength is the highest. The functionalization of specific facets is therefore an effective avenue to improve the sensitivity of single-particle sensors. Protocols already exist to specifically functionalize the tips of nanorods [25] by introducing a surfactant in solution during the NP functionalization (Fig. 3.9). Surfactants assemble into dense bilayers on flat surfaces, but these bilayers are more open near asperities or on surfaces with a high curvature radius (such as the tips of a nanorod). Due to the reduced steric hindrance, thiolated receptors diffuse more effectively to the tips of the nanorod, where the field is highest. Also the edges and vertex sites of Au nanoplates can be selectively functionalized by a thiol-exchange reaction, which occurs preferentially at the edges of the Au NP again because of the reduced steric hindrance [26]. The above described optimization of the sensitivity is an active area of research that will eventually enable researchers to routinely detect individual molecules without the need for labeling.

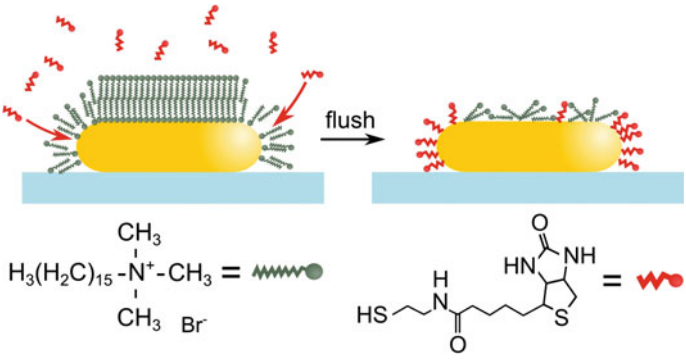

Fig. 3.9 Schematic showing the site-specific functionalization of gold nanorods. A dense bilayer of a surfactant (cetyltrimetheylammonium bromide, in *green*) provides steric hindrance that prevents the efficient functionalization of the side faces of a nanorod with thiolated biotin (*red*). This results in a particle that is mainly functionalized at its tips, which is also the area where the field-enhancement and thus the sensitivity to molecular binding is the highest. Note that the difference in surfactant density between the sides and the tip is exaggerated. Reprinted with permission from [25], Copyright (2012) Wiley-VCH

3.4.5 Emission Enhancements

Analogous to radio-frequency (RF) antennas, optical antennas efficiently convert free propagating optical radiation into localized energy, and vice versa. When an emitter, such as an organic dye or a semiconductor nanocrystal, is placed at the proper location in this high local field, the coupling between antenna and the emitter leads to enhanced single-fluorophore emission (Fig. 3.10). This enhancement near a plasmonic NP may arise from two factors:

(i) The lightning-rod effect (a non-resonant field-enhancement due to increased surface charge and crowding of electric field lines around sharp features) in combination with the presence of a surface plasmon leads to a high field enhancement in the vicinity of the NP. The excitation rate of the emitter can be enhanced by this high local field.

(ii) The antenna can also enhance the emission rate of a fluorophore. This Purcell effect arises from an enhanced density of optical states accessible for decay for a dipole, or, equivalently, from the enhancement of the dipole moment by electric currents in the NP antenna. The Purcell effect may not only change the intensity of the emission, but also its spectral shape, decay rate, and quantum yield. As metals also enhance non-radiative decay rates, they may also quench the emission [27] (Fig. 3.10). Quenching typically occurs for emitters placed within a few nanometers of the NP. The dipole field of the emitter then exhibits a strong field gradient at the location of the NP, causing the excitation of higher order plasmon modes. In contrast to the dipolar plasmon mode, higher order modes are poor radiators in small particles and

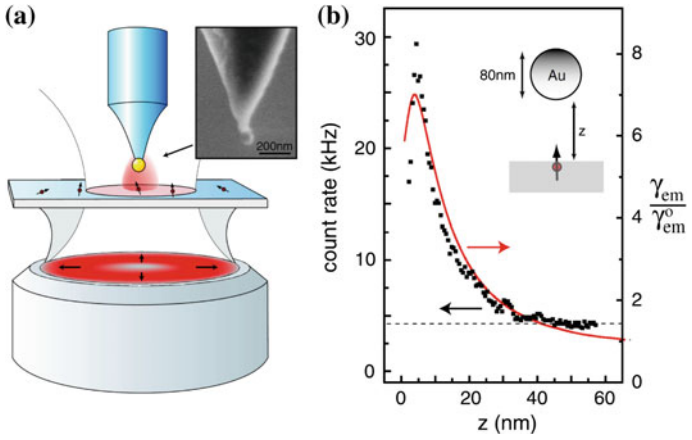

Fig. 3.10 **a** Optical setup used to characterize single-molecule fluorescence in the vicinity of a single 80 nm gold sphere attached to an optical fiber. **b** Fluorescence count-rate as a function of distance (z) between the fluorophore and the metal NP. The ratio between the emission rates in the presence (γ_{em}) and in the absence of the Au NP (γ^0_{em}) is also given (both enhancement and quenching are observed depending on z). Reprinted with permission from [27], Copyright (2006) by The American Physical Society

result in quenching of the fluorophores emission, and the energy is simply dissipated in the metal as heat. The balance between enhancement and quenching depends on the exact position and orientation of the fluorophore with respect to the NP, as well as on the NP size [28].

The main parameter that characterizes the emission enhancement is the magnitude of the local electric field, i.e. the degree to which the optical field is concentrated around the antenna (see also Sect. 3.3.1). For single NPs the field enhancements are modest: ~5 for a 20 nm Au sphere and ~50 for a 14 nm × 57 nm Au nanorod [29]. The field enhancement at asperities and metal tips can be significantly higher than for spherical particles due to the lightning rod effect (see above). Larger field enhancements are predicted in dimer junctions due to the hybridization of the plasmons of the two particles (see Sect. 3.5).

When assessing whether an antenna with its large field enhancement will enhance or reduce the brightness of a fluorophore, it is not enough simply to analyze the local field at the excitation and emission wavelengths. In addition, one has to take into account the intrinsic quantum yield (QY) of the isolated fluorophore. For "good" emitters (i.e., QY ≅ 1), any photon that is absorbed leads to exactly one output photon, and no further increase in QY is possible. Therefore, the antenna enhances brightness by increasing the effective excitation rate, directly resulting in a higher emission intensity (at least as long as no quenching of the emission occurs). In contrast, for "poor" emitters (i.e., QY << 1), the antenna can enhance both the excitation rate and the QY. A poor QY implies that for the isolated fluorophore the radiative rate is not competitive with nonradiative decay processes,

which are for instance enabled by the vibrational degrees of freedom in the emitter (organic fluorophores) or by Auger recombination processes (semiconductor nanocrystals). Accelerating the radiative decay through Purcell enhancement at fixed nonradiative decay rates means that radiative decay becomes more competitive, therefore effectively increasing the QY. Fluorescence intensity enhancements of 1,000 or more are easily reached when a poor emitter is positioned close to a single gold nanorod or a dimer antenna composed of two triangles in a bowtie-antenna configuration [30]. Nano-antennas therefore form a promising route to generalize single-molecule fluorescence imaging to emitters with low QYs.

Emission processes that scale nonlinearly with the local intensity profit enormously from the field enhancement around a nanoantenna. For example, surface enhanced Raman scattering (SARS) typically employs corrugations on a rough metal surface to enhance the Raman scattering signal, which scales as E^4. Enormous field enhancements of up to 10^3 are needed to amplify and detect Raman signals from single molecules. These enhancements are not easily obtained, and require selected asperities or sharp features on a rough metal film.

The large optical fields near a metal NP are also commonly employed for near-field imaging [31]. Near-field imaging is an approach to beat the diffraction limit in optical microscopy. The essential idea is that one of the ways to beat the diffraction limit of Abbe (resolution $\lambda/2NA$) to which far field optics are subject is to place a local nanoscopic reporter directly inside the sample under inspection. A plasmonic NP can be used as a near-field probe to interact locally with the sample. In a scattering based approach the evanescent component of the optical field at the sample is converted into propagating radiation by the scattering probe. By collecting this scattered radiation and mapping its strength, a spatial image can be collected by raster scanning the position of the probe. The region where the field is significantly enhanced is of the order of the size of the antenna, and sub-diffraction limited resolutions of 10–50 nm can be routinely achieved.

3.5 Clusters and Lattices of Metal Nanoparticles

While single NPs in isolation already provide a wealth of properties and applications, combining them into clusters or lattices provides even further benefits. When plasmonic NPs are brought together within distances of well below the wavelength, the plasmon resonances of the individual building blocks couple to form collective plasmon modes with novel properties. Following a seminal paper by Prodan et al. [32] this phenomenon is commonly known as plasmon hybridization. Plasmon hybridization allows to:

- Control at what wavelength collective plasmon resonances occur. Large shifts compared to the limited range of wavelengths achievable with just single particles are possible.
- Control the spectral linewidth of plasmon resonances.

- Introduce a strongly polarization dependent response.
- Achieve ultrahigh field strength.
- Control the directionality with which scattered light is reradiated.

In this section we first describe the concept of plasmon hybridization, and explain how spectral resonances can be tuned using hybridization (Sect. 3.5.1). Next, we validate the intuition of the plasmon hybridization approximation against exact calculations, and explain the relevance of plasmon hybridization for resonance linewidth (Sect. 3.5.2, applications in Sect. 3.5.3). In Sect. 3.5.4 the use of plasmonics to achieve ultrahigh field strengths is discussed. Directional antennas are treated in Sects. 3.5.5, and 3.5.6 finally discusses the extension of insights for finite clusters to infinite periodic lattices.

3.5.1 Plasmon Hybridization

By way of example, let us consider the physics of a plasmon dimer, a cluster of two identical plasmon particles with a volume V at a short center-to-center separation d from each other. In Sect. 3.3 we have established that a single plasmon particle responds to an incident field of strength $\boldsymbol{E}_{\text{in}}$ as a dipole with a dipole moment $\boldsymbol{p}$ set by a polarizability α that shows a clear resonance, according to (3.17). At very small separations d, one can approximate the field that the induced dipole $\boldsymbol{p}$ in a particle generates by its dominant near field term

$$\boldsymbol{E}_{\text{dipole}} = \frac{3(\boldsymbol{p}\cdot\boldsymbol{r})\hat{r} - \boldsymbol{p}}{4\pi\varepsilon_0 r^3} e^{-i\omega t}. \tag{3.22}$$

This equation contains the following physics: the scatterer oscillates at the same driving frequency ω as the incident field, falls off monotonically as $1/r^3$ as a function of distance r away from the center of the scatterer and has a distinct orientation dependence. On the axis along $\boldsymbol{p}$, the field is exactly parallel to $\boldsymbol{p}$, while on the axis transverse to $\boldsymbol{p}$, the field is antiparallel to $\boldsymbol{p}$ and twice weaker in strength. It is important to realize that this expression is approximate and only valid in the near field. Indeed, any radiating dipole also has a $1/r^2$ and $1/r$ field contribution that are both weaker at close range, but dominate further from the scatterer. Furthermore, at a distance larger than a fraction of the wavelength one should take into account that the radiated field is not everywhere in phase, but undergoes a retardation due to the distance it has to travel (replacing $e^{-i\omega t}$ by $e^{ikr-i\omega t}$). Suppose now that we quantify the response of a plasmon dimer where the dimer is illuminated with an incident field that is polarized along the dimer axis. Both particles will be driven directly by the incident field, and by each other. The responses of the two particles 1 and 2 hence follow from

$$\begin{aligned} \boldsymbol{p}_1 &= \alpha_1[\boldsymbol{E}_{\text{in}}(\boldsymbol{r}_1) + \frac{2\boldsymbol{p}_2}{4\pi\varepsilon_0 d^3}], \quad \text{and} \\ \boldsymbol{p}_2 &= \alpha_2[\boldsymbol{E}_{\text{in}}(\boldsymbol{r}_2) + \frac{2\boldsymbol{p}_1}{4\pi\varepsilon_0 d^3}]. \end{aligned} \tag{3.23}$$

Since the two particles will be polarized along the axis of the dimer, this coupling scenario is termed *longitudinal*. The above two equations can be rewritten in a matrix form as follows

$$\begin{pmatrix} 1/\alpha_1 & -2/4\pi\varepsilon_0 d^3 \\ -2/4\pi\varepsilon_0 d^3 & 1/\alpha_2 \end{pmatrix} \begin{pmatrix} \boldsymbol{p}_1 \\ \boldsymbol{p}_2 \end{pmatrix} = \begin{pmatrix} \boldsymbol{E}_{\text{in}}(\boldsymbol{r}_1) \\ \boldsymbol{E}_{\text{in}}(\boldsymbol{r}_2) \end{pmatrix}. \tag{3.24}$$

Substituting the Lorentzian form of the polarizability for each particle that is appropriate for a Drude metal (Eq. 3.11), one recognizes

$$\begin{pmatrix} \omega_{SPR}^2 - \omega^2 - i\omega\gamma & -6V\omega_{SPR}^2/d^3 \\ -6V\omega_{SPR}^2/d^3 & \omega_{SPR}^2 - \omega^2 - i\omega\gamma \end{pmatrix} \begin{pmatrix} \boldsymbol{p}_1 \\ \boldsymbol{p}_2 \end{pmatrix} = 3V\omega_{SPR}^2 \begin{pmatrix} \boldsymbol{E}_{\text{in}}(\boldsymbol{r}_1) \\ \boldsymbol{E}_{\text{in}}(\boldsymbol{r}_2) \end{pmatrix}. \tag{3.25}$$

We have now arrived at a linear set of equations that is formally equivalent to the physics of two pendulums that are coupled via the off diagonal term in the coupling matrix. In this analogy, the dipole moment $\boldsymbol{p}$ is equivalent to the pendulum amplitude, the driving force is the electric field $\boldsymbol{E}_{\text{in}}$ due to externally incident radiation, and the off-diagonal term essentially implies a coupling rate $6V/d^3\omega_{SPR}$. As in the pendulum case, this linear set of equations should be viewed as an eigenvalue problem, in which the eigenvalues $\omega_{\pm}$ correspond to the eigenfrequencies of the normal modes in the system. By bringing two identical plasmon particles close to each other, one expects the degenerate plasmon resonances to split into two distinct resonances. One of the resonances corresponds to a symmetric dipole configuration $\boldsymbol{p}_1 = \boldsymbol{p}_2$, where the dipole moments are aligned, while the second resonance corresponds to an antisymmetric configuration of dipole moments $\boldsymbol{p}_1 = -\boldsymbol{p}_2$. In analogy to the theory of hybridization of molecular orbitals, the symmetric mode is referred to as a *bonding* resonance, and the antisymmetric mode is called *antibonding*. The bonding mode is lower in energy, i.e., red-shifted relative to the bare plasmon frequency while the antibonding mode is blue-shifted. The eigenfrequencies (taking damping γ as zero) are

$$\omega_{\pm} = \omega_0\sqrt{1 \pm 6\frac{V}{d^3}}, \tag{3.26}$$

showing that the magnitude of the shift can be easily estimated by the dimensionless ratio V/d^3 of particle volume to the inverse separation cubed.

Figure 3.11 summarizes the level splitting in a graphical diagram. That the bonding combination is shifted to lower energy is intuitively understood simply by considering electrostatic energy arguments. Evidently, in the symmetric configuration, the

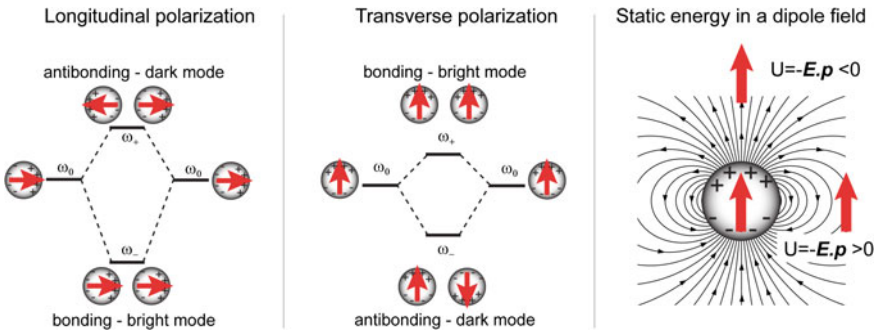

Fig. 3.11 (*Left panel*) Level scheme used to understand resonance hybridization in a plasmon dimer consisting of two identical particles in case of longitudinal polarization. (*Center panel*) Same in case of transverse excitation. The general intuition (*right panel*) is that the electrostatic interaction energy of a probe dipole in the field of a first dipole sets if a resonance redshifts or blue shifts. Whether a mode is bright or dark, simply depends on whether the total dipole moment vanishes, or is twice that of the single entities

dipoles are arranged head to tail, in such a fashion that each dipole moment is aligned with the field of its neighbor. Conversely, for the antisymmetric mode, a blue shift occurs due to the energy penalty that is associated with the antiparallel alignment of each dipole with the field of its neighbor. It should be noted in Fig. 3.11 that we have not drawn the energy splitting as symmetric around the unperturbed level. Firstly, this serves as a reminder that, different to first order perturbation theory for energy levels in quantum mechanics, in optics a square root enters (Eq. 3.26), which reduces the blue shift for large perturbations. Secondly, as the high-energy mode shifts towards the blue, the approximation that only the dipole mode contributes is increasingly violated, as the mode enters the range where the particles also have, e.g., a quadrupole resonance. Analysis including these multipoles indicates that the blue-shift is reduced compared to dipole intuition. Figure 3.11 also summarizes the level splitting for the so-called *transversely* coupled case. Suppose that we start from the same dimer, but that we illuminate it from a different direction and with a different polarization. If the incident field is polarized perpendicular to the dimer axis, both particles will obtain a dipole moment transverse to the dimer axis. The dipoles will again drive each other; however the interaction term reverses in sign and halves in strength for transverse coupling. In this case the symmetric eigenmode (dipole aligned) is blue shifted, while the antisymmetric eigenmode (antiparallel dipoles) is red shifted. In general, for illumination of a plasmon dimer under arbitrary polarization and incidence, a superposition of the longitudinal bonding and antibonding, as well as the transverse bonding and antibonding modes will be excited simultaneously.

This model is by no means rigorous, as it is limited to near field interactions, and a dipolar approximation. The intuition derived from hybridization will, however, generally be useful to interpret scattering spectra as well as exact numerical calculations, as long as we can consider plasmon particles to be small enough (radius $a \ll \lambda/2\pi$), close enough together for coupling to be via near fields (center-to-center

distance $d \ll \lambda/2\pi$), yet far enough apart that mutual driving yields no multipoles ($d > 2a$). Thus, plasmon hybridization has been applied to larger oligomers, clusters of anisotropic plasmon particles as well as 1D chains of particles at subwavelength spacing. Several authors have even used plasmon hybridization to understand more complex systems that do not have an obvious decomposition into dipolar scattering constituents. A prime example treated in the original work by Prodan et al. [32] is the core-shell NP that consists of a dielectric core, such as SiO_2, surrounded by a thin Au shell. If one views such a core-shell NP as the subtraction of a solid gold particle and a hole in a solid block of gold, one can view the shell resonances as a hybridization of the solid gold particle and the hole.

3.5.2 Validating Plasmon Hybridization Intuition

It is instructive to compare the simple formalism of plasmon hybridization as outlined above with the actual physics of coupled plasmon systems, as obtained from experiment or from rigorous calculations. Figure 3.12 shows rigorous calculations of the extinction of a plasmon dimer as a function of wavelength and as a function of separation, both for transverse and for longitudinal polarization [33].

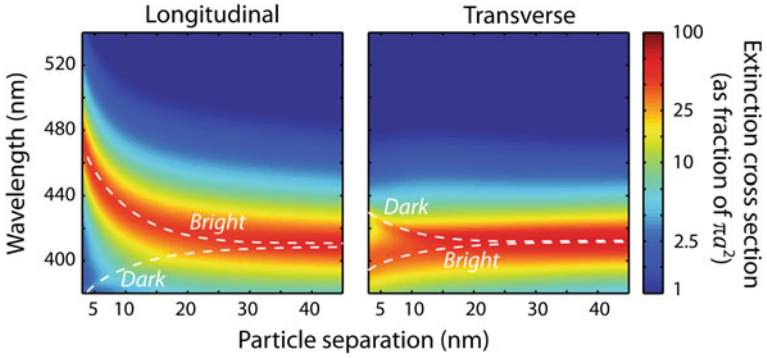

Fig. 3.12 Exact calculation using a generalized multipole expansion method of the extinction cross section of a plasmon dimer (NPs of radius a = 15 nm, embedded in a host of index 1.5, assuming a Drude model with $\hbar\omega p = 7.5$ eV and damping $\hbar\gamma = 0.05$ eV) for two excitation cases. The extinction cross section is normalized to the geometrical cross section of a single NP and plotted on a logarithmic color scale. *Left* excitation by a plane wave incident at almost normal incidence from the dimer symmetry axis, with polarization along the dimer axis. This polarization induces longitudinal dipole moments. The *left panel* hence shows the longitudinal hybridized resonances. At exact normal incidence the dark mode is not excited at all—at 10° off as in this calculation it is faintly visible. Right panel: excitation with polarization transverse to the dimer axis. By choosing an incidence angle at 45° off the dimer axis, both the bright and dark mode are excited. Note how the longitudinal case shows much larger frequency shift, and how the sign of the shift is reversed between the longitudinal and transverse (anti) bonding cases. *White dashed lines* are a guide to the eye. Calculations follow the method reported in [33]

The color scales clearly evidence the presence of two resonances that are degenerate at large separation, and split as the plasmon NPs approach. This basic result confirms the intuition gained by plasmon hybridization theory. For a quantitative comparison several hurdles need to be overcome.

The plasmon hybridization theory as we outlined above only predicts eigenfrequencies, and not the actual values of observables such as extinction. Nonetheless, the extinction calculated rigorously contains further features that we can qualitatively explain using the plasmon hybridization model. In particular we note that the two hybridized resonances are characterized by a highly unequal strength and a large difference in linewidth. To understand this difference we return to the arrangement of dipole moments that we identified as underlying the distinct resonances. Turning to the longitudinal resonance, the red-shifted mode corresponds to the symmetric combination $\boldsymbol{p}_1 = \boldsymbol{p}_2$ of dipole moments. This combination has a very large effective dipole moment $\boldsymbol{P} = \boldsymbol{p}_1 + \boldsymbol{p}_2 = 2\boldsymbol{p}_1$. Thereby, this mode radiates exceptionally well, and is easily excited using outside radiation. In contrast, the blue-shifted mode is antisymmetric $\boldsymbol{p}_1 = -\boldsymbol{p}_2$, and therefore has zero net dipole moment ($\boldsymbol{P} = \boldsymbol{p}_1 + \boldsymbol{p}_2 = 0$). The antisymmetric mode is hence a poor radiator. Moreover, it is not easily excited using external radiation, as it requires the incident field on the two closely spaced NPs to be applied out-of-phase. On basis of the magnitude of the total dipole moment, the symmetric longitudinal mode is called a *bright* plasmon resonance, while the antisymmetric mode is called *dark*.

In an extinction experiment, the difference between bright and dark plasmon resonances stands out in two ways. First, the bright resonance is most easily observed, due to the fact that coupling of the bright plasmon to incident radiation is strongest. Secondly, the bright and dark resonances have very different linewidths. The large difference in linewidth is easily understood if we consider the mechanisms by which the two eigenmodes lose energy. In case of the dark plasmon mode, the plasmon resonance only loses energy due to dissipation as heat as a consequence of the Ohmic damping of the metal. The damping of the dark plasmon can thereby be even less than the damping of the individual constituent particles: radiative damping that each NP may have is effectively canceled due to destructive interference of the radiated fields of the two dipole moments. Thereby the dark plasmon is referred to as "sub-radiant" (radiative loss lower than that expected for just one NP) and presents a rather narrow linewidth that is only limited by the Ohmic damping rate. Conversely, the bright plasmon loses energy both by Ohmic damping and by radiation damping. Owing to constructive interference of the radiated fields of the two dipole moments the radiative loss of the bright mode exceeds that of the individual NPs significantly. This effect is called *superradiant damping* and is easily understood as follows. Suppose we have N dipoles each with identical dipole moment $\boldsymbol{p}$. The radiated power is proportional to the total dipole moment squared and hence scales as $N^2|\boldsymbol{p}|^2$. The quadratic instead of linear scaling points to an interference effect that occurs when we coherently add the radiation of two dipoles. The fact that the loss *per dipole* increases proportional to N results in a broadening of the resonance, i.e., an increase in the radiative damping rate. For the dimer, the radiation damping doubles compared to a single particle.

3.5.3 Observation and Use of Dark Modes

Narrow linewidths could be especially desirable for spectroscopic and sensing applications. Firstly, when for instance sensing an analyte via frequency shifts, it is easiest to sense small shifts if the spectral feature that shifts is narrow. Secondly, by having lower loss and higher quality factors, dark resonances potentially store higher field densities in their near field. While dark modes can also be engineered in single NPs, i.e., by using higher multipole moments, plasmon hybridization provides a constructive design tool to engineer dark modes.

As a poignant illustration of the importance of dark modes that has been well studied in the plasmon literature, let us consider plasmon hybridization in a heptamer consisting of 7 plasmon NPs [34, 35]. This structure consists of a hexagon of NPs, surrounding a central one. Strictly speaking, since each plasmon NP has a 3-fold degenerate resonance (one for each axis), the heptamer has 21 normal modes. However, as the heptamer has the same symmetry as a benzene molecule, the 21 modes can be easily classified by symmetry. If we focus on modes that couple to excitation offered by in-plane polarized plane waves (as would be excited in a normal incidence optical experiment) only a small subset of eigenmodes participate. These are the combinations that in the vibrational spectroscopy of benzene would be coined 'infrared active'. Figure 3.13 shows the three infrared active eigenmodes that couple to *y*-polarized plane waves (in total there are 6 modes that couple to plane waves). The other 3 are obtained by a 90° rotation of all arrows in Fig. 3.13a). Due to the coupling between NPs, these three normal modes have both different eigenfrequencies and very different damping constants. The first mode has all 7 dipole moments approximately aligned and hence has a large damping

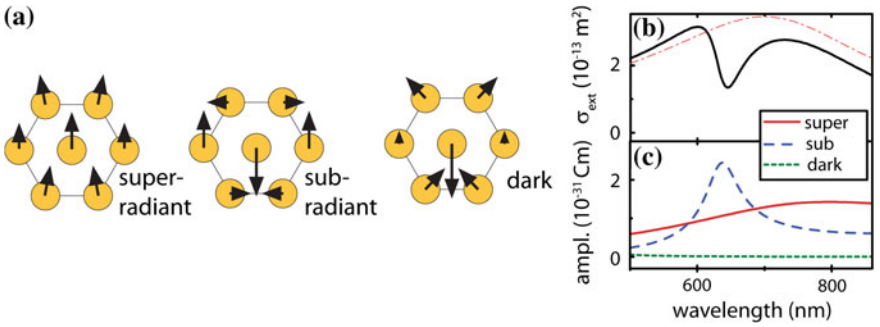

Fig. 3.13 Plasmon hybridization in a heptamer. **a** Arrows indicate the dipole orientation and strength for the three (out of 21) hybridized plasmon modes of a plasmonic heptamer (calculated for 100 nm Au NPs, spaced by 150 nm, in the irreducible representation E_{1u} that couples to normally incident plane waves with polarization oriented from *top* to *bottom* in this plot). **b** Extinction of the plasmon heptamer versus excitation wavelength. Dotted line indicates the extinction one would have in absence of the sub-radiant mode. **c** Amplitudes with which the three modes are excited (at 1 V/m incident field strength). Figure adapted with permission from [36]

corresponding to a 'bright' or 'superradiant' mode. The other two modes in contrast, have dipole moments that are not all parallel, and hence have a much smaller net dipole moment. One of these truly has zero net dipole moment and is hence 'dark'. The other has a residual net dipole moment that is not zero and is best described as 'subradiant'.

Figure 3.13b shows the calculated scattering spectrum of a plasmon heptamer [36] using a dipole model, which is in excellent agreement with, for instance, the experiment and full calculations of Hentschel et al. [35]. The scattering has a broad peak, due to the heavily damped superradiant mode. On top of this peak is a narrow feature, due to the subradiant mode. The one feature that is remarkable is that, although on the subradiant mode resonance the incident field causes a strong excitation of *two* modes instead of one, the scattering is *suppressed* and not enhanced. The physics is that of interference. The incident light drives a coherent superposition of two modes, which reradiate light out to the far field. The total scattered intensity is determined by the squared absolute value of the total reradiated field, i.e., the fields reradiated by the superradiant and subradiant mode. In this particular case, the interference of these fields is destructive, giving rise to an apparent *transparency* of the heptamer in scattering around the frequency where the subradiant mode is efficiently driven. As the phase of the response of the subradiant mode actually sweeps through 180^{o} as the frequency is swept through resonance, this interference reverses sign from constructive in the red part of the spectrum, to destructive in the blue part of the spectrum, as is evident when we compare the extinction in the presence and absence of the subradiant mode (dashed line in Fig. 3.13b). Due to the fact that interference between a broad and a narrow contribution is hidden in this scattering spectrum, the transparency window has been likened to 'electromagnetically induced transparency', as well as to the mathematics of Fano interference. Fano interference is the phenomenon that in any system of coupled oscillators with a broad and a narrow oscillator, the response to driving either one of the oscillators can show dispersive non-Lorentzian lineshapes as a consequence of a change from constructive to destructive interference in interaction with the second oscillator. The remarkably narrow plasmonic lineshapes of Fano interference due to plasmonic dark modes are attractive for sensing and spectroscopy applications, especially given that at transparency a substantial excitation energy is in the near-field, i.e. in the subradiant resonance.

3.5.4 Narrow Gaps Yield High Fields

For separations larger than a few nanometers, the dimer plasmons are well described by classical electromagnetic theory and field enhancements depend on the material, size and spacing of the particles. In the examples for single NPs and NP clusters that we have discussed so far, the field strength right at the interface of the metal is not exceedingly large. According to Eq. (3.13) the field strength right at the interface of a metal NP compared to the incident field strength $|E_{in}|$, is

approximately $3V\omega_0/\gamma r^3 \approx 4\pi\omega_0/\gamma$, which at optical frequencies amounts to about 10–50, depending on the choice of metal. Generally, improvements do occur with elongated NPs, giving rise to somewhat higher field enhancements at the sharpest ends. According to the simple plasmon hybridization theory outlined in Sect. 3.5.1, the field that is expected inside the gap of a plasmon dimer may exceed the single NP value by at most a factor 2 or so. If we examine a rigorous classical electrodynamic calculation of the electric field induced in a plasmon dimer when exciting it on resonance with the bonding mode, we indeed find a field enhancement in the gap that is larger than that for a single NP. Surprisingly, the enhancement significantly exceeds that predicted by the simple dipole model: the enhancement in fact reaches very high values that diverge to infinity for zero gap size in between the particles.

This observation points at the fact that a dipole approximation fails to describe the response of plasmon NPs when they are very close to each other. The approximately dipolar response of metal NPs in Sect. 3.3 was derived on the assumption that the driving fields are constant over the particle size. When the driving field has a strong gradient, multipoles are induced as well. For plasmon NPs such multipoles become increasingly important as the gap between NPs becomes less than their radius. In this regime, at very small separation, a large field enhancement occurs over a very small spatial range confined to the gap, corresponding to excitation of very high order multipoles. While the singular nature of touching geometries and sharp asperities make a general scaling argument to estimate field enhancements difficult, classical electrodynamic numerical simulations have shown that field enhancements $|E|/|E_0|$ of 100–1,000 times compared to the incident field strength can be reached in realistic scenarios, taking into account the radiative and Ohmic losses of metals. For gaps below 1 nm, quantum mechanical effects such as electron tunneling across the dimer junction and screening [37] significantly modify the optical response and drastically reduce the electromagnetic field enhancements relative to classical predictions, removing the divergence that occurs at zero separation. The high field-enhancements have been among the main drivers in the plasmon field, as they would allow spectroscopies such as Raman spectroscopy, which are characterized by weak signals that are very often masked by unwanted strong signals (e.g., fluorescence of the specimen), to be enhanced by many orders of magnitude. While the actual mechanisms that underlie so-called Surface Enhanced Raman Spectroscopy (SERS) on plasmon substrates are still under debate, there is consensus that high electric field enhancement in narrow gaps of up to $|E|^2/|E_0|^2 \sim 10^4$ or above can be routinely achieved.

By way of illustration, we discuss two examples of the use of plasmon oligomers, both shown in Fig. 3.14. The first concerns the well-known 'bowtie' antenna [38], that consists of two triangular metal particles in a bowtie arrangement, with a narrow gap in between them. Bowtie antennas combine the electromagnetic properties of sharp metal tips with those of coupled plasmon resonant NP pairs [30]. A closely related geometry is an antenna consisting of two metal nanorods placed tip-to-tip [39]. The coupling between the plasmon resonances in these geometries induces field enhancements in the gap region of up to 1,000. Such bowties can be

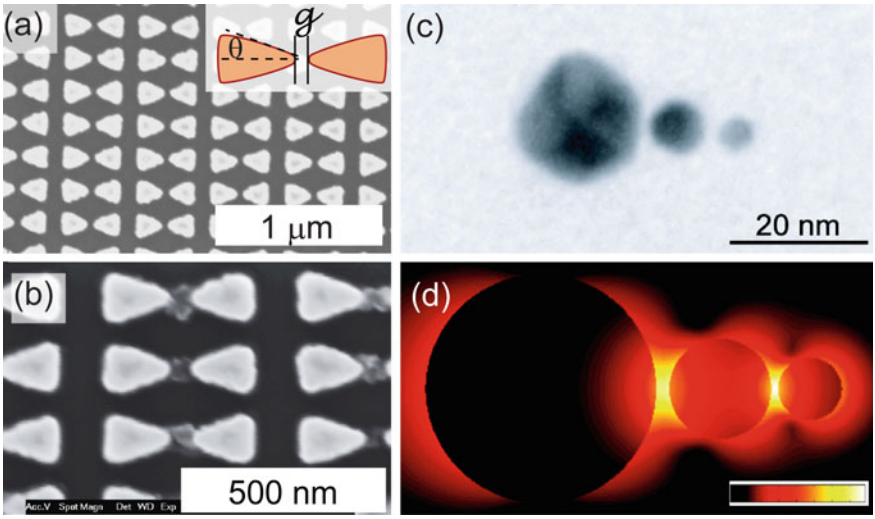

Fig. 3.14 Antenna geometries. *Left* SEM image of an array of bowtie antennas. In panel **b** we have visualized the field enhancement using a photopolymerizable resist (SU8 in this example). After exposure and development of the resist, polymer remains at the hot spots, i.e., in the antenna gaps. *Right panels* TEM image of a three-NP antenna created by functionalizing three Au NPs with complementary DNA strands. Hybridization of the strands allows selective formation of trimers with NPs of 20, 8 and 5 nm size, and 1–2 nm gaps. An electromagnetic simulation of the field intensity (|E|^2, on a logarithmic color scale covering 4 orders of magnitude) shows a tightly confined hotspot with 10^4 times enhancement of |E|^2. Note how inhomogeneous the field is inside the particles, evidencing that high order multipoles are at play. Panels (a, b) are modified with permission from [38], Copyright (2011) Optical Society of America. Panels (c, d) are reprinted with permission from [40], Copyright (2008) American Chemical Society

fabricated using state-of-the-art top-down lithography techniques with gaps that can reproducibly be smaller than 20 nm. Consistent with the ideas of plasmon hybridization, such antennas have a very strong response to incident light when excited with light polarized along the bowtie axis. The excitation drives the symmetric bright antenna mode, which is resonant typically at around 800 nm for gold bowties of $\sim$300 nm overall size. This resonance is red-shifted from that of the individual triangles, due to the elongated single particle shape and the longitudinal dipole moment alignment. The charge separation across the narrow gap implies that a very strong electric field is generated in the gap region. The high field enhancement of bowtie antennas has been evidenced in a set of experiments that include plasmon enhanced Raman scattering, fluorescence lifetime control, and the usage of bowtie antennas as near field scanning probes.

Instead of top-down lithographic fabrication of nano-antennas, an alternative approach uses self-assembly of colloidal NPs that have been synthesized in solution. A major advantage of using colloidal NPs for bottom-up fabrication of antennas is the crystalline nature of the NPs. The (near) absence of crystal defects reduces electron scattering and minimizes the additional damping of the plasmon oscillation. This can

result in higher field enhancements compared to lithographically fabricated structures, which are typically polycrystalline or amorphous. For example, experiments on an individual single-crystalline Au nanorod have shown fluorescence enhancements larger than 1,000-fold for single dye molecules (Sect. 3.4.5).

To achieve even higher enhancements, antennas consisting of multiple colloidal NPs can be assembled in solution and subsequently deposited on a substrate. Using thiol-linkers, Au NPs can be functionalized with single stranded DNA. By functionalizing NPs with complementary strands, oligomers of controlled composition can be formed, where the spacing between the NPs is set by the length of the DNA strand (on the order of 5 nm). For instance, this approach was used by Bidault et al. [40] to construct plasmon trimers consisting of Au NPs of diameter 20, 8 and 5 nm attached in a linear string with gaps of just 1–2 nm. The excitation of the large NP is converted into a strong hot spot in the gap with the next smaller NP. By virtue of the self-similarity, an even stronger hot spot is found in the opposing gap at the smallest NP. According to electrodynamic calculations, the field enhancement in the 1–2 nm gaps can be as high as 100, corresponding to a 10^4 times enhancement. Recent measurements of spontaneous emission of dye molecules localized in the gap [41] confirm the presence of very strongly enhanced fields. The compatibility of Au with DNA chemistry and the emergence of techniques like DNA origami means that arbitrary scaffolds for bottom-up fabrication of plasmon structures with ultrasmall gaps can be created.

3.5.5 Directional Scattering

As discussed above, plasmon oligomers are often called 'optical antennas' and likened to radio antennas. A large benefit of radio antennas is that they provide *directionality* to the process of sending and receiving radiowave signals. Plasmonic antennas can likewise impart directionality to emission and absorption of photons by single molecules, and other emitters such as semiconductor nanocrystals. To understand the physics, let us revisit the workings of the archetypical antenna for radio/TV waves that was designed by Yagi and Uda, which is treated in many antenna handbooks [42] and depicted in Fig. 3.15. The Yagi-Uda antenna consists of a set of dipolar scatterers that surround a single active element, i.e. a single current-carrying wire. The total size of a Yagi-Uda antenna is a few wavelengths, while the pitch between the elements is approximately λ/3. Scaled to optical frequencies, a Yagi-Uda antenna would hence be approximately 1 micron in size, and consist of plasmon NPs at pitches of 150 nm or so.

Let us try to assess how directionality comes about in such an array antenna. In the far zone, the field of N dipoles is the sum of far field dipole radiation of each scatterer. Let us consider a chain of N dipoles at equidistant separations d along the x axis, and with dipole moments of equal magnitudes $|\boldsymbol{p}|$ but different phases φ_m excited along the z-axis. In this case the far field factorizes as a spherical wave $\frac{e^{ikR}}{R}$,

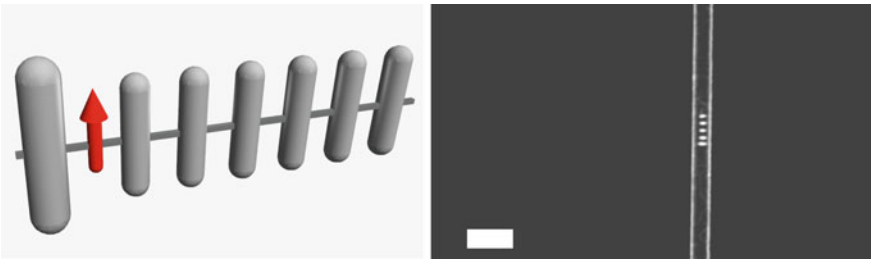

Fig. 3.15 *Left* cartoon of a Yagi-Uda antenna. For radio and TV waves such an antenna is meter sized, and consists of a single active element (*red arrow*, connected to current receiver/source) and a set of rods mounted on a linear mechanical support (thin rod). The vertical rods are cut to approximately λ/4 length, and the antenna pitch is at most λ/3. The longer rod is called 'reflector', while the set of smaller rods are called 'directors'. When driven (current through red element, which alone would be an isotropic radiator), the antenna radiates strongly along the axis of the antenna while no radiation emerges on the reflector side. *Right* scanning electron micrograph of a Yagi-Uda antenna with a response at optical wavelengths. The total length of the structure is just 1 micron. The five gold NPs (reflector on lower side of antenna) are fabricated using electron beam lithography on top of an optical waveguide, which is a 500 nm wide silicon nitride strip on a quartz surface. The antenna can interface nanoscale sources and detectors to guided modes that propagate in the dielectric strip

multiplied by the radiation pattern specific to z-oriented dipoles, multiplied by a *structure factor*

$$S = \sum_{m=1}^{N} e^{ik\hat{\boldsymbol{r}}\cdot\boldsymbol{r}_m} e^{i\varphi_m} \tag{3.27}$$

that accounts for the coherent addition of radiation of the N dipoles. The coherent addition contains both geometrical phase differences $e^{ik\hat{\boldsymbol{r}}\cdot\boldsymbol{r}_m}$ and the phase differences φ_m. Suppose for instance that one would be able to excite the N plasmon NPs with phase differences that increase linearly from element to element by an amount βd such that $\varphi_m = \beta m d$. At a viewing angle θ relative to the x-axis, the structure factor yields

$$|S|^2 = \left| \sum_{m=1}^{N} e^{imd[k\cos\theta+\beta]} \right|^2 = \left[\frac{\sin\frac{N}{2} d[k\cos\theta+\beta]}{\sin\frac{1}{2} d[k\cos\theta+\beta} \right]^2 . \tag{3.28}$$

This structure factor is very strongly peaked in a particular direction, namely the direction set by $k\cos\theta + \beta = 0$, especially when many elements are present. Figure 3.16 shows the structure factor for different array lengths. The sharpness of the structure factor around the peak emission angle increases with the number of dipoles N in the array, allowing for very narrow beams using long arrays. The reasoning outlined above for the radiation pattern of coherently radiating dipoles is commonly used as a design tool in radio antenna engineering. In radio antenna

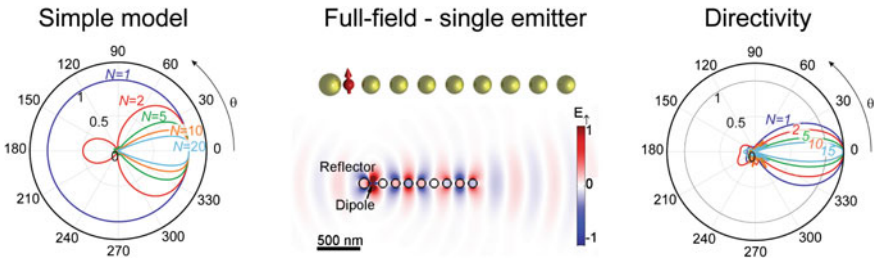

Fig. 3.16 (*Left panel*) Polar plot of the structure factor in Eq. (3.28) for a phased array in which the phase advance βd (with d the array pitch) from one dipole to the next is chosen exactly such that βd = kd = 2πd/λ. A single source is an isotropic emitter that radiates equally into all angles. A strong forward lobe develops for growing number of dipoles N. The angle θ is measured relative to the antenna axis. (*Center panel*) Electromagnetic field generated by a single emitter (radiating point dipole representing a single molecule) inside a plasmon antenna consisting of Au NPs embedded in a glass matrix, assuming a NP size of 100 nm and pitch of 150 nm. The field clearly shows that all NPs in the array are excited and carry large dipole moments, with a phase difference from NP to NP commensurate with the free space wavelength. The radiation of all these dipole moments plus that of the molecule itself add together in the far field to give a directional radiation pattern. (*Right panel*) Polar plot of the radiated intensity versus angle relative to the antenna axis for various numbers N of director NPs (note that there is always a reflector). Beyond N = 10 the radiation pattern does not improve further, as the number of NPs that the molecule can drive is limited. Figure adapted with permission from [46]

engineering, very often one can actually realize driving electronics that rigorously imposes a phase and amplitude on each of *N* dipoles in an array by controlling the magnitude and relative phase of currents driving each radiating wire in the radio antenna. No such luxury is available in plasmonics, as optics only allows a few distinct forms of driving, namely either by a local point source in the form of a fluorescent emitter, or in the form of an externally supplied incident beam. Controlling the phase of individual elements directly is hence impossible, since multiple fluorescent sources would not be coherent. However, the essence of plasmon antennas is that metal NPs that are near each other couple via dipole-dipole coupling. If we embed a single fluorophore in an array of NPs, it drives not only the metal NP that it is closest to, but the whole NP chain is excited. The field from the molecule, plus radiation from all the plasmon NPs finally need to be added together, and a directional radiation pattern ensues. In such a scenario the control parameters are firstly the choice of distances between NPs, and secondly a suitable choice of NP size and shape to engineer the magnitude and phase of the complex polarizability of each plasmon NP.

As discussed above, a particularly powerful example of the physics of such array antennas is the Yagi-Uda antenna [43–46]. Scaled to optical frequencies, it consists of a single emitter surrounded by a NP array. If the pitch of the array is chosen to be around a third of the operation wavelength, and the NPs are chosen to be just blue-shifted in resonance compared to the emitter, the molecule sets up a travelling wave in the NP array that has wave vector β almost equal to the free space wavelength. As a consequence, the antenna has a structure factor that is very highly peaked in

the forward direction, causing over 90 % of emission to be pointed in a forward lobe of small opening angle (around 20°). This type of optical antenna could be useful for creating single photon sources for secure quantum communication that are integrated in networks of dielectric waveguides. The benefit for microscopy on single molecules or single semiconductor nanocrystals, could be that fluorescence into a narrow radiation cone yields one to two orders of magnitude better collection efficiency, which would alleviate the need for expensive high NA microscope objectives. In principle, the antennas could be cheaply printed on a substrate using imprint nanolithography to replicate them from a lithographic master [47]. Thereby plasmon array antennas could potentially be useful to realize microscopy substrates that allow rapid fluorescence collection with cheap optics, and may improve the brightness of single photon sources that are based on single emitters. That the physics of Yagi-Uda plasmon antennas indeed works has been verified by Curto et al. [48]. In this experiment, Yagi-Uda antennas were fabricated on a glass slide, and one or a few quantum dots were lithographically grafted onto a single antenna element. The radiation pattern was found to be strongly peaked in a forward lobe. Due to the substrate, and contrary to the idealized calculation, this lobe is not, however, along the antenna axis, but points into the substrate under a 45° angle. While the structure factor for the Yagi-Uda antenna strongly peaks in the forward direction along the antenna axis, it is not sufficiently peaked to overcome the fact that on a substrate the single dipole radiation pattern is exceptionally strongly peaked into the direction of the critical angle (45° downwards into the glass).

The Yagi-Uda antenna is just one example of the usefulness of NP clusters to provide directivity to emission. Recently it has also been shown that 2D clusters of particles, as well as 2D clusters of holes in metal films, can similarly impart directionality on scattering and on emission by single fluorophores. The advantage of 2D systems is that directivity enhancement perpendicular to the substrate on which the cluster is deposited can be achieved, making such structures useful for fluorescence enhancement in microscopy applications. In general, current efforts in this direction use lithographically prepared structures because lithography allows to make structures with controlled dimensions (down to 5 nm error) at the required overall sizes that are approximately twice the wavelength (total size 1 or 2 μm). In principle, assembly of linear chains of metal NPs with a single emitter at a controlled location could also be possible using self-assembly techniques.

3.5.6 Lattices of Plasmonic Particles

Finally, we discuss infinite periodic lattices of plasmon scatterers. From our review of finite plasmon NP clusters, it is evident that arraying multiple objects together allows to sharpen resonances, shift resonances, and to obtain very high directionality. In particular, we mention the possibility to enhance sensing and spectroscopy through collective lattice resonances. The new physics in lattices compared to that of finite clusters is the appearance of very sharp optical features that are well known

in the physics of gratings as 'Wood's anomalies' and 'Rayleigh anomalies'. In the context of plasmonics these types of effects have been studied both in systems composed of metal particles in a transparent background, and in systems that possess the inverse geometry, i.e. holes perforated in thin metal films. This second case has opened the new field of 'Extraordinary Optical Transmission' spawned by the pioneering work of Ebbesen [49], but falls outside the scope of this book. We refer the reader to reviews on this subject [50, 51]. Here we discuss periodic arrays of plasmon NPs, a subject first studied in detail by the groups of Schatz and Van Duyne, and by Rivas et al. [52, 53].

The physics of two-dimensional periodic systems of NPs is best appreciated by turning once again to a point dipole model. Suppose that we have a lattice of identical NPs located on sites $\boldsymbol{r}_{pq} = p\boldsymbol{a}_1 + q\boldsymbol{a}_2$ where $\boldsymbol{a}_{1,2}$ are basis vector, and p, q are both integers. If the lattice is illuminated under normal incidence, this will cause all the polarizable particles to obtain the *same* dipole moment. This dipole moment is once again given by the incident field, plus the field of all dipoles in the lattice, such that (with θ_{pq} the angle between the induced moments $\boldsymbol{p}$ and the vectors $\boldsymbol{r}_p - \boldsymbol{r}_q$)

$$p = \alpha(\omega)\left[\boldsymbol{E}_{in} + \sum_{p\neq q} e^{ikr_{pq}}\left[\frac{3\cos^2\theta_{pq}-1}{4\pi\varepsilon_0 r_{pq}^3}\left(1-ikr_{pq}\right) + k^2\frac{\sin^2\theta_{pq}}{4\pi\varepsilon_0 r_{pq}}\right]p\right]. \quad (3.29)$$

This equation can be rewritten as

$$p = A(\omega)\boldsymbol{E}_{in},$$

with

$$A(\omega) = \frac{1}{1/\alpha(\omega) - S}, \quad (3.30)$$

i.e., as if we deal with a lattice of uncoupled particles, but with a renormalized polarizability $A(\omega)$that is determined by interactions in the lattice quantified by the lattice sum S

$$S = \sum_{p\neq q} e^{ikr_{pq}}\left[\frac{3\cos^2\theta_{pq}-1}{4\pi\varepsilon_0 r_{pq}^3}\left(1-ikr_{pq}\right) + k^2\frac{\sin^2\theta_{pq}}{4\pi\varepsilon_0 r_{pq}}\right]. \quad (3.31)$$

Note how the lattice sum S depends on the lattice geometry but *not* on any property of the single NPs. In case of oblique incidence with parallel wave vector $\boldsymbol{k}_{|,\mathrm{in}}$, i.e. under angle θ = asin ($|\boldsymbol{k}_{|,\mathrm{in}}|/k$), the phase factor $e^{ikr_{pq}}$ in the lattice summands is further modified to read $e^{ikr_{pq}+\boldsymbol{k}_{\|,\mathrm{in}}\boldsymbol{r}_{pq}}$. The lattice sum is not entirely trivial to calculate, as it requires a technique borrowed from solid state physics called 'Ewald lattice summation'. Indeed, readers may recognize the lattice summations from the well-

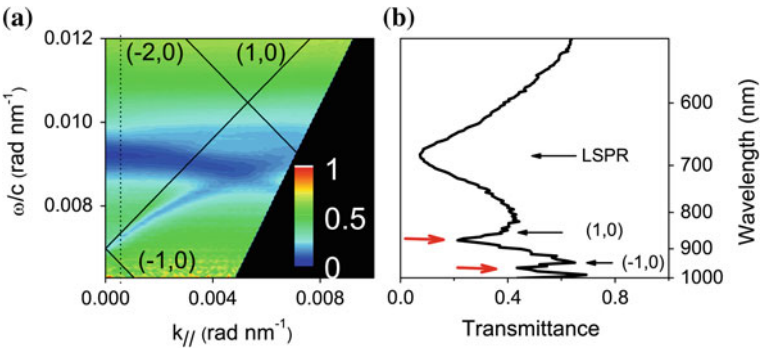

Fig. 3.17 Measured extinction for a lattice of plasmonic nanorods excited along their long axis as a function of incidence angle ($k_{//} = 2\pi/\lambda \sin\theta$) and incident wavelength. Panel B shows a cross cut at normal incidence. Figure reprinted with permission from [53], Copyright (2009) by The American Physical Society

known summation of electrostatic dipole interactions that occurs in evaluating Madelung constants.

An example of the measured extinction through a square grating of plasmon NPs on a substrate is shown in Fig. 3.17 as a function of wavelength ($2\pi/\lambda$ on the vertical axis) and incidence angle (actually $2\pi/\lambda\sin\theta$) on the horizontal axis. The measurement shows two distinct features. Firstly at around 680 nm wavelength (0.0092 rad/nm) a broad almost angle independent band appears in which transmission is suppressed. This band corresponds to the single NP resonance and is due to the resonance in $\alpha(\omega)$. Secondly, a narrow line crosses obliquely through the diagram. This narrow line is contributed by the lattice sum S, and occurs exactly when the lattice allows diffraction of the incident beam into a diffracted beam that lies in the lattice plane. Importantly, the lattice sum is strongly structured near each of these diffraction conditions, and furthermore is a *complex* quantity with both a real and an imaginary part. The real part causes the resonances of the array, i.e., the collective hybridized mode frequencies, to be shifted compared to the single NP plasmon resonance at each crossing between the angle-independent plasmon band and the angle-dependent resonances in S. The imaginary part of the lattice sum can cause a change in linewidth of the collective lattice plasmon resonance. For lattices with pitch *below* half the wavelength, i.e., lattices so dense that no grating diffraction can occur, the radiative damping is typically larger than that of single scatterers. This is caused by coherently oscillating dipoles that are in phase and are superradiantly damped, in analogy to the bright plasmon modes of a dimer (Sect. 3.5.2).

Remarkably, under certain conditions the lattice sum can completely cancel the radiative damping of the plasmon particle, giving rise to narrowing of resonance features. The physics is that just prior to the emergence of a diffraction order, the lattice supports a bound mode that is delocalized in 2D over the entire lattice, but bound in the third dimension. Since a significant proportion of the electromagnetic

field energy resides just *outside* the metal NPs, the loss rate is even lower than the Ohmic damping rate of the metal, giving rise to very sharp resonances.

Surface lattice resonances in 2D plasmonic arrays are pursued for a variety of applications. In optical sensing, the sensitivity is often expressed as a figure-of-merit (FOM) according to Eq. (3.21) that we defined for a single particle plasmon sensor. The FOM is greatly boosted for arrays by the fact that resonance lines can have a linewidth that is an order of magnitude below that of single NPs. Thereby 2D plasmonic arrays are very suited to measure surface covering layers of analytes that present a small index difference. In Sect. 3.4.4 we saw that single plasmon NP sensing can even register the binding and unbinding of single proteins through a resonance shift. In plasmon NP arrays this is fundamentally impossible, as one relies on probing an extended area. Nonetheless, fractions of a monolayer of deposited material can be in principle detected as a resonance shift.

Advantageously, large field enhancements outside the NP can be obtained due to the collective lattice resonance effect. Indeed, the first pursuits of plasmon lattices were focused on realizing substrates for reproducible SERS measurements. The groups of Schatz and Van Duyne were among the first to propose that so-called Fischer patterns, regularly used in the scanning probe microscopy community as topographical calibration samples, could be used for this purpose. Fischer patterns are obtained by first growing self-assembled hexagonally ordered close-packed monolayers of colloidal NPs on a glass substrate, and subsequently evaporating metal through the voids. Very reproducibly, a lattice of triangular particles with sharp tips and arranged in a pattern with hexagonal symmetry inherited from the colloidal lattice results. SERS signals from sub-monolayers of molecules (e.g. the DNA base adenine in [54]) can be obtained reproducibly in this manner.

Plasmonic lattices have also attracted interest as structures to improve the in- and outcoupling of light into high-index semiconductor structures. For instance, in the large emerging technology of solid state lighting, materials such as GaN and InGaN form the basis of powerful Light Emitting Diodes (LEDs). A significant problem in such LEDs is that the light is generated in a layer with very high refractive index (well above 2). Since the angle of incidence on the interface normal beyond which total internal reflection of light occurs is small for high refractive indices, most of the generated light is trapped, unless roughness or scattering layers are used to improve light outcoupling. Diffractive plasmonic lattices can be easily fabricated using for instance nano-imprint lithography on top of LED surfaces. The specific angle- and wavelength dependent resonances of such surface texturing can then be used to improve overall light extraction from LEDs for particular colors, as well as causing a redistribution of emitted light into particular emission angles. These strategies likewise extend to organic light emitting diode layers, where plasmon lattices help to enhance spontaneous emission decay rates.

Conversely to the case of improving light emitting devices, plasmon lattices have also been proposed for improving absorption of light by placing a lattice directly on top of, e.g., silicon photodiodes. Owing to their ability to redirect light via diffraction, plasmonic lattices increase the overall efficiency of thin photovoltaic cells [55]. Also, by suitable engineering of the shape resonances of the individual

particles narrowband color filter arrays have been fabricated directly onto the pixels of CMOS camera devices [56].

3.6 Exercises

1. Drude model for silver:
   (a) Calculate the plasma frequency from the electron density of silver.
   (b) What is the Drude damping rate, given the conductivity of silver at DC?
   (c) Prove that the polarizability of a silver sphere is a Lorentzian resonance.
   (d) Prove that inclusion of radiation damping (3.16) is formally equivalent to adding extra damping to the Ohmic damping. How large is the extra damping term? Plot the linewidth of the resonance as a function of particle diameter
   (e) Prove that the optical theorem holds if you use the polarizability of Eq. (3.16) in the limit of zero Ohmic damping: Scattering cross section = extinction cross section
   (f) Plot the "albedo", as a function of particle size, using the damping rate from (b), on resonance. The albedo (latin for "whiteness") denotes the ratio of scattering to extinction.
2. Silicon is a semiconductor that can be doped with both electrons and holes either by implanting donor/acceptor species, or by creating carriers thermally.
   (a) Suppose we consider n-type dopes silicon. What level of doping do we need to obtain a plasma frequency of 1 THz? Is this level of doping realistic?
   (b) For what size of particle is the dipole approximation still reasonable?
   (c) Plot the extinction cross section of an n-doped Si sphere with the doping from (a) and the size from exercise (b).
3. The optical properties of gold nanorods (which can be synthesized in large quantities in solution) are often approximated by assuming the shape to be prolate spheroidal (semi-major axis a, two equal semi-minor axes $b = c$).
   (a) Calculate the plasma frequency of gold. How does it compare to the plasma frequency for silver found in (1a)?
   (b) Plot the depolarization factors $L_{1,2,3}$ in the range of aspect ratios 1…5. What is the depolarization factor for an aspect ratio of 1, i.e. a sphere?
   (c) Calculate the scattering and extinction cross sections of a prolate spheroid with $a = 30$ nm and $b = c = 10$ nm, immersed in water (n = 1.33). Use the

Drude dielectric function for gold without radiation damping (see the caption of Fig. 3.1 for the relevant Drude parameters).

(d) How does the linewidth of this spheroid plasmon compare to the scattering linewidth of the 80 nm spherical particle plotted in Fig. 3.2b? What causes the broader linewidth for the sphere?

4. A single metal particle as a plasmonic biosensor.

(a) What determines the figure-of-merit (FOM) of a plasmon biosensor? Which shape gold particle would have a higher FOM, a sphere or a prolate spheroid with aspect ratio 4? Is the same true for silver?

(b) Assuming a Drude dielectric function, calculate the plasmon wavelength in the scattering spectrum for a gold prolate spheroid immersed in water (n = 1.33) with a semi-major axis of 20 nm and a semi-minor axis of 5 nm. Repeat the calculation for the same spheroid immersed in ethanol (n = 1.36).

(c) Calculate the FOM for this spheroid (Eq. 3.21).

5. Consider a dimer of two identically sized particles of volume V, at distance d. We use a Lorentzian expression for the polarizability and consider longitudinal coupling, as in Eq. 3.25

(a) Convince yourself that Eq. 3.25 is correct.

(b) In the text we set damping to zero to derive the resonances, and ignored radiation damping. The resonances are found by taking the determinant of the coupling matrix M (LHS of Eq. 3.25), and finding the roots. Here we consider a simple method to judge resonances in hybridization *including* damping. We use normalized units with $\omega_{SPR} = 1$, $\gamma_{Ohmic} = 0.01\ \omega_{SPR}$, V = 0.1 (meaning $V = 0.1(c/\omega_{SPR})^3$). Use a program such as Matlab, Octave or Mathematica to plot $1/|\det(M)|$ for various values of d between $\lambda/2\pi$ and $3\lambda/2\pi$ (i.e. d = 1 and 3 in normalized units) for frequencies from $0.5\ \omega_{SPR}$ to $1.5\ \omega_{SPR}$. Explain the resulting diagrams. What is the width of each peak?

(c) Now we introduce radiation damping through Eq. (3.16), which is equivalent to replacing the damping rate γ with

$$\gamma_{Ohmic} + 2/3\,\omega^2[V(\omega_{SPR})^2/c^3] = \omega_{SPR}[\gamma_{Ohmic} + 2/3\,(\omega/\omega_{SPR})^2[V(\omega_{SPR})^3/c^3]\,.$$

In our normalized units this means γ is replaced by $\gamma = 0.01 + 0.0667\,(\omega/\omega_{SPR})^2$. Again plot the absolute value of the inverse determinant. What happens to the peak height and width compared to c?

(d) In Fig. 3.12, which plots the response of a dimer upon plane wave excitation, the blueshifted mode is hardly visible. However, in (d), the blueshifted mode appears as a very narrow strong peak. Why does the blue-shifted

mode not appear in plane wave driving? Would it appear under other forms of driving?

References

1. Mie, G.: Beiträge zur Optik trüber Medien, speziell kolloidaler Metallösungen. Ann. Phys. **330**, 377–445 (1908)
2. Kreibig, U., Vollmer, M.: Optical Properties of Metal Clusters. Springer-Verlag, Berlin (1995)
3. Ashcroft, N.W., Mermin, N.D.: Solid State Physics. Brooks Cole (1976)
4. Johnson, P.B., Christy, R.W.: Optical constants of the noble metals. Phys. Rev. B. **6**, 4370–7379 (1972)
5. Palik, E.D.: Handbook of Optical Constants of Solids. Academic Press, Boston (1998)
6. Bohren, C.F., Huffman, D.R.: Absorption and Scattering of Light by Small Particles. Wiley-VCH, Weinheim (1998)
7. Kelly, K.L., Coronado, E., Zhao, L.L., Schatz, G.C.: The optical properties of metal nanoparticles: the influence of size, shape, and dielectric environment. J. Phys. Chem. B. **107**, 668–677 (2003)
8. Osborn, J.A.: Demagnetizing factors of the general ellipsoid. Phys. Rev. **67**, 351–357 (1945)
9. Sönnichsen, C., Franzl, T., Wilk, T., Von Plessen, G., Feldmann, J., Wilson, O., Mulvaney, P.: Drastic reduction of plasmon damping in gold nanorods. Phys. Rev. Lett. **88**, 77402 (2002)
10. Zijlstra, P., Orrit, M.: Single metal nanoparticles: optical detection, spectroscopy and applications. Rep. Progr. Phys. **74**, 106401 (2011)
11. Yguerabide, J., Yguerabide, E.E.: Light-scattering submicroscopic particles as highly fluorescent analogs and their use as tracer labels in clinical and biological applications—I. Theory. Anal. Biochem. **262**, 137–156 (1998)
12. Klar, T., Perner, M., Grosse, S., Von Plessen, G., Spirkl, W., Feldmann, J.: Surface-plasmon resonances in single metallic nanoparticles. Phys. Rev. Lett. **80**, 4249–4252 (1998)
13. McMahon, J.A., Wang, Y.M., Sherry, L.J., Van Duyne, R.P., Marks, L.D., Gray, S.K., Schatz, G.C.: Correlating the structure, optical spectra, and electrodynamics of single silver nanocubes. J. Phys. Chem. C **113**, 2731–2735 (2009)
14. Lindfors, K., Kalkbrenner, T., Stoller, P., Sandoghdar, V.: Detection and spectroscopy of gold nanoparticles using supercontinuum white light confocal microscopy. Phys. Rev. Lett. **93**, 37401 (2004)
15. Boyer, D., Tamarat, P., Maali, A., Lounis, B., Orrit, M.: Photothermal imaging of nanometer-sized metal particles among scatterers. Science **297**, 1160–1163 (2002)
16. Mooradian, A.: Photoluminescence of metals. Phys. Rev. Lett. **22**, 185–187 (1969)
17. Fujiwara, T., Ritchie, K., Murakoshi, H., Jacobson, K., Kusumi, A.: Phospholipids undergo hop diffusion in compartmentalized cell membrane. J. Cell Biol. **157**, 1071–1081 (2002)
18. Lasne, D., Blab, G.A., Berciaud, S., Heine, M., Groc, L., Choquet, D., Cognet, L., Lounis, B.: Single nanoparticle photothermal tracking (SNaPT) of 5-nm gold beads in live cells. Biophys. J. **91**, 4598–4604 (2006)
19. Ruijgrok, P.V., Verhart, N., Zijlstra, P., Tchebotareva, A.L., Orrit, M.: Brownian fluctuations and heating of an optically aligned gold nanorod. Phys. Rev. Lett. **107**, 37401 (2011)
20. Kyrsting, A., Bendix, P.M., Stamou, D.G., Oddershede, L.B.: Heat profiling of three-dimensionally optically trapped gold nanoparticles using vesicle cargo release. Nano Lett. **11**, 888–892 (2011)
21. Seol, Y., Carpenter, A.E., Perkins, T.T.: Gold nanoparticles: enhanced optical trapping and sensitivity coupled with significant heating. Opt. Lett. **31**, 2429–2431 (2006)

22. Zijlstra, P., Paulo, P.M.R., Orrit, M.: Optical detection of single non-absorbing molecules using the surface plasmon resonance of a gold nanorod. Nature Nanotechnol. **7**, 379–382 (2012)
23. Ament, I., Prasad, J., Henkel, A., Schmachtel, S., Sönnichsen, C.: Single unlabeled protein detection on individual plasmonic nanoparticles. Nano Lett. **12**, 1092–1095 (2012)
24. Sannomiya, T., Hafner, C., Voros, J.: In situ sensing of single binding events by localized surface plasmon resonance. Nano Lett. **8**, 3450–3455 (2008)
25. Zijlstra, P., Paulo, P.M.R., Yu, K., Xu, Q.-H., Orrit, M.: Chemical interface damping in single gold nanorods and its near elimination by tip-specific functionalization. Angew. Chem. Int. Ed. **51**, 8352–8355 (2012)
26. Beeram, S.R., Zamborini, F.P.: Selective attachment of antibodies to the edges of gold nanostructures for enhanced localized surface plasmon resonance biosensing. J. Amer. Chem. Soc. **131**, 11689–11691 (2009)
27. Anger, P., Bharadwaj, P., Novotny, L.: Enhancement and quenching of single-molecule fluorescence. Phys. Rev. Lett. **96**, 113002 (2006)
28. Mertens, H., Koenderink, A.F., Polman, A.: Plasmon-enhanced luminescence near noble-metal nanospheres: comparison of exact theory and an improved Gersten and Nitzan model. Phys. Rev. B. **76**, 1–12 (2007)
29. Liu, M.Z., Guyot-Sionnest, P., Lee, T.W., Gray, S.K.: Optical properties of rodlike and bipyramidal gold nanoparticles from three-dimensional computations. Phys. Rev. B. **76**, 235428 (2007)
30. Kinkhabwala, A., Yu, Z.F., Fan, S.H., Avlasevich, Y., Mullen, K., Moerner, W.E.: Large single-molecule fluorescence enhancements produced by a bowtie nanoantenna. Nature Photon. **3**, 654–657 (2009)
31. Novotny, L., Stranick, S.J.: Near-field optical microscopy and spectroscopy with pointed probes. Ann. Rev. Phys. Chem. **57**, 303–331 (2006)
32. Prodan, E., Radloff, C., Halas, N.J., Nordlander, P.: A hybridization model for the plasmon response of complex nanostructures. Science **302**, 419–422 (2003)
33. García De Abajo, F.J.: Multiple scattering of radiation in clusters of dielectrics. Phys. Rev. B. **60**, 6086–6102 (1999)
34. Fan, J.A., Wu, C., Bao, K., Bao, J., Bardhan, R., Halas, N.J., Manoharan, V.N., Nordlander, P., Shvets, G., Capasso, F.: Self-assembled plasmonic nanoparticle clusters. Science **328**, 1135–1138 (2010)
35. Hentschel, M., Saliba, M., Vogelgesang, R., Giessen, H., Alivisatos, A.P., Liu, N.: Transition from isolated to collective modes in plasmonic oligomers. Nano Lett. **10**, 2721–2726 (2010)
36. Frimmer, M., Coenen, T., Koenderink, A.F.: Signature of a fano resonance in a plasmonic metamolecule's local density of optical states. Phys. Rev. Lett. **108**, 077404 (2012)
37. Zuloaga, J., Prodan, E., Nordlander, P.: Quantum description of the plasmon resonances of a nanoparticle dimer. Nano Lett. **9**, 887–891 (2009)
38. De Hoogh, A., Hommersom, B., Koenderink, A.F.: Wavelength-selective addressing of visible and near-infrared plasmon resonances for SU8 nanolithography. Opt. Express **19**, 11405–11414 (2011)
39. Muskens, O.L., Giannini, V., Sánchez-Gil, J.A., Gómez Rivas, J.: Strong enhancement of the radiative decay rate of emitters by single plasmonic nanoantennas. Nano Lett. **7**, 2871–2875 (2007)
40. Bidault, S., García De Abajo, F.J., Polman, A.: Plasmon-based nanolenses assembled on a well-defined DNA template. J. Amer. Chem. Soc. **130**, 2750–2751 (2008)
41. Busson, M.P., Rolly, B., Stout, B., Bonod, N., Bidault, S.: Accelerated single photon emission from dye molecule-driven nanoantennas assembled on DNA. Nature Commun. **3**, 962 (2012)
42. Balanis, C.A.: Antenna theory: Analysis and design. Wiley Asia (2005)

43. Hofmann, H.F., Kosako, T., Kadoya, Y.: Design parameters for a nano-optical Yagi-Uda antenna. New J. Phys. **9**, 217 (2007)
44. Li, J., Salandrino, A., Engheta, N.: Optical spectrometer at the nanoscale using optical Yagi-Uda nanoantennas. Phys. Rev. B. **79**, 195104 (2009)
45. Taminiau, T.H., Stefani, F.D., Van Hulst, N.F.: Enhanced directional excitation and emission of single emitters by a nano-optical Yagi-Uda antenna. Opt. Express **16**, 10858–10866 (2008)
46. Koenderink, A.F.: Plasmon nanoparticle array waveguides for single photon and single plasmon sources. Nano Lett. **9**, 4228–4233 (2009)
47. Ji, R., Hornung, M., Verschuuren, M.A., Van de Laar, R., Van Eekelen, J., Plachetka, U., Moeller, M., Moormann, C.: UV enhanced substrate conformal imprint lithography (UV-SCIL) technique for photonic crystals patterning in LED manufacturing. Microelectron. Eng. **87**, 963–967 (2010)
48. Curto, A.G., Volpe, G., Taminiau, T.H., Kreuzer, M.P., Quidant, R., Van Hulst, N.F.: Unidirectional Emission of a quantum dot coupled to a nanoantenna. Science **329**, 930–933 (2010)
49. Ebbesen, T.W., Lezec, H.J., Ghaemi, H.F., Thio, T., Wolff, P.A.: Theory of extraordinary optical transmission through subwavelength hole arrays. Nature **391**, 667–669 (1998)
50. García De Abajo, F.J.: Colloquium: light scattering by particle and hole arrays. Rev. Mod. Phys. **79**, 1267–1290 (2007)
51. Garcia-Vidal, F.J., Ebbesen, T.W., Kuipers, L.: Light passing through subwavelength apertures. Rev. Mod. Phys. **82**, 729–787 (2010)
52. Zou, S., Janel, N., Schatz, G.C.: Silver nanoparticle array structures that produce remarkably narrow plasmon lineshapes. J. Chem. Phys. **120**, 10871–10875 (2004)
53. Vecchi, G., Giannini, V., Gómez Rivas, J.: Shaping the Fluorescent emission by Lattice resonances in plasmonic crystals of nanoantennas. Phys. Rev. Lett. **102**, 146807 (2009)
54. Hennemann, L.E., Kolloch, A., Kern, A., Mihaljevic, J., Boneberg, J., Leiderer, P., Meixner, A.J., Zhang, D.: Assessing the plasmonics of gold nano-triangles with higher order laser modes. Beilstein J. Nanotechnol. **3**, 674–683 (2012)
55. Atwater, H.A., Polman, A.: Plasmonics for improved photovoltaic devices. Nature Mater. **9**, 205–213 (2010)
56. Yokogawa, S., Burgos, S.P., Atwater, H.A.: Plasmonic color filters for CMOS image sensor applications. Nano Lett. **12**, 4349–4354 (2012)

Chapter 4
Nanoporous Materials and Confined Liquids

Petra E. de Jongh and Tamara M. Eggenhuisen

Abstract Nanoporous materials comprise zeolites, metal organic frameworks, disordered mesoporous oxides, ordered mesoporous oxides and carbon nanostructures. This chapter addresses the synthesis, structure and functional properties of each of these groups. Moreover, the changes in the physical properties of liquids confined in nanoporous materials are discussed. The altered properties of confined phases also form the basis for two important techniques to characterize nanoporous materials: physisorption and thermoporometry.

4.1 Introduction

Nanoporous materials contain pores with diameters up to 100 nm. Porosity is typically characterized by the specific pore volume (in cm^3/g) or porosity (in vol%), and the pore size distribution. As we will discuss below, the pore wall surface properties and specific surface area (in m^2/g) are also relevant parameters. Following IUPAC nomenclature, nanoporous materials are divided into three classes according to their dominant pore size range: ***microporous*** (up to 2 nm pores), ***mesoporous*** (2–50 nm pores) and ***macroporous*** materials (pores larger than 50 nm). This division is not always straightforward, as a single material can contain pores of different sizes (hierarchical porosity), and sometimes broad pore size distributions are found. Another important distinction is between ***ordered*** **and** ***disordered*** **porosity**. Ordered porous materials have a well–defined pore size, shape, and orientation. These materials are of great relevance for fundamental scientific research. Disordered materials have a random pore orientation, and generally wide pore size distributions. They are much easier to produce at low cost,

P.E. de Jongh (✉) · T.M. Eggenhuisen
Inorganic Chemistry and Catalysis, Debye Institute for Nanomaterials Science,
Utrecht University, Utrecht, The Netherlands
e-mail: p.e.dejongh@uu.nl

C. de Mello Donegá (ed.), *Nanoparticles*,
DOI 10.1007/978-3-662-44823-6_4

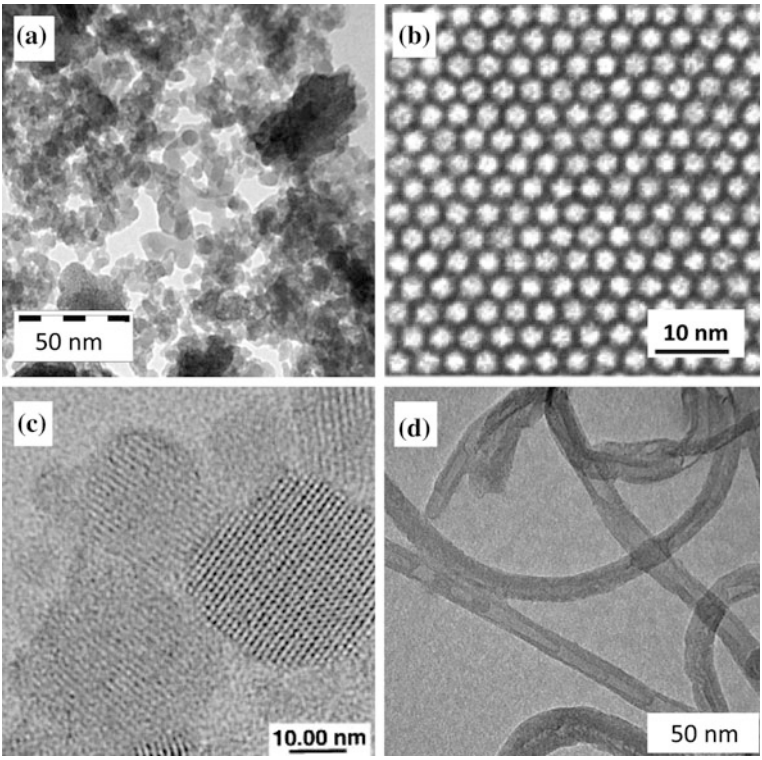

Fig. 4.1 Transmission electron micrographs illustrating the micro-structure of **a** disordered silica gel, adapted with permission from Ref. [1]; **b** ordered mesoporous silica (SBA-15), adapted with permission from Ref. [1]; **c** nanocrystals of microporous zeolite, reprinted from Ref. [2] with permission from the American Association for the Advancement of Science; and **d** an assembly of single walled carbon nanotubes. Note the different scale bars

and hence more relevant for practical applications. A few examples of porous materials are shown in Fig. 4.1.

Micropores have dimensions of the order of that of small molecules. Zeolites (crystalline aluminosilicates) form a prominent class of microporous materials. They can act as size-selective sieves or sorbents for small molecules. Most common mesoporous materials are ordered or disordered metal oxides, but also mesoporous carbons, nitrides, carbides, and metals are known. The mesopore range is the most interesting pore size range to study fundamental size and confinement effects. Mesopores allow the incorporation of nanoparticles, bulky organic molecules, biological species, and enzymes. Macroporous materials generally are not size-selective; their pores allow easy diffusion of even large molecules. They can be interesting for optical applications, but are also widely used as support or sorbent. In the second subsection of this chapter we will treat four main classes of nanoporous materials: zeolites, molecular microporous materials, ordered and disordered mesoporous oxidic materials, and nanostructured carbon materials.

Liquids may be confined in the pores of nanoporous materials, which significantly changes the physical properties of the liquid, such as the boiling and freezing points. Wetting and capillarity are key concepts to understand these changes, and will be discussed in detail in Sect. 4.3.

4.2 Classes of Nanoporous Materials

4.2.1 Zeolites

Zeolites are crystalline microporous aluminosilicates with pore sizes up to 1.5 nm. The term "zeolite" was first used by a Swedish mineralogist called Cronstedt in 1756, and is derived from the Greek words "ζεω" (to boil) and "λιθος" (stone). It refers to the large amount of water released upon heating zeolites. The water is present in the pores at ambient conditions due to the small pore size and high hydrophilicity. Zeolites can be mined in vulcanic regions, but have also increasingly been produced synthetically since the 1940–1950s. Nowadays almost 200 zeolite structures are known. Detailed information about zeolite structures and properties can be found at the authoritative website of the International Zeolite Association (IZA) [3]. Zeolite structures are identified by 3-letter codes, which are abbreviations of their full name. The structures of sodalite (SOD), faujasite (FAU, also called "zeolite Y") and mordenite (MOR) are shown in Fig. 4.2. New zeolite structures are still being discovered and accepted by the IZA Structure Commission after proof of synthesis details and structural characterisation. Although most structures are based on Si frameworks containing Al, a few all-silica as well as differently composed zeolitic structures are known, for instance alumina-phosphates (ALPO's) with Al^{3+} and P^{5+} alternating in the lattice. Zeolites find many applications: on a scale of several million tons/year in detergents, as selective sorbents in the food and pharmaceutical industry, agriculture, as ion-exchangers, and as catalysts and catalyst supports.

Zeolites are synthesized hydrothermally from precursors such as amorphous alumino-silicates or metal organic molecules [4]. Porosity is induced by the presence of templates (for instance alkyl ammonium ions, small molecules or ion pairs) during the crystal growth. The formation of zeolites takes place in three stages, similar to those observed in the formation of colloidal nanoparticles (see Sect. 6.3.3, Chap. 6 for details). In the ***induction stage*** the solution is equilibrated at lower temperature. ***Nucleation*** is critical: for a synthesis solution with a given composition often several different zeolite structures can be grown depending on experimental conditions (kinetic control). Therefore, meticulous control over the synthesis conditions is required and the solution should be very homogeneous in pH, concentrations, and temperature. Often seeds are used to steer the nucleation process. ***Crystal growth*** is slow, and generally takes several hours up to days even at the typical hydrothermal conditions (100–150 °C, autogeneous steam pressure).

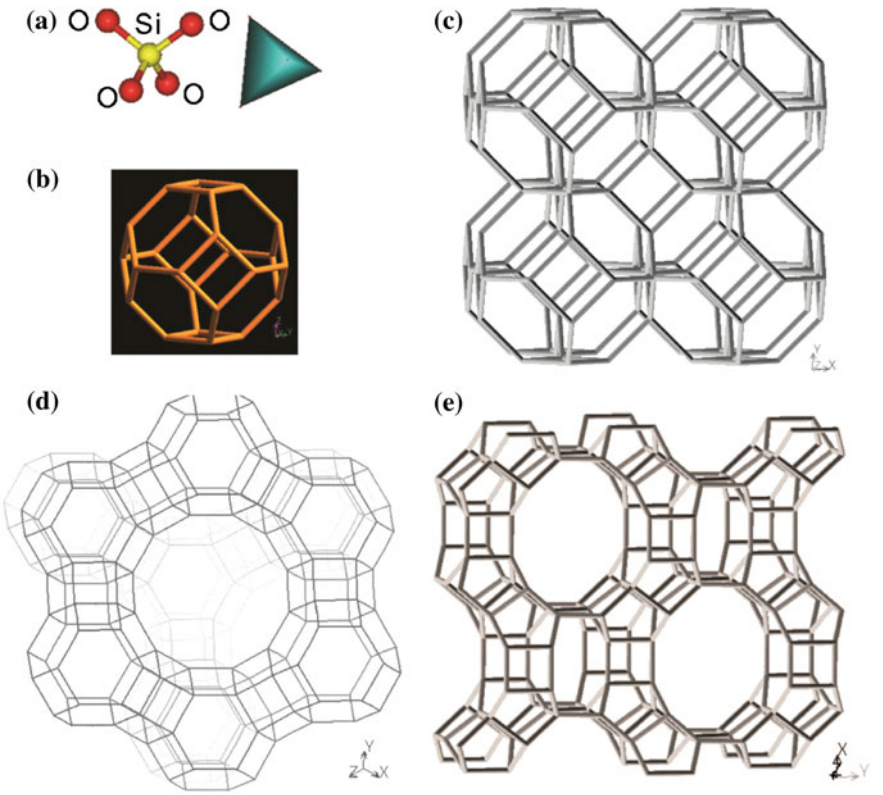

Fig. 4.2 TO_4 unit (**a**) is the primary building block that is used to construct larger composite building units such as the sodalite cage (**b**). These units can be arranged in different crystalline structures: (**c**) sodalite (SOD), (**d**) faujasite (FAU) and (**e**) mordenite (MOR). The structural models are not space filling: lines connect the metal cations in the structure, the oxygen anions are not represented. Images adapted with permission from Ref. [3]

After cooling, washing and filtering, the template is usually removed from the pores of the zeolite by heat treatment under air or inert atmosphere.

The primary building block of the zeolite structure is the TO_4 unit, a tetrahedron consisting of a central metal cation (usually Si^{4+}) and four (much larger) oxygen anions. The tetrahedra can be connected in different ways to form a 3-dimensional structure by sharing corners, edges or planes. Figure 4.2a schematically illustrates how different zeolitic structures can be assembled. By combining primary building blocks, secondary building blocks can be constructed, such as flat 4- or 6-rings. These can then be further assembled in larger composite building units, such as the sodalite cage (Fig. 4.2b), which consists of 4 flat 6-rings of tetrahedra (or alternatively 6 flat 4-rings). Arrangement of these larger units into the crystalline zeolite structure determines the porosity of the zeolite, comprising cages, cavities and/or

channels. Sodalite (Fig. 4.2c) and faujasite (Fig. 4.2d) structures are both based on sodalite cages, but have different porosities. In Fig. 4.2e we see mordenite, another common zeolite, which is constructed out of 5-1 building blocks (a five-ring of tetrahedra with one extra tetrahedron connected).

An important parameter is the *size* of the pores, cages or cavities in the structure, which can be derived from the number of tetrahedra forming them. Another important characteristic is the ***dimensionality of the porosity***: in how many dimensions can a small molecule (about 0.3 nm wide) cross the zeolite through the pores. The sodalite cage has an inner diameter of 0.63 nm, which is large enough to host an organic molecule. However the 6-ring entrances only offer an opening of 0.25 nm; no molecule larger than water can travel through sodalite hence sodalite has zero-dimensional porosity. In contrast, the sodalite cages in faujasite are arranged such that larger cavities and windows are created. The cages can host species up to 1.12 nm, while the windows are 0.74 nm. Faujasite, like most other zeolites, has a 3-dimensional porosity. Mordenite has parallel channels of about 0.65 nm, and hence one-dimensional porosity.

A last important feature that describes a zeolite structure is the *symmetry* of the porosity, which is also relevant for metal organic frameworks and ordered mesoporous materials. Like the symmetry of a crystal lattice, the symmetry of an ordered nanoporous material provides information about the spatial arrangement of the pores. It is based on the smallest unit cell that can be used (by translation) to describe the entire 3D pore structure (space filling). For sodalite (Fig. 4.2c) the centres of 8 sodalite cages form the corners of the cubic unit cell. The full symmetry (space group) of each structure is denoted by 4 symbols, which give the symmetry elements that can be found in the unit cell. As an example: sodalite is designated "*Im3 m*", which means that its cubic unit cell has inversion symmetry ("*I*") as well as mirror planes ("*m*") and a three-fold rotation axis along the body diagonal ("*3*"). Identification of pore symmetries is based on X-ray crystallographic data, and in recent years has been supplemented by advanced electron microscopy methods.

The exact chemical composition of zeolites can vary, a property that is the basis for two major applications. Though the structure is based on SiO_2, the Si^{4+} ions can be replaced by other metal cations that are small enough to favor tetrahedral coordination. Most common is replacement of part of the Si^{4+} ions by Al^{3+} ions. This leaves a net negative charge on the framework, which is compensated by cations present inside the pores, typically protons or small alkaline or alkali earth ions such as Na^+ or Li^+. These cations are easily exchanged by other cations. For instance when zeolites are applied as "softener" in detergents, they exchange the Ca^{2+} or Mg^{2+} cations in "hard" water for cations that lead to more soluble salts (e.g., Na^+). Another major industrial application of zeolites is as acid catalyst for instance for (hydro)cracking and isomerisation reactions, in which intrapore protons provide acid catalytic sites.

4.2.2 Metal-Organic and Organic Microporous Materials

Zeolites are found in nature and have been known for centuries. In contrast, metal-organic frameworks (MOF) form a relatively new class of materials, which can only be obtained synthetically [5, 6]. Like zeolites, MOF are ordered microporous crystalline materials but they consist of metal ion complexes ("nodes") that are connected by organic bridging ligands ("linkers"). Although polymeric porous materials had been known for some time, only in 1995 compounds containing dicarboxylate units were reported that were structurally stable upon removal of the solvent and thermal treatment.

Figure 4.3 shows the structure of MOF-5, one of the most studied MOF's, which consists of $Zn_4O_6^+$ nodes and benzene-1,4-dicarboxylate linkers, forming a cubic lattice with cages of 1.2 nm that are accessible via 0.8 nm windows. The pore size, geometry and also the chemical and physical properties of MOF can be varied by choosing different linkers and nodes, and the theoretical number of structures that can be formed is enormous. 15 years after their discovery already more than 10,000 structures are known. One of the important structural differences with zeolites is that the primary building blocks are not limited to tetrahedra. A node can be connected to 2, 3, 4, 5, 6 or 8 linkers in different geometric configurations, while the linkers can bridge 2 nodes or more, allowing for an almost unlimited variety in structures.

The nodes in MOF are complexed metals (Zn, Cu, Co, Ni, Mg), while the linkers are organic ligands which often comprise N atoms. Some MOF can be synthesized hydrothermally, but solvothermal synthesis (growth in non-aqueous solution) is more common. Generally growth of the crystal is slow (in the course of days) starting from solutions containing metal precursor salts such as nitrates, and organic ligands. Additional templates can be used to induce porosity, but often the solvent molecules themselves act as template.

Post-synthesis modification is widely applied to induce functionality by covalently attaching extra groups to the organic ligands, or by incorporating nanoparticles or ions. MOF can be surprisingly stable upon solvent removal and further heating, but

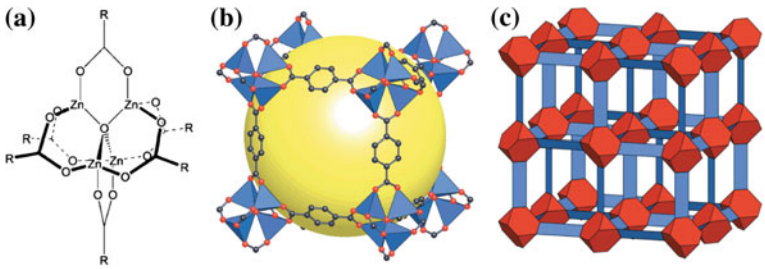

Fig. 4.3 **a** Structure of the Zn_4O node and carboxylic linkers in MOF-5; **b** MOF-5 cage of 1.2 nm (indicated by the sphere) which is accessible via 0.8 nm windows; **c** MOF-5 has a cubic unit cell arrangement. Reprinted by permission from Macmillan Publishers Ltd: Nature, **423**, 705–714 (Ref. [6]), copyright (2003)

generally only in inert atmosphere (without water or oxygen). As they are composed of light elements, MOF can reach pore volumes as high as 2–3 cm^3/g, and specific surface areas up to 3,000–6,000 m^2/g. They are considered for a variety of applications in separation and reversible gas storage, as well as for catalytic, optical, and magnetic applications. The functionality is either inherent to the metal-organic framework, or due to guest species that are introduced into the cages. However, practical relevance still has to be proven. At present MOF are expensive, as most organic linkers are not commercially available. Also the limited stability and poor mechanical properties are a disadvantage for many applications.

In 2005 it was reported that also all-organic ordered nanoporous frameworks (Covalent Organic Frameworks, COF) could be synthesized [7]. An example is COF-1, which is based on diboronic acid units which are connected by a condensation reaction to form covalently bound planar and rigid sheets. These sheets self-assemble (bound by mostly van der Waals and also electronic interactions) into ordered 3-dimensional porous structures. Because COF are made of light elements, their porosity and specific surface area rival those of MOF (e.g. ~ 1 cm^3/g and $\sim 1{,}600$ m^2/g for COF-5). A porous network that is covalently bound in three dimensions can be formed when using building units with four connections such as tetra(4-di-hydroxylborylphenyl)methane (TBPM).

Shortly after the discovery of COF's another class of crystalline microporous solids was reported: zeolitic imidazolate frameworks (ZIF's). The stability of these materials is quite high compared to MOF. For instance, ZIF-8 and ZIF-11 are stable if boiled in alkaline solution, or heated up to temperatures of 550 °C. ZIF combine some of the properties of zeolites with those of MOF. They are based, like MOF, on metals (usually Zn, Co or Cu) and organic linkers. However, the organic linker is always an imidazolate unit, a conjugated 5-ring which contains 2 nitrogen atoms. The imidazolate unit binds to two transition metal atoms with a fixed bond angle very close to that of the Si–O-Si bonds in crystalline silica and zeolites (109^o). As a result the framework structures, and hence pore symmetries, follow those of the zeolites. For instance ZIF-67 and ZIF-8 have the same framework and pore symmetry as the zeolite sodalite (*Im3 m*), but contain Zn (ZIF-67) or Co (ZIF-8) metal ions. By choosing different imidazolate linkers the pore or cage size can be tuned systematically. The number of ZIF is rapidly expanding, with close to 100 reported within the first 5 years after discovery.

4.2.3 Disordered Mesoporous Metal Oxides

Disordered metal oxides form a class of nanoporous materials that is widely used in industry. The nanoporosity of these materials is typically formed by interparticle spaces: primary particles of a few to a few tens of nanometres aggregate into μm-sized secondary particles. This results in an interparticle mesoporosity of 0.1–0.3 cm^3/g. The porosity is not well-defined; it comprises different pore shapes and generally a wide pore size distribution. Therefore, these materials are of less

interest for fundamental studies than the ordered mesoporous materials that will be treated in the next Sect. 4.2.4. Two synthesis strategies are generally employed to prepare disordered metal oxide materials: solution (usually aqueous phase) synthesis or gas phase synthesis. Porous silica (used as filler material, desiccant, chromatography stationary phase, and catalyst support) is used as an example, but other porous metal oxides can be prepared in similar ways, and especially the solution-based route is also relevant for the ordered mesoporous oxides discussed below (Sect. 4.2.4).

A first preparation strategy is gelification from aqueous silicate solutions [8]. Natural sodium silicates can be dissolved in alkaline solution, forming a multitude of species such as $Si_2O_7^{6-}$, $Si_3O_{10}^{8-}$ and cyclic structures such as $Si_4O_{12}^{8-}$. Solubility in neutral and acid solution is low, hence acidification of the solution (for instance by adding H_2SO_4) or alternatively evaporation of the solvent, leads to the formation of a solid by condensation:

$$\equiv \text{Si-OH} + \text{HO--Si} \equiv \rightarrow \equiv \text{Si--O--Si} \equiv + H_2O$$

The condensation is governed by parameters such as temperature, concentration of the different species, and especially pH. At high pH the silicate species or hydroxyl surface groups of formed silica particles are deprotonated and hence negatively charged. As a result they repel each other. As the silicate solubility is also high, the dominating growth mechanism is Ostwald ripening by the preferential addition of monomeric silicates (which might originate from the dissolution of smaller particles) to larger particles, leading to spherical crystalline SiO_2 particles. At a low pH, close to the isoelectric point of silica (pH = 2–3), the species and particles are net uncharged. As condensation is slow and the growing species are not stabilized by electric repulsion, 3D aggregated networks with small pores are formed.

Very pure (and more expensive) porous silica can be obtained starting from metal-organic precursors, such as tetra-ethoxy-silane, $Si(OC_2H_5)_4$ (TEOS). In this case the condensation reaction is preceded by hydrolysis of the precursor:

$$Si(OR)_4 + H_2O \rightarrow Si(OH)_4 + 4ROH$$

but still the final product is SiO_2 as the organic group is removed as an alcohol. This route also allows the formation of hybrid inorganic-organic materials with a lower degree of condensation, by introducing non-hydrolysable groups such as methyl-trimethoxy-silane in the precursor. The incorporation of organic groups leads to higher hydrophilicity and different mechanical properties (more flexibility) of the material.

Nanoparticles can be observed once they have grown large enough to induce light scattering, while the formation of 3D networks becomes evident from a viscosity increase of the solution and gel formation upon prolonged reaction. It should be noted that the reaction can be stopped at the early stages allowing the preparation of free-standing allowing the preparation of colloidal silica nanoparticles as small as

10–20 nm as well as encapsulation of nanoparticles of other materials (e.g. gold or semiconductors) inside silica shells (see Chap. 6 for details). A very suitable technique to follow the progress of condensation is ^{29}Si NMR, which detects quantitatively the concentration of Si in different condensation states: e.g. Si(O) (not bound to any other Si atom via an oxygen), Si(I) (having formed one Si–O-Si bond), and fully condensed Si(IV) (forming the tetrahedral Si–O-Si coordination also found in quartz). After reaction the solid product is filtered and washed, and generally heated in inert atmosphere to further increase the degree of condensation in the materials. A wide range of metal oxides can be prepared via sol-gel chemistry in aqueous solutions. However most metal ions are more electropositive than silicon, leading to faster reaction and limited control over the particle morphology and hence porosity.

An alternative preparation route for metal oxide nanoparticles is via a gas phase reaction. A good example is the so-called Aerosil® process in which the starting material is a macroscopic silica such as sand. It is converted into the silica precursor by carbo-chlorination:

$$SiO_2 + C + 2Cl_2 \rightarrow SiCl_4 + CO_2$$

In a second step the gaseous silicon tetrachloride is converted into silicon dioxide at high temperatures (typically $\sim$1,000 °C) by reaction with methane and oxygen, or alternatively with water ("flame hydrolysis") which is formed in situ by co-feeding H_2 and O_2:

$$SiCl_4 + H_2O \rightarrow SiO_2 + 4\ HCl$$

The primary particle size (and hence the pore size in the resulting aggregates) is tuned by choosing the reaction conditions such as temperature, concentrations, and residence time in the flow through reactor. In addition to SiO_2, TiO_2, Al_2O_3 and ZrO_2 are also routinely prepared by flame hydrolysis.

For the production of nanoparticulate metal oxides it is important to realize that for many of them different polymorphs exists. Preparation of the final material generally involves heat treatment, and phase transitions can occur leading to a rearrangement of atoms and loss of the porosity that had been induced at room temperature. Typical examples are the anatase to rutile phase transition of TiO_2, and the different polymorphs of Al_2O_3 sequentially formed upon heating.

4.2.4 Ordered Mesoporous Materials

In 1992 a new type of mesoporous material was reported that cannot be found in nature: ordered mesoporous silica. To prepare them, silica is grown in aqueous solution in the presence of surfactant molecules that have been added in such a high concentration that they form ordered micellar structures [9]. After filtering and

drying the template molecules are removed (combusted by heating in air, or leached out with, for instance, an acid). The imprint left by the micellar structure leads to 3D ordered mesoporosity in the silica. An important difference with zeolites (Sect. 4.2.1) is the size of the pores. Zeolites are microporous, having pores up to about 1.5 nm, while the pore sizes of ordered mesoporous silica are in the 1.5 to 50 nm range. Also, although the pore structure is ordered, the silica itself that forms the pore walls is amorphous, in contrast to zeolites which are crystalline. This limits the (hydro)thermal and mechanical stability of these materials.

Ordered mesoporous materials are commonly used for fundamental studies as their pore geometry and size are well defined and can be easily tuned by varying surfactant chain length, concentration, pH, temperature and solvent. Above the critical micelle concentration, surfactant molecules form isotropic micelles which upon further increase in concentration arrange into hexagonal, cubic or lamellar arrays. This provides a wealth of possible geometries, which can be "inverted" by using an apolar rather than a polar solvent to grow the metal oxides. Lamellar structures are generally not stable after surfactant removal.

The ordered mesoporous silica material MCM-41 is one of the earliest and most prominent examples. MCM-41 stands for "Mobil-Composition of Matter—No 41", as Exxon Mobil was the first to report its synthesis in open literature [10]. As illustrated in Fig. 4.4, MCM-41 is templated by a cationic surfactant: cetyltriammoniumbromide (CTAB, cetyl = hexadecyl). These template molecules form tubular micelles, resulting in parallel pores aligned in a hexagonal symmetry (*P6 mm*). The pore size distribution is narrow and around 2 nm. The pore walls ($\sim$0.5 nm thick) are smooth and no intrawall porosity is present. Using the same surfactant molecules but different experimental conditions other structures can also be synthesized such as MCM-48 (a cubic structure) and MCM-50 (a lamellar structure).

In 1998 it was reported that also block-copolymers could be used as templates [11]. The first material synthesized was SBA-15. SBA stands for "Santa Barbara Acid", as it was a group at this university that first reported the synthesis, which is

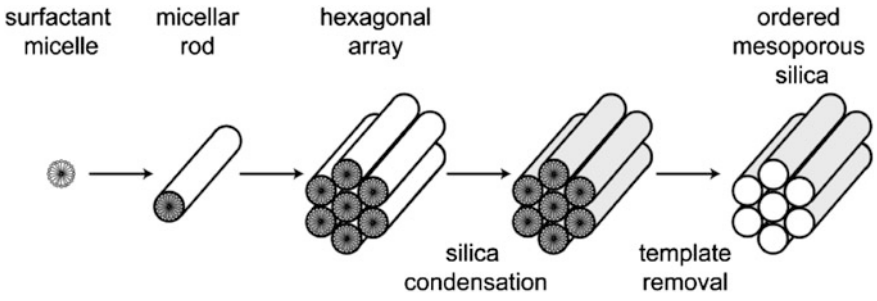

Fig. 4.4 The formation of ordered mesoporous silica (MCM-41): at high surfactant concentrations the micelles pack into rods, and the rods pack into regular hexagonal structures. Upon deposition of silica from the aqueous phase (which is excluded from the hydrophobic inner core of the micelles) a nanocomposite is formed. After removal of the micelles by heat treatment, a highly porous silica structure remains. Figure based on Ref. [10]

executed in acid solutions, rather than the alkaline conditions under which MCM type materials are grown. In the presence of a tri-block-copolymer, polyethyleneoxide-polypropyleneoxide-polyethyleneoxide (PEO_{20}-PPO_{70}-PEO_{20}) hexagonally ordered mesoporous silica with cylindrical pores was prepared. Key is the difference in hydrophilicity between PPO and PEO. Micelles form with a PPO hydrophobic core, while silica can grow in the aqueous phase that is intermixed with the more hydrophilic PEO units. After silica condensation, drying, and removal of the template, relatively large pores result, typically 5–10 nm. The former presence of the polyethyleneoxide chains is marked by micropores in the silica pore walls. The pore walls are typically 1.5–2 nm. Also, for SBA type materials the pore walls are corrugated (curved on a nm scale) and the ordering of the pores on the longer length scales is not rigid resulting in wormlike particles.

Ordered mesoporous silica is easy to prepare. Also other metal oxides can be prepared in a similar way, but generally less ordered mesoporosity is obtained. Nevertheless a range of ordered mesoporous oxides, such as Al_2O_3, TiO_2, MgO, Co_3O_4, TiO_2 has been reported by now. An alternative route to ordered mesoporous materials was first reported in 1999: nanocasting [12]. In this synthesis method an ordered mesoporous silica structure is used as a mold. Carbon replicas are prepared by filling the pores with a carbon precursor, such as sucrose or furfuryl alcohol. The negative carbon replica of the silica structure is obtained by polymerization and carbonization of the carbon source in the pores, followed by removal of the silica by leaching with an HF containing or alkaline solution. Alternatively vapor-phase deposition can be used for instance using N-containing carbon precursors, as well as other techniques such as electroless deposition or electrodeposition.

The invention of ordered mesoporous materials has been very important for fundamental studies on the properties of nanoporous materials, and gases, liquids and solids confined in the pores of these materials. The flexibility and control over the porosity of these materials is unprecedented. For instance the pore size can be varied from 1.5 to 30–50 nm. A wide variety of compounds has been prepared via the nanocasting method. Inorganic-organic hybrid materials can be grown by choosing partly non-hydrolysable precursors, mixed oxides can be formed by using mixed precursors and post-synthesis grafting allows tuning of the surface chemistry.

4.2.5 Nanostructured Carbon Materials

A range of nanostructured carbon materials exist with varying surface chemistries and porosity. The industrially most relevant are the “activated carbons”. These materials are produced from low-cost natural products, such as wood, olive pits, coconut shell, or bones by heating to high temperatures (800–1,500 °C) in an inert atmosphere. Usually an “activation” treatment follows where additional porosity is introduced by acid or KOH leaching, steam treatment, or both. Activated carbons have a high microporosity with slit–like pores, but typically also some additional meso- and macroporosity. The pore size distribution is broad and due to the natural

origin of the starting materials there is often a relatively high amount of contamination (for instance with metal oxides, carbonates or sulfates). The high specific surface areas up to 1,000–1,500 m^2/g and facile manufacture of activated carbons makes them widely applied for instance as absorbents (such as in potable and waste water treatment, decoloration of food products and air purification), automotive emission abatement and industrial processes such as solvent vapor recovery. The wide pore size distribution and poor control over the physicochemical properties make these materials less interesting from a research point of view. Carbon materials with higher purity can be obtained from synthetic precursors. For instance "carbon black" is produced by burning hydrocarbons in a low oxygen concentration. Aggregates of spherical particles with a size of a few nanometers are formed, hence analogous to disordered mesoporous silica the porosity arises from the interparticle spaces.

For fundamental studies, well-defined nanostructured carbons are much more attractive. Since their discovery in the early 1990s carbon nanotubes have attracted much attention [13]. They consist of a graphitic sheet, rolled up into a cylindrical tube. Nanotubes can have a diameter between 2 and 200 nm, while the length can be in the order of micrometers. They can be semiconducting or metallic, and have extraordinary mechanical strength. A variety of nanostructured carbon materials based on graphitic sheets exists. Multiwalled carbon nanotubes consist of multiple concentric graphitic cylinders. Furthermore, in herringbone type and platelet-like carbon nanofibres the graphitic sheets are not oriented parallel to the tube axis, but rather inclined and perpendicular respectively. Buckyballs or fullerenes and graphene sheets also attract much attention due to their exceptional properties.

Carbon nanotubes and fibers are generally produced by vapor phase processes and can be grown from CH_4 or CO and H_2 using supported metal nanoparticles as growth catalysts. The metal catalysts are usually removed by acid leaching, but it is difficult to remove all contamination. More expensive methods are carbon arc discharge or laser ablation processes. Processing carbon nanomaterials is more cumbersome than oxides as carbon nanotubes cannot be dispersed in aqueous solutions or organic solvents, and generally rapid precipitation occurs forming nanoporous materials consisting of entangled networks or bundles of individual nanostructures. An important difference between all carbon materials and the metal oxides discussed earlier is the nature of their surface. Graphite is hydrophobic, and has a very low surface energy. As a consequence its interaction with gases, liquids and solids is weak. As we will see later (Sect. 4.3), this has important implications when trying to deposit a material, whether liquid or solid, inside the pores.

4.3 Liquids Confined in Nanopores

In this section we discuss liquids confined in nanopores, and how the confinement influences the physical properties of the liquid phase, and the liquid-gas and liquid-solid transitions. Figure 4.5 (solid lines) gives a schematic representation of a phase

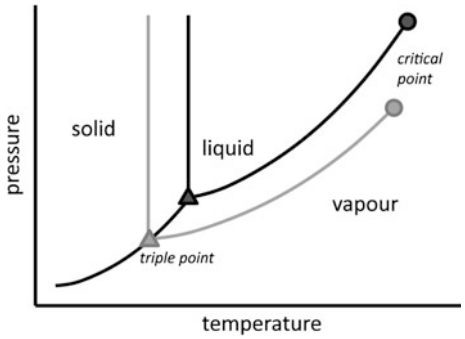

Fig. 4.5 Schematic phase diagram showing the solid, liquid and vapour phases as a function of temperature and pressure. *Solid line* a typical bulk material; *dotted line* confinement of the same material in nanopores leads to a depression of the melting point and an increase in the boiling point

diagram for a typical material with phase transitions from solid to liquid to the vapour phase occurring with increasing temperature or decreasing pressure. The triple point indicates the pressure and temperature at which solid, liquid and vapour phases co-exist. The critical point indicates the temperature and pressure above which liquid and vapour form a single continuous phase.

The dotted line indicates the changes in the phase diagram if the same material is confined in nanopores. Nanoconfinement generally results in a shift of the triple point to lower temperature and pressure. Concomitantly, the temperature for the solid-liquid equilibrium (melting/freezing point) decreases and the temperature of the liquid-vapor equilibrium (boiling/condensation point) increases. In rare cases due to a specific combination of matrix and liquid, a reverse shift can be observed. The origin of these effects lies in the interaction of confined liquids with the pore walls and will be discussed in more detail qualitatively and quantitatively in the following paragraphs, using the concepts of ***wetting*** and ***capillary condensation***.

4.3.1 Wetting

Wetting is a crucial factor in determining not only the magnitude but also the sign/direction of changes in the physicochemical properties when confining a liquid in nanopores. An experimentally easily accessible measure for wetting is the contact angle θ. This is schematically illustrated in Fig. 4.6 which depicts a droplet of a liquid on top of a solid substrate. The terms γ_{sv}, γ_{lv}, and γ_{sl} denote the surface free energies of the solid and of the liquid, and the solid-liquid interfacial free energy, respectively. Please note that generally the term "*surface energy*" (given in J/m^2) is used for solids, while often "*surface tension*" (given in N/m) is used for liquids, although both units are interchangeable. All of these energies are fixed for a given combination of solid and liquid material (and gas atmosphere). The droplet will

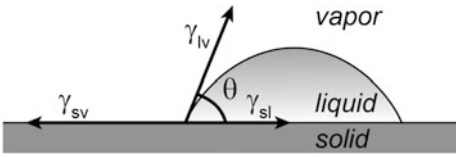

Fig. 4.6 Schematic illustration of a drop of liquid wetting a planar solid surface, with contact angle θ, and γ_{SV}, γ_{LV}, γ_{SL} being the interfacial energies [*courtesy* Rudy Wagemans]

adopt such a shape that the contact angle reflects the balance between the interfacial energies. As the contributions of the solid-vapour and liquid-solid interfacial energies exert forces parallel to the surface, it is easy to derive that in equilibrium the contact angle is defined by the Young equation:

$$\gamma_{sv} = \gamma_{sl} + \gamma_{lv} \cos \vartheta \tag{4.1}$$

Depending on the magnitude of the interfacial tensions, cos θ can be either positive (i.e., $\theta < 90^{o}$) corresponding to wetting, or negative (i.e., $\theta > 90^{o}$) corresponding to dewetting. For instance water on a hydrophilic surface will easily wet: if a droplet is applied it will spread over the surface until in equilibrium the contact angle is far below 90º. On the contrary if the liquid is repelled by the surface, such as in the case of water on a hydrophobic surface, the droplet retracts, resulting in a final contact angle higher than 90º. Solids with polar surfaces, such as hydroxylated metal oxides, have high solid surface free energies, and are thus more easily wetted than solids with an apolar surface and hence low surface energy, such as graphitic materials. In general, apolar solvents (such as hexane, γ_{lv} = 0.018 N/m) have a lower surface tension and hence spread more easily on a given surface than polar liquids (e.g., water, having a surface tension of γ_{lv} = 0.072 N/m) or even molten metals (such as mercury, having a surface tension of γ_{lv} = 0.5 N/m).

We can now understand qualitatively that if the wetting of a solid surface with a liquid is favourable, confining this liquid into a nanoporous matrix of the solid material will enhance the stability of the liquid phase. Therefore, for wetting liquids confined in nanopores a decrease of the triple point will occur leading to a depression of the melting point and an increase of the boiling point. However, if a non-wetting situation occurs, the opposite is true, and the stability domain of the liquid phase becomes smaller as a result of the pore-confinement. The extent of these effects depends strongly on the pore size, and this is discussed in a more quantitative manner in the following sub-sections.

4.3.2 Capillarity and Capillary Condensation

At a fixed temperature the liquid-vapour equilibrium occurs at a pressure different than the standard condensation pressure p_0 if the interface between the two phases

is curved. The pressure difference Δp across an interface with an effective radius of curvature r_{eff} is described by the *Laplace equation*:

$$\Delta p = \frac{2\gamma_{\text{lv}}}{r_{\text{eff}}} \tag{4.2}$$

Δp is defined as the pressure difference between the liquid and the vapour phase, and the effective radius is positive for convex liquid surfaces and negative for concave surfaces. This means that for a convex liquid surface (e.g., a small liquid droplet in the gas phase) a positive value Δp is found. The pressure inside the droplet is larger than outside the droplet, and compensates the surface forces trying to further contract the droplet in order to minimise the surface area. For a concave surface (e.g., a gas bubble in a liquid) a negative pressure difference is found.

Filling nanopores with a liquid generally leads to curved liquid-vapour phase interfaces. In the simplest case, assuming cylindrical pores, a hemispherically shaped meniscus is present, for which the effective radius is determined by the pore radius r_{p} and wetting angle θ. Equation (4.2) can easily be modified to give the capillary pressure difference Δp across a liquid-vapour interface for a liquid confined in cylindrical pores with a radius r_{p} as described by the *Young-Laplace equation*:

$$\Delta p = \frac{2\gamma_{\text{lv}} \cdot \cos\theta}{r_{\text{p}}} = \frac{2}{r_{\text{p}}}(\gamma_{\text{sv}} - \gamma_{\text{sl}}) \tag{4.3}$$

We refer to the capillary pressure Δp as the pressure difference between the liquid and the vapour phase induced by the confinement in pores. If we assume perfect wetting ($\theta = 0^{\text{o}}$) and cylindrical pores, the Young-Laplace equation reduces to Eq. (4.2). The capillary pressure can be an important driving force to fill pores. An everyday example is the absorption of water into a sponge, and the mechanism that carries water up the microscopic tubes (xylem) inside a tree. Capillary pressure can be measured in capillaries by comparing the liquid level inside a capillary with that of the same liquid outside, as illustrated in Fig. 4.7. The capillary pressure causes a rise or fall in the liquid level which is balanced by gravity. In the case of, for instance, water in a glass capillary, a strong rise of the liquid level in the capillary results. On the contrary, if the capillary is placed in liquid mercury, the liquid level in the capillary will be significantly lower than that of the surrounding liquid.

An important consequence of the capillary pressure is that a liquid can condense in pores at vapour pressures much lower than the standard condensation pressure p_0 (compare in Fig. 4.5 the liquid-vapour transition pressure at a given temperature for the bulk and confined material). We refer to this phenomenon as ***capillary condensation***. The condensation pressure for a perfectly wetting liquid is given by the ***Kelvin equation***:

$$p = p_0 e^{-\frac{2v\gamma_{\text{lv}}}{r\text{RT}}} \tag{4.4}$$

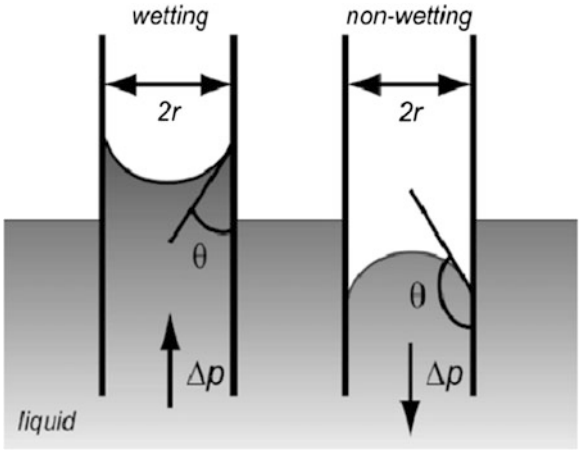

Fig. 4.7 Schematic illustration of the liquids levels in capillaries as a result of capillary pressure, illustrating the wetting case (*left frame*) for instance occurring for water in a glass capillary, as well as the dewetting case (*right frame*) which occurs for liquid mercury in glass [*courtesy* Rudy Wagemans]

in which v_l denotes the molar volume of the liquid. The Kelvin equation is directly derived from the Laplace equation (Eq. 4.2) assuming ideal gas behaviour and a liquid molar volume that is independent of pressure. As expected, a high surface tension of the liquid will lead to a large deviation from the standard condensation pressure. Also, the smaller the pores, the larger the effect.

As an example, condensation of water vapour at 100 °C in pores of 1 μm occurs at a pressure very close to the standard condensation pressure (p/p_0 = 0.9999). However, in nanopores, water already condenses at significantly lower pressures: p/p_0 = 0.998 for 100 nm radius pores, p/p_0 = 0.981 for 10 nm pores, and only p/p_0 = 0.826 for 1 nm pores. The Kelvin equation can easily be modified to take non-ideal wetting into account by adding the term cosθ. However, most often this is not needed if we are studying liquid-vapour equilibria. The interaction of gas molecules with solid surfaces is generally strong enough to allow adsorption of a monolayer of molecules or atoms at pressures much lower than the condensation pressure. As a result, vapour typically condenses onto an internal pore surface which is already covered by a monolayer of the corresponding liquid, leading to low effective contact angles.

It is good to realize that the Kelvin equation is based on a macroscopic approach and hence inevitably breaks down for pores in the lower size range. For instance, it is not reasonable in this case to assume that the shape of the meniscus (which now consists of a limited number of molecules or atoms) is exactly hemispherical, or that the surface tension of such a highly confined liquid is the same as that for a bulk liquid. Nevertheless the Kelvin equation gives a very reasonable quantitative approximation of the impact of pore confinement on the liquid-gas equilibrium, and the shift in pressure (or, equivalently, in condensation temperature) associated with it.

4.3.3 Gas Physisorption

The influence of pore size on capillary pressure is the basis for the most common method of porosity determination: nitrogen physisorption [14]. It measures the equilibrium amount of adsorbed N_2 in a sample at liquid nitrogen temperature (−196 °C or 77 K) as a function of the relative pressure. A typical measurement is started in vacuum. Then for every measurement point a known amount of nitrogen is dosed to the sample container, and after equilibration the pressure is measured. The expected pressure for the given free volume if there would be no interaction at all between the nitrogen vapour and the solid is known. The difference between this reference value and the experimentally measured pressure directly yields the amount of nitrogen that is adsorbed by the sample. Measurement points are taken at increasing relative pressures up to the condensation pressure p_0 (1 bar for N_2 at −196 °C). Subsequently, the desorption isotherm is recorded by stepwise decreasing the vapour pressure/amount of nitrogen in the system and recording the equilibrium pressures.

Physisorption gives a wealth of information about the porosity of the material. An example of a measurement is given in Fig. 4.8 for ordered mesoporous silica (MCM-41). The left frame shows the equilibrium amount of nitrogen adsorbed as a function of the relative pressure. As wetting is favourable, at low relative pressures gas molecules start adsorbing at the large SiO_2 surface, leading to a gradually increasing amount of adsorbate with pressure. From this part of the measurement the specific surface area (m^2/g) can be derived, which is dominated by the internal surface area of the nanopores. At a certain pressure, given by the Kelvin equation (Eq. 4.4), capillary condensation takes place, and liquid nitrogen suddenly condenses inside the nanopores leading to a steep increase in adsorption at a relative pressure of ∼0.3 bar. This proves that a significant amount of mesoporosity is present. The specific

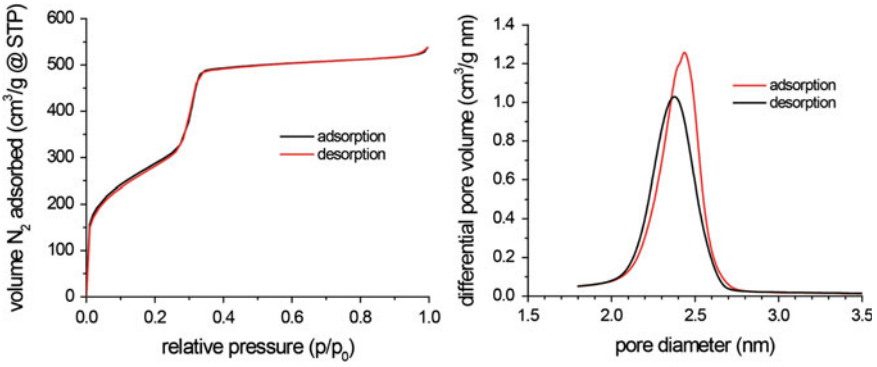

Fig. 4.8 N_2 physisorption isotherm measured at −196 °C for MCM-41. (*left*) Experimental N_2 uptake (expressed as the volume that the gas would have at standard T and p). (*right*) Pore size distribution derived from this measurement

mesopore volume is directly derived from the amount of nitrogen condensed in the pores. The pore size and pore size distribution (Fig. 4.8, right frame) are obtained by analysing this step in detail and using the Kelvin equation. Upon further increasing the pressure the adsorbed amount does not change much, as only some nitrogen adsorbs on the (small) external surface area of the particles. The shape of the physisorption isotherm, and specifically the hysteresis that is often observed (difference between adsorption and desorption branches of the physisorption isotherm) also contains information on pore shape and connectivity.

4.3.4 Changes in Melting Behaviour

Not only the liquid-vapour, but also the solid-liquid phase transition is affected by pore-confinement [15]. The melting point depression, ΔT, is inversely related to the effective radius of curvature r_{eff}, as described by the ***Gibbs-Thomson equation*** for a cylindrical pore (note that Thomson is Lord Kelvins given name):

$$\Delta T = T_0 - T_{\mathrm{m}}(r_{\mathrm{eff}}) = \frac{2T_0(\gamma_{\mathrm{ws}} - \gamma_{\mathrm{wl}})v_{\mathrm{l}}}{\Delta H_{\mathrm{m}} r_{\mathrm{eff}}} \tag{4.5}$$

where T_0 is the bulk melting temperature, ΔH_{m} is the melting enthalpy and γ_{ws} and γ_{wl} are the pore wall-solid and pore wall-liquid interface energies. For a perfectly wetting liquid $\gamma_{\mathrm{ws}} - \gamma_{\mathrm{wl}} = \gamma_{\mathrm{sl}}$. In this case the solid-liquid transition shifts to lower temperatures, and the Gibbs-Thomson equation can be simplified to:

$$\Delta T = \frac{\mathrm{C_{GT}}}{r_{\mathrm{p}} - t} \tag{4.6}$$

with $\mathrm{C_{GT}}$ a constant, and t the thickness of a non-freezing layer.

The surface tension, melting enthalpy and liquid molar volume are considered to be independent of the temperature. Even though this is a simplification (it is known that, for instance, the melting enthalpy of water decreases with decreasing temperature), it gives a reasonably good description of experimental results. Also, a non-freezing layer with thickness t is taken into account. Indeed, for water the existence of a non-ordered layer of molecules between the pore wall and ice core has been demonstrated, but there is no consensus on its thickness, as values between 0.20 and 1.05 nm are reported.

4.3.5 Thermoporometry

The influence of the pore size on the melting temperature is the basis for a second important technique to obtain information about porosity: thermoporometry. The

advent of ordered mesoporous silica materials has facilitated precise determination of the melting point depression as a function of mesopore size. These phase transitions can be measured by *Nuclear Magnetic Resonance* (NMR) or alternatively by *Differential Scanning Calorimetry* (DSC). With DSC the difference between the heat flows to either an empty container or to a sample-filled container is measured as a function of temperature, thereby detecting phase transitions occurring in the sample. Figure 4.9 shows the experimental data for the melting of ice confined in a series of ordered mesoporous silica with pore radii spanning from 1.5 to 6.2 nm. It shows that water confined in an SBA-15 material with a pore radius of 4 nm melts at −16 ºC, while water confined in a MCM-41 silica with a pore radius of 2 nm has a melting point depression of 43 ºC (see gray dashed lines in Fig. 4.9).

Thermoporometry is classically performed using water as adsorptive, allowing determination of melting points with a precision of ∼0.04 ºC. For water in silica mesopores a lower pore diameter limit of ∼2 nm has been observed, below which the formation of ice was no longer detectable. However, also other adsorptives can be used, depending on the range of pore diameters under study and the nature of the porous material. Confined organic liquids including cyclohexane, nitrobenzene and various aromatic molecules also show pore size dependent phase transition temperatures. For these molecules a larger melting point depression as a function of the pore radius as compared to water is observed, enhancing the resolution at larger pore diameters.

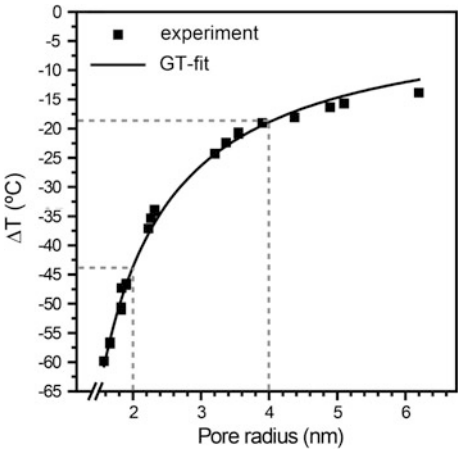

Fig. 4.9 Melting point depression as function of the pore radius. Symbols are experimental values for the melting point onset temperature of water confined in ordered mesoporous silica determined calorimetrically. The solid line represents best fit for the Gibbs-Thomson equation with C_{GT} = 66.5 ºC nm and t = 0.48 nm

4.4 Outlook

Nanoporous solids are an important class of nanomaterials, with a wide variety in chemical composition (e.g., carbon or metal oxides), porosity (e.g., microporous or mesoporous) and properties. Although some materials, such as zeolites and activated carbons, have been known for centuries, the last few decades have seen remarkably the "invention" of new classes of materials that cannot be found in nature. Most of these materials, such as ordered mesoporous silica and metal organic frameworks, possess a very high structural order, which means that pore size, shape and orientation are well-defined. As a result, they give access to a fundamental exploration of the structure of nanoporous materials, and the impact of confining phases inside well-defined nanopores.

A first very important result of the availability of ordered nanoporous materials has been a significant progress in characterization techniques such as physisorption and thermoporometry. These techniques are based on intriguing fundamental changes when confining phases inside nanopores, such as changes in melting and boiling points of confined liquids, which are increasingly being investigated and understood. The availability of ordered porous materials has also greatly facilitated understanding the fundamentals of the preparation and functionality of supported nanoparticles, as will be treated in detail in Chap. 5.

Many ordered nanoporous materials have only recently been synthesized and described, hence it is difficult to predict what the future will bring. Though deemed very promising for a myriad of applications and functionalities, very few practical applications have actually been realised yet. Regarding fundamentals, many changes upon confining phases in nanopores are still not understood. Examples include changes in the solubility of salts in confined liquids, phase nucleation in confined solutions, and changes in crystallisation behaviour (for instance, why different crystal structures of ice are formed in confinement). Nanoporous materials will undoubtedly remain a very active research area in the years to come.

4.5 Exercises

1. An important advantage of ordered mesoporous materials is that their pore diameter can vary, allowing fundamental studies as a function of pore size. Suggest at least two strategies to tune the pore size of ordered mesoporous silica prepared by sol-gel synthesis in aqueous solutions.
2. (a) How high could a tree grow if it relies only on capillary pressure to transport water up to its leafs? Assume that the tree is composed of a single capillary tube with a diameter of 12 μm (a typical pore diameter for xylem). Start by calculating the force of gravity as a function of height, and then equalling it to the

attractive force due to the capillary force (interaction between water and pore wall). Assume perfect wetting ($\theta = 0^o$).
(b) What other mechanisms help trees to grow even taller?
(c) And in comparison: how high is water lifted against gravity in a nanoporous material with 2 nm pore diameter?

3. The IUPAC officially distinguishes 6 different classes of N_2 adsorption isotherms based on their shape [14]. Shown below (Fig. 4.10) are schematic representations of the adsorption profiles of these 6 classes (if only one line is shown, the adsorption and desorption branches of the isotherm exactly overlap). Class II is a typical non porous solid, which is wetted well by the N_2 (e.g., silica).

   a. Which class would represent a material with the same structure that is not wetted by N_2?
   b. Which isotherm would represent a zeolite?
   c. And which isotherm MCM-41?
   d. Can you guess which material could lead to an isotherm such as represented in VI?

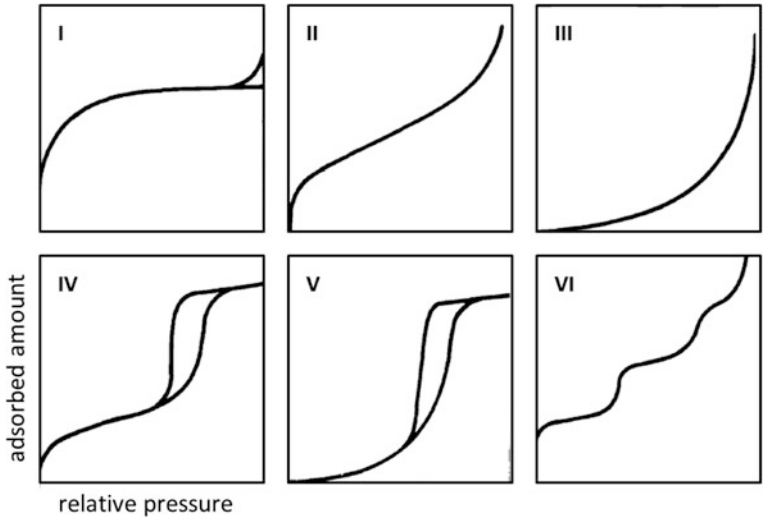

Fig. 4.10 Schematic representations of the 6 classes of N_2 adsorption isotherm profiles recognized by the IUPAC

References

1. Jong, K.P.: Support materials and characterization tools for nanostructured catalysts. Oil & Gas Sci. Technol. **61**, 527–534 (2006)
2. Mintova, S., Olson, N.H., Valtchev, V., Bein, T.: Mechanism of zeolite A nanocrystal growth from colloids at room temperature. Science **283**, 958–960 (1999)
3. Database of Zeolite Framework Types as provided by the Structure Commission of the International Zeolite Association (IZA-SC) which can be accessed via http://www.iza-structure.org/databases/
4. Cundy, C.S., Cox, P.A.: The hydrothermal synthesis of zeolites: History and development from the earliest days to the present time. Chem. Rev. **103**, 663–701 (2003)
5. James, S.L.: Metal-organic frameworks. Chem. Soc. Rev. **32**, 276–288 (2003)
6. Yaghi, O.M., O'Keefe, M., Ockwig, N.W., Chae, H.K., Eddaoudi, M., Kim, J.: Reticular synthesis and the design of new materials. Nature **423**, 705–714 (2003)
7. Cŏté, A.P., Benin, A.I., Ockwig, N.W., O'Keefe, M., Matzger, A.J., Yaghi, O.M.: Porous, crystalline, covalent organic frameworks. Science **310**, 1166–1170 (2005)
8. Brinker, C.J.; Scherer, G.W.: Sol-Gel Science: the Physics and Chemistry of Sol-Gel Processing. Academic Press, New York (1990)
9. Ciesla, U., Schüth, F.: Ordered mesoporous materials. Microporous Mesoporous Mater. **27**, 131–149 (1999)
10. Kresge, C.T., Leonowicz, M.E., Roth, W.J., Vartuli, J.C., Beck, J.S.: Ordered mesoporous molecular sieves synthesized by a liquid-crystal template. Nature **359**, 710–712 (1992)
11. Zhao, D., Feng, J., Huo, Q., Melosh, N., Fredrickson, G.H., Chmelka, B.F., Stucky, G.D.: Triblock copolymer synthesis of mesoporous silica with periodic 50 to 300 angstrom pores. Science **279**, 548–552 (1998)
12. Jun, S., Joo, S.H., Ryoo, R., Kruk, M., Jaroniec, M., Liu, Z., Shsuna, T., Terasaki, O.: Synthesis of new, nanoporous carbon with hexagonally ordered mesostructure. J. Am. Chem. Soc. **122**, 10712–10713 (2000)
13. Baughman, R.H., Zakhidov, A.A., de Heer, W.A.: Carbon nanotubes: the route towards applications. Science **297**, 787–792 (2002)
14. Sing, K.S.W.: Reporting physisorption data for gas/solid systems. Pure Appl. Chem. **54**, 2201–2218 (1982)
15. Alba-Simionesco, C., Caosne, B., Dosseh, G., Dudziak, G., Gubbins, K.E., Radhakrishnan, R., Sliwinska-Bartowiak, M.: Effects of confinement of freezing and melting. J. Phys. Condens. Matter **18**, R15–R68 (2006)

Chapter 5
Supported Nanoparticles

Tamara M. Eggenhuisen and Petra E. de Jongh

Abstract A collection of free standing individual nanoparticles is difficult to handle. Hence, in functional applications nanoparticles are often stabilized by deposition in a nanoporous scaffold, which provides mechanical strength and chemical- and sinter-resistance, while preserving their accessibility. A range of deposition strategies, such as solution impregnation and melt infiltration, is available for supported nanoparticle preparation. Standard solid state characterization techniques provide structural information, while a few specific techniques are able to measure for instance the size distribution and location of the supported nanoparticles. Common applications of these nanostructured materials include catalysis, gas separation and storage, and energy storage and conversion.

5.1 Preparation Strategies

Nanoparticles (NPs)are intrinsically much less stable than the corresponding bulk materials due to their large specific surface area (see Chap. 1 for details). For most practical applications, such as in the fields of catalysis and energy conversion and storage, they lack resistance against sintering, ripening or dissolution under practical operating conditions (often chemical conversions, high temperatures, reactive atmospheres, cycling, etc.). Hence NPs are typically stabilized, either in solution by adding appropriate ligands (Chap. 6), or in the solid phase by embedding in a nanocomposite or by confinement in a nanoporous support.

Although it is possible to incorporate pre-existing colloidal NPs into nanopores, more typically the NPs are prepared in the presence of, and with the help of, a support [1]. The size and shape of the NPs is then to a large extent influenced by the support. Electronic interaction and specific interfacial bonding between NPs and

T.M. Eggenhuisen (✉) · P.E. de Jongh
Inorganic Chemistry and Catalysis, Debye Institute for Nanomaterials Science,
Utrecht University, Utrecht, The Netherlands
e-mail: tm.eggenhuisen@gmail.com

C. de Mello Donegá (ed.), *Nanoparticles*,
DOI 10.1007/978-3-662-44823-6_5

scaffold material may also play an important role. On a larger scale the support should allow accessibility of the supported NPs and provide mechanical, thermal and chemical stability to the overall system.

Figure 5.1 illustrates three main strategies to deposit particles in a nanoporous matrix. An approach that is widely used is loading a nanoporous matrix with a precursor solution, such as aqueous solutions of metal nitrates or chlorides. After drying and decomposition typically metal oxide or hydroxide NPs have formed, which can subsequently be reduced to metallic NPs, or further reacted to form hydrides, sulphides, etc. Another possibility is filling the porous matrix directly with a melt of the desired phase, or with a molten precursor. It is also possible to start from a suspension of colloidal NPs which are then introduced into the porous matrix. Application of this last route is steadily gaining importance, especially in academic research, because it allows exact control of the NP size. However, it is difficult to preserve the exact properties of the colloidal NPs upon deposition. Less used alternative deposition techniques are for instance chemical vapour, atomic layer, and glow discharge plasma deposition. These techniques are generally not suitable for the large scale production of 3D supported NPs. We hence discuss in this Chapter only the three main preparation pathways.

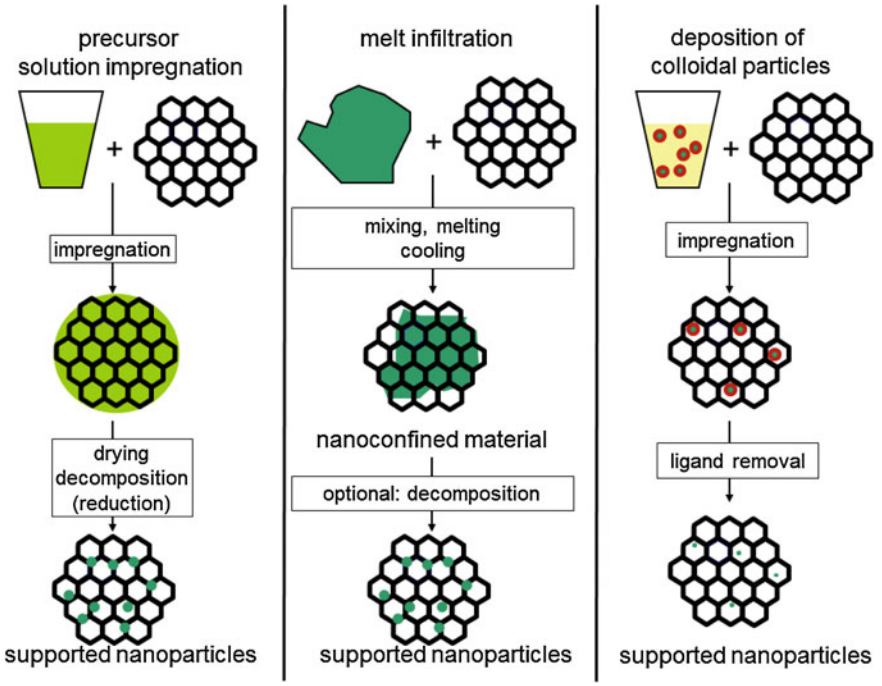

Fig. 5.1 Illustration of the three main pathways to obtain nanoparticles confined in a nanoporous matrix: (*left*) impregnation with a precursor solution followed by decomposition into the desired compound; (*middle*) melt infiltration of either a pure phase or a precursor; (*right*) incorporation of colloidal nanoparticles

5.1.1 Precursor Solution Impregnation

Solution impregnation is based on contacting a nanoporous matrix with a solution containing a precursor (complex) of the active species. A first important prerequisite is that the solution does wet the nanoporous matrix (see also Sect. 4.3.1), so that it enters the pores. Often aqueous precursor solutions are used. Oxidic nanoporous materials are generally easily wetted, due to interaction of the water molecules with the surface hydroxyl groups, and in that case infusion of the liquid into the pores by capillary forces is rapid. It can be assisted by thoroughly drying the matrix before applying the precursor solution. Sometimes first vacuum is applied to the solid, and then the precursor solution is introduced. Specifically for carbon-based matrices, or apolar solvents, proper care has to be taken to ensure that the precursor solution enters the nanopores of the support material. In some cases, first a less polar solvent is introduced into the pores, and is subsequently gradually replaced by an aqueous solution via a series of miscible solvents.

Another important factor is the interaction between the precursor (complex) and the internal surface of the support, which is mostly based on electrostatic interaction. In general it is favourable to choose a precursor that is oppositely charged compared to the support surface. Most solids have a charged surface in aqueous solutions, with the charge density and sign depending on the pH. For instance, a hydroxylated silica surface contains ~ 5 hydroxyl (–OH) groups per nm^2. In very acidic solutions these groups will be protonated ($–OH_2^+$ groups) and hence positively charged, while in alkaline solutions they will be fully deprotonated ($–O^-$ groups) and hence negatively charged. It is important to note that this proton exchange between surface groups and the solution can significantly change the pH of the solution, especially locally, due to the large specific surface area of the nanoporous supports and hence large number of exchangeable surface protons.

An important parameter is the point of zero charge (PZC) of the surface: the pH at which the surface groups have no net charge. The PZC depends on the chemical composition of the solid, mainly on the electronegativity of the metal atom. For example, silica has a PZC at pH 2–3 and if contacted with a platinum(IV)-chloride precursor solution at pH 3, the $Pt(Cl)_6^{2-}$ ions will have only weak interaction with a silica surface, as the surface silanol groups are hardly (de-)protonated. However, using an alumina support (with a PZC around pH 8–9) the $Pt(Cl)_6^{2-}$ ions adsorb strongly on the protonated, and hence positively charged, alumina surface. Graphite, carbon nanotubes, and fullerenes are hydrophobic, as there are virtually no functional groups at the surface. On the other hand, oxygen containing surface groups are present in activated carbon. Their number and nature can vary widely, which means that the PZC of carbon materials ranges from acidic to basic pH.

Experimental parameters such as solvent, precursor concentration, support, infiltration procedure and drying strongly influence the final NP size and distribution. Depending on the desired loading, the active phase or precursor complex should have sufficiently high solubility in the solvent. On the other hand, at high concentrations an increased viscosity may slow down the capillary flow. Multiple impregnation steps

might be applied to achieve the desired particle loading. If there is a too strong interaction between the precursor and the surface of the porous support particles, the active phase adsorbs onto the surface groups it will encounter first and may be only deposited at the pore mouths and on the outer rim of the support particle. If the interaction is weak, redistribution of the active phase during further drying or heat treatments is likely. Three strategies to make use of the interaction between support and precursor in solution are briefly discussed below: "impregnation and drying", "electrostatic adsorption", and "deposition-precipitation".

The most straightforward approach is ***impregnation and drying*** (Fig. 5.2). 'Incipient wetness-', 'dry-' or 'pore volume-' impregnation involves the addition of a solution volume equal to the pore volume. For "wet" impregnation an excess of solution is added, which is removed by filtration or evaporation. A highly dispersed precursor or active phase inside the pores is obtained after removal of the solvent. Thermal treatment in inert atmosphere or air ("calcination") is applied to decompose precursors into metal oxide nanoparticles. For instance starting from a metal nitrate solution, after drying, solvent evaporation and decomposition would lead to gaseous water and nitric oxides, while a solid metal oxide phase is formed. Oxidic nanoparticles can then be reduced to metallic nanoparticles (for instance by heating in 5 % H_2 in N_2) or reacted to form nanoparticulate hydrides, sulfides, etc. Impregnation and drying is a simple and low-cost method. However, the resulting nanoparticles' sizes and their distribution over the support are difficult to control. Thermal treatment steps often lead to a redistribution of the active phase.

Electrostatic adsorption is a similar technique, but in this case a large amount of solution is used, and specifically only a monolayer of metal precursor complexes is bound to the support's surface groups. The pH of the solution determines whether the surface groups of the support are protonated or deprotonated. It is chosen such that the surface charge is opposite to that of the metal ion. The NPs loading is limited by the specific surface area of the support, its density of charged surface groups, and the adsorption strength at the applied pH. In some cases the metal ions are reduced in situ, while it is also possible to decompose precursor complexes

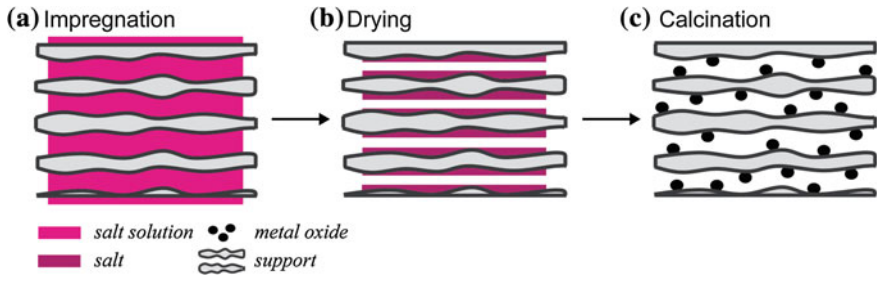

Fig. 5.2 Supported nanoparticle preparation by impregnation and drying. **a** a solution containing the metal precursor is absorbed by a porous support, **b** solvent removal results in the metal salt deposited inside the pores and **c** the precursor salt is decomposed to form metal oxide nanoparticles, which can be converted to other nanoparticulate phases

upon heating after solvent removal followed by reduction. Generally, small metal NPs which are uniformly distributed over the porous support are obtained, but only in loadings up to 2–5 wt%.

For ***deposition-precipitation*** a support is suspended in a large volume of solution containing the metal precursor complex. By a controlled change in the pH (e.g., by thermal hydrolysis of urea resulting in the gradual formation of OH^-) gradual supersaturation is created uniformly in the solution. As a result of the slight supersaturation, species precipitate (e.g., metal hydroxides), preferentially nucleating on the suspended support since the activation energy for heterogeneous nucleation is lower than for homogeneous nucleation (see Sect. 6.3.3.2 for details). This method is applicable to a wide variety of metals and small metal NPs (<10 nm) and high metal loadings (e.g., up to 17 wt% Ni/SiO_2) can be achieved. However, due to the small particle size and strong bonding of the precipitated hydroxides to the support, it is often very difficult to reduce them to the corresponding metal NPs.

5.1.2 Melt Infiltration

Precursor solution impregnation is especially suitable for large scale production of supported nanoparticulate materials with small particle sizes. However, solubility of the precursor in the solvent poses a fundamental limit to the loading that can be obtained in a single impregnation step. Preparation by infiltration of the support with the pure molten phase or its precursor can achieve (almost) complete filling of the pore volume. The method involves mixing a nanoporous matrix with the metal (precursor) of interest and heating the mixture to above the melting point of the metal (precursor). If wetting occurs, the pores fill by capillary infusion with the molten phase. After cooling (and, if relevant, decomposition) a nanoconfined solid phase results.

The absence of solvents allows for higher loadings in a single step and circumvents the need of drying procedures. However, the method is only relevant for materials or their precursors that melt at relatively low temperatures. For instance light metals, such as Li, Na, Mg or Al can be molten at temperatures (181, 98, 649 and 660 °C respectively) at which nanoporous matrices (oxides or carbon materials) are stable. Several hydrides, especially complex metal hydrides such as $LiBH_4$ and $NaAlH_4$, melt at low temperatures (280 and 180 °C, respectively). Also hydrated salts such as metal nitrate hydrates can be molten into a porous structure.

A second important practical consideration for the application of melt infiltration is whether the melt and the matrix are stable under the infiltration conditions. For example, hydrated transition metal nitrate salts have relatively low melting points, but loss of water at melt infiltration temperatures may cause the formation of partially dehydrated solid species. Complex metal hydrides have relatively low melting points, but should be molten under hydrogen pressure to prevent decomposition before melting. Furthermore, molten metals are quite reactive with most oxidic materials, so in this case inert nanoporous carbon matrices are often preferred.

The degree of pore filling is controlled by the ratio of the components, but limited by the wetting of the matrix with the infiltrate. The viscosity of the melt and the support pore diameter also affect the capillary flow. Preferably the melt has a low viscosity, low melting point and a low vapour pressure. Mesoporous metal oxides have a high surface energy. Therefore infiltration with inorganic metal precursor salts, such as hydrated transition metal nitrate salts, occurs rapidly and completely. On the other hand, infiltration of carbon supports with metals is more difficult. Molten metals typically have relatively high surface tensions (in the order of 0.2–0.4 J/m^2), while carbon supports have a low surface energy. This means that often the situation occurs that no energy would be gained if a carbon surface would be covered by a thin layer of molten metal. For carbon nanotubes for example, it has been established that infiltration does not occur for liquids with surface tensions exceeding 0.1 J/m^2 as there is no net energy gain. Pore filling can be improved by applying external pressure, while wetting properties can be improved by modification of the surface energy of the matrix (by introducing functional groups, or depositing a wetting layer) or by alloying the infiltrate.

Melt infiltration is particularly relevant for the preparation of catalysts with high metal loadings, such as transition metal catalysts. For these catalysts, high volumetric loadings of the active phase are desired allowing smaller reactor volumes to obtain the same level of production. Also for energy storage materials, such as electrodes for batteries or hydrogen storage systems, high loadings are often required to minimize the volume and weight, especially for mobile applications.

5.1.3 Deposition of Colloidal Nanoparticles

Precursor solution impregnation and melt infiltration are low-cost methods, but neither of them allows the control over particle size and composition that is offered by the growth of nanoparticles as colloids in suspension (see Chap. 6). Hence substantial efforts are on-going to deposit colloidal NPs onto high surface area supports. A first potential obstacle are the solvent and ligands used for NP growth. These are often amphiphilic organic molecules (see Sect. 6.2.2) which bind their polar head to the NP surface and expose their apolar tail to the solvent. This leads to unfavourable interaction with the polar surfaces of oxidic matrices. Several methods have been developed in recent years to perform ligand and solvent exchange (see Sect. 6.2.3) and stabilizing colloidal NPs into aqueous-based systems. Another practical issue with introducing colloidal NPs into a nanoporous structure is their size; though the colloidal NPs themselves can be a few nm in size, the capping ligand shell increases the effective size substantially; hence infiltration with the colloidal suspension is only possible for relatively large pores.

The next step is removal of the solvent and the capping ligands. This is a critical step. Nanoparticles in colloidal suspension are typically stabilized by organic ligands, which completely coat the NPs and are relatively strongly bound to their surface atoms. A fundamental challenge is to remove the stabilizing ligands from

the colloidal NPs, while at the same time achieving a stable interaction between the NPs and the support. Careful evaporation of the solvent at low temperatures may be necessary to avoid premature aggregation of the colloidal NPs.

The most effective method to remove the organic ligands is combustion of the organic compounds at relatively high temperatures. Unfortunately this generally results in strong aggregation and sintering of the nanoparticles, as in this stage there is no strong interaction (yet) between the NPs and the support. Alternatively, methods such as leaching of the ligands, and reductive removal are being explored. Although the deposition of nanocolloids onto supports is not straightforward at all, it is a very active area of research. The potential benefit of combining the advantages of 3D supported systems with those of the high precision in defining the shape, size and composition of NPs offered by colloidal synthesis makes it worth the effort.

5.2 Characterization

Structural characterization of confined NPs is paramount to allow insight into the relation between structural properties and functionality, and to develop optimum synthesis methods. Roughly two types of analysis are possible: specifically looking at the confined NPs, or accessing the overall properties of the resulting nanocomposite. It is not possible to treat all characterization methods in detail in this section. We mention a few of the most important techniques, and focus on how they are specifically used to determine the particle size or particle location in the case of 3D supported nanoparticulate materials. Next to the techniques mentioned below, most standard techniques that are applied for the characterisation of the structural properties of solids, such as vibrational spectroscopy (IR or Raman), optical spectroscopy in the UV-Visible, solid state NMR, X-Ray absorption techniques, etc., can also be used to characterize nanocomposites.

Regarding the NPs, a most obvious structural property of interest is the particle size and shape (see Fig. 5.3). Visualization by ***electron microscopy*** techniques (Fig. 5.3 left frame, see Chap. 7 for details) provides quantitative information on nanoparticle sizes, size distribution and shape. It also allows mapping the chemical composition and distribution of the phases with nm resolution. However, a bias is often introduced by sample preparation, and it is only possible to look at very small amounts of sample (typically a few femtograms). This means that it is not straightforward to obtain statistically relevant information. Furthermore, the structure is assessed ex situ and requires sample transfer through air. ***Neutron*** and ***X-ray diffraction*** *(XRD)* are also used to characterize nanoconfined solids. Using the Scherrer equation, a volume average crystallite size is derived from the line broadening in the X-ray powder diffraction pattern (Fig. 5.3 right frame).

Particle sizes are indirectly accessed by determining the surface area of the active phase. For instance, a metal surface area can be determined by hydrogen chemisorption, which measures the amount of dissociatively adsorbed hydrogen per gram

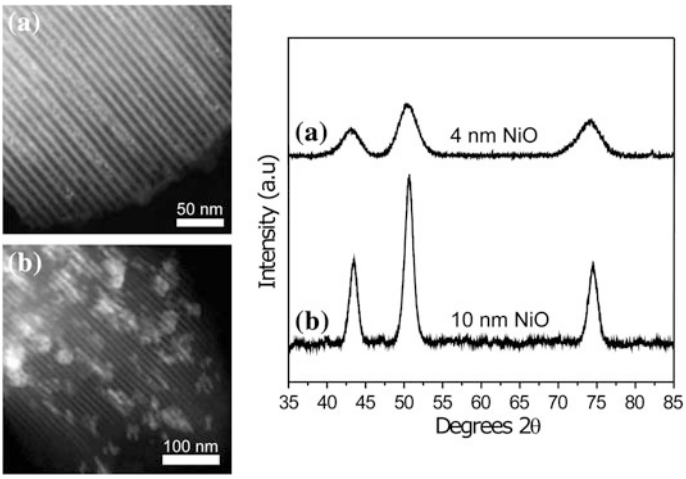

Fig. 5.3 NiO nanoparticles in ordered mesoporous silica either 4 nm in size and homogeneously distributed over the pores (**a**) or 10 nm in size and clustered in high density regions (**b**). *Left* dark field transmission electron microscopy shows the NiO crystallites (*bright dots*) and their distribution inside the pores. *Right* XRD identifies the crystalline phase as NiO (the ordered mesoporous silica is amorphous) and from the line broadening the average crystal sizes are obtained; the smaller the crystallites, the broader the lines. Adapted with permission from Ref. [9]

of sample. Assuming a certain stoichiometry for the reaction (for instance one hydrogen atom per one metal surface atom) the fraction of metal atoms that resides at the surface is derived from the experimental data. The average NP size is obtained by assuming a given geometry of the metal particles, usually hemispherical. Other molecules than H_2 can also be used to probe the active surface area, for example N_2O titration is often applied for Cu. Please be aware that the crystallite size does not necessarily correspond to particle size, and that it is also very important to note whether a technique yields volume-, surface-, or number-averaged sizes.

Information that is far from trivial to access is the location of the NPs. ***Electron microscopy*** does give information on the NP distribution over the support, but is hampered by the fact that conventional electron microscopy only gives a 2-dimensional projection (it looks through the material). Electron tomography (or "3D electron microscopy") does give information in 3 dimensions (it looks inside the material), but requires substantial experimental and image analysis effort. For details on electron microscopy related techniques we refer to Chap. 7. An important question is typically whether the particles are located inside the nanopores or not. The maximum loading of a porous support can be determined by measuring samples with a series of loadings, and detecting overfilling. For instance nanopore confined phases are nanocrystalline or even X-ray amorphous, hence XRD can detect surpassing the maximum loading by determining the onset of the presence of large crystallites.

Instead of specifically looking at the confined phase, we can also monitor changes in the porosity of the support upon deposition of this active phase. The most standard technique to measure porosity is ***N_2-physisorption*** (see Sect. 4.3.3) to assess the decrease of the pore volume upon addition of the nanoparticles to the matrix. The pore volume of the empty support and the nanocomposite material should be compared per gram of support. However, the possibility of loss of pore volume by pore destruction or pore blockage needs to be considered as well. The presence of NPs in pores can also be detected from delayed desorption and a change in the hysteresis loop. As has been discussed in Sect. 4.3.1, confining a solid in a nanoporous matrix affects its phase behaviour. Therefore, studying the phase transitions of a nanocomposite material with ***differential scanning calorimetry*** provides information on the actual confinement of the material. Quantitative information on pore filling can be obtained by determining the amount of residual extraporous phase. In addition, the presence of nanomaterials in pores can be detected by studying the altered phase transition behaviour of the confined material itself, or studying the open space left in the pores with a probe such as water/ice.

X-ray diffraction at low angles ***Small Angle X-ray Scattering*** (SAXS) can also be used to follow changes in properties in ordered mesoporous materials. Analogue to diffraction patterns caused by a regular arrangement of atoms in solids with Å distances, distinct diffraction patterns at low diffraction angles arise due to the regular arrangement of pore walls in ordered mesoporous materials on a nm scale. Filling of the pores can be detected as a decrease of the amplitude of this diffraction signal (due to a decreased contrast in electron density between pore walls and empty pores *versus* filled pores). Also any destruction of the order of the porous structure due to the impregnation/deposition of the nanophase will become immediately evident. However, accurately measuring diffraction at such low angles often requires the use of synchrotron radiation and specialized equipment.

5.3 Supported Nanoparticles as Catalysts

Nanoparticles confined in porous materials are applied on a large scale in the chemical industry as catalysts for the production of fuels, chemicals and materials [2]. It is often stated that about 85 % of all industrial chemical conversions involves a catalyst to optimize the reaction. Most of these catalysts are “heterogeneous” catalysts, which means that the catalytic materials are in a different (solid) phase than the reactants and products (gas or liquid phase). Typically catalytically active metal (or sometimes metal oxide, sulfide or carbide) NPs are supported on a porous material. The catalyzed reaction takes place at the surface of the catalyst, which binds reactants and intermediates. The effective activation barrier for the reaction is lowered, for instance by donating electron density to the antibonding orbitals, and hence facilitating the dissociative adsorption of molecules. Catalysts can steer reactions in a certain direction (selectivity) and increase the rate of reaction (activity) not only by lowering the activation barriers, but also by concentrating the

reactive species at its surface compared to the gas or liquid phase. Most catalytically active materials are transition metals, for which the specific contribution of the d-electron density to adsorbed species gives rise to a variety of catalytic functionalities.

As the catalytic action takes place at the surface, it is essential to have a large surface to volume ratio of the catalytic phase. To minimize the cost in terms of material, energy and capital (often expensive metals such as Pd and Pt are used) typically NPs < 10 nm are used. However, chemical reactions occur at elevated temperatures (typically 200–400 °C) and in reactive atmosphere, so stabilizing the small size of the catalyst NPs is vital. This is the most important role of the nanoporous support, which generally consist of disordered metal oxides or (activated) carbon materials. However, the support also facilitates facile preparation of the NPs, and sometimes also influences the reactivity by altering electronic or structural properties of the metal NPs or acting as a co-catalyst in the reaction.

In Fig. 5.4 two examples of supported catalysts are shown. The left frame shows 5 nm Cu NPs that have been deposited inside the pores of SBA-15 (ordered mesoporous silica, see Chap. 4 for details) by impregnation with an aqueous copper nitrate solution, followed by drying, decomposition and reduction. This illustrates that the controlled synthesis of complex nanostructures is possible by relatively straightforward preparation methods. On the right frame, the catalyst consists of Pt NPs on a carbon nanofibre support. It was prepared by deposition precipitation of Pt $(NH_3)_4(NO_3)_2$ from an aqueous solution. After decomposition of the precursor salt, it was treated at 700 °C in N_2 for 2 h, which led to an increase in the particle size only from 1.4 nm to 2.0 nm. This clearly illustrates the strongly stabilizing effect of the support.

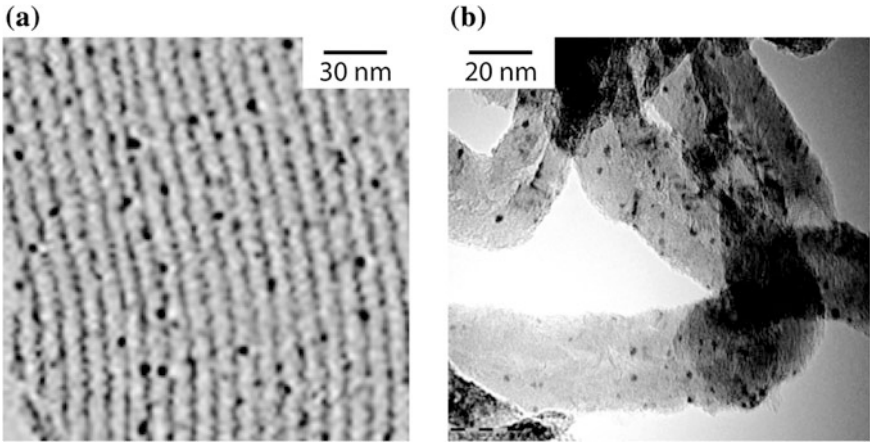

Fig. 5.4 Supported nanoparticle catalysts: **a** electron tomography slice of 5 nm Cu particles prepared by impregnation inside SBA-15 ordered mesoporous silica [10]. **b** Electron micrograph showing 2 nm Pt nanoparticles on carbon nanofibres prepared by deposition precipitation. Adapted with permission from Ref. [11]. Copyright (2004) American Chemical Society

5.3.1 Particle Size Effects

Smaller NPs have a higher surface-to-volume ratio, and hence, for most reactions, a higher catalytic activity per weight basis. The fraction of atoms at the surface is proportional to the inverse of the particle radius, thus the same relationship might be expected for the activity of catalyst NPs. However, not all adsorption sites on a metal surface have the same properties. Therefore, a more meaningful measure for catalyst activity is the turnover frequency (TOF), which is the average number of chemical conversions per second per metal surface atom, which may vary for the types of active sites present on a NP surface. For many reactions the most relevant active sites are those that involve metal atoms having a lower coordination number than for atoms in planar surfaces, such as at step sites or on corners. For NPs smaller than 10 nm the surface becomes more and more dominated by these lower-coordinated atoms. This is illustrated in Fig. 5.5 which shows different types of atoms: corner, edge, step or terrace atoms. The coordination number of the surface atoms has a large influence on the adsorption of reactant, intermediate and product molecules and atoms, and hence on the catalystic activity and selectivity.

For macroscopic particles, the shape can be predicted rather accurately via a "Wulff construction"(see Sect. 6.3.3.3, for details). This construction is based on a minimalization of the total surface energy, by taking the macroscopic surface energies of the different crystal faces into account. However, its value for prediction the shapes of supported NPs smaller than 10 nm is limited for several reasons. Nanoparticle shapes are strongly influenced by reactive gases or liquids present, and stabilizers, dopants and supports. For catalytically active metals, such as Pt, Pd and

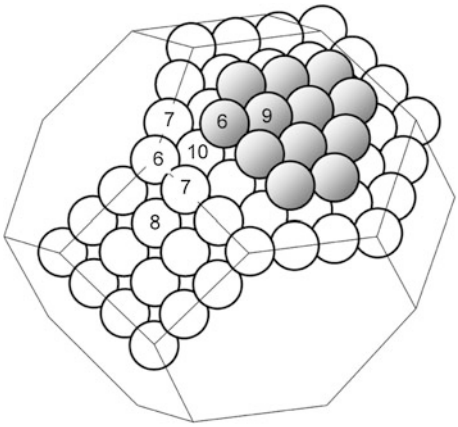

Fig. 5.5 Geometrical model of a nanoparticle with cuboctahedral geometry. Corner, edge and step atoms have a decreased coordination number as compared to terrace atoms. Reprinted with permission from Ref. [12]. Copyright (2009) American Chemical Society

Au, the common most stable shapes for NPs of a few nanometres are cuboctahedral (corresponding to a face-centred cubic crystal lattice), icosahedral and decahedral. The last two are "quasicrystals": their lattice lacks translational periodicity, bond distances vary slightly as a function of position in the particle. NPs can accommodate significant lattice strain, this is much less the case for bulk crystal structures. Furthermore, Wulff constructionsyield the thermodynamically calculated most stable particle shapes, assuming the surfaces are exposed to vacuum. Surface/interfacial energies play a decisive role. It is difficult to predict the real shape of supported NPs under reactive gas atmosphere. Supported NPs have even been observed to reversibly change shape upon exposure to different gas atmospheres [3]. The support might provide a very favourable interaction ("wetting" and hence flattening the particle) or less favourable interaction, and also this interaction can be influenced by the gas atmosphere.

Though depending on the specific catalyst, reaction, and reaction conditions, it is possible to sketch a general picture of the influence of particle size on catalytic activity and selectivity. Figure 5.6a illustrates three general cases of the relation between catalytic activity (expressed as turn-over-frequency, TOF) and particle size. The TOF is generally independent of the particle size in a certain region (**curve a** Fig. 5.6a), at least for the largest particles. However, for a certain class of reactions the TOF decreases sharply for small particles (**curve b in** Fig. 5.6a). This could for instance be the case for a reaction that needs a binding site coordinated by a number of specifically organized metal atoms, such as 4 or 6 terrace atoms, or a combination of multiple step-terrace atoms which are rare in the smallest particles. An increasing TOF with decreasing particle size (**curve c in** Fig. 5.6a) may occur for instance when single surface atoms with low coordination numbers form the active sites. Figure 5.6b shows experimental results for the turn-over-frequency for the formation of hydrocarbons from CO and H_2 (Fischer-Tropsch synthesis)

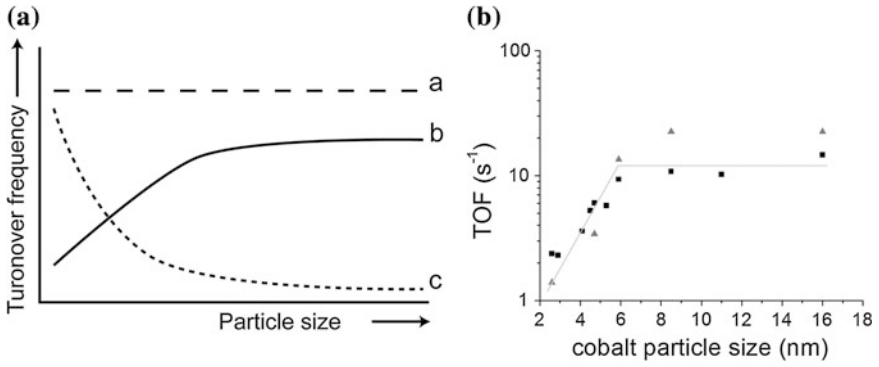

Fig. 5.6 a Possible trends in particle-size dependence of the turnover frequency (TOF). **b** experimentally measured particle-size dependence for carbon supported Co metal nanoparticles used as catalysts for the synthesis of hydrocarbons from H_2 and CO. Reprinted with permission from Ref. [12]. Copyright (2009) American Chemical Society

catalysed by supported Co NPs. The decrease in activity for smaller NPs is due to the fact that irreversible adsorption of CO on step and corner atoms occurs, leadings to an intrinsic decrease of activity for smaller NPs.

5.3.2 Nanoparticle Stability

Deactivation of catalysts can occur by poisoning of the metal (a change of surface properties for instance by reaction with sulphur), fouling by, e.g., deposition of coke, or mechanical failure. However, one of the most detrimental deactivation pathways for supported catalysts is NP sintering. The loss of active surface area due to crystallite growth is often irreversible. For a few specific cases the possibility of regeneration by oxidation/reduction cycling has been reported, resulting in fragmentation of larger particles into smaller ones. However, typically after deactivation by crystal growth, the complete catalyst bed has to be replaced.

Sintering of supported NPs may occur by either migration and coalescence of complete particles, or via Ostwald ripening. In the last case mobile species are released by the small particles, and after diffusion recombine with larger particles, effectively resulting in shrinking and disappearance of the smaller particles, and growth of the larger particles (Ostwald ripening and coalescence also commonly occur for colloidal NPs and are discussed in more detail in Chap. 6). Metals often show a relatively high mobility, especially the low-melting metals such as Ag, Cu and Au. A rule of thumb: metal surface atoms gain significant mobility above a temperature which is half the melting temperature (in Kelvin); the so-called "Tamman temperature". A high atom mobility is expected for NPs, as their melting point is significantly lower than that for the corresponding bulk metals.

Surprisingly little is known about the mobile species in Ostwald ripening in most common catalytic systems. Due to the high energy barrier, transport by metal atoms in the gas phase seems unlikely. Most probably metal complexes, either bound to the surface, in solution or volatile, are responsible for the mass transport. The porous support plays an important role in restricting mobility, by anchoring the NPs to the support (e.g. by the reaction of the metal NP with surface hydroxyl groups) and by influencing the electronic and structural properties of the supported NPs. Another general strategy to prevent sintering is increasing the melting point of the catalytically active metal by alloying with a higher melting point metal. It is important to spread the NPs uniformly over the support, maximizing the nearest neighbour distance, to reduce the sintering. More sophisticated strategies are also being employed, such as encapsulating individual catalytic NPs in porous shells [4], or use supports with cage porosity to trap the nanoparticles in separate cavities [5].

5.3.3 Support Interaction

The main role of the support is to provide mechanical stability for the NPs. A first requirement is hence that the support itself is stable under reaction conditions. For instance, a porous carbon material will not resist elevated temperatures (>200–300 °C) under a significant pressure of O_2 or H_2, as it will then react to form either CO_2 or CH_4. This process is especially fast if metal NPs are present in the nanoporous carbon material that can catalyse this reaction, such as Ni or Co. Silica supports are suitable for most gas phase reactions. However, they have poor hydrothermal stability. If water is a reactant, intermediate or product, collapse of the porous silica is likely. Alumina has somewhat higher hydrothermal stability, but metal cations (especially divalent ones) can easily migrate into the alumina structure.

It is well known that metal-support interaction influences the catalytic functionality of supported NPs. For instance the catalytic activity of noble metal particles for hydrogenation reactions is much larger if they are supported on an acidic material (having a high concentration of acidic –OH groups at the surface) than if supported on materials with neutral or basic surface groups. The interaction of the precursor phases and the supported NPs with the support influences the distribution of NPs over the support as well as their shape and size. Pore confinement can restrict particle growth. In general, the influence of the support on the properties of the NP will be higher if the NP is more strongly bound to the surface of the support material. Alkali and alkaline earth metals typically bind through Coulomb interaction, while transition metals form more covalent bonds by mixing metal 3d orbitals with O 2p orbitals from the support. Noble metals (having filled d-orbitals) show intermediate orbital mixing. Generally the interaction with carbon materials is weaker than for oxidic materials. A strong interaction between the metal and the support is favourable, as it restricts mobility and NP growth. However, if the interaction is too strong part of the NP may form inactive species by reaction with the support, loosing catalytic activity.

In addition to the structural effects, supports may also influence the catalytic properties of the NP by electronic effects, i.e. a shift in the Fermi level of the supported NP as compared to the bulk state. It is not always clear whether actual electron density is transferred between NPs and support, or whether the electronic effect is a result of the Coulomb interaction between the support's surface oxygen groups and the metal NPs.

The porous support material can also be directly involved in the catalytic action. In some cases a discrete reaction step is catalysed by the support and another by the supported metal NP ("bifunctional catalysis"). A prominent example is zeolite supported Pt NPs used for the hydrocracking/isomerization of oil. In this case the cracking of larger molecules and isomerization is catalysed by the acid sites of the zeolite support, while the (de)hydrogenation steps are performed by the supported Pt NPs, and close coupling of these different steps is a prerequisite for effective reaction. In other cases the support might assist in the catalysis by inducing a specific orientation of the adsorbed molecules which favours the desired

reaction catalysed by the metal NPs. In this case typically the selectivity of the reaction depends strongly on the nature of the support. As a last case, sometimes the catalytic sites are specifically those at the interface between metal and support. For instance, Au NPs supported on TiO_2 show surprisingly high activity for the oxidation of CO, and specific catalytic sites at the interface between Au and TiO_2 is one of the proposed explanations for this phenomenon.

5.4 Nanomaterials for Gas Separation and Storage

An increasingly important application area for nanomaterials is in the field of gas separation and reversible gas storage. The gases of interest are generally relatively small molecules, such as hydrogen, oxygen, methane, ammonia, carbon dioxide and short-chain alkanes, alkenes and alkynes. High specificity of gas adsorption requires very uniform materials. Hence most relevant for these applications are ordered microporous materials such as metal organic frameworks and zeolites. However, also supported NPs can play an important role in specific and reversible gas adsorption. In this section, we first discuss the principles and a few selected examples of gas separation materials. In the second part we discuss the relevance of reversible gas storage applications, and treat reversible hydrogen storage in both nanoporous materials and supported NPs in more detail as a showcase.

5.4.1 Gas Separation

Industrial gas separation of small molecules is currently still mostly done by selective freezing: cooling the gas mixture to a temperature at which one component is still a gas while the other becomes liquid. However, this is expensive and consumes much energy, mainly due to the required compression. Also, some gases are very difficult or impossible to separate due to similar or extremely low specific boiling points. Polymeric membranes are used for liquid separations, but are limited in thermal and mechanical stability. A few non-porous inorganic membranes are used for specific applications, such as Pd as a H_2 selective membrane (H-atoms diffuse as interstitials through the metal lattice) and perovskites for O_2 separation (defect-mediated diffusion). The use of inorganic microporous membranes for gas separation is currently emerging. For instance, Linde Type A (LTA) zeolites are now used for dewatering alcohol. Shape-selective zeolites such as MFI are used in combination with catalysis to steer the reaction products, for instance for isomerization and addition reactions (see Sect. 4.1.1 for more details on zeolite porosity). Intensive research activity focuses on metal organic frameworks, which are potentially able to achieve separations, such as between ethane and ethene, that cannot be separated with any other gas separation material.

The most straightforward mechanism for gas separation is by *molecular exclusion*: a membrane can have pores that are large enough to allow certain molecules to pass, but too small for others. For instance the zeolite Silicalite has cages that are accessible only via 0.25 nm windows, which means that water is able to pass (slowly) through the zeolite, while for instance ethanol is not. More commonly gas separation is based on differences in rates with which molecules permeate through the porous material. A first aspect is that of ***specific adsorption interaction***: if the first gas is very strongly adsorbed, it will be selectively held in the pores while a second gas can pass through more rapidly. Also ***different molecular mobilities*** of the two gases can play a role. One gas can experience a much longer effective diffusion pathway than another gas through the same nanoporous material if part of the porosity is only accessible to one of the two. Tuning the materials properties allows playing with these aspects and choosing whether larger or smaller, or specific molecules, are the fastest to pass through nanoporous materials.

Two material systems are currently being used for separation purposes: membranes and beds. Membranes seem ideal, as they can be thin they require little material, and they can in theory be extremely selective. However, it is far from trivial to prepare membranes of zeolites or metal organic framework materials. These membranes should be absolutely crack-free, as otherwise cracks would offer a preferential pathway for molecules transport and cause loss of selectivity. The membranes should also be very thin (hundreds of nm to a few μm thick) to allow high permeation rates as generally molecules diffuse relatively slowly through pores of a similar size. Often high pressures have to be applied to achieve practically relevant permeation rates. Microporous membranes are typically supported on a thicker layer such as macroporous alumina, which has porosity to allow passing of the gases or liquids but is mechanically strong and typically several hundreds of μm thick.

Another option for larger scale gas separation is the use of beds of powders of porous materials. A mixture of gases is fed into the bed containing the powder. One of the gases will pass much faster through the bed than the other gas, which is preferentially held by the porous powder. This means that for a long time only the second gas is found at the outlet of the bed. Only after a certain time, also the first gas will come out ("breakthrough point"). Figure 5.7 shows a schematic of the principle. When a mixture of for instance 3-methylpentane and n-hexane enters a bed of zeolite with pores large enough to contain n-hexane, but too small for 3-methylpentane, the n-hexane enters the pores of the zeolite, and experiences a very long diffusion pathway. On the other hand the 3-methylpentane passes the zeolite crystals and directly flows through the reactor bed. Only when the pores of the zeolite are almost saturated with n-hexane, also the n-hexane will be detected in the outflow of the zeolite bed. In a swing process, the gas flow can be stopped after a certain time of collecting only the second gas at the end of the powder bed, after which the first gas can be recovered by purging and/or heating the bed. This can be important for instance for upgrading fuels, as 3-methyl pentane has much better combustion properties than n-hexane.

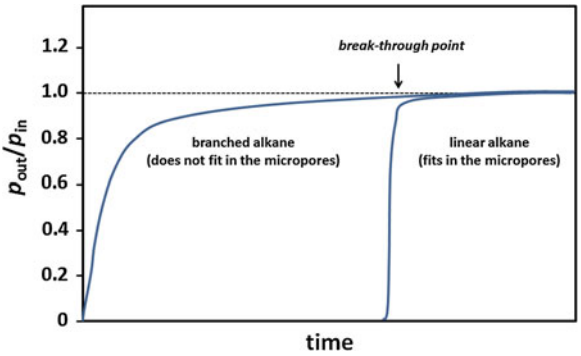

Fig. 5.7 Schematic illustration how two gases can be separated based on molecular size using a zeolite reactor bed. If a gas consist of molecules that are too large to enter the zeolite pores (for instance a branched alkane), it flows straight through the bed, hence the outflow partial pressure p_{out} is soon identical to the inflow partial pressure p_{in}. However a gas that enters the pores (for instance a linear alkane) is retarded by the zeolite [14]

5.4.2 Reversible Gas Storage

A rapidly expanding research area is concerned with the ability of solid materials to *reversibly* bind gases [6]. In principle, temporary storage can be achieved by pressurizing gases, or liquefying them. However, this involves high energy costs, as well as large storage volumes and safety issues. Reversible gas storage in solid materials can offer significant advantages related to volumetric density, safety, handling, controlled release, and selective scavenging. Examples are applications in the field of energy (storing gases that are energy carriers such as CH_4 and H_2), medical applications (such as for controlled administration of NO), and environmental applications (such as in the scavenging of CO_2, SO_2 and NH_3 from exhaust gases).

General requirements for storing gases are high storage capacities (both in weight and volume), cycling stability, and practical issues such as cost, mechanical properties, and safety. Additionally it is crucial to be able to control the gas uptake and release. Typically, gases are released by applying a trigger, such as increasing the temperature, decreasing the pressure, or more specific stimuli, such as by applying UV light, a certain pH, or contact with a replacing species.

Two mechanisms can lead to reversible gas sorption: ***physisorption*** and ***chemisorption***. Physisorption involves the van-der-Waals binding of molecules to solid surfaces. Many metals, and in particular transition metals, can bind gases to their surface. Generally the bond strength of gas molecules is in the range of 2–20 kJ/mole. Nanoporous materials are specifically suitable for physisorption. Molecules can either bind to the (large) internal pore surface, or are adsorbed in the pores by capillary condensation. Chemisorption involves the breaking and formation of chemical bonds. A molecule can specifically bind to a surface atom by

forming a new chemical bond (for instance the dissociative adsorption of H_2 onto Co involves the breaking of the H–H bond, and the formation of two Co–H bonds). Alternatively gases can be absorbed, forming new compounds (hydrides), for instance as in the formation of MgH_2 from Mg and H_2. Metal hydride formation enthalpies are generally larger than 40 kJ/mol.

Which properties do materials need to make them suitable for reversible gas storage? A first important parameter is ***adsorption capacity***. Gas physisorption takes place at a surface. This means that very high specific surface areas are required, as can be found in nanoporous materials and in supported metal NPs. If pores are filled with the gas, the pore volume is also an important parameter. A second requirement is fast ***kinetics***, as gas uptake and release has to occur within a reasonable time span, depending on the specific application. Also to meet this requirement, high specific surface areas, and small particle sizes are favourable. A last very important requirement is related to ***thermodynamics***. Gas uptake and release should be possible at practically relevant conditions in terms of temperature, pressure, and concentration.

Let us in somewhat more detail consider the case of reversible hydrogen storage. Hydrogen is expected to play an important role as an energy carrier in a future society based on more sustainable energy use. Sustainable energy sources such as wind and solar, often yield electricity, rather than liquid or gaseous energy carriers, hence the ability to store large amounts of electricity is crucial if we move towards more sustainable energy sources. However, no attractive options exist to store electricity on a large scale (though batteries are very efficient for small-scale storage). Hydrogen can be produced by electrolysis from water, and in a fuel cell it can be reacted with (oxygen from) air to regenerate the electricity on demand. The gravimetric energy density of hydrogen (released upon combustion) is about three times as large as that of petrol. However it is the lightest gas, and as a consequence has a very low gravimetric density. Furthermore, it is difficult to compress, and only becomes liquid at very low temperatures (−253 °C). Reversible hydrogen storage in nanomaterials is thus an attractive option.

Microporous materials, such as activated carbon materials, zeolites, ordered or disordered mesoporous oxides, as well as metal organic frameworks, are able to reversibly bind appreciable amounts of hydrogen by ***physisorption*** [7]. Especially metal organic frameworks and zeolitic imidazolate frameworks have very high surface areas (up to 2,000–6,000 m^2/g reported) and porosities (up to 2–3 cm^3/g), potentially offering high capacities (Fig. 5.8 a). However, the adsorption enthalpy is relatively low, typically 5–10 kJ/mol [H_2]. As a result, reversible hydrogen storage is only possible at cryogenic conditions (liquid nitrogen temperature), or under high pressures at room temperature. Nevertheless, the range of molecular materials such as metal organic frameworks is certainly not yet fully explored. The adsorption interaction with gases can be tuned by the choice of symmetry, metal atoms and organic linkers.

A second opportunity for reversible hydrogen storage is offered by ***chemisorption***. Many metals are able to reversibly form hydrides. Alkali and alkaline earth metals form ionic hydrides, such as NaH, LiH, and MgH_2, in which the

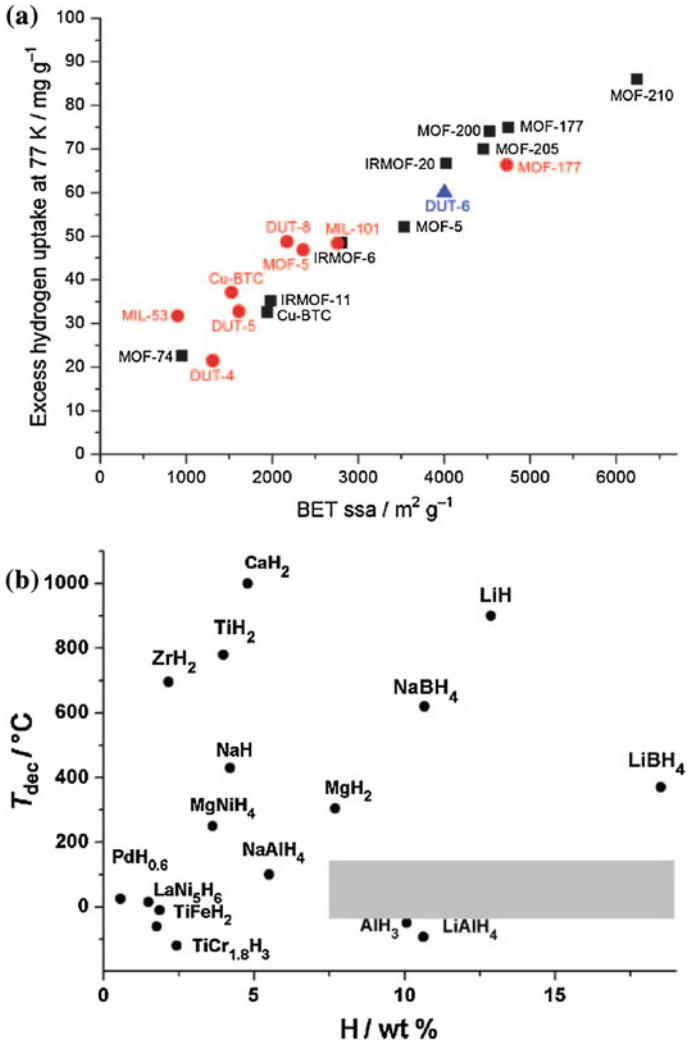

Fig. 5.8 **a** Hydrogen uptake at −196 °C by physisorption in metal organic frameworks with varying specific surface area. Reprinted with permission from Ref. [13]. Copyright © 2011 WILEY-VCH Verlag GmbH & Co. KGaA, Weinheim. **b** Equilibrium hydrogen absorption temperature under 1 bar pressure in different metal hydrides plotted versus the hydrogen capacity. The *grey square* indicates a favourable situation for practical application. Reprinted with permission from Ref. [8]. Copyright © 2010 WILEY-VCH Verlag GmbH & Co. KGaA, Weinheim

hydrogen is present as a hydride anion. Several transition metals (but by far not all) form metallic hydrides, in which hydrogen atoms are present at interstitial positions in the metal lattice, such as for PdH_x and YH_x. Let us return to an important requirement for reversible gas storage: uptake and release of the gas should occur

under practical conditions in terms of temperature and pressure. This relates to the sorption energy of the hydrogen. As an example, we treat the reaction between a metal M and hydrogen, forming a metal dihydride MH_2:

$$M(s) + H_2(g) \leftrightarrow MH_2(s)$$

The Gibbs free energy change of this reaction ΔG_r is determined by the enthalpy of reaction ΔH_r, the entropy of reaction ΔS_r, and the temperature T:

$$\Delta G_r = \Delta H_r - T\Delta S_r$$

Comparing the situation to standard conditions (p = 1 bar, T = 298 K, a = 1), the equilibrium temperature T_{eq} of this reaction in 1 bar gas pressure can be given by:

$$\Delta T_{eq} = \frac{\Delta H_r^0}{\Delta S_r^0}.$$

This is not entirely correct, as the enthalpy and entropy are slightly temperature dependent, but the error is small. Furthermore, the entropy differences between solid phases are generally much smaller than the entropy of the gas phase components, hence the reaction entropy is dominated by that of hydrogen (130 J K^{-1} mol^{-1}). A simple calculation then shows that equilibrium under 1 bar pressure is reached between room temperature and 100 °C if the sorption enthalpy (which is the negative of the formation enthalpy of the metal hydride) is between 39 and 52 kJ mol^{-1}.

Unfortunately, no metal hydride ideal for hydrogen storage has yet been identified (see Fig. 5.8b). Most metal hydrides known are either too stable (requiring high temperatures for release), too heavy or expensive, or hydrogen uptake and release is low. Complex systems such as $NaAlH_4$, $LiBH_4$ and mixtures of different hydrides and metals are currently being investigated. However, having such multiphase systems inevitably decreases the cycling ability of the materials, due to phase segregation and the need for solid state diffusion.

An effective strategy to enhance hydrogen sorption properties is decreasing the particle size. This is traditionally done by high energy ball milling. A more recently developed strategy is using NPs confined in porous matrices. Nanosizing (<10 nm) and nanoconfinement have been found to result in a large enhancement of the hydrogen sorption kinetics [8]. Furthermore, also significant changes in hydrogen sorption equilibrium pressures are observed. Though theoretically particle size effects are expected to be significant if NPs of 1–2 nm or smaller are used, the physical confinement of metal hydrides in nanopores, and the interaction with the support material seem to be at least as important as particle size effects. Very relevant for a practical application is also that nanoconfinement clearly enhances the reversibility, specifically for complex systems, and facilitates hydrogen absorption under milder conditions. As no ideal material system fulfilling all practical requirements regarding equilibrium, kinetics, reversibility and price has yet been identified, this is a very active area of research.

5.5 Outlook

Nanoparticles have a low intrinsic stability, and especially at higher temperatures or under reactive conditions tend to grow into larger crystallites. Hence often NPs are stabilized by embedding them in mesoporous oxides or nanoporous carbon materials. The most common method to prepare supported NPs is to start from a precursor solution, and use the properties of the support, such as surface charge and porosity, to induce the formation of small NPs upon decomposition of the precursor. Despite the long history of these methods, the past decades have nevertheless seen important progress in allowing more control over particle size (distribution) and location or ordering of the NPs. Alternatively, designing strategies to insert preformed colloidal NPs into existing porous scaffolds, or assembling porous scaffolds around existing NPs is a strongly emerging research field.

The combination of NPs and supports offers a wide range of possibilities to tune the functional properties of the nanocomposite materials. By far the most important application of these materials is as heterogeneous catalysts. Advancement of the structural and electronic analysis, such as based on electron microscopy or synchrotron-techniques, yields steady progress in the level of understanding of the behaviour of these materials, but many fundamental aspects are still to be explored. Another exciting field of study is in applications related to renewable energy, such as for reversible gas storage, solar fuel production and rechargeable battery materials to name a few, fields that will undoubtedly gain even more importance in the coming decades.

5.6 Exercises

1. Different methods to prepare supported NPs are solution impregnation, deposition precipitation, melt infiltration and colloidal deposition. You would like to prepare Cu NPs of about 4 nm size in the pores of an ordered mesoporous SiO_2 with pores of about 10 nm.

   (a) Which of the above mentioned methods would in your view be most suitable to prepare these supported NPs? Explain in at most five sentences the principle of the chosen method. Explain why this method would be suitable to prepare the above mentioned material.
   (b) Which of the four above methods would *not* be suitable to prepare this material? List at least two arguments why this method is clearly less suitable than the others.
   (c) Propose two characterisation methods that can be used to determine the particle size of the supported Cu NPs. For each method explain:

   - which information you can exactly derive from it
   - at least one limitation/disadvantage

2. Hydrogen might be stored in magnesium reversibly by forming magnesium dihydride:

$$Mg(s) + H_2(g) \leftrightarrow MgH_2(s)$$

The enthalpy of formation of MgH_2 is −75 kJ/mol. Its molar weight is 26.32 g/mol and its density is 1.45 g/cm^3.

(a) What is the approximate equilibrium temperature under 1 bar H_2 pressure?
(b) Which enthalpy of formation would be needed to achieve an equilibrium hydrogen pressure at 1 bar pressure and room temperature (298 K)? What particle diameter would be needed to have 1 bar H_2 pressure equilibrium at room temperature? Assume spherical particles and a surface energy of MgH_2 that is 0.5 J/m^2 higher than that of Mg. Neglect volume expansion due to hydrogen uptake.

3. Below are electron microscopy images of a Cu NP supported on a ZnO substrate (Fig. 5.9). The nanoparticle changes shape reversibly if the gas atmosphere above the sample is changed. It is more flat if H_2 is present, and more spherical if H_2O is introduced into the gas atmosphere.

(a) Give two reasons why the gas atmosphere can influence the shape of a supported NP. Explain your answer.
(b) If instead of a ZnO support a flat carbon support would have been used, what would you expect for the shape of the NP compared to that on a ZnO support? Why?

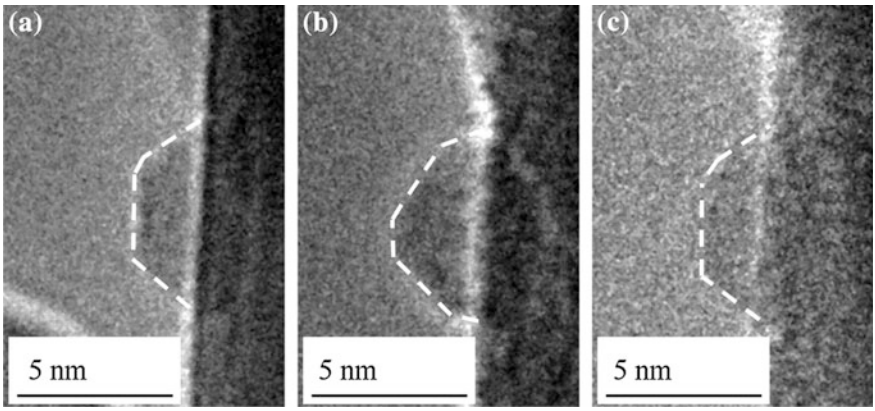

Fig. 5.9 TEM images showing the reversible shape change of a Cu nanocrystal. The same Cu nanocrystal is imaged at 220 °C under **a** H_2 at 1.5 mbar, **b** H_2:H_2O (3:1) at a total pressure of 1.5 mbar, and **c** H_2 at 1.5 mbar. Reprinted from Ref. [3] with permission from AAAS

References

1. De Jong, K.P. (ed.): Synthesis of Solid Catalysts. Wiley-VCH, Weinheim (2009)
2. Beller, M., Renken, A., van Santen, R. (eds.): Catalysis—From Principles to Applications. Wiley-VCH, Weinheim (2012)
3. Hansen, P.L., Wagner, J.B., Helveg, S., Rostrup-Nielsen, J.R., Clausen, B.S., Topsoe, H.: Atom-resolved imaging of dynamic shape changes in supported copper nanocrystals. Science **295**, 2053–2055 (2002)
4. Yan, W.F., Mahurin, S.M., Pan, Z.W., Overbury, S.H., Dai, S.: Ultrastable Au nanocatalyst supported on surface-modified TiO_2 nanocrystals. J. Am. Chem. Soc. **127**, 10480–10481 (2005)
5. Li, L.Y., King, D.L., Liu, J., Huo, Q.S., Zhu, K.K., Wang, C.M., Gerber, M., Stecens, D., Wang, Y.: Stabilization of metal nanoparticles in cubic mesostructured silica and its application in regenerable deep desulfurization of warm syngas. Chem. Mater. **21**, 5356–5364 (2009)
6. Morris, R.E., Wheatley, P.S.: Gas storage in nanoporous materials. Angew. Chem. Int. Ed. **47**, 4981–4996 (2008)
7. Hirscher, M. (ed.): Handbook of Hydrogen Storage. Wiley-VCH, Weinheim (2010)
8. De Jongh, P.E., Adelhelm, P.: Nanosizing and confinement: new strategies towards meeting hydrogen storage goals. ChemSusChem **3**, 1332–1348 (2010)
9. Sietsma, J.R.A., Meeldijk, J.D., den Breejen, J.P., Versluijs-Helder, M., van Dillen, A.J., de Jongh, P.E., de Jong, K.P.: The preparation of supported NiO and Co3O4 nanoparticles by the nitric oxide controlled thermal decomposition of nitrates. Angew. Chem. Int. Ed. **46**, 4547–4549 (2007)
10. Prieto, G., Zečević, J., Friedrich, H., De Jong, K.P., De Jongh, P.E.: Towards stable catalysts by controlling collective properties of supported metal nanoparticles. Nat. Mater. **12**, 34–39 (2013)
11. Toebes, M.L., Van Der Lee, M.K., Tang, L.M., In't Veld, M.H.H., Bitter, J.H., van Dillen, A. J., De Jong, K.P.: Preparation of carbon nanofiber supported platinum and ruthenium catalysts: Comparison of ion adsorption and homogeneous deposition precipitation. J. Phys. Chem. B **108**, 11611–11619 (2004)
12. Den Breejen, J.P., Radstake, P.B., Bitter, J.H., Froseth, V., Holmen, A., de Jong, K.P.: On the origin of the cobalt particle size effects in fischer-tropsch catalysis. J. Am. Chem. Soc. **131**, 7197–7203 (2009)
13. Hirscher, M.: Hydrogen storage by cryoadsorption in ultrahigh-porosity metal-organic frameworks. Angew. Chem. Int. Ed. **50**, 581–582 (2011)
14. Chorkendorff, I., Niemantsverdriet, H.: Concepts of modern catalysis and kinetics. Wiley-VCH, Weinheim (2007)

Chapter 6
The Challenge of Colloidal Nanoparticle Synthesis

Esther Groeneveld and Celso de Mello Donegá

Abstract Inorganic nanoparticles have developed into one of the main pillars of Nanoscience. Colloidal nanoparticles are particularly attractive as they consist of inorganic particles that are coated with a layer of organic ligand molecules. The hybrid nature of these nanostructures greatly expands the possibilities for property tailoring, since both components can be independently manipulated. The inorganic particle dictates the optoelectronic and magnetic properties, while the organic surfactant layer controls physical-chemical properties such as colloidal stability, making processing in solution extremely facile. This chapter addresses the essential physical-chemical concepts needed to understand the preparation of colloidal inorganic nanoparticles, and the remarkable degree of control that has been achieved over their composition, size, shape and surface.

6.1 Introduction

Inorganic nanoparticles (NPs) have developed into one of the main pillars of Nanoscience, allowing scientists to understand fundamental nanoscale effects and to exploit them to engineer the functionality of materials. Colloidal NPs are particularly attractive as they consist of inorganic particles that are coated with a layer of organic ligand molecules, and can therefore be regarded as solution-grown inorganic-organic hybrid nanomaterials (Fig. 6.1). The hybrid nature of these nanostructures greatly expands the possibilities for property tailoring, since both components can be independently manipulated [1]. The inorganic NP dictates the optoelectronic and magnetic properties, while the organic surfactant layer controls physical-chemical properties such as colloidal stability, making processing in solution extremely facile. In addition, synergistic interactions between the inorganic and organic components may give rise to novel properties. This makes colloidal

E. Groeneveld · C. de Mello Donegá (✉)
Debye Institute for Nanomaterials Science, Utrecht University, Utrecht, The Netherlands
e-mail: c.demello-donega@uu.nl

C. de Mello Donegá (ed.), *Nanoparticles*,
DOI 10.1007/978-3-662-44823-6_6

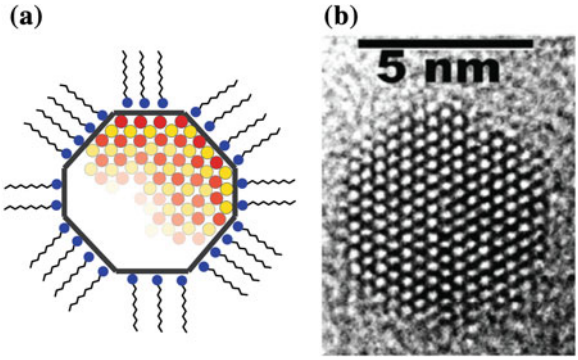

Fig. 6.1 **a** Schematic illustration of a colloidal NP consisting of an inorganic crystal coated with a layer of organic molecules. **b** High-resolution Transmission Electron Microscopy (HR-TEM) image of a colloidal CdSe nanocrystal

chemistry preparation methods highly versatile, and also lower-cost and easier to upscale than other nanomaterial fabrication techniques (e.g., MBE or MOCVD, see Chap. 1). The combination of versatility in property-tailoring and ease of fabrication has turned colloidal NPs into promising materials for a variety of applications (optoelectronics, photonics, catalysis, biomedicine, solar energy harvesting, etc.), spurring an intense research activity over the past decades. As a result, a remarkable degree of control has been achieved over the composition, size, shape and surface of colloidal NPs. In this Chapter, we discuss the essential physical-chemical concepts needed to understand the preparation of colloidal NPs. We will first address the organic layer and subsequently focus on the synthesis of colloidal NPs. Several excellent reviews and books covering various aspects of colloidal NP research have been published over the last few years [1–20], and provide the basis for this Chapter.

6.2 Colloidal Nanoparticles: When the Whole Is Greater than the Sum of Its Parts

The hybrid organic-inorganic nature of colloidal NPs implies that they can be described as a two component system (Fig. 6.1), consisting of an inorganic core and an organic shell. The properties of colloidal NPs are dictated not only by the individual characteristics of the inorganic and organic components, but also by their mutual interaction. The organic-inorganic interface and the interplay between the organic surfactant molecules are also of crucial importance during the synthesis of colloidal NPs, being the driving forces behind the remarkable control achieved over the size, shape and architecture of NPs (Sect. 6.3).

6.2.1 The Inorganic Core

Colloidal inorganic nanoparticles (NPs) may be amorphous (e.g., SiO_2) or crystalline (e.g., TiO_2). Due to the high surface to volume ratio of NPs (Chap. 1) the overall surface free energy can dramatically modify the stability of crystalline phases, making it possible to obtain NPs with crystal structures that are metastable for the bulk material (Sect. 6.3). The crystal structure is important since it not only affects the electronic structure of the material, but also defines which facets will be exposed on the surface of the NP. The nature of the facets may have a large impact on NP growth, as will be discussed in Sect. 6.3.

Moreover, NPs can be obtained with a variety of shapes (e.g., spheres, cubes, pyramids, rods, multipods, etc.) and compositions (Fig. 6.2). They can be made of single materials (metals, e.g. Au, semiconductors, e.g. InP, or insulators, e.g. SiO_2), alloys (e.g., FePt, $Cd_{1-x}Zn_xS$), doped materials (e.g., ZnSe:Mn, $NaYF_4$:Yb, Er), or combinations of two (or more) different materials joined by one or more interfaces (e.g., a CdSe core surrounded by a ZnS shell) [1]. The latter category of NPs is usually referred to as heteronanocrystals (HNCs). The nature of the materials connected by heterojunctions in HNCs can be widely different [1–5]. Consequently, HNCs can be made combining metals (e.g., Ag-Au), metals and semiconductors (e.g., Au-CdSe), metals and insulators (e.g., Au-SiO_2), or different semiconductors (e.g., CdSe-ZnS). Multicomponent colloidal HNCs combining different types of materials have also been obtained (e.g., CdSe/(Cd,Zn)S/ZnS core/multishell quantum dots embedded in SiO_2 NPs) [1].

The ability to join different materials in the same HNC opens up a rich realm of possibilities for property engineering [1]. For example, magnetic and optical functionalities can be combined in a single HNC (e.g., FePt/PbSe dumbbell HNCs). Alternatively, an inert material can be used to add chemical stability and/or modify the solubility of a colloidal HNC without affecting its optical properties (e.g., encapsulation of NCs in silica). Moreover, novel properties may arise from the

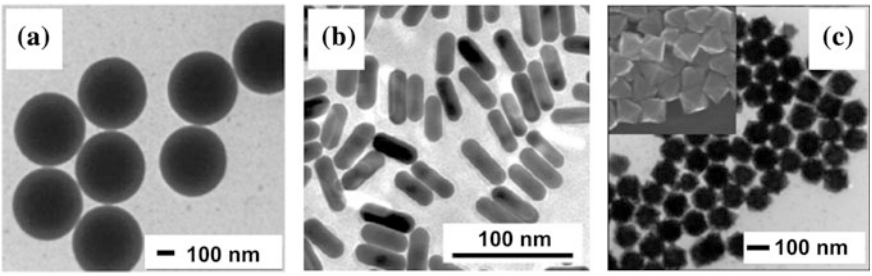

Fig. 6.2 Gallery of TEM images of colloidal NPs of various shapes and compositions. **a** SiO_2. Reprinted with permission from Ref. [21], Copyright (2000) American Chemical Society. **b** Gold. Reprinted with permission from Ref. [22], Copyright (2007) American Chemical Society. **c** PbSe. Reprinted with permission from [23], Copyright (2006) American Chemical Society

interaction between the different components of the HNC. The properties of NPs of semiconductors and metals have been addressed in Chaps. 2 and 3, respectively.

6.2.2 The Organic Shell

The organic molecules that coat the surface of colloidal NPs, forming the surfactant (or capping) layer, consist of a polar head group and a non-polar hydrocarbon tail (i.e., they are *amphiphilic*). These molecules perform a number of essential roles. First, ligand molecules are crucially important during the synthesis of colloidal NPs in order to control their size, shape and architecture. Second, several physical-chemical properties are directly determined by the surfactant layer, and can thus be manipulated by a judicious choice of ligands. This section focuses on the latter aspect. The synthesis of colloidal NPs is discussed in Sect. 6.3.

Amphiphilic molecules as surfactants. The functionality of the surfactant molecule depends on both the polar head group and the non-polar hydrocarbon tail. The apolar tail determines the interaction of the surfactant layer with the surrounding medium, while the polar head coordinates to metal atoms in solution and at the NP surface. Moreover, both domains strongly influence the diffusion rates of the free surfactant molecules. These characteristics have a large impact on the nucleation and growth rates of colloidal NPs (Sect. 6.3) and on their properties after growth, and must thus be carefully considered when designing syntheses or post-preparation processing procedures.

Surfactant-Surface bond. The ability of the head group to bind to the NP surface originates from the presence of donor atoms (e.g., N, O, S, P), which possess unshared electron pairs and are thus capable of forming coordinating bonds with metal atoms or ions. This is why the surfactant molecules employed during the colloidal synthesis of NPs are commonly referred to as coordinating ligands or coordinating solvents. The variety of chemicals suitable for use as coordinating ligands is very large (Fig. 6.3): alkylamines (R-NH_2, e.g., hexadecylamine—HDA), fatty acids (R-COOH, e.g., oleic acid—OA), alkylphosphine oxides (R_3PO, e.g., trioctylphosphineoxide—TOPO), phosphonic acids (R-PO_3H_2, e.g., *n*-octadecylphosphonic acid—ODPA), alkylthiols (R-SH, e.g., hexanethiol—HT). These chemicals bind primarily to metal atoms (e.g., Cd, Zn, In). The choice of coordinating ligands for the non-metal components of the NP (e.g., S, Se, Te, P) is more limited, and typically alkyl phosphines (e.g., trioctylphosphine, TOP) are used. It is also possible to use ligands with two polar heads separated by a hydrocarbon chain (e.g., dithiols, HS-R-SH, mercapto *n*-alkyl acids, HS-R-COOH, hydroxyalkylphosphines, or peptides). These ligands are used to cross-link NPs together or to render them water soluble, either by post-preparative ligand exchange procedures or by directly synthesizing them in aqueous medium [1, 11, 17]. Amphiphilic multidentate polymeric ligands and dendrons may also be used, leading to NP encapsulation [1, 24]. Fully inorganic molecules or ions (e.g., metal chalcogenide complexes such as $Sn_2S_6^{-4}$, or ions such as S^{2-} or OH^-) have also been shown to work as NP surfactants [1, 11, 25].

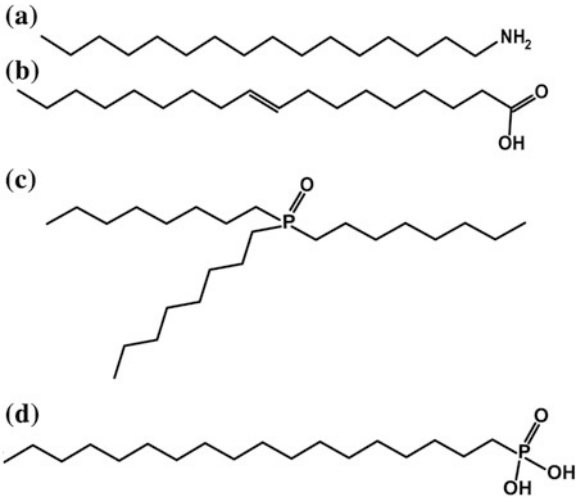

Fig. 6.3 Examples of organic amphiphilic molecules commonly used as ligands in colloidal NP synthesis: **a** hexadecylamine (HDA), **b** oleic acid (OA), **c** trioctylphosphine oxide (TOPO), **d** octadecylphosphonic acid (ODPA)

The **metal-ligand binding strength** is a very important parameter, being largely responsible for the effectiveness of the surfactant molecule. For example, a strong bond may be useful to provide stability and surface passivation to the NP after the synthesis, but may hinder its growth, therefore being undesirable during the synthesis. On the other hand, too weak bonds result in uncontrolled growth and/or insufficient colloidal stability. Coordination chemistry and organic chemistry provide a number of useful principles that can be used as guidelines for the rational choice of surfactants [1]. The bond between the donor atom of the polar head group and the metal atom can be rationalized in terms of a Lewis acid-base interaction, whose strength is determined by both electrostatic and covalent contributions. Smaller and/or more charged metal ions (i.e., hard Lewis acids, e.g., Zn^{2+}) will form stronger bonds with donors capable of strong electrostatic interactions (i.e., hard Lewis bases, which are characterized by large electronegativities and small polarisabilities, e.g., Oxygen). Conversely, larger and/or less charged metal ions (i.e., soft Lewis acids, e.g., Cd^{2+} or Pb^{2+}) will favor larger and more polarisable ligand atoms (i.e., soft Lewis bases, e.g., Sulfur). Phosphines differ from the other commonly used surfactants because they bind to metals by a combination of σ donation from the P atom and π back-bonding from the metal atom. Therefore, they will bind strongly to chalcogenides and transition metals in their low oxidation states, but interact only very weakly with IIB, IIIA and IVA metals (e.g., Cd, Zn, In, Pb). Further, the bond strength increases with the number of donor atoms (i.e., monodentate < bidentate < tridentate, and so forth). The length of the hydrocarbon tail is also an important parameter, since shorter alkyl chains result in weaker metal-ligand bonds and weaker interactions between the surfactant molecules, leading to more dynamic NP-surfactant interactions and higher diffusion rates at relatively lower temperatures. Steric effects are also relevant and should be considered when utilizing bulky surfactants, such as tertiary phosphineoxides and amines.

Surfactants and colloidal stability. The capping layer prevents the aggregation of the NPs by means of repulsive Van der Waals or electrostatic interactions (steric stabilization and charge stabilization, respectively). The first mechanism is responsible for the colloidal stability of NPs coated with hydrophobic surfactants in apolar solvents, while the second confers stability to dispersions of NPs coated with hydrophilic or charged ligands in polar media. The colloidal stability can be manipulated to narrow the size distribution of ensembles of NPs via post-preparative size-selective precipitation. This is achieved by slowly adding a non-solvent to a colloidal suspension of NPs (e.g., methanol to a colloidal suspension of NPs in toluene). Larger NPs exert greater attractive forces over each other and thus destabilize with smaller volumes of non-solvent than smaller NPs. Therefore, the gradual addition allows different NP sizes to be sequentially separated.

Surfactants and self-assembled monolayers. Amphiphilic molecules are known to form self-assembled monolayers (SAM's) on surfaces [26] (Fig. 6.4a). The surfactant monolayer that coats a colloidal NP can be envisioned as a three-dimensionally constrained SAM of tightly packed organic amphiphilic molecules [1] (Fig. 6.4b). It is becoming increasingly evident that the morphology and organization of the surfactant layer plays an essential role in defining the properties of colloidal NPs. For example, phase transitions in the surfactant layer have been shown to affect the optical properties of CdSe and CdTe colloidal quantum dots (QDs) [27], and the kinetics of heteronucleation of Au NPs on CdSe/CdS nanorods [28]. Moreover, Van der Waals, electrostatic or covalent interactions with the native surfactant layer can be utilized to assemble new molecules around a colloidal NP, thereby introducing new functionalities or modifying properties. For example, the van der Waals interactions between lipid molecules and the octadecylamine coating layer of CdSe/(Cd,Zn)S/ZnS core/multishell (CSS) QDs has been successfully used to self-assemble a multifunctional lipid monolayer around the QD, yielding labels for bimodal biomedical imaging (Fig. 6.4b) [29].

Surfactants and optical properties. The photoluminescence (PL) quantum efficiency (PL QE) of colloidal NPs is strongly dependent on the nature of the surfactant layer [1]. For example, the PL QE of colloidal CdSe quantum dots (QDs)

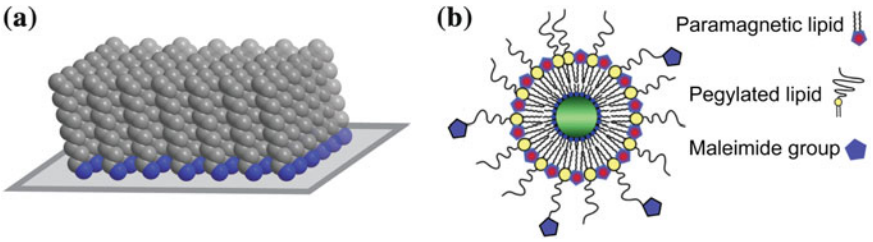

Fig. 6.4 **a** Schematic representation of a self-assembled monolayer (SAM) of amphiphilic molecules on a surface **b** Schematic representation of a nanolabel for bimodal (optical and MRI) biomedical imaging, obtained by self-assembly of a multifunctional lipid monolayer around an organically capped CdSe/(Cd,Zn)S/ZnS core/multishell colloidal QD [29]. Courtesy of Dr. W. J. M. Mulder (Mount Sinai School of Medicine, USA)

increases by one order of magnitude (from ≤5 to ≥50 %) after the exchange of the native trioctylphosphineoxide capping layer by primary alkylamines, such as hexadecylamine. In contrast, organic ligands have also been reported to decrease the PL QEs of colloidal QDs (see item c below). The influence of organic ligands on the PL QEs of semiconductor NPs is due to several mechanisms:

(a) **Surface passivation**. The bond formed between the donor atom of the ligand molecules and the dangling orbitals at the NP surface shifts the energy of the surface (and trap) states away from the HOMO-LUMO gap, thereby preventing nonradiative relaxation via these states. Linear monodentate ligand molecules (e.g., primary alkylamines) provide a more efficient surface passivation than bulky ligands (e.g., TOPO), because they lead to a higher surface coverage density, allowing dangling orbitals to be fully passivated.

(b) **Surface relaxation and reconstruction**. Surface states can also be shifted away from the HOMO-LUMO energy gap by a reorganization of the surface atoms in such a way that the dangling orbitals of neighbouring atoms partially overlap, leading to a redistribution of electronic density. This is referred to as surface self-passivation and can be achieved by surface relaxation and/or reconstruction. Surfactant molecules are likely to strongly affect surface relaxation and reconstruction processes, since they modify the surface free energies and thereby may hinder or facilitate the reorganization of surface atoms. The interaction between the surfactant molecules and their collective effect is also crucial, making the surfactant layer a very active player in the relaxation and reconstruction of the surfaces of colloidal NPs [1].

(c) **Carrier trapping**. Some ligands efficiently scavenge photogenerated electrons or holes from NPs, thereby leading to PL quenching, since this precludes the exciton radiative recombination. Well-known examples of such ligands are alkylthiols and methylviologen, which efficiently trap holes and electrons, respectively, from CdSe QDs [1].

6.2.3 The Organic–Inorganic Interface and Ligand Dynamics

The interface between the surfactant layer and the inorganic NP is defined by the coordinating atoms of the surfactant molecules and the surface atoms of the NP (Fig. 6.5). The driving force for its organization is the minimization of the interfacial free energies, which results from the interplay between several forces acting within and across the interface (e.g., intermolecular interactions between the surfactants, attractive forces between the NP surface and the surfactant polar heads, interactions between the surface and the interior atoms of the NP). Therefore, the organic-inorganic interface is a very dynamic structure that strongly influences a number of key properties of colloidal NPs, making them highly responsive to their environment, during and after their synthesis.

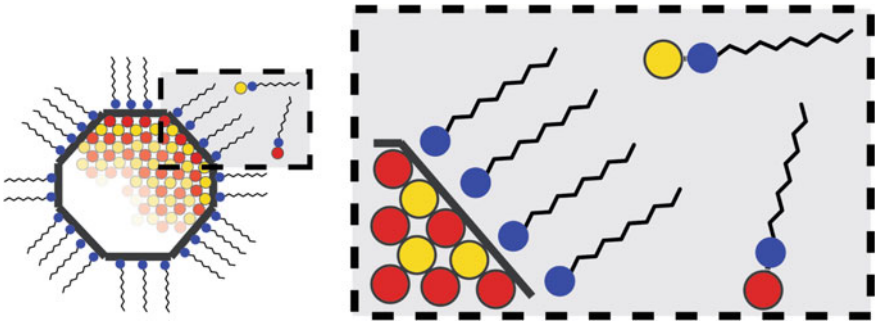

Fig. 6.5 Schematic representation of a colloidal NC showing the crystalline and multifaceted nature of the inorganic core and the monolayer of amphiphilic organic molecules (the ligand shell) bound to the surface. The right panel emphasizes the essential interactions taking place between the atoms within the NC, at the surface and in the growth medium

Theoretical calculations of the surface free energies of NPs have been carried out only for a few selected facets of CdSe and PbSe [30, 31]. The results indicate that the various crystallographic facets of a NP can have quite different free energies, arising from different arrangements and densities of atoms, polarity and number of surface dangling bonds. Further, the energies of individual crystallographic facets can be modified differently by surface relaxation (or reconstruction) and binding of surfactant molecules. As it will be discussed below (Sect. 6.3), this has important consequences for the growth kinetics and shape control of NPs, and implies that the faceting of a colloidal NP, and therefore its shape, may be largely determined by the organic-inorganic interfacial energies due to the large surface to volume ratio of NPs.

The impact of surfactant molecules on the equilibrium shape of colloidal NPs has been demonstrated by in situ high-temperature HRTEM studies on PbSe NPs [31]. Hexylamine capped PbSe NPs are observed to have a nearly spherical, multifaceted morphology, in which a considerable fraction of the surface consists of {111} polar facets. Upon removal of the capping molecules through gentle in situ heating (393 K) under vacuum, the NPs reconstruct into cubes with predominantly {100} non-polar facets (Fig. 6.6). This is consistent with the theoretical prediction that the non-polar {100} surface is the most stable under vacuum, and demonstrates that the dominance of the polar {111} facets in the surface of the capped NC is due to the hexylamine surfactant molecules, which lower the free energies of these facets with respect to the {100} facets [31].

Ligand Exchange and Ligand dynamics. The native surfactant molecules can easily be exchanged by different ligands. Post-preparative ligand exchange is a valuable and widely used tool for property control, since the surfactant layer affects several properties of colloidal NPs [1, 11]. For example, NPs can be readily transferred from apolar solvents into water by exchanging the native hydrophobic ligands by hydrophilic or charged ones [1, 24]. Further, the most widely procedure for surface functionalization of colloidal NPs involves the displacement of the native surfactant with difunctional molecules containing a surface-binding head

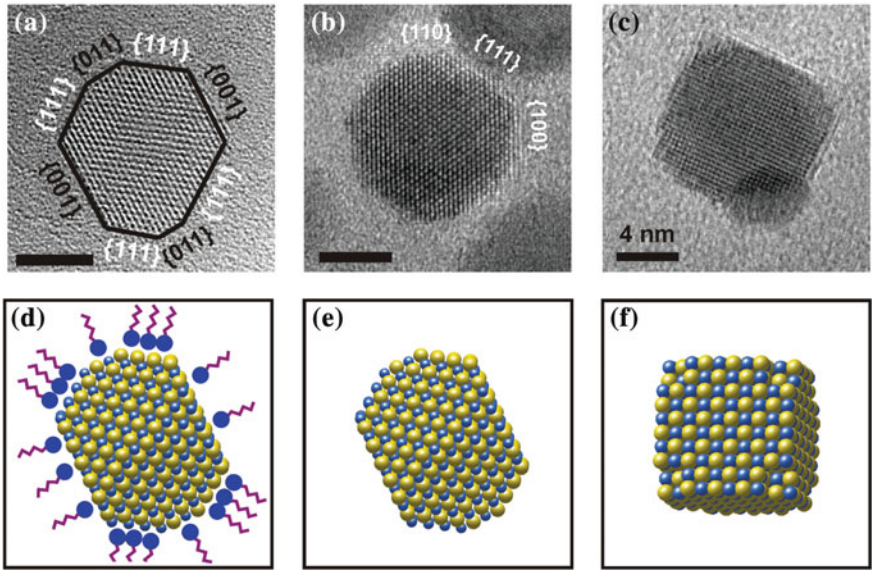

Fig. 6.6 High-resolution TEM images showing the morphology of PbSe NCs in a near-110 projection showing non-polar {001} and {011} surfaces and polar {111} surfaces **a**, and in a 011 projection, showing the {100}, {110}, and {111} surfaces **b**. Cubic NCs start to dominate after longer annealing times as the surfactants evaporate **c**. The process of morphological reconstruction induced by the loss of surfactants is schematically illustrated in panels **d** to **f** [31]. Courtesy of Dr. M. A. van Huis (Utrecht University, Netherlands). Reproduced by permission of the Royal Society of Chemistry from Ref. [1]

group at one end and the desired functional group at the other end. This is also useful to attach NPs to surfaces (e.g., mesoporous oxide layers in QD sensitized solar cells). Ligand exchange can also be used to increase the photoluminescence quantum yields of colloidal NPs.

The exchange of weaker by stronger ligands (e.g., amines by thiols) occurs very easily and can be carried out immediately after the synthesis, with the NPs still in the original crude reaction mixture [1]. To exchange the native ligand by a weaker one (e.g., fatty acids by amines) or by one with a comparable binding strength (i.e., the same functional head group) it is necessary to use a large excess of the new ligand, which requires the purification of the NPs by precipitation prior to adding the new ligand. After allowing the exchange reaction to reach equilibrium (which may take up to several days for weak ligands) the NPs can be precipitated and isolated. Surfactants with low boiling points (e.g., pyridine or allylamine) can also be used, since the ligand exchange procedure is carried out at mild temperatures (≤50 °C). These ligands are often used as weak and labile surfactants that can be easily replaced by other surfactants (regardless of their affinity for the NP surface) or stripped off the surface by vacuum treatment [1, 11].

The success of ligand exchange protocols provides a clear demonstration that the surfactant layer is very dynamic. Nevertheless, the dynamics of ligands bound to

NP surfaces have only recently been quantitatively investigated [1]. The results show that the surfactant molecules bind and unbind to the NP surface on a time-scale that is dependent on their binding strength. Weaker ligands, such as amines, bind on and off the surface at faster rates (viz., ≥0.05 ms^{-1}), while stronger ligands (e.g., oleic acid) have much longer residence times at the surface (viz., s^{-1} range) [32] (see Chap. 10 for details). Therefore, the exchange rates of amines can be orders of magnitude faster than those of more tightly bound ligands (viz., seconds versus. hours). Ligand-ligand interactions are also important and are reflected in slower exchange rates for bulkier ligands, due to a combination of more pronounced steric hindrance and slower diffusion times away from the surface (or towards the surface, for incoming ligands). It is also clear that the tendency of leaving the NP surface increases with decreasing chain length for a given head group [33]. It has also been demonstrated that the ligand exchange rates are strongly site-dependent, being much faster at defect sites in the surfactant monolayer (e.g., vertices [34]).

6.3 Colloidal Nanoparticle Synthesis

6.3.1 Synthesis Methodologies

As mentioned above (Sect. 6.2.1), colloidal inorganic NPs may have a variety of shapes and compositions, and be made of single materials, alloys, doped materials, or different materials joined by one or more interfaces (i.e., heteronanocrystals, HNCs). In this section we will focus on synthesis strategies for single composition NPs and HNCs.

Colloidal Nanoparticles. Colloidal NPs are synthesized in liquid-phase by carrying out chemical precipitation reactions under conditions that allow the growth to be controlled and arrested while the particle size is still in the nanoscale [6], yielding colloidal sols. This is achieved by combining **precursors** that contain the constituent elements (viz., organometallic compounds or inorganic salts) at sufficiently high temperatures and/or concentrations, in the presence of surfactant molecules (or stabilizers). For example, CdSe NPs can be synthesized by reacting dimethylcadmium (or cadmium oleate) and trioctylphosphineselenium dissolved in hexadecylamine at 300 °C. Thermal decomposition of the **precursors** or dissociation of the salts releases a high concentration of the constituent elements over a short period of time, leading to a temporally short **nucleation** event followed by slower **growth** on the existing nuclei (see 6.3.3). In most cases the precursor chemicals are quickly injected into the reaction media (water or nonpolar organic solvents containing surfactants or stabilizers) to ensure that the nucleation event takes place over a narrow and well-defined time window. In water (or alcohol) based systems the injection is carried out at room temperature, but the majority of the synthesis protocols uses the so-called "**hot-injection**" **technique** (Fig. 6.7a), which involves relatively high injection temperatures (viz., ∼100 to ∼300 °C) in

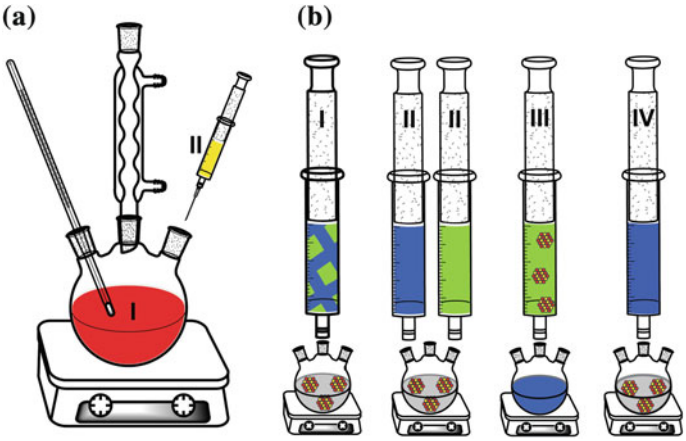

Fig. 6.7 **a** Schematic representation of a typical colloidal nanocrystal synthesis by the hot injection method: one of the two precursors (*I*) is in the reaction flask at high temperatures while the other precursor (*II*), which is at room temperature, is swiftly injected into the reaction flask. **b** Schematic overview of several strategies to synthesize colloidal HNCs: (*I*) dropwise addition of mixed precursor, (*II*) alternate addition (dropwise/injection) of precursors, (*III*) seeded injection, (*IV*) cation exchange

high boiling point apolar solvents. It is also possible to achieve a temporally narrow nucleation stage by quickly increasing the temperature of the reaction system (the "**heating up**" **technique**) or by injecting a small concentration of a chemical that catalyses the decomposition of the precursors. A well-known example of the latter is the preparation of SiO_2 NPs by hydrolysis and polycondensation of tetraethylorthosilicate in ethanol, which is catalysed by bases or acids (e.g., ammonia or HCl solutions).

The **surfactants** present in the reaction medium **control the nucleation and growth rates** by dynamically binding to the surface of the NPs and to the constituent elements in solution, and are thus essential to control the size and shape of NPs (see 6.3.3). The functionality of the surfactant molecules depends on both the polar head and the apolar tail. Surfactants can be introduced explicitly, either as the solvent itself (coordinating solvent) or diluted in a non-coordinating solvent (e.g., octadecene—ODE), but can also be part of the precursor compound (e.g., cadmium oleate). There are also amphiphilic molecules that can simultaneous play the role of solvent, surfactant and precursor. A well-known example is dodecanethiol (DDT), which reacts with metal ions at sufficiently high temperatures (<180 °C) to produce metal sulphide NPs that are stabilized by intact DDT molecules. Another example are phosphines, which can be used as coordinating solvents, surfactants, reducing agents and P-source (at temperatures above 300 °C).

The NP size can also be controlled by carrying out the reaction inside confined volumes, such as micelles or reverse micelles (**microemulsion synthesis**) [35]. In this case the maximum size is limited by the micelle dimensions. This method is no longer widely used for the synthesis of semiconductor and metal NCs, since it offers

a smaller degree of size and shape control than that achieved by other synthesis strategies. However, it is the method of choice to synthesize NPs of metal oxides such as TiO_2 and SiO_2, and one of the best methods available to encapsulate NCs into silica NPs.

ColloidalHeteronanocrystals. Colloidal HNCs are obtained by growing a different material over pre-existing NPs (i.e., seeds). There are essentially two strategies for the synthesis of colloidal HNCs (Fig. 6.7b): the **single-stage** (or "one-pot") approach, and the **multistage seeded growth approach**. In the first one the HNC is fabricated by sequentially adding the precursors of the different components in the same reaction flask. Although this approach may be appealing for its simplicity, it cannot provide the degree of control required for the targeted synthesis of high-quality colloidal HNCs. As will be discussed (6.3.3), the heteroepitaxial growth of high-quality shells (or branches) on seed NPs requires physical-chemical conditions that substantially differ from those needed for the growth of single composition NPs. Moreover, uncontrolled interfacial alloying is usually unavoidable in a single-stage synthesis, since the concentration of monomers of the first component should still be substantial when the second component is added (otherwise inter-NP ripening would have set in, see 6.3.3). In contrast, the **multistage approach** is highly versatile and provides several **advantages** over the single-stage strategy [1]:

1. The addition of preformed nuclei to the reaction mixture (i.e., seeded growth) is a very effective way of separating nucleation and growth, and leads to a better control over the growth stage.
2. Different conditions can be used to grow each segment of the HNC. Therefore, the targeted synthesis of complex multicomponent HNCs, in which NPs of different composition and shape are sequentially combined, becomes possible.
3. The seeds (NPs or HNCs) can be subjected to post-synthetic processing (purification, size-selection, ligand exchange or annealing). This can be used to improve the quality of the seeds and allows for judicious surface manipulation. This is a key advantage, as the seed characteristics have a decisive impact on the final shape of the HNCs.
4. The heterointerface is better controlled, since the possibility of unintentional interfacial alloying is almost eliminated (provided the temperature is low enough and the excess of unreacted precursors has been removed from the surface of the seed NPs).

Two techniques can be used to mix the NP seeds and the precursors of the second component in the multistage approach (Fig. 6.7b):

(I) **Precursor addition to seeds**. This is the most commonly used technique to grow HNCs, being particularly well suited when slow growth is required. The precursor solution for the new component of the HNC is added to the seed NPs dissolved in a suitable surfactant mixture and under vigorous stirring. The reaction temperature is typically set prior to the precursor addition, but it may also be increased following it (the so-called "heating-up" or "thermal cycling"

method [1, 8]). The precursor addition must keep relatively constant growth rates, while preventing homogeneous nucleation, and can be performed in several ways: (a) dropwise addition of mixed precursors, (b) alternate injections of each precursor separately (the so-called Successive Ion Layer Adsorption and Reaction method, "SILAR"), or (c) dropwise and alternate addition. The effectiveness of each method depends primarily on the precursor reactivity. If the precursor is highly reactive, all three methods will fail to completely suppress homogeneous nucleation, but (c) is the most effective. Conversely, if the precursor is too stable, the differences between (a) and (c) vanish, and all three methods will fail if the time allowed for growth between two subsequent additions is too short (i.e., if the addition rates exceed the consumption rates). In this case the concentration of unconsumed precursors builds up, eventually exceeding the threshold for homogeneous nucleation.

(II) **Seeded injection**. In this method seed NPs and one of the precursors are injected together in a hot solution containing the second precursor and surfactants, under vigorous stirring. This leads to very fast heteroepitaxial growth over the seeds, preventing homogeneous nucleation and leading to comparable growth rates for all the HNCs in the ensemble. Anisotropic growth can be ensured by using a high concentration of precursors and suitable surfactants (see 6.3.3). This technique has been successfully used to obtain anisotropic HNCs with well-defined length and diameter for a number of compositions (viz., dot core/rod shell nanorods: CdSe/CdS, ZnSe/CdS; tetrapods: CdSe/CdS, CdSe/CdTe, ZnTe/CdTe, ZnTe/CdSe, ZnTe/CdS, CdTe/CdSe) [1–3, 11].

Heteronanocrystals and single compound nanocrystals can also be prepared by using **Cation Exchange** [1, 36–39]. This method consists of adding the cation precursor of the new component to a solution of the parent NP in a solvent (e.g., methanol, toluene, or a coordinating solvent), under conditions that favour a place exchange reaction in which the new cation diffuses into the parent NP and displaces the parent cation. Very often the anionic sublattice is not affected, leading to a topotactic reaction, through which the size and shape of the parent NPs are preserved in the product NPs.

Cation exchange reactions consist of a number of inherently linked elementary kinetic steps [36–38]. The thermodynamic driving force is determined by the energy balance of the overall reaction. Nevertheless, since the elementary steps must proceed in a concerted manner, the energy input or output involved in each step is important, so that the rate limiting step will be the least favoured elementary step [37, 38]. Consequently, the exact conditions to achieve topotactic cation exchange depend on the nature of the incoming and outgoing cations, and their relative stabilities in the nanoparticle and in solution. Therefore, some exchange reactions can happen at room temperature and with stoichiometric amounts of the replacing cation (e.g., Cd^{2+} for Ag^{+} exchange in CdS NCs), while others require higher temperatures and large excesses of the replacing cation (e.g., Pb^{2+} for Cd^{2+}

in PbSe NCs). Cation exchange reactions can thus be controlled by choosing suitable solvents and ligands, and tuning the temperature, reaction time, and the ratio between parent and replacing cations.

This allows also the extent of the conversion to be controlled, leading to partial or total replacement of the native cation [36–39]. In the case of partial exchange, the elemental profile distribution within the product NP can also be tailored, so that core/shell heteronanocrystals [36–38], homogeneous or gradient alloy nanocrystals [36], and doped nanocrystals [37, 38] can be obtained, depending on the chemical system and reaction conditions.

The exchange rates may also strongly depend on the crystallographic facets, as observed for CdS/Cu_2S and PbSe/CdSe [37, 38]. Moreover, the NP composition can be controlled through successive exchange reactions (e.g., first Cd^{2+} by Cu^{+}, and subsequently Cu^{+} by Pb^{2+} or Zn^{2+}) [37–39]. Cation exchange thus offers an attractive route to shape-controlled NCs and HNCs that are not attainable by direct synthesis methods.

6.3.2 The Hidden Variable: Adventitious Impurities

The complex nature of the reaction systems typically used in the colloidal synthesis of NPs renders many synthetic protocols difficult to reproduce. The variability in the synthesis can partially be traced to unintentional variations in the reaction parameters. Nevertheless, the largest source of irreproducibility is the presence of adventitious impurities in the chemicals used, since impurities may be much stronger ligands than the intended surfactants and may therefore dominate the NP nucleation and growth kinetics [1].

The critical role of impurities was recognized already in the early years. Phosphonic acids were originally adventitious impurities in technical TOPO, bringing a bit of alchemy to the nascent field of colloidal nanoscience, and giving rise to a rich scientific lore, full of anecdotal tales about "good" and "bad" batches of TOPO. After their presence and impact was recognized they became essential additives to control the shape of colloidal NPs. The intentional addition of ligands presumed to be analogous to the impurities in technical TOPO (i.e., alkylphosphonic acids) led to the first controlled synthesis of colloidal QRs and tetrapods, initiating extensive research activities on understanding and controlling the anisotropic growth of NPs [1]. The reproducibility problems associated with the use of TOPO as a surfactant became more and more evident over the years, despite the improved purity of commercially available TOPO (99 %). Up to now, ten different impurities have been identified in commercially available TOPO (99 %) [40], going from simple molecules such as H_3PO_3 to larger molecules such as 1-methylheptyl-di-*n*-octylphosphineoxide. More importantly, some of those impurities have turned out to be essential for the synthesis of high-quality shape controlled CdSe NPs (e.g., di-*n*-octylphosphinic acid, at levels of 0.2 wt%, for nanowires) [40]. It is also worth mentioning that the composition of the surfactant layer on colloidal CdSe NPs prepared in technical TOPO has been

shown to consist primarily of P-containing impurities (viz., *n*-octylphosphonate and P,P′-(di-*n*-octyl)dihydrogen pyrophosphonic acid) [41]. The impact of impurities has also been identified in other commonly used surfactants, such as TOP [1]. Impurities may also be inadvertently introduced during the preparation of the precursors (e.g., traces of acetic acid may be left when converting Cd acetate into Cd oleate) or heating of the organic surfactant mixture [1].

It should also be realized that the early work on the synthesis of colloidal NPs was affected by the limited purity of the chemicals available at the time. The extent to which impurities in the surfactants are still biasing the conclusions currently published in the literature is unclear. To improve the reproducibility of synthetic protocols, some groups advocate the purification of the starting chemicals and intentional addition of impurities. An alternative is the use of protocols based on diluted surfactant systems (e.g., octadecylamine in 1-octadecene), which are less sensitive to impurities than those based on neat surfactant systems [1], since the impurities are then diluted to levels that no longer affect the reaction kinetics.

6.3.3 *Colloidal Nanoparticle Synthesis: Fundamental Concepts*

The parameter space for controlling the nucleation and growth rates of colloidal NPs is quite large: nature and concentration of precursors, rate (and method) of addition of precursors, temperature (which may be different at different reaction stages), and composition of the coordinating solvent (i.e., nature and concentration of surfactants). This complexity renders the nucleation and growth kinetics quite sensitive to variations and inhomogenities in concentrations, temperature, and heating/cooling rates. Therefore, the preparation of high-quality colloidal NPs is far from trivial, since small variations may tip the system out of control, limiting the reproducibility of many synthetic protocols. Nevertheless, this complexity is also an attractive feature, since it allows for judicious and systematic manipulation.

The colloidal synthesis of NPs has been extensively investigated over the last three decades and has developed into a rather mature field. Nonetheless, the underlying mechanisms leading to nucleation and growth are still not fully understood and, consequently, a general theoretical model that accurately describes the formation of colloidal NPs has yet to emerge. Therefore, the design of synthesis protocols is still a largely empirical endeavour, which is guided by a number of fundamental principles that evolved from a few classical models for nucleation and growth [42–46] and a large body of rationalized empirical knowledge. These principles will be outlined and discussed below.

Elementary steps. The formation of colloidal NPs consists of a long chain of chemical steps, in which earlier events determine the fate of later events. However, the overall process can be divided into a small number of elementary kinetic steps [1–3, 18, 47]. Basically, four consecutive stages can be recognized (Fig. 6.8):

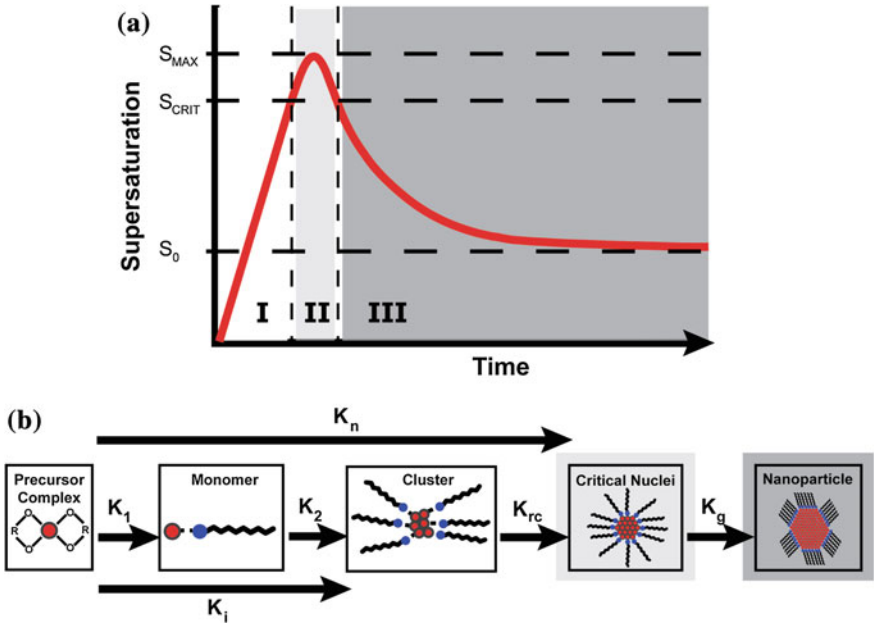

Fig. 6.8 **a** Temporal evolution of the supersaturation degree S during the three stages in NC synthesis (*I* induction; *II* nucleation; *III* growth). S_0 is equal to the solubility limit of the solute material. **b** Graphic illustration of the different steps in NC synthesis and corresponding reaction rates. K_1 is the rate of formation of monomers from precursors. K_2 is the formation rate of subcritical nuclei. The length of the induction period is inversely proportional to K_i. K_{rc} is the nucleation rate (formation of critical nuclei). K_n is the effective nucleation rate. K_g is the average growth rate of NCs from critical nuclei

I. **Induction or pre-nucleation period**. This period starts with the addition of the precursors and ends when stable crystal nuclei are formed. This stage encompasses a complex chain of coupled chemical reactions, the first of which being the formation of monomers from precursors at rate $\boldsymbol{k_1}$ (see Sect. 6.3.3.1 for details). The term "**monomer**" is used here to indicate the basic building units of the crystal (e.g., Au^0 for Au crystals or one [CdSe] unit for CdSe crystals, probably stabilized by a number of ligand molecules). As the monomer concentration increases, small and unstable clusters (i.e., **sub-critical nuclei** or **crystal embryos**) start to form by assembly of monomer units (or coalescence of smaller clusters) at rate $\boldsymbol{k_2}$. The rate limiting step will determine the overall rate $\boldsymbol{k_i}$.

II. **Nucleation stage** (Sect. 6.3.3.2). **Nucleation** is defined here as a single step process through which the **sub-critical crystal nuclei** formed during the induction period are converted into nuclei that are sufficiently large to become viable, i.e., capable of growing to mature crystals. The size at which the probabilities of growth and dissolution of the crystal nucleus become equal is referred to as **critical radius ($\boldsymbol{r_C}$)**. The nucleation stage is thus the time period

in which crystal nuclei with radius r equal to or larger than r_C are formed with a rate $\boldsymbol{k_{rc}}$, either by the addition of one more monomer unit to the largest possible subcritical nucleus forming a critical nucleus, or by the coalescence of two (or more) subcritical nuclei into a nucleus with $\boldsymbol{r \geq r_C}$ (i.e., **critical or super-critical nuclei**). The nucleation rate $\boldsymbol{k_{rc}}$ may be larger or smaller than the overall induction rate $\boldsymbol{k_i}$. The effective nucleation rate $\boldsymbol{k_n}$ will then be equal to the slower rate ($\boldsymbol{k_{rc}}$ or $\boldsymbol{k_i}$). Critical (and super-critical) nuclei are only formed at **monomer supersaturations** higher than a critical value ($\boldsymbol{S_{crit}}$) (Fig. 6.8). A supersaturated solution is a thermodynamically unstable system in which the solute concentration becomes higher than its solubility limit. The degree of supersaturation $\boldsymbol{S}$ is thus the ratio between the actual (transient) solute activities in the reaction medium and the solute solubility under the reaction conditions (temperature, solvent composition, etc.). Because monomers are still produced during the nucleation stage (with rate $\boldsymbol{k_1}$, see above) the supersaturation levels will keep increasing until the monomer consumption rates exceed the monomer production rates and S starts to decline, eventually reaching a level that is too low to sustain nucleation. As a result, the nucleation stage will have a temporal width that is determined by the balance between the monomer production and consumption rates.

III. **Growth Stage** (Sect. 6.3.3.3). Growth of the critical (and supercritical) crystal nuclei proceeds, at an average rate $\boldsymbol{k_g}$, by sequential addition of monomer units to the growing NP, by coalescence of smaller NPs, or by a combination of both processes. If allowed, growth proceeds until the monomer concentration reaches the solubility equilibrium level. However, this will usually result in larger size and shape distributions due to Ostwald ripening (i.e., growth of larger NPs at the expenses of smaller NPs). Therefore, growth is typically terminated before reaching equilibrium, by quickly cooling the reaction mixture.

Separation between nucleation and growth. In order to achieve a **narrow size distribution** it is necessary to **temporally separate** the **nucleation and growth** stages [1–3, 11, 12, 45, 47]. This can be achieved by the so-called **hot-injection** technique, which involves the rapid injection of a cold solution of precursors into a hot coordinating solvent, or by steady heating of the reaction mixture (**heating-up** method). It should also be realized that the monomers available for growth are those not consumed during the nucleation stage. Therefore, nucleation and growth rates should be **kinetically balanced** in order to yield good control over the size and shape of the NPs. The final size is related to the rate constants $\boldsymbol{k_n}$ and $\boldsymbol{k_g}$, as well as the initial precursor concentration $\boldsymbol{[P]_0}$, so that when $\boldsymbol{k_g[P]_0/k_n}$ is large relatively few nuclei grow quickly into larger NPs, whereas when $\boldsymbol{k_g[P]_0/k_n}$ is small a larger concentration of smaller NPs is obtained. If the kinetic imbalance is too large the synthesis fails, leading to either uncontrolled growth of large crystals or no NPs at all. As will be discussed below (Sect. 6.3.3.3), the monomer concentration during the growth stage strongly affects the growth rates, thereby determining the final size and shape of the NPs.

These elementary kinetic stages can also be identified in the colloidal synthesis of heteronanocrystals (HNCs), but the nature of the nucleation stage is fundamentally different, since in this case the second component is grown over pre-existing NPs of a different material. Therefore, homogeneous nucleation (i.e., the formation of critical nuclei of the second component directly in the growth solution) is undesirable, but instead nucleation directly over the seed NP (i.e., heterogeneous nucleation) is preferred. These two types of nucleation will be discussed in more detail (6.3.3.2). In some cases (e.g., to synthesize concentric core/shell HNCs), it is necessary to prevent both homogeneous and heterogeneous nucleation, in order to allow the reaction to start directly in the growth stage, which will take place via heteroepitaxy. The growth mechanisms will be discussed in more detail in Sect. 6.3.3.3.

6.3.3.1 Induction Period: The Monomer Formation

As mentioned above, the induction period involves two distinct kinetic steps: (a) formation of monomers from precursors, and (b) monomer assembly into subcritical crystal nuclei of increasing size. The latter step is better discussed in the context of the nucleation process, so we will focus here on the first step. The mechanism of monomer formation and the nature of the monomer itself are often not well understood, since comprehensive mechanistic studies have been undertaken only for very few cases. It should be noted that, depending on the chemical nature of the precursor and the reaction media, the monomer formation may involve either association (e.g., metal salts in aqueous media) or decomposition reactions (e.g., complexes in apolar coordinating solvents), or a combination of both (e.g., formation of [CdSe] units from Cd oleate and TOPSe). In some cases redox reactions are required to convert precursors into monomers (e.g., formation of Au^0 units from Gold salts).

As an illustrative example, we will briefly discuss the mechanism of formation of colloidal ME nanocrystals (M = Cd or Zn; E = S, Se, Te) from ML_2 and R_3P-E in 1-octadecene (R = butyl or octyl, L = oleic acid, OA, or octadecylphosphonic acid, ODPA), which has been investigated in detail [48]. The cleavage of the P = E bond is activated by the Lewis acidic character of the metal centre. This activation facilitates the nucleophilic attack by the L^- group. Evidence is presented for a bimolecular decomposition mechanism, i.e., a second L^- group must bind to the P atom for the cleavage to take place. The reaction rates increase with increasing temperature. Further, the cleavage rates increase from S to Te (S < Se < Te), as a result of the weakening of the P = E bond (the binding energy decreases from 403 to 218 kJ/mol from TBP-S to TBP-Te [49]). Oleate complexes are observed to be more reactive than phosphonate complexes. This is in agreement with the general principles discussed above (Sect. 6.2.2), since phosphonate coordinates via three oxygen atoms (tridentate), while oleate possesses only two oxygen donor atoms (bidentate). Moreover, Zn-complexes are observed to be less reactive than Cd-complexes, consistent with the stronger and harder Lewis acid character of Zn^{2+}.

The concentration of surfactants (i.e., free OA, ODPA or R_3P) in the reaction mixture affects the P = E cleavage rate. This has a large impact on both the nucleation and growth rates, showing that the rate limiting step in the formation of colloidal ME NCs from ML_2 and R_3P-E is the monomer formation. This also implies that the monomer consists of at least one [ME] unit stabilized by a number of surfactant molecules ($[ME]L_x$). The general validity of the conclusions from this mechanistic study is supported by the observation that the induction periods observed for the colloidal syntheses of semiconductor NCs vary dramatically depending on the reactivity of the precursors (e.g., ≤40 ms, ~1 s, and ~10 s, for CdSe NPs from TOP-Se and $Cd(CH_3)_2$, $Cd(OA)_2$, or $Cd(TDPA)_2$, respectively). It should also be noted that these investigations highlight the role of surfactants as reagents capable of modulating the precursor reactivity, in agreement with several other experimental studies. Considering that the intrinsic reactivity of the precursors available for the synthesis of colloidal NPs varies dramatically depending on their chemical nature (e.g., organometallic compounds, metal carboxylate salts, single-source precursors, etc.) and structural characteristics such as carbon chain length (precursors with shorter chains are typically more reactive than their longer chain counterparts) [1], it becomes clear that the combination "surfactant system-precursor" is one of the key parameters to be considered when designing synthesis protocols for colloidal NCs.

6.3.3.2 Nucleation Stage

Nucleation is stochastic in nature, and can be homogeneous or heterogeneous [1–3, 11, 12] (Fig. 6.9). Heterogeneous nucleation occurs at surfaces of foreign nuclei, bubbles or pre-existing NCs. Homogeneous nucleation requires spontaneous density fluctuations of the medium that lead several atoms to assemble into a crystal nucleus.

Homogeneous Nucleation

Various models have been used in the past to describe the NP formation process: classical nucleation theory (CNT), single particle growth laws, and rate equation

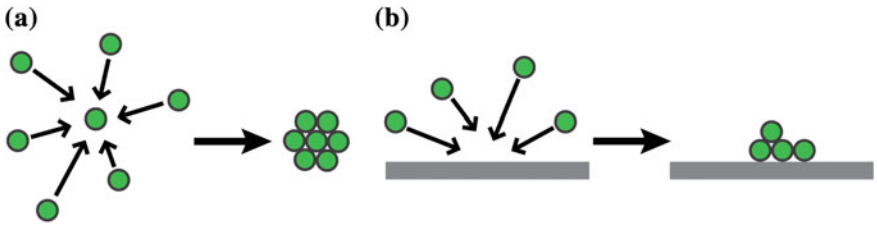

Fig. 6.9 Schematic illustration of **a** homogeneous nucleation **b** heterogeneous nucleation

based models. Each of these models has advantages, drawbacks and limitations [1, 50]. Nevertheless, the basic physics of nucleation is best illustrated with the help of the simplest, and possibly the most inaccurate, of these models: CNT. CNT is described in a number of books and reviews [51], so we will not address it here in detail, but merely use it to qualitatively discuss the underlying principles involved in the nucleation of colloidal NPs, and to rationalize the large body of empirical knowledge available. However, one should keep in mind that CNT has several shortcomings, even for the seemingly simple case of nucleation of liquid droplets from gas, and therefore cannot provide a quantitative description. These shortcomings will be briefly addressed at the end of this subsection.

As mentioned (6.3.3.2), the first requisite for nucleation is supersaturation. The supersaturated state can be reached by a sudden increase in the monomer concentration (e.g., by injection of precursors or by raising the temperature), or by a sudden decrease in the solubility of the solute (e.g., by a drop in temperature). The driving force for nucleation is the difference in free energy between the crystal components (monomers) in the crystal and in solution. The total change in free energy, $\Delta \boldsymbol{G_{TOT}}$, for the formation of a spherical crystal nucleus of radius r with n monomers M (viz., an atom, molecule, or ionic pair) from a solution of M is given by

$$\Delta G_{TOT} = \Delta G_V + \Delta G_S = \frac{4}{3}\pi r^3 \rho \Delta\mu + 4\pi r^2 \gamma \tag{6.1}$$

where $\Delta \boldsymbol{G_V}$ is the volume excess free energy and $\Delta \boldsymbol{G_S}$ is the surface excess free energy. $\Delta \boldsymbol{G_V}$ is negative due to the energy freed by the chemical bonds formed in the crystal nucleus, which largely compensates the energy spent to break the bonds between the monomers and the solvent (or surfactant) molecules. $\Delta \boldsymbol{G_S}$ is positive due to the fact that monomers at the surface have unsaturated bonds. The term $\boldsymbol{\rho}$ gives the density of the crystalline phase and $\boldsymbol{\Delta\mu}$ represents the chemical potential difference between the nucleus and the monomers in solution, which can be approximated to $-kT \ln S$. As described (6.3.3.2, Fig. 6.8), the parameter $\boldsymbol{S}$ is a measure for the degree of oversaturation, and can be expressed as $\boldsymbol{S = a/a_0}$, where $\boldsymbol{a}$ is the monomer activity in the growth solution at temperature T and $\boldsymbol{a_0}$ is the monomer activity in equilibrium with a macroscopic crystal at temperature T (i.e., the solubility constant). For a multicomponent compound, such as a binary semiconductor ME (e.g., CdSe), $\boldsymbol{a}$ will be determined by the product of the activities of each component in the growth solution ($\boldsymbol{a = a_M a_E}$), while $\boldsymbol{a_0}$ is equivalent to the solubility product constant K_{sp} at T.

The term $\boldsymbol{\gamma}$ is the interfacial tension between the nascent crystal and the supersaturated solution. Because $\Delta \boldsymbol{G_V}$ and $\Delta \boldsymbol{G_S}$ have opposite signs and different size dependences, $\Delta \boldsymbol{G_{TOT}}$ will reach a maximum for nuclei with critical radius $\boldsymbol{r_C}$ and then decrease with increasing radius (Fig. 6.10). This imposes an energy barrier for nucleation, $\Delta \boldsymbol{G_C}$, as it implies that crystal embryos with $r < r_C$ redissolve to monomers, while those with $r > r_C$ grow out to mature NCs, or even macroscopic crystals if no constraints are imposed on the growth process. The coordinates of the

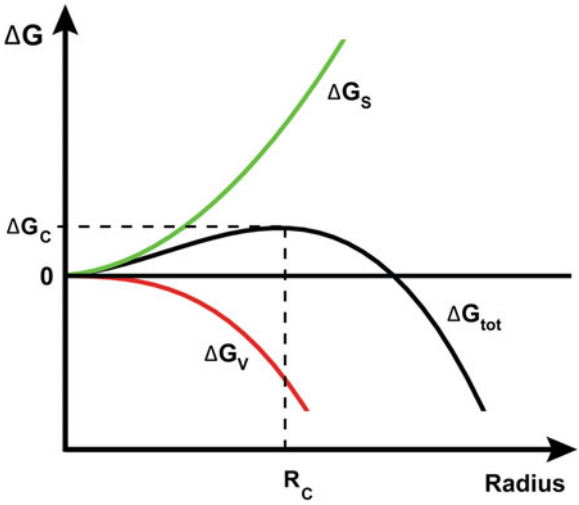

Fig. 6.10 Change in free energy during the formation of a spherical crystal nucleus. ΔG_V gives the volume excess free energy, ΔG_S the surface excess free energy, and ΔG_{TOT} is the free energy change. ΔG_c indicates the activation energy for nucleation

saddle point of the nucleation barrier correspond to the variables of state of a critical nucleus, which is in unstable equilibrium with the surrounding monomer solution. The crystal embryos overcome the nucleation barrier by means of fluctuations, but this does not necessarily happen exactly over the saddle point. The critical radius is given by:

$$r_c = -\frac{2\gamma}{\rho kT \ln S} \tag{6.2}$$

Equation (6.2) shows that higher T and/or higher supersaturations lead to smaller $\boldsymbol{r_C}$, in agreement with experimental results [1, 52]. Also, the concentration of critical nuclei formed during the nucleation stage is directly proportional to the monomer concentration [12]. Supersaturations larger than a critical value $\boldsymbol{S_{CRIT}}$ are needed because nucleation is a rare event process. Consequently, a solution that is just slightly supersaturated will not yield crystals because the probability of formation of critical nuclei is vanishingly small given a reasonable amount of time and volume of solution.

By analogy to Arrhenius expressions used to describe thermally activated processes, the steady state nucleation rate $\boldsymbol{J}$ (number of critical nuclei per unit time in a unit volume of solution) can be expressed as

$$J = J_0 \exp\left(-\frac{\Delta G_C}{kT}\right) \cong J_0 \exp\left[-\frac{16\pi\gamma^3}{3(kT)^3(\ln S)^2}\right] \tag{6.3}$$

The pre-exponential factor $\boldsymbol{J_0}$ depends on the number of monomer units per critical nucleus $\boldsymbol{c}$ and the degree of supersaturation ($\boldsymbol{J_0 = S^c}$) [8]. Equation (6.3) is only qualitatively valid, but provides useful guidelines for the manipulation of the

nucleation rates, since it shows that J is strongly dependent on the interfacial tension γ, the reaction temperature T, and the degree of supersaturation S.

Separation between nucleation and growth. Equation (6.3) clearly explains the success of the hot-injection technique, since supersaturation at high temperature results in small $\boldsymbol{r_C}$ and high nucleation rates, leading to a burst of nucleation, which lowers $\boldsymbol{S}$ and is accompanied by fast cooling, since the injected solution of precursors is at room temperature. The combination of lower $\boldsymbol{S}$ and lower T decreases the nucleation rates $\boldsymbol{J}$ to negligible values, effectively separating the nucleation and growth stages. It is interesting to note that separation between nucleation and growth also occurs in the "heating-up" method [1, 8]. In this case, the burst of nucleation is caused by the sudden increase in the monomer concentration due to the fast thermal decomposition of the precursors, which were quickly brought above their decomposition temperature. The consumption of monomers by the nucleation process decreases $\boldsymbol{S}$ to levels that are too low to sustain nucleation (Fig. 6.8).

The separation between nucleation and growth is further facilitated by using less reactive precursors and suitable surfactants. As discussed above (Sect. 6.3.3.1), the monomer formation from the precursors is likely the rate limiting step in the induction period and nucleation stages, and is also thermally activated. Therefore, a drop in T will also slow down the monomer formation, increasing the impact of the drop in S. This is probably the reason why less reactive precursors (e.g., Cadmium oleate, $Cd(OA)_2$) require a relatively smaller T drop than more reactive precursors (e.g., $Cd(CH_3)_2$). A similar reasoning applies to the adjuvant role of surfactants in separating nucleation and growth, since the binding between surfactants and metal atoms is also stronger at lower T's.

Impact of surfactants on homogeneous nucleation. Surfactants may lower or increase the nucleation rates, depending on the nature of both the precursor and the surfactant. As mentioned above, the surfactant molecule may modify the precursor reactivity. If the precursor reactivity is enhanced by the surfactants (e.g., primary alkylamines on Cd(II) carboxylate complexes [33]) the nucleation rate increases due to higher rates of monomer formation [1, 53]. Conversely, if the surfactant depresses the precursor reactivity (e.g., amines on In(III) myristate complexes [54]) the nucleation rate decreases. Additionally, the surfactant molecules affect the nucleation rates by coordinating to the monomer species, which increases the stability of the monomers in solution with respect to the nucleus. This translates into a lower $\Delta\boldsymbol{\mu}$ and a larger $\boldsymbol{r_C}$, therefore increasing $\Delta\boldsymbol{G_C}$ and lowering the nucleation rate. Consequently, a higher surfactant concentration will lower the concentration of nuclei and increase their size [1, 52, 53]. The stronger the interaction surfactant-monomer, the more pronounced the effect.

CNT shortcomings. It should be noted that the validity of the qualitative conclusions drawn above is not affected by the shortcomings of CNT. The greatest flaw of CNT is that it treats nuclei as bulk material having macroscopic properties [51]. The key assumptions are: nuclei are spherical particles with sharp boundaries and uniform and size-independent bulk-like physical-chemical properties. The interfacial tension $\boldsymbol{\gamma}$ is also assumed to be size independent. Further, interactions

with surfactants and solvents are neglected. These assumptions become unreasonable when considering a nucleus of only several atoms. Most likely, both ΔG_V and γ are size dependent [1, 12, 51], varying considerably with the size and inherent structure of the growing nuclei, as well as with the particular arrangement of the surface atoms and the surfactant molecules. However, the exact structure and composition of critical nuclei remains largely unknown, due to the small sizes and inherently transient nature of the nuclei present at the early stages of NP formation. It remains a critical challenge to identify and monitor subcritical nuclei, as this requires techniques capable of tracking in situ the growth dynamics of very small clusters with fast temporal-resolution. An additional complication is that the nature of the monomer species that participate in the nucleation and growth is still poorly understood, since studies aiming at unravelling the chemical mechanism of colloidal NC formation are scarce. As a result, a quantitative and general picture of what happens during the nucleation of NPs in solution has yet to emerge, although remarkable advances in this direction have been made in the last few years.

Heterogeneous Nucleation

Nucleation is facilitated by surfaces. The nucleating agent provides a low-energy interface with the crystal phase, thereby lowering the activation energy for nucleation ΔG_C [1–3] (Fig. 6.11). Heterogeneous nucleation thus happens at lower supersaturations and/or lower T's than homogeneous nucleation, making it possible

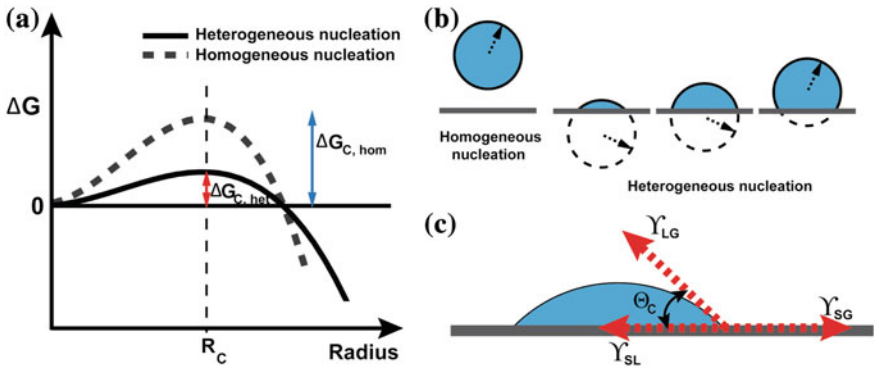

Fig. 6.11 **a** Change in free energy during the formation of a spherical crystal nucleus for heterogeneous and homogeneous nucleation. ΔG_c indicates the activation energy for nucleation. R_C indicates the critical radius, which is the same for homogeneous and heterogeneous nucleation under identical conditions (i.e., temperature, degree of supersaturation and interfacial tension, see Eq. 6.2). **b** The volume of material required to form a critical nucleus of radius r_C is much larger for homogenous nucleation, and decreases further for heterogeneous nucleation as the wetting angle θ_C decreases. **c** Illustration of the wetting angle θ_C between the nucleating material and the substrate, and the three different interfacial energies involved in the heterogeneous nucleation process γ_{LG}, γ_{SL}, γ_{SG}, which represent the solution-nucleus, the nucleus-substrate, and the substrate-solution interfacial tensions, respectively (see Eq. 6.5)

to use reaction conditions that effectively suppress homogeneous nucleation. ΔG_C for heterogeneous nucleation is given by [1, 2]:

$$\Delta G_C(\text{het}) = \Delta G_C(\text{hom}) \times f(\theta) \tag{6.4}$$

where $f(\theta)$ is a parameter that depends on the contact angle θ between the nucleating crystal and the adjuvant surface ($f(\theta) = 0.25[(2 + \cos\theta)(1 - \cos\theta)^2]$). The contact angle is related to the ability of the growing material to wet the substrate, which increases with decreasing interfacial tension. Higher wettabilities result in lower contact angles (e.g., complete wettability leads to $\theta = 0$ and minimum $f(\theta)$), leading to more pronounced reduction in the nucleation barrier, and faster nucleation rates.

The essential difference between homogeneous and heterogeneous nucleation is that only one type of interface occurs in the former (i.e., the solution-nucleus interface with interfacial energy γ_{LG}), while the latter involves three different types of interface, each with its own interfacial energy: (a) solution-nucleus (γ_{LG}); (b) nucleus-substrate (γ_{SL}); and (c) substrate-solution (γ_{SG}). The interplay between the three interfacial energies determines the wetting angle θ, since the shape adopted by the nucleus will be the one that minimizes the total interfacial energy:

$$\gamma_{SL} + \gamma_{LG}\cos\theta = \gamma_{SG} \tag{6.5}$$

The interfacial tension in solid-solid interfaces is primarily related to the lattice mismatch between the two materials. Therefore, heterogeneous nucleation will be more effective if the lattice mismatch between the nascent nanocrystal and the substrate is small. Considering that different crystallographic facets differ in terms of free energies and interatomic distances, it is clear that the activation energy for heterogeneous nucleation will be strongly dependent on the nature of the adjuvant facet. Moreover, the crystallographic orientation of the nucleating crystal will be imposed by the substrate in order to minimize the interfacial tension. It should also be noted that heterogeneous nucleation is facilitated on high energy sites, such as defects and corners.

Impact of surfactants on heterogeneous nucleation. As discussed in the previous section, surfactants have an essential role in homogeneous nucleation, performing a number of functions. Their impact on heterogeneous nucleation is even more dramatic, since they will not only regulate the monomer chemical potential in solution, but also the free energy and accessibility of the adjuvant surfaces. The surfactant molecules modify the free energies of the different facets of the seed NC, thereby enhancing or depressing the heterogeneous nucleation rates on specific facets. Moreover, surfactant molecules sterically hinder incoming monomers, and may therefore limit or even block the access to certain facets or surface sites, if their binding strength is strongly facet or site dependent. This makes it possible to use surfactants to control the accessibility of adjuvant surfaces, thereby accelerating, slowing down, or preventing heterogeneous nucleation on selected facets of a NC seed.

6.3.3.3 Growth Stage

NP growth is a deterministic process, whose outcome is dictated by the initial conditions at the onset of the growth stage: temperature, composition of the reaction medium (surfactant system and solvents), concentration, size, shape and structure of the NP seeds, remaining concentration of monomers and precursors. It is thus clear that the fate of the NPs is largely determined by the nucleation stage. However, one should realize that these initial conditions are not sharply defined, as a result of a spread in nucleation time and fluctuations or inhomogeneities in the reaction conditions during the induction period and nucleation stage. Most importantly, the reaction flask in which the synthesis of colloidal NPs is taking place is not a thermodynamically isolated system, since its temperature must be tightly controlled. In fact, it nearly always is an open system, either due to addition of fresh precursors or simply because the reaction is carried out under an inert gas flow. This makes it a very dynamic system, and offers plenty of opportunities for judicious manipulation.

The growth rate of a NP increases with the monomer concentration and the temperature, and is strongly size dependent. It is also strongly affected by the presence of surfactants, which slow down the growth. The specific impact of a surfactant system, however, depends on its nature and concentration. To understand the effect of the various reaction parameters on the growth rates it is necessary to consider the growth mechanism.

A colloidal NP can grow either by monomer addition to an existing seed or by coalescence of smaller NPs into larger ones [45, 46] (Fig. 6.12). The possibility of growth through NP coalescence is often overlooked, based on the assumption that the surfactant molecules provide an effective steric barrier to NP aggregation. However, there is substantial evidence that particle coalescence or even oriented attachment can also play an important role in the growth and shape control of colloidal NPs [46, 47, 55]. This will be discussed in section “Oriented Attachment and Shape Control” . In the case of growth by monomer addition the crystallographic orientation of the growing monolayer is dictated by the substrate facet, resulting in homo- or heteroepitaxial growth, depending on whether or not the compositions of the growing material and the NC seed are the same. The essential aspects involved in the growth of NPs by monomer addition will be addressed in section “Growth by Monomer Addition”. The dramatic impact of the growth kinetics over the shape of a colloidal NP will be discussed in detail in sections

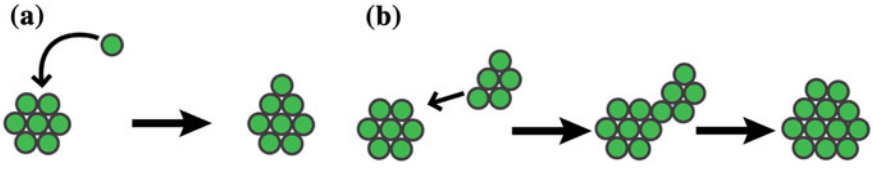

Fig. 6.12 Growth mechanisms of NPs: **a** growth by monomer addition, **b** growth by coalescence of smaller NPs

"Homoepitaxial Growth and Shape Control" and "Heteroepitaxial Growth and Shape Control " for the specific cases of homoepitaxial and heteroepitaxial growth, respectively.

Oriented Attachment and Shape Control

Oriented attachment of smaller NCs into larger nanostructures has been proposed to explain the formation of anisotropic and complex shaped colloidal NCs of a number of different materials (viz., TiO_2, PbSe, CdSe, CdTe, Au, MnO, etc.) [1, 56]. For example, the formation of asymmetric PbSe nanocrystals, such as nanowires, nanorings, and nanorods, has been attributed to growth through oriented attachment, since PbSe has the centrosymmetric rock-salt structure [57]. There are also reports on the formation of narrow nanowires ($\sim$1.5–3 nm diameter and up 200 nm long) by oriented attachment of NCs during growth at mild temperatures ($\sim$100–150 °C) and long times (4–70 h) (e.g., ZnSe:Mn nanowires by heating-up single-source precursors in HDA [1, 58], CdSe nanowires by reacting Cd acetate and selenourea in amines [1, 58]). The spontaneous formation of single-crystalline CdSe and CdTe nanowires by oriented attachment has also been observed during post-preparative treatments at room temperature [1, 59]. Surfactants have been observed to play a decisive role in the growth of NCs by oriented attachment, possibly by destabilizing or selectively exposing certain facets [56].

Three different stages have been identified in the growth of CdSe and CdTe nanowires through oriented attachment [1, 59] (Fig. 6.13). Initially, small NCs are generated or added to the growth medium. This is followed by oriented attachment of the parent NCs in pearl necklace aggregates, which subsequently reorient and fuse, yielding single crystalline nanowires. The diameter of the wires is determined by the diameter of the parent NCs. The fusion process is accompanied by recrystallization from zincblende to wurtzite structures. The overall process is probably driven by the reduction of the surface and interfacial energy, thereby minimizing the total free energy of the system. Most likely, these three stages are a general feature in the mechanism of formation of NPs through oriented attachment. Indeed, this general mechanism is corroborated by in situ studies of the unification of PbSe NCs through oriented attachment, which allowed the direct observation of a complex chain of processes: NC coalescence, followed by multiple rotations to achieve proper lattice orientation, interfacial relaxation to eliminate misfits, and finally fusion into larger single-crystalline NCs [60].

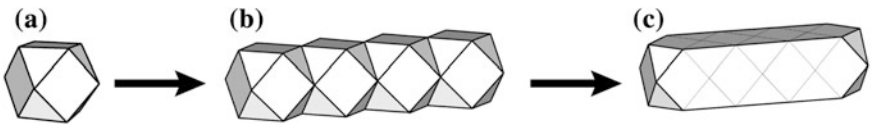

Fig. 6.13 Schematic illustration of the formation of nanorods by oriented attachment: parent NPs (**a**) self-organize into pearl necklace aggregates (**b**), which subsequently reorient and fuse, yielding single crystalline nanorods (or nanowires) (**c**)

It is generally accepted that the oriented attachment process is driven by a dipolar interaction between the parent NCs. The observation of the transient formation of short strings of NCs in solutions of both PbSe and CdSe colloidal NCs provides further support to this idea [61]. A size-dependent permanent dipole moment has been reported for wurtzite CdSe NCs and nanorods, and ascribed to the intrinsic polar character of the wurtzite lattice [61]. However, dipole moments have also been observed for NCs of materials with centrosymmetric crystal structures, such as PbSe (rock-salt) [61]. The origin of these dipole moments is at present still under debate, but it is generally attributed to an asymmetric distribution of the polar facets [56, 57, 60, 61] or to shape asymmetry [62].

Growth by Monomer Addition

Two sequential elementary steps can be distinguished in the growth process of a colloidal NP via monomer addition [1, 2, 14]: **(I) monomer diffusion** to the NP surface, and **(II) incorporation of the monomer** into the NP (Fig. 6.14). It should be noted that the competing process of NP dissolution (removal of monomers from

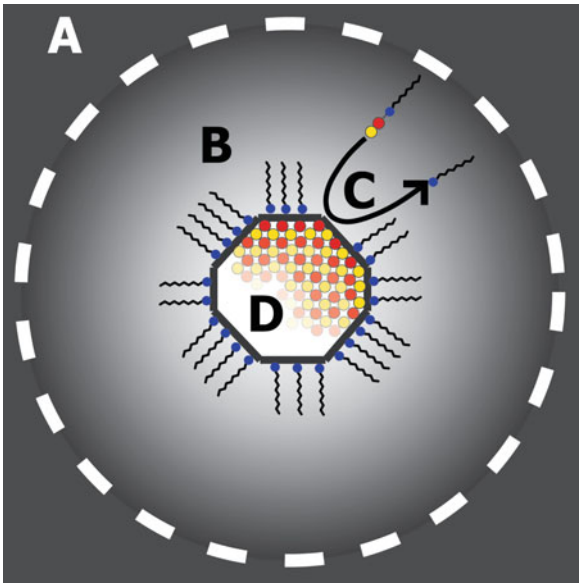

Fig. 6.14 Schematic representation of growth via monomer addition. The *dashed white circle* marks the onset of the diffusion sphere for the monomers. Region *A* is the bulk of the solution, where the monomer concentration is independent of the distance from the NP surface. *B* indicates the diffusion sphere, where a monomer concentration gradient occurs due to consumption of monomers at the NP surface. The *arrow C* indicates the diffusion of the monomer-surfactant complex to the NP surface, followed by monomer incorporation into the NP (*D*), and diffusion of the released surfactant molecule away from the NP

the NP followed by diffusion away from the NP surface) will also occur, but will become important only at low monomer concentrations.

The **growth rate** of a nanoparticle in solution is then given as [2, 7, 8, 44]:

$$\frac{dr}{dt} = \frac{DV_m(a_b - a_r)}{r - (D/K_S)} \tag{6.6}$$

D is the diffusion coefficient of the monomers, V_m the molar volume of the solid, a_b the monomer activity in the bulk of the solution (i.e., far from any NC), a_r the monomer activity on the surface of a NP of radius r (equivalent to the NP solubility), and K_S the reaction constant between the monomers and the NP surface. The monomer activity is used instead of its concentration to account for the fact that the growth solution strongly deviates from the ideal behavior (as defined by Henry's law).

The driving force for diffusion (step I) is the concentration gradient between the NP surface and the bulk of the solution. Therefore, the monomer diffusion rate is determined by the monomer activity and the diffusion coefficient in the reaction medium, which is a function of the temperature and the composition of the growth solution (solvents, surfactants, precursors). Diffusion rates can be increased by increasing temperature and/or monomer concentration, or decreasing the surfactant concentration in the growth medium.

If the rate limiting step is the monomer diffusion ($D \ll K_S r$) the growth is said to be in the **diffusion controlled regime** and Eq. (6.6) can be approximated to

$$\frac{dr}{dt} = \frac{DV_m(a_b - a_r)}{r} \tag{6.7}$$

The incorporation of the monomer into the NP (step II) involves a reaction between the monomer-surfactant complex and the NP surface, and implies the release of at least one surfactant molecule (Fig. 6.14). The rate of this process is determined by the reaction rates between the monomers and the NP surface sites. It is also possible that precursors decompose directly at the NP surface. If the rate limiting step is the incorporation of monomers into the NP ($D \gg K_S r$), the growth is under **reaction control** and Eq. (6.6) becomes

$$\frac{dr}{dt} = V_m K_S(a_b - a_r) \tag{6.8}$$

Equation (6.8) shows that dr/dt is size independent and that the size distribution Δr remains constant throughout the growth. Consequently, the relative size distribution decreases during the growth. The assumption that K_S is size independent is justified because the reaction rate depends primarily on the local site where the monomer and the surface of the nanoparticle make contact, i.e. the monomer binding site. Therefore the reaction rate averaged out over all possible binding sites will depend only on the surface area of the NP. Because the growth rate is also proportional to the surface area, the overall growth rate constant under reaction controlled conditions becomes size independent.

The **reaction-controlled regime dominates at high monomer activities**, when the diffusion rates become so fast that the diffusion process can be neglected. Therefore, it may be expected that the initial NC growth will be primarily reaction controlled. As the growth proceeds, the monomer activity in solution decreases, until the monomers in the immediate vicinity of the growing NP are depleted. Under these conditions **monomer diffusion** is expected to **become the rate limiting step**. Moreover, due to the low monomer activity in the growth solution the dissolution rates of the NP will increase and become comparable to the deposition rates. The effective growth rate will then be determined by the diffusion rates and the balance between the rates of deposition and dissolution.

The **dissolution rates**, however, are extremely sensitive to the size of the NP. According to the Gibbs-Thomson relation a spherical particle with radius r has extra chemical potential, which increases its solubility in a size dependent fashion:

$$a_r = a_0 \exp(2\gamma V_m / r k_B T) \tag{6.9}$$

where a_0 gives the monomer activity in equilibrium with the bulk material and k_B is Boltzmann constant. The coefficient $2\gamma V_m / k_B T$ is much larger for nanoparticles than for bulk surfaces due to the pronounced increase of the interfacial tension γ at the nanoscale.

The Gibbs-Thomson relation can be used to define a critical size r^* that is in equilibrium with the monomer activity in the bulk of the solution ($r = r^*$ when $a_r = a_b$). The growth rate can thus also be expressed in terms of the critical size r^* as follows

$$\frac{dr}{dt} = \frac{2\gamma D a_0 V_m^2}{k_B T r} \left(\frac{1}{r*} - \frac{1}{r} \right) \tag{6.10}$$

The critical size r^* is characterized by a zero growth rate, since a NP of this size is in equilibrium with the solution. NPs smaller than r^* have a negative growth rate (i.e., dissolve) while those larger than r^* grow. It should be noted that r^* is actually equivalent to the critical size for nucleation r_C and can be defined in the same way (Eq. 6.2).

Equation (6.10) implies that the **monomer activity during the growth stage** will **determine the size distribution of the NPs** [2, 3, 14]. At **high monomer activities** an initially broad size distribution can undergo **size distribution focusing** (Fig. 6.15). Due to the high activity (concentration), r^* is small (see Eq. 6.2), and all NPs grow. However, since the growth rates are proportional to the surface area of the NP, smaller NPs grow relatively faster than larger ones, causing the size distribution to narrow while the average size increases. As the monomer activity decreases the critical size r^* increases, eventually becoming larger than a fraction of the NPs previously formed. At **lower monomer activities** the dissolution rates accelerate, and smaller NPs will dissolve faster due to their higher surface/volume ratio. As a result, the size distribution broadens, since NPs larger than r^* grow at expense of the smaller ones (**defocusing regime or Ostwald ripening**) [2, 14].

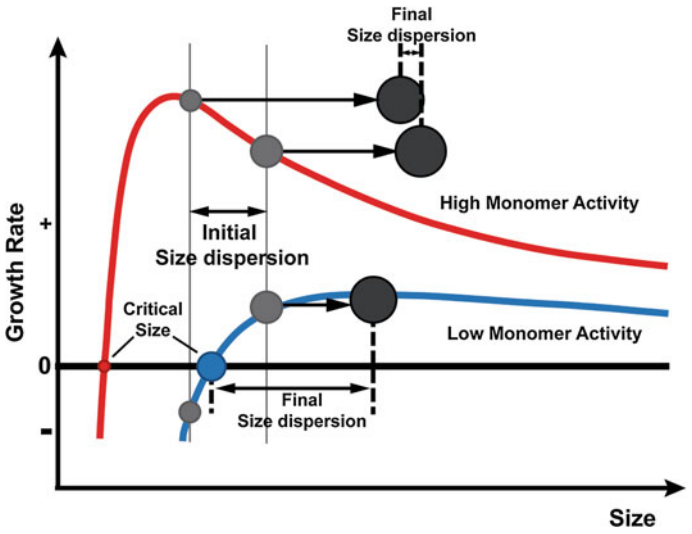

Fig. 6.15 Size dependence of the NP growth rates for reaction mixtures in two representative monomer activity limits: low (*lower curve*) and high (*upper curve*) [2, 14]. The high activity limit allows for size focusing to occur, while in the low activity limit size defocusing occurs, through which the size dispersion broadens

The driving force for this ripening process is the minimization of the surface free energy. It should be noted that ligands and surfactants that accelerate the dissolution of NPs will enhance this process and are therefore typically referred to as ripening agents. A well-known example of such a ligand is oleic acid, which is a very effective ripening agent for NCs of II–VI semiconductors (e.g., CdSe or PbSe).

Size defocusing can be prevented by two strategies: (a) growth is terminated while the monomer activity is still in the focussing regime; and (b) the monomer activity is maintained high. To maintain activities in the focussing regime some groups use repeated injections of fresh precursors [2]. However, this may lead to new nucleation events (secondary nucleation) if the monomer activity exceeds the homogeneous nucleation threshold. An alternative is to use a large excess of one of the precursors [1]. In this case, growth will be limited by depletion of one of the NP components, but the initial oversaturation and the final activity product of monomers will still be sufficiently high to prevent defocusing [1], since at high monomer activity products the NP dissolution is hampered. Under such conditions, inter-NP mass transport processes (i.e., Ostwald ripening) and growth rates are negligible, but the surface atoms still have enough mobility if the temperature is sufficiently high. This allows surface annealing to take place, leading to high photoluminescence quantum efficiencies [1, 62].

Kinetic and Thermodynamic growth control [1]. In the kinetic control model, growth occurs under conditions far from equilibrium, so that the size and shape of the NP are determined by the kinetic balance between several competing processes. In contrast, the thermodynamic control model is based on the concept of equilibrium

and assumes that the binding between the surfactant molecules and the NP surface is sufficiently strong to thermodynamically drive the system toward a particular average size under a given set of conditions. Both models are valid, depending on the growth conditions.

Crystal Structure of NPs. Due to the high surface to volume ratio of NPs the overall surface energy can dramatically modify the stability of crystalline phases, making it possible to obtain NPs with crystal structures that are metastable for the bulk material. The most common reaction parameter to control the crystalline phase of a NP is the growth temperature. Typically, growth at higher T's (thermodynamic control) yield the phase that is thermodynamically stable for bulk at ambient conditions, while NPs produced at sufficiently low T's crystallize in the metastable phase (e.g., CdSe NPs are wurtzite, WZ, and zinc-blende, ZB, at high and low T's, respectively) [9].

Surfactants and growth. Surfactants affect the NP growth by binding to monomer species in solution and to the NP surface, thereby decreasing both the reaction and the diffusion rates. Further, the surfactant layer also depresses the reaction rates by limiting access to the NP surface and by actively competing with the monomers for the reaction sites. As mentioned above (Sect. 6.2.2), the functionality of the surfactant molecules depends on both the polar head (coordinates to metal atoms) and the apolar tail (affects the diffusion properties). The interactions between the surfactant molecules will also have a profound impact on the growth rates, because they determine the surfactant dynamics in the reaction medium and at the NP surface.

Faster dynamics result in faster growth, since the residence times of the surfactant at the NP surface will be shorter (see Sect. 6.2.2), thus making the surface more accessible to monomers. The surfactant dynamics are determined both by the polar head group and the apolar chain length, so that weakly coordinating head groups and/or shorter chains result in faster dynamics, and consequently faster growth at relatively lower T's [33]. The dynamics also depend on the concentration of the surfactant and the temperature, so that higher T's or lower concentrations lead to faster dynamics. However, for surfactants capable of enhancing the precursor reactivity, concentrations below a certain threshold will depress the growth rates [33]. This emphasizes the important role of surfactants as reagents (Sect. 6.3.3.1), which may strongly affect the growth rates by determining the monomer availability, given that the precursor conversion into monomers may continue throughout the growth stage. High precursor stabilities may thus decrease the growth rates and enhance the differences between the growth rates of different crystallographic facets [1, 33, 40, 53]. Surfactants can also have a large impact on the crystal structure of a NC, by modifying the surface energies of the facets, thereby changing the relative stability of a given phase.

Homoepitaxial Growth and Shape Control

The ability to control the shape of colloidal NCs is highly developed, yielding a plethora of 0-dimensional (e.g., cubes, stars, pyramids), 1-dimensional (e.g.,

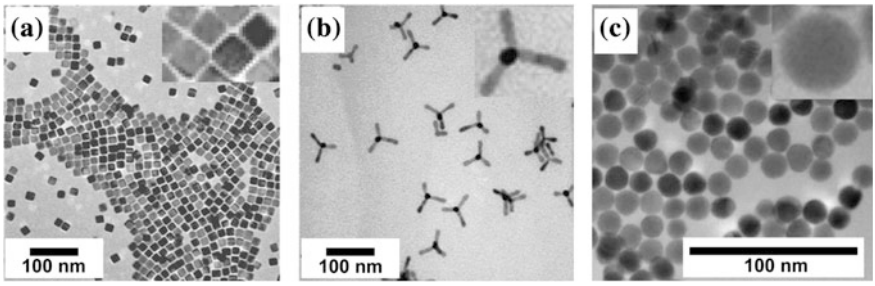

Fig. 6.16 Gallery of transmission electron microscopy images of colloidal NPs of various shapes and compositions. **a** PbSe cubes. Reprinted with permission from Ref. [11], Copyright (2010) American Chemical Society. **b** CdTe tetrapods. Reprinted with permission from Ref. [11], Copyright (2010) American Chemical Society. **c** CdTe spheres

straight or zig-zag wires), and 2-dimensional (e.g., platelets and disks) NCs, as well as more complex morphologies (e.g., multipods and nanorings) [1–3, 14, 16] (Fig. 6.16). Although colloidal NCs are very often referred to as spherical, they are never truly so, since a NC is always highly facetted, and therefore should better be described as nearly spherical. In fact, NCs frequently present shapes that, albeit isotropic, cannot be approximated to spherical (e.g., cubes, tetrahedra, octahedra, truncated cubes, etc.). Therefore, to understand the mechanisms underlying the shape control of colloidal NCs, it is more insightful to classify the morphology of a NC in just two categories: nearly-spherical or isotropic (i.e., low aspect ratio) and anisotropic (i.e., high aspect ratio).

Equilibrium shape. The equilibrium shape of a nanoparticle is the one that minimizes the overall surface free energy. For an amorphous NP the equilibrium shape will thus be a sphere, as indeed observed for colloidal silica NPs (see, e.g., Fig. 6.2a). However, for nanocrystals the equilibrium shape is constrained by the free energy of the different crystallographic facets, and will thus be dictated by the relative surface energies of the various facets, as stated by Wulff's theorem. This is illustrated in Fig. 6.17, which shows a number of Wulff shape constructions for a hypothetical crystal of cubic symmetry constrained to expose only two sets of facets with free energies γ_1 and γ_2 [2].

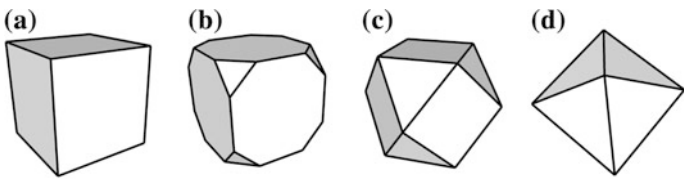

Fig. 6.17 Different Wulff shape constructions for a crystal of cubic symmetry showing only two sets of facets. R gives the ratio between the free energies of the facets [2]. **a** $R \geq 1.73$, **b** $R = 1.73$, **c** $R = 1.15$, **d** $R = 0.58$

The variety of equilibrium shapes for a real NC is much larger, since several different crystallographic facets may be available for a given material. Moreover, the free energy of the different facets may be substantially modified by surfactant molecules, further extending the number of possible equilibrium shapes. Therefore, under thermodynamic control, when the growth rates are sufficiently slow to allow equilibrium to be achieved, the shape of colloidal NCs and HNCs will be isotropic, although facetted, both because this minimizes surface area and because low-energy facets of the NC are relatively close to each other in energy [2, 14].

Kinetic shape control. It should be noted, however, that the shape of colloidal NCs or HNCs is frequently not the equilibrium one, because the growth is often quenched while the growth rates are still significant, resulting in metastable anisotropic morphologies that are kinetically controlled [1, 2, 14]. The growth rate of a crystal facet depends exponentially on the surface free energy [14], so that at high growth rates high-energy facets grow more quickly than low-energy facets, typically yielding high aspect ratio shapes. These shapes can still be rationalized in terms of Wulff constructions, by replacing free energies by growth rates, since fast growing facets tend to disappear [2]. It is worth noting that the NC shape is ultimately determined by the surface free energies, both under thermodynamic and kinetic control, since in the first case the NC surface consists primarily of low-energy facets, while in the latter the high-energy facets exhibit the fastest growth rates [1].

Shape dynamics. It is thus clear that the shape of a colloidal NC (or HNC) reflects a compromise between the growth rates and the relative stabilities of all possible crystallographic facets of a growing NP, which are competing with each other for the limited monomer supply in the growth solution. The shape of a colloidal NP is thus very dynamic, evolving continuously during the growth in response to changes in the reaction parameters. These changes result from the growth process itself and from the interplay between monomers, precursors, surfactants and surface atoms. To control the shape of a colloidal NP one must thus judiciously select a set of initial reaction conditions and then allow the growth to proceed until the intended shape is obtained. The parameter space from which the initial conditions can be selected is quite large: temperature, concentration and nature of precursors, concentration and nature of the surfactants, crystal structure of the growing material, and characteristics of the seeds (concentration, size and faceting). Despite the complexity inherent to such a wide parameter space, the shape control of NCs and HNCs can be rationalized in terms of a balance between just two fundamental quantities: the monomer flux towards the surface of the growing nanocrystal, and the capacity of the individual crystallographic facets to incorporate the available monomers. In other words, the shape of a growing colloidal NP is determined by the balance between "monomer diffusion" and "monomer consumption" rates, and is therefore related to the concepts of "diffusion-controlled" and "reaction-controlled" growth discussed in the previous section.

Monomer fluxes and shape. The monomer flux is defined by the monomer diffusion rate, which increases with the temperature and the monomer activity in the reaction medium (typically referred to in the literature as "effective monomer

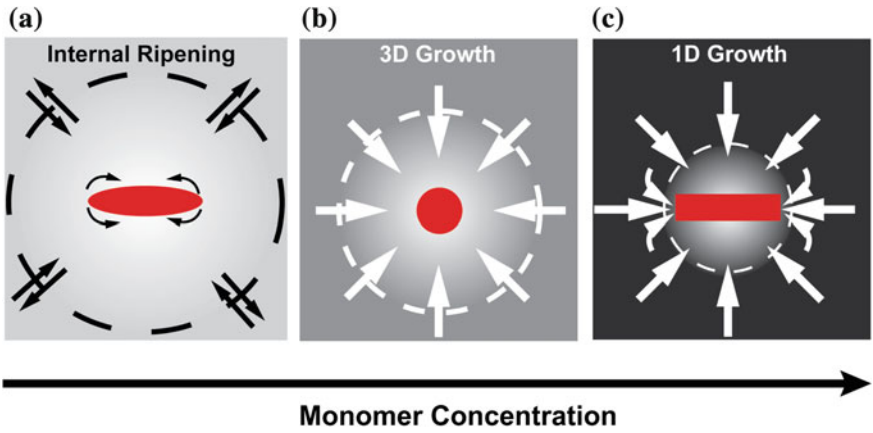

Fig. 6.18 Schematic illustration of the influence of the monomer fluxes on the shape of a colloidal NC [53]: **a** very low monomer flux, **b** low monomer flux, **c** high monomer flux

concentration"). The "effective monomer concentration" is determined not only by the concentration and stability of the precursors at the reaction temperature, but also by the surfactant-precursor and surfactant-monomer interactions. High monomer fluxes favour anisotropic growth (1D-growth, Fig. 6.18c), while low fluxes lead to isotropic growth (3D-growth, Fig. 6.18b). Monomer fluxes that are too low to sustain growth, but are still sufficiently high to prevent NC dissolution, lead to a process of internal ripening in which material is transported from high-energy facets to low-energy facets, causing the aspect ratio to slowly decrease towards a roughly isotropic shape (Fig. 6.18a) [1–3, 63]. Very low fluxes result in inter-NC ripening (Ostwald ripening), because the dissolution rates increase (see "Growth by Monomer Addition").

It should be noted that this makes the growth stage strongly dependent on the nucleation stage, as discussed above (Sect. 6.3.3). Slow nucleation leads to fewer nuclei and higher residual monomer activity, and therefore favours anisotropic growth. Conversely, fast nucleation leads to higher concentration of smaller nuclei and lower residual monomer activity, thereby favouring isotropic growth. Moreover, it should be realised that the high monomer fluxes required to achieve anisotropic growth will result instead in homogenous nucleation if the energy barrier for nucleation is too low. Therefore, strongly coordinating surfactants (e.g., phosphonic acid) are typically used to produce anisotropic shapes [1–3] due to their ability to decrease the nucleation rates, while allowing high monomer fluxes to be achieved.

It is interesting to note that the anisotropic growth observed under high monomer fluxes is caused by the fact that the monomer feeding rates largely exceed the monomer consumption rates (reaction-controlled limit). Therefore, the free energy differences between different crystallographic facets become more discriminatory, since high energy facets can incorporate monomers at faster rates. Very high monomer fluxes are also known to induce branching, leading to the formation of multipods or even hyperbranched NCs (dendritic shapes similar to those of snowflakes).

To understand this phenomenon one has to consider that the growing NC is facetted, but is embedded inside an isotropic diffusion sphere, so that different parts of the NC may be exposed to different concentration gradients [2]. These differences are negligible at low monomer activities, but increase dramatically with increasing activities, because the spatial extension of the diffusion layer is inversely proportional to the diffusion rates. At sufficiently high activities, this will lead to self-sustained branching from high-energy facets or sites (e.g., corners, edges or defects) of the NC and may lead to hyperbranching, since any defect (e.g., kinks, stacking faults) in the fast growing branches will serve as a heterogeneous nucleation site.

Surfactants and shape. As mentioned above, the surface free energies of the various crystallographic facets of a NP can be remarkably different and may be strongly modified by surfactants. This affects the equilibrium shape of the NC [1, 2, 31], and also kinetically controls the NC shape during growth. Further, some surfactants may bind more strongly to certain facets, thereby restricting their accessibility to monomers and increasing the activation energy for monomer addition to surface sites located on these facets [1–3, 16]. The different bonding strengths of the surfactants to different facets will enhance or depress their relative growth rates, which may lead to highly anisotropic shapes, particularly under high monomer fluxes and/or lower T's (Fig. 6.19). The decisive role of preferential adhesion in the shape control of colloidal NCs has been clearly established on a number of studies, leading to rods, tetrapods, platelets, bullets, and other complex shapes [1–3, 16]. The impact of the surfactant molecule on the NC shape depends on the head group and the apolar tail. For strongly binding head groups the ability to boost anisotropic growth and branching increases with decreasing chain length [1, 64, 65]. This is due to a combination of factors [1]. First, shorter alkyl chains result in lower precursor stability (e.g., reactivity of Cd-hexylphosphonate is *ca*. 3 orders of magnitude larger than that of Cd-tetradecylphosphonate) and faster diffusion rates, leading to faster growth. Further, shorter chain ligands may bind more tightly to certain facets of the NC, thereby decreasing their growth rates more effectively than their longer chain counterparts.

Crystal structure and shape. The crystalline phase of the NC seed also influences the final shape of the NP [2, 9], since this will expose different sets of crystallographic facets to the growth medium. This is particularly important for the growth of HNCs, and will thus be discussed in more detail in the following subsection. Non-centrosymmetric crystal structures, such as wurtzite (e.g., CdSe, CdTe), are inherently polar and tend to grow anisotropically, easily yielding rods

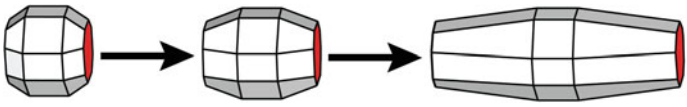

Fig. 6.19 Schematic illustration of the impact of the selective adhesion of ligands on the final shape of a colloidal nanocrystal. *Red (dark grey) facets* are coated by weakly bound ligands, while white facets are covered by strongly bound ligands. As a result of the difference in binding strength, anisotropic growth occurs

and multipods under kinetically controlled growth conditions. Conversely, centrosymmetric crystal structures, such as zincblende (e.g., ZnS, CdTe, CdS) and rock-salt (e.g., PbSe, MnS), tend to grow isotropically along the three crystalographic axes, resulting in nearly spherical facetted NCs, cubes or tetrahedra (commonly with truncated edges).

Heteroepitaxial Growth and Shape Control

Shape control has been extended to colloidal HNCs, producing a wide variety of sophisticated nanostructures, in which the composition, morphology, and connectivity of the individual segments of the HNC can be varied (viz., concentric core/multishell QDs, heterodimers, nanodumbbells, heteronanorods and multipods, Fig. 6.20) [1–5]. The principles discussed above for homoepitaxial growth also apply to heteroepitaxial growth, but shape control of HNCs is inherently more challenging, since the requirement for lattice matching at the heterointerface imposes larger constraints on the morphology of a HNC. The essential difference between homo- and heteroepitaxial growth is that the latter depends on both the surface and the heterointerfacial free energies. Therefore, the shape of a colloidal HNC is extremely sensitive to the characteristics of the seed (crystal structure, size, shape and faceting, surface defects, etc.) and the nature of the growing material. Nevertheless, the current understanding of the impact of the seeds on the shape of HNCs is still limited, although it is clear that misfit strain at the heterojunction is very relevant. Nevertheless, several other mechanisms, such as solid-state atomic diffusion and/or exchange, redox processes, phase separation, and oriented attachment may intervene in the heteroepitaxial growth process [1–3].

The composition and shape of the overgrowing segment are chosen based on the properties desired for the HNC and the role to be fulfilled by the new segment. From this perspective, the essential parameters to be considered are the nature (viz., metal, semiconductor, etc.), chemical composition, and properties (e.g., band positions, electron and hole effective masses, magnetic susceptibility, optical transitions, etc.) of the overgrowing material. The choice of composition is ample but not unrestricted, as the overgrowing material must be chemically and structurally compatible with the seed surface. Moreover, the composition of the HNC imposes limitations on the morphologies attainable. These constraints are particularly strict if the overgrowing material is intended to form a concentric shell around the seed NC, since this requires small lattice mismatches (see below). However, there are strategies to circumvent or minimize compatibility issues. Some of these strategies will be discussed below.

Interfacial strain due to lattice mismatch is an important issue in nanostructures grown by heteroepitaxy, as the wealth of data on QDs and quantum wells grown by vapour phase (VP) deposition methods clearly illustrates [66]. The growth mode and shape evolution is dictated by the interfacial strain, which is in turn determined by the interface free energies and the lattice mismatch. Depending on the latter, three different heteroepitaxial growth modes can be distinguished: (a) layer-by-layer

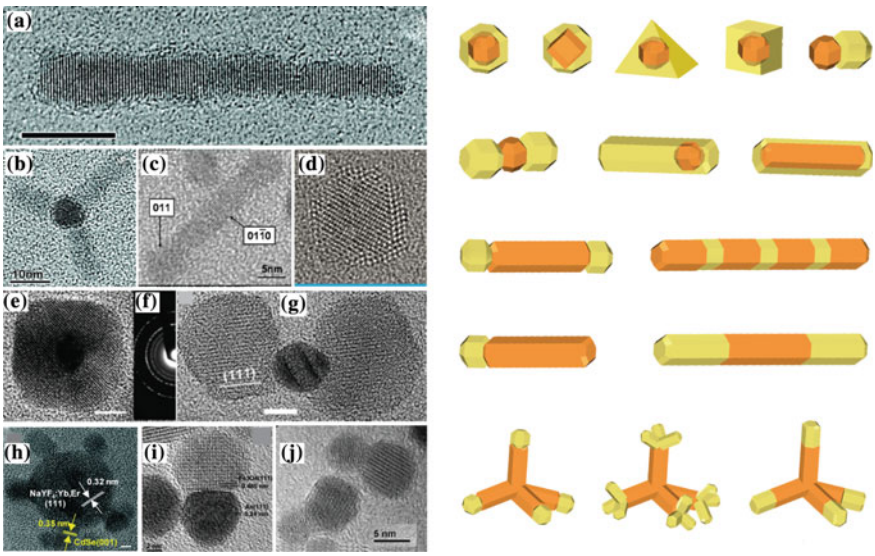

Fig. 6.20 *Left* Gallery of HRTEM images of colloidalheteronanocrystals (HNCs) of various compositions and architectures: **a** dot core/rod shell CdSe/CdS nanorod (*scale bar* 5 nm). Reprinted with permission from Ref. [68], Copyright (2007) American Chemical Society. **b** CdSe/CdS nanotetrapod. Reprinted with permission from Ref. [68], Copyright (2007) American Chemical Society. **c** CdTe-CdSe-CdTe dumbbells. The images show that the CdTe dots are neither wurtzite nor oriented along the c-axis of the CdSe rod. Reprinted with permission from Ref. [69], Copyright (2006) American Chemical Society. **d** PbSe/CdSe core/shell QDs. Courtesy of M.A. van Huis, Utrecht University, Netherlands. **e** Au-Fe_3O_4 core/shell HNCs (scale bar: 4 nm). Reprinted with permission from Ref. [70], Copyright (2006) American Chemical Society. **f** electron diffraction pattern of the HNC shown in **e**. Reprinted with permission from Ref. [70], Copyright (2006) American Chemical Society. **g** Fe_3O_4-Au-Fe_3O_4 HNC (scale bar: 4 nm). Reprinted with permission from Ref. [70], Copyright (2006) American Chemical Society. **h** CdSe NCs grown onto a $NaYF_4$:Yb,Er NC (*scale bar* 3 nm). Reprinted with permission from Ref. [71], Copyright (2010) American Chemical Society. **i** Au-Fe_3O_4 (*scale bar* 2 nm). Reprinted with permission from Ref. [72], Copyright (2005) American Chemical Society. **j** γ-Fe_2O_3-CdS. Reprinted with permission from Ref. [73], Copyright (2005) American Chemical Society. *Right* Schematic survey of colloidal HNC architectures (for clarity the surfactant layer is not represented). Courtesy of Dr. M. Casavola (Utrecht University, Netherlands). Reprinted by permission of the Royal Society of Chemistry from Ref. [1]

growth (Frank van der Merwe mode, FM, for lattice matched systems); (b) layer growth followed by self-organization in islands (Stranski-Krastanow mode, SK, for lattice mismatched systems with relatively small mismatches, i.e., ≤10 %); and (c) island growth (Volmer-Weber mode, VW, for lattice mismatched systems with larger mismatches, i.e., ≥10 %). In the case of the FM mode the strain is negligible and therefore the thickness of the heteroepitaxial layer is in principle unlimited. Conversely, in the VW mode the growing material will minimize the interfacial area, therefore growing as islands. In the SK mode a thin heteroepitaxial layer grows, but is strained due to the lattice mismatch. Strain builds up as the thickness

increases, and, as a result, self-reorganization of the layer into islands will occur to relieve strain if the thickness exceeds a critical value. This critical thickness is determined by the strain energy and is therefore smaller for larger mismatches, but is typically just a few monolayers (MLs). For example, the critical thickness for the growth of InAs over GaAs (7 % lattice mismatch) is only 2 MLs [67].

Strain relaxation in VP-grown layers can occur by energy minimization mechanisms that yield defect free islands, such as elastic relaxation on facet edges and renormalization of the surface (or interface) free energy, but it can also occur through the formation of misfit dislocations and other defects, especially as the islands grow larger [67]. Colloidal HNCs are much smaller than their VP-grown counterparts. Consequently, colloidal HNCs are able to accommodate larger degrees of interfacial strain, and therefore heteroepitaxial growth may occur for larger lattice mismatches [1]. For example, ZnS shells can be grown over CdSe cores despite the large lattice mismatch (viz., 12 %), although the shell thickness is limited to $\sim$3 MLs [5]. To minimize the strain field in the shell, the chemical bonds in the HNC core become also partially strained. It should be noted that strain relaxation is a dynamic process that occurs concomitantly with the growth, and therefore is under strong kinetic control. As a result, relaxation by formation of misfit dislocations and other defects is favoured under fast growth conditions, because they involve the reorganization of fewer atoms than interface and surface reconstruction processes and island formation. The resulting shape and structure of the overgrown material will then be the one that is more effective in terms of dynamically minimizing the overall strain energy. Therefore, under fast growth conditions the synthesis of concentric HNCs is prevented, and very often homogeneous nucleation followed by homoepitaxial growth prevails. It is also possible that under fast growth conditions and/or large mismatches the deposited material grows as an amorphous shell [2, 3].

The multifacetted nature of colloidal NCs makes the heteroepitaxial growth over colloidal NC seeds much more complex than under VP conditions, since different facets not only have different free energies and reactivities, but also offer different lattice mismatches. Further, as discussed above, surfactant molecules may bind more strongly to certain facets of the NC seed, thereby decreasing their growth rates and availability for heteroepitaxial growth, irrespective of their suitability in terms of lattice mismatch. The combination of these constraints may result in anisotropic growth or the formation of complex morphologies even under conditions that would yield isotropic growth under homoepitaxy. For instance, it has been experimentally demonstrated that anisotropic HNCs, such as heterorods, can accommodate much larger lattice mismatches (as large as 11 %) than concentric structures such as core/shell QDs [74]. Consequently, the length of colloidal heteronanorods or multipods is less limited than the shell thickness of core/shell HNCs and typically reach several tens of nm, or even hundreds, allowing the fabrication of narrow colloidal nanowires. Strain relaxation in this case occurs primarily by the periodical formation of stacking faults and dislocations, which do not preclude the continued growth of the nanorod or nanowire.

The different susceptibilities to heteroepitaxial growth of the various facets of a NC seed can be exploited to fabricate complex HNCs. The choice of seeds is in

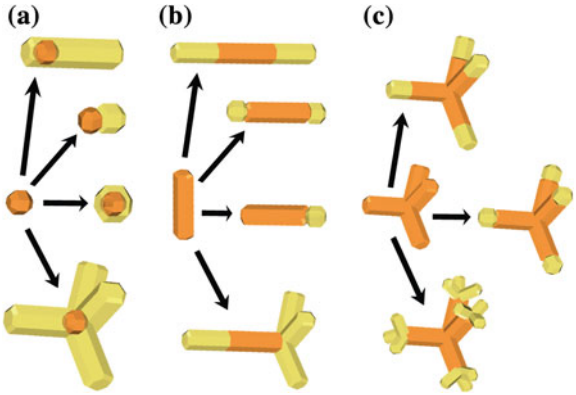

Fig. 6.21 Scheme showing the HNC morphologies that can be obtained by seeded growth using shape controlled CdSe nanocrystals as seeds: **a** nearly spherical NCs, **b** nanorods, and **c** tetrapods. Courtesy of Dr. M. Casavola (Utrecht University, Netherlands). Reproduced by permission of the Royal Society of Chemistry from Ref. [1]

principle unlimited, since any colloidal NC can be used, regardless of shape or composition (single-component, alloy, doped or hetero-NCs). However, the characteristics of the seeds strongly influence the final morphology of the HNC and impose constraints on the nature of the overgrowing segment. CdSe NCs and CdSe based HNCs have been workhorses of colloidal nanoscience since the inception of the field, and are therefore ideal to illustrate the decisive role of the seeds in the colloidal synthesis of HNCs. As shown in Fig. 6.21, the use of shape controlled seeds and suitable growth conditions has allowed the preparation of a large variety of sophisticated CdSe based HNCs (e.g., concentric core/shell QDs, heterodimers, heterotetrapods, dot core/rod shell HNCs, heterorods, dumbbells, matchsticks, etc.) [1–5].

The use of nearly spherical NCs as seeds may lead to a variety of HNC shapes depending on the specific faceting of the seed, the growth conditions, and the lattice mismatch between the seed and the overgrowing materials (Fig. 6.21a) [1]. Concentric shells can only be obtained by slow heteroepitaxial growth of materials with a small lattice mismatch with respect to the seed. Alternatively, the lattice mismatch can be gradually adapted by using gradient shells and a multishell strategy (e.g., CdSe/CdS/(Cd,Zn)S/ZnS core/multishell QDs [5]). In case the lattice mismatch between the NC seed and the overgrowing material is too large, preferential nucleation may occur on selected facets that offer the smallest possible mismatch, yielding heterodimers or oligomers (e.g., CdSe-Au or CdSe-Fe_2O_3 [2, 3]. Alternatively, the material can initially grow as an amorphous shell, thereby circumventing the lattice mismatch problem. Subsequent annealing induces crystallization of the shell, accompanied by a de-wetting and retraction process which leads to the formation of a heterodimer (e.g., CdSe-FePt) [2]. Anisotropic HNCs (Fig. 6.21a), such as dot core/rod shell CdSe/CdS nanorods and heterotetrapods [1, 2, 68], can be obtained by using growth conditions that promote anisotropic growth (viz., high monomer activity and surfactants that selectively bind to the non-polar facets of

II-VI semiconductors). Under such conditions, the morphology of the HNC is dictated by the crystal structure and shape of the seed (wurtzite yields rods [1, 2, 68], while zincblende leads to tetrapods [1, 68, 75] or octapods [75], for tetrahedral or cuboctahedral seed NCs, respectively).

Nanorods and tetrapods can also be used as seeds (Fig. 6.21b, c). The tips of nanorods and pods with the wurtzite structure typically consist of the polar facets, which are more reactive than other facets. Therefore, the heteroepitaxial growth will be faster in these facets, leading to a variety of complex morphologies. Dumbbell or matchsticks HNCs (e.g., Au-CdSe [2, 3]) are obtained under conditions that favour isotropic growth (viz., low monomer activities and lower T's). If conditions that promote 1-dimensional growth are used, heteronanorods and heterotetrapods will form, with branched heterojunctions dominating at very high precursor activities [1–3, 74]. Due to the different reactivities of the anion-terminated and cation-terminated polar facets linear heteroepitaxial growth may occur on one tip of the nanorod while branching takes place at the other. Growth on tetrapod seeds will result in either a linear extension of each pod or in branching at the tips of the pods, depending on the precursor activity [1–3, 74]) (Fig. 6.21c).

Finally, it should be noted that different synthesis techniques may be adopted depending on the intended morphology and composition of the HNC. The CdSe-PbSe combination offers an insightful illustration. The lattice mismatch between CdSe and PbSe is very small (viz., 1 %), and alloying between the two materials is prevented due to a lattice-type mismatch (CdSe is wurtzite or zincblende, while PbSe is rock-salt). Nonetheless, concentric PbSe/CdSe core/shell HNCs cannot be obtained by seeded heteroepitaxial growth, because the temperatures needed are too high for PbSe NCs, leading to dissolution and Ostwald ripening. This difficulty can be circumvented by using low temperature cation exchange processes, which convert PbSe NCs into PbSe/CdSe core/shell NCs while preserving the diameter and shape of the parent NC [36].

6.4 Outlook

The past decades have witnessed remarkable progress in the colloidal synthesis of shape-controlled NCs and HNCs. Several fundamental principles have emerged from these studies, and are discussed in detail in this Chapter. The utility of this set of concepts as guidelines for the rational design of preparation protocols for novel colloidal NCs and HNCs was also briefly addressed, and has been extensively discussed and demonstrated in the literature. The field is now moving towards more sophisticated nanostructures where size, shape, composition and connectivity of multiple segments of a HNC must be tailored in an independent and controllable way. However, there are still a number of challenges that must be addressed before the targeted synthesis of complex multicomponent colloidal HNCs reaches its full potential.

The most critical of these challenges is the development of a coherent theoretical framework that allows the rational design and fabrication of colloidal NCs and

HNCs. As discussed in this Chapter, the understanding of a number of fundamental issues is still quite fragmentary, despite the large body of accumulated knowledge. Therefore, future progress in the field will require further research on a variety of topics. First, the dynamics of the NC surface and of the organic-inorganic interface must be better understood and controlled. Second, the reaction mechanisms for the formation of colloidal NCs and HNCs are largely unknown, and should be investigated in more detail. Further, the elucidation of the nucleation and growth mechanisms remains a critical challenge, which only recently became addressable. Moreover, the role of strain and alloying on nanoheterojunctions and the correlation between atomic scale structure and the properties of HNCs are crucial issues that merit a systematic and comprehensive investigation. Future work will certainly shed more light on these issues, paving the way to a myriad of novel colloidal HNCs that will in turn give rise to new phenomena and open up many application possibilities.

6.5 Exercises

1. Describe the basic steps in the formation of colloidal inorganic nanoparticles. Which physical-chemical variables are important to control each of these steps?
2. What is the role of surfactants (also referred to as stabilizers or capping ligands) in the synthesis of colloidal nanoparticles?
3. Explain why the so-called "hot-injection" method provides a very efficient route for the preparation of nanocrystals with a small distribution in size.
4. What is the difference between the "diffusion-controlled" and the "reaction-controlled" growth regimes? How do the temperature and the precursor concentration affect each of these regimes?
5. Explain the differences between the "size-focusing" and the "size-defocusing" regimes during nanocrystal growth in solution? How can we prevent size defocusing (i.e., Ostwald ripening)?
6. Explain the essential concepts involved in the shape control of colloidal NCs.
7. What is the main difference between the growth of nanocrystals and heteronanocrystals?

References

1. Donega, C.D.M.: Synthesis and properties of colloidal heteronanocrystals. Chem. Soc. Rev. **40**, 1512–1546 (2011) (this review was used as the starting point for the present chapter and is therefore an useful source of additional details and references)
2. Manna, L., Kudera, S.: Mechanisms underlying the growth of inorganic nanoparticles in the liquid phase. In: Cozzoli, P.D. (ed.) Advanced Wet-Chemical Synthetic Approaches to Inorganic Nanostructures, pp. 1–53. Transworld Research Network, Kerala (2008)

3. Carbone, L., Cozzoli, P.D.: Colloidal heterostructured nanocrystals: Synthesis and growth mechanisms. Nano Today **5**, 449–493 (2010)
4. Costi, R., Saunders, A.E., Banin, U.: Colloidal hybrid nanostructures: a new type of functional materials. Angew. Chem. Int. Ed. **49**, 4878–4897 (2010)
5. Reiss, P., Protière, M., Li, L.: Core/shell semiconductor nanocrystals. Small **5**, 154–168 (2009)
6. Burda, C., Chen, X., Narayanan, R., El-Sayed, M.A.: Chemistry and properties of nanocrystals of different shapes. Chem. Rev. **105**, 1025–1102 (2005)
7. Rogach, A.L., Talapin, D.V., Shevchenko, E.V., Kornowski, A., Haase, M., Weller, H.: Organization of matter on different size scales: monodisperse nanocrystals and their superstructures. Adv. Funct. Mater. **12**, 653–664 (2002)
8. Kwon, S.G., Hyeon, T.: Formation mechanisms of uniform nanocrystals via hot-injection and heat-up methods. Small **7**, 2685–2702 (2011)
9. Jun, Y.-W., Choi, J.-S., Cheon, J.: Shape control of semiconductor and metal oxide nanocrystals through nonhydrolytic colloidal routes. Angew. Chem. Int. Ed. **45**, 3414–3439 (2006)
10. Roduner, E.: Size matters: why nanomaterials are different. Chem. Soc. Rev. **35**, 583–592 (2006)
11. Talapin, D.V., Lee, J., Kovalenko, M.V., Shevchenko, E.V.: Prospects of colloidal nanocrystals for electronic and optoelectronic applications. Chem. Rev. **110**, 389–458 (2010)
12. Donega, C.d.M., Liljeroth, P., Vanmaekelbergh, D.: Physico-chemical evaluation of the hot-injection method, a synthesis route for monodisperse nanocrystals. Small **1**, 1152–1162 (2005)
13. Rogach, A.L., Klar, T.A., Lupton, J.M., Meijerink, A., Feldmann, J.: Energy transfer with semiconductor nanocrystals. J. Mater. Chem. **19**, 1208–1221 (2009)
14. Yin, Y., Alivisatos, A.P.: Colloidal nanocrystal synthesis and the organic–inorganic interface. Nature **437**, 664–670 (2005)
15. Choi, C.L., Alivisatos, A.P.: From artificial atoms to nanocrystal molecules: preparation and properties of more complex nanostructures. Annu. Rev. Phys. Chem. **61**, 369–389 (2010)
16. Kumar, S., Nann, T.: Shape control of II–VI semiconductor nanomaterials. Small **2**, 316–329 (2006)
17. Gaponik, N., Hickey, S.G., Dorfs, D., Rogach, A.L., Eychmüller, A.: Progress in the light emission of colloidal semiconductor nanocrystals. Small **6**, 1364–1378 (2010)
18. Park, J., Joo, J., Kwon, S.G., Jang, Y., Hyeon, T.: Synthesis of monodisperse spherical nanocrystals. Angew. Chem. Int. Ed. **46**, 4630–4660 (2007)
19. Rogach, A.L. (ed.): Semiconductor nanocrystal quantum dots: synthesis, assembly, Spectroscopy and Applications. Springer, New York (2008)
20. Scholes, G.D.: Controlling the optical properties of inorganic nanoparticles. Adv. Funct. Mater. **18**, 1157–1172 (2008)
21. Smith, D.D., Sibille, L., Cronise, R.J., Hunt, A.J., Oldenburg, S.J., Wolfe, D., Halas, N.J.: Effect of microgravity on the growth of silica nanostructures. Langmuir **16**, 10055–10060 (2000)
22. Durr, N.J., Larson, T., Smith, D.K., Korgel, B.A., Sokolov, K., Ben-Yakar, A.: Two-photon luminescence imaging of cancer cells using molecularly targeted gold nanorods. Nano Lett. **7**, 941–945 (2007)
23. Houtepen, A.J., Koole, R., Vanmaekelbergh, D., Meeldijk, J., Hickey, S.G.: The hidden role of acetate in the PbSe nanocrystal synthesis. J. Am. Chem. Soc. **128**, 6792–6793 (2006)
24. Medintz, I.L., Mattoussi, H., Clapp, A.R.: Potential clinical applications of quantum dots. Int. J. Nanomed. **3**, 151–167 (2008)
25. Jiang, C., Lee, J.-S., Talapin, D.V.: Soluble precursors for CuInSe2, CuIn1–xGaxSe2, and Cu2ZnSn(S, Se)4 based on colloidal nanocrystals and molecular metal chalcogenide surface ligands. J. Am. Chem. Soc. **134**, 5010–5013 (2012)
26. Schwartz, D.K.: Mechanisms and kinetics of self-assembled monolayer formation. Annu. Rev. Phys. Chem. **52**, 107–137 (2001)

27. Donega, C.d.M., Bode, M., Meijerink, A.: Size- and temperature-dependence of exciton lifetimes in CdSe quantum dots. Phys. Rev. B **74**, 085320 (2006)
28. Menagen, G., Macdonald, J.E., Shemesh, Y., Popov, I., Banin, U.: Au growth on semiconductor nanorods: photoinduced versus thermal growth mechanisms. J. Am. Chem. Soc. **131**, 17406–17411 (2009)
29. Mulder, W.J.M., Koole, R. Brandwijk, R.J. Storm, G., Chin, P., Strijkers, G.J., de Mello Donegá, C., Nicolay, K., Griffioen, A.W.: Quantum dots with a paramagnetic coating as a bimodal molecular imaging probe. Nano Lett. **6**, 1–6 (2006)
30. Manna, L., Wang, L.W., Cingolani, R., Alivisatos, A.P.: First-principles modeling of unpassivated and surfactant-passivated bulk facets of wurtzite CdSe: a model system for studying the anisotropic growth of CdSe nanocrystals. J. Phys. Chem. B **109**, 6183–6192 (2005)
31. Fang, C., Van Huis, M.A., Vanmaekelbergh, D., Zandbergen, H.W.: Energetics of polar and nonpolar facets of PbSe nanocrystals from theory and experiment. ACS Nano **4**, 211–218 (2010)
32. Fritzinger, B., Moreels, I., Lommens, P., Koole, R., Hens, Z., Martins, J.C.: In situ observation of rapid ligand exchange in colloidal nanocrystal suspensions using transfer NOE nuclear magnetic resonance spectroscopy. J. Am. Chem. Soc. **131**, 3024–3032 (2009)
33. Pradhan, N., Reifsnyder, D., Xie, R., Aldana, J., Peng, X.: Surface ligand dynamics in growth of nanocrystals. J. Am. Chem. Soc. **129**, 9500–9509 (2007)
34. Devries, G.A., Brunnbauer, M., Hu, Y., Jackson, A.M., Long, B., Neltner, B.T., Uzun, O., Wunsch, B.H., Stellaci, F.: Divalent metal nanoparticles. Science **315**, 358–361 (2007)
35. Eastoe, J., Hollamby, M.J., Hudson, L.: Recent advances in nanoparticle synthesis with reversed micelles. Adv. Coll. Interf. Sci. **128–130**, 5–15 (2006)
36. Groeneveld, E., Witteman, L., Lefferts, M., Ke, X., Bals, S., van Tendeloo, G., de Mello Donega, C.: Tailoring ZnSe-CdSe colloidal quantum dots via cation exchange: from core/shell to alloy nanocrystals. ACS Nano **7**, 7913–7930 (2013)
37. Rivest, J.B., Jain, P.K.: Cation exchange on the nanoscale: an emerging technique for new material synthesis, device fabrication, and chemical sensing. Chem. Soc. Rev. **42**, 89–96 (2013)
38. Beberwyck, B.J., Surendranath, Y., Alivisatos, A.P.: Cation exchange: a versatile tool for nanomaterials synthesis. J. Phys. Chem. C **117**, 19759–19770 (2013)
39. Li, H., Zanella, M., Genovese, A., Povia, M., Falqui, A., Giannini, C., Manna, L.: Sequential cation exchange in nanocrystals: preservation of crystal phase and formation of metastable phases. Nano Lett. **11**, 4964–4970 (2011)
40. Wang, F., Tang, R., Kao, J.L.-F., Dingman, S.D., Buhro, W.E.: Spectroscopic identification of Tri-*n*-octylphosphine oxide (TOPO) impurities and elucidation of their roles in cadmium selenide quantum-wire growth. J. Am. Chem. Soc. **131**, 4983–4994 (2009)
41. Kopping, J.T., Patten, T.E.: Identification of acidic phosphorus-containing ligands involved in the surface chemistry of CdSe nanoparticles prepared in tri-*N*-octylphosphine oxide solvents. J. Am. Chem. Soc. **130**, 5689–5698 (2008)
42. LaMer, V.K., Dinegar, R.H.: Theory, production and mechanism of formation of monodispersed hydrosols. J. Am. Chem. Soc. **72**, 4847–4854 (1950)
43. Reiss, H.: The growth of uniform colloidal dispersions. J. Chem. Phys. **19**, 482–487 (1951)
44. Sugimoto, T.: Preparation of monodispersed colloidal particles. Adv. Colloid Interface Sci. **28**, 65–108 (1987)
45. Sugimoto, T.: The theory of the nucleation of monodisperse particles in open systems and its application to AgBr systems. J. Colloid Interf. Sci. **150**, 208–225 (1992)
46. Besson, C., Finney, E.E., Finke, R.G.: A mechanism for transition-metal nanoparticle self-assembly. J. Am. Chem. Soc. **127**, 8179–8184 (2005)
47. Watzky, M.A., Finney, E.E., Finke, R.G.: Transition-metal nanocluster size vs formation time and the catalytically effective nucleus number: a mechanism-based treatment. J. Am. Chem. Soc. **130**, 11959–11969 (2008)

48. Owen, J.S., Chan, E.M., Liu, H., Alivisatos, A.P.: Precursor conversion kinetics and the nucleation of cadmium selenide nanocrystals. J. Am. Chem. Soc. **132**, 18206–18213 (2010)
49. Saruyama, M., So, Y., Kimoto, K., Taguchi, S., Kanemitsu, Y., Teranishi, T.: Spontaneous formation of Wurzite-CdS/Zincblende-CdTe heterodimers through a partial anion exchange reaction. J. Am. Chem. Soc. **133**, 17598–17601 (2011)
50. Rempel, J.Y., Bawendi, M.G., Jensen, K.F.: Insights into the kinetics of semiconductor nanocrystal nucleation and growth. J. Am. Chem. Soc. **131**, 4479–4489 (2009)
51. Finney, E.E., Finke, R.G.: Nanocluster nucleation and growth kinetic and mechanistic studies: A review emphasizing transition-metal nanoclusters. J. Colloid Interface Sci. **317**, 351–374 (2008)
52. Bullen, C., Mulvaney, P.: Nucleation and growth kinetics of CdSe nanocrystals in octadecene. Nano Lett. **4**, 2303–2307 (2004)
53. Peng, X.: Mechanisms for the shape-control and shape-evolution of colloidal semiconductor nanocrystals. Adv. Mater. **15**, 459–463 (2003)
54. Allen, P.M., Walker, B.J., Bawendi, M.G.: Mechanistic insights into the formation of InP quantum dots. Angew. Chem. **122**, 772–774 (2010)
55. Zheng, H., Smith, R.K., Jun, Y., Kisielowski, C., Dahmen, U., Alivisatos, A.P.: Observation of single colloidal platinum nanocrystal growth trajectories. Science **324**, 1309–1312 (2009)
56. Zhuang, Q., Liu, S.-J., Yu, S.-H.: Recent advances in oriented attachment growth and synthesis of functional materials: concept, evidence, mechanism, and future. J. Mater. Chem. **19**, 191–207 (2009)
57. Koh, W., Bartnik, A.C., Wise, F.W., Murray, C.B.: Synthesis of monodisperse PbSe nanorods: A case for oriented attachment. J. Am. Chem. Soc. **132**, 3909–3913 (2010)
58. Groeneveld, E., van Berkum, S., van Schooneveld, M.M., Gloter, A., Meeldijk, J.D., van den Heuvel, D.J., Gerritsen, H.C., de Mello Donega, C.: Highly luminescent (Zn,Cd)Te-CdSe colloidal heteronanowires with tunable electron-hole overlap. Nano Lett. **12**, 749–757 (2012)
59. Tang, Z., Kotov, N.A., Giersig, M.: Spontaneous organization of single CdTe nanoparticles into luminescent nanowires. Science **297**, 237–240 (2002)
60. van Huis, M.A., Kunneman, L.T., Overgaag, K., Xu, Q., Pandraud, G., Zandbergen, H.W., Vanmaekelbergh, D.: Low-temperature nanocrystal unification through rotations and relaxations probed by in situ transmission electron microscopy. Nano Lett. **8**, 3959–3963 (2008)
61. Klokkenburg, M., Houtepen, A., Koole, R., De Folter, J.W., Erné, B.H., Van Faasen, E., Vanmaekelbergh, D.: Dipolar structures in colloidal dispersions of PbSe and CdSe quantum dots. Nano Lett. **7**, 2931–2936 (2007)
62. de Mello Donega, C., Hickey, S.G.; Wuister, S.F.; Vanmaekelbergh, D.; Meijerink, A.: Single-step synthesis to control the photoluminescence quantum yield and size dispersion of CdSe nanocrystals. J. Phys. Chem. B **107**, 489 (2003)
63. Nair, P.S., Fritz, K.P., Scholes, G.D.: Evolutionary shape control during colloidal quantum-dot growth. Small **3**, 481–487 (2007)
64. Jiang, Z., Kelley, D.F.: Role of magic-sized clusters in the synthesis of CdSe nanorods. ACS Nano **4**, 1561–1572 (2010)
65. Wang, W., Banerjee, S., Jia, S., Steigerwald, M.L., Herman, I.P.: Ligand control of growth, morphology, and capping structure of colloidal CdSe nanorods. Chem. Mater. **19**, 2573–2580 (2007)
66. Bhattacharya, P., Ghosh, S., Stiff-Roberts, A.D.: Quantum dot opto-electronic devices. Annu. Rev. Mater. Res. **34**, 1–40 (2004)
67. Ovidko, I.A., Sheinerman, A.G.: Misfit dislocations in nanocomposites with quantum dots, nanowires and their ensembles. Adv. Phys. **55**, 627–689 (2006)
68. Talapin, D.V., Nelson, J.H., Shevchenko, E.V., Aloni, S., Sadtler, B., Alivisatos, A.P.: Seeded growth of highly luminescent CdSe/CdS nanoheterostructures with rod and tetrapod morphologies. Nano Lett. **7**, 2951–2959 (2007)
69. Halpert, J.E., Porter, V.J., Zimmer, J.P., Bawendi, M.G.: Synthesis of CdSe/CdTe nanobarbells. J. Am. Chem. Soc. **128**, 12590–12591 (2006)

70. Shi, W., Zeng, H., Sahoo, Y., Ohulchanskyy, T.Y., Ding, Y., Wang, Z.L., Swihart, M., Prasad, P.N.: A general approach to binary and ternary hybrid nanocrystals. Nano Lett. **6**, 875–881 (2006)
71. Yan, C., Dadvand, A., Rosei, F., Perepichka, D.F.: Near-IR photoresponse in new up-converting CdSe/$NaYF_4$:Yb. Er Nanoheterostructures. J. Am. Chem. Soc. **132**, 8868–8869 (2010)
72. Yu, H., Chen, M., Rice, P.M., Wang, S.X., White, R.L., Sun, S.: Dumbbell-like bifunctional Au-Fe_3O_4 nanoparticles. Nano Lett. **5**, 379–382 (2005)
73. Kwon, K.-W., Shim, M.: γ-Fe_2O_3/II − VI sulfide nanocrystal heterojunctions. J. Am. Chem. Soc. **127**, 10269–10275 (2005)
74. Milliron, D.J., Hughes, S.M., Cui, Y., Manna, L., Li, J., Wang, L., Alivisatos, A.P.: Colloidal nanocrystal heterostructures with linear and branched topology. Nature **430**, 190–194 (2004)
75. Deka, S., Miszta, K., Dorfs, D., Genovese, A., Bertoni, G., Manna, L.: Octapod-shaped colloidal nanocrystals of cadmium chalcogenides via "one-pot" cation exchange and seeded growth. Nano Lett. **10**, 3770–3776 (2010)

Chapter 7
Electron Microscopy Techniques

Marijn A. van Huis and Heiner Friedrich

Abstract This chapter introduces the basic concepts of electron microscopy, which comprises an extensive toolbox for characterizing the size, three-dimensional shape, composition, and crystal structure of nanoparticles, nanoparticle superstructures and nanostructured materials.

7.1 Introduction: Imaging Nanoparticles with Electrons

The most characteristic property of nanoparticles (NPs) is their nanoscale size. It is this small scale that results in interesting physical properties (optical, magnetic, electronic, opto-electronic, etc.), which differ from the properties of their bulk counterparts (see Chap. 1). The simple fact that the particles are of nanometer size renders observation by light microscopy impossible, as the dimensions of the NPs are much smaller than the typical wavelength of light (hundreds of nanometers). Therefore, electrons—which have a much smaller wavelength than light—are much better suited to study the structural properties of NPs. Nowadays, electron microscopes (EM) are available with a spatial resolution of 50 pm, which is considerably smaller than the typical distance between atoms (200 pm or 2 Å). Because of this superior resolution, the structure of surfaces and interfaces of NPs can now be imaged with atomic resolution. As the incident electrons interact with the atoms in the sample in very diverse ways (scattering, diffraction, electron energy losses, induced X-ray emission), a large variety of methods and techniques have been developed that can be used to obtain additional information on the material under

M.A. van Huis
Soft Condensed Matter, Debye Institute for Nanomaterials Science, Utrecht University, Princetonplein 5, 3584 CC Utrecht, The Netherlands

H. Friedrich (✉)
Laboratory of Materials and Interface Chemistry, Eindhoven University of Technology, P.O. Box 513, 5600 MB Eindhoven, The Netherlands
e-mail: h.friedrich@tue.nl

C. de Mello Donegá (ed.), *Nanoparticles*,
DOI 10.1007/978-3-662-44823-6_7

study. In this chapter we provide only a brief overview of the most commonly used methods. The book *Transmission Electron Microscopy—A Textbook for Materials Science* by D.B. Williams and C.B. Carter [1] can be found in EM facilities all over the world and provides a very comprehensive introduction to the field. A very complete overview of EM is given in the *Handbook of Nanoscopy*, edited by G. van Tendeloo et al. [2]. It should be stressed that one can learn electron microscopy only by spending many hours behind the microscopes in a continuous effort to obtain the best images possible. Finally, it is strongly recommended to collaborate with experienced electron microscopists for the interpretation of the data. *What you see is not always what you get*: the way the image looks depends strongly on the settings of the microscope, and the interpretation of images is sometimes far from trivial.

In the next Sect. 7.2 we will explain the distinction between scanning electron microscopy (SEM) and transmission electron microscopy (TEM). While SEM can be used to study large, micrometer scale assemblies of NPs, TEM is mostly used to analyze individual NPs and smaller assemblies because of its superior resolution. We will conclude Sect. 7.2 with some remarks on sample preparation.

In the remainder of this Chapter, the main imaging modes of the TEM instrument will be discussed: regular TEM imaging, and *scanning* transmission electron microscopy (STEM) (Sect. 7.3). We will then proceed to describe at a basic level the most important interaction mechanisms of electrons with matter: ***electron diffraction*** (Sect. 7.4), and scattering events which enable a number of viewing modes (Sect. 7.5). To bring relief to the restriction that conventionally only two-dimensional images are recorded, we will discuss ***electron tomography*** in Sect. 7.6, a method which allows three-dimensional reconstruction of NPs and their assemblies. In Sect. 7.7 ***analytical TEM*** will be described as a means to map the local chemical composition of the NPs. The study of particles and molecules in liquids, and of very soft materials, in general requires *cryo-TEM*, whereby the sample is analyzed at liquid nitrogen temperatures ($\sim$77 K). This technique is discussed in Sect. 7.8. Finally, in Sect. 7.9 we discuss **in situ *TEM***: performing experiments such as heating and gas exposure inside the electron microscope, before concluding with some general remarks on future developments (Sect. 7.10).

7.2 Scanning Electron Microscopy (SEM) and Transmission Electron Microscopy (TEM)

The basic scheme of the SEM and TEM setups and representative images are shown in Fig. 7.1. In ***Scanning Electron Microscopy*** (SEM), the acquired image is built up from electrons that are reflected (backscattered electrons, BSE) or emitted (secondary electrons, SE) from the surface of the material under investigation. The electron beam is focused into an electron probe, which is scanned over the surface in a raster scan pattern. Therefore, the pixels in a SEM image originate from electrons that are collected sequentially point by point in a detector (usually an

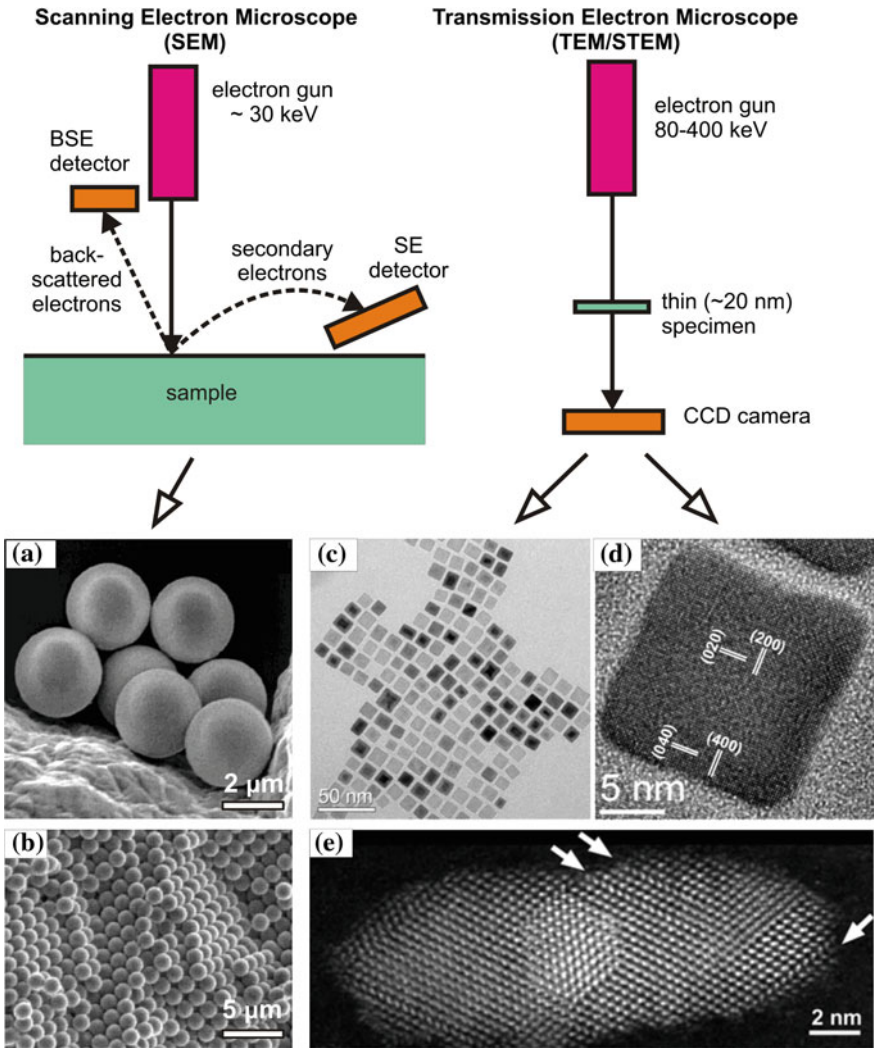

Fig. 7.1 *Top* schematic showing the basic principle of scanning and transmission electron microscopes (SEM and TEM, respectively). Images recorded in the SEM display surfaces. **a** ZnS NPs on a support. **b** Silica NPs assembled in a superstructure. TEM imaging provides two-dimensional projections of the NPs. **c** Deposited cubical $FeO_x/CoFe_2O_4$ core/shell NPs. **d** High-resolution image of a NP in **c** with atomic planes indicated. **e** High-resolution HAADF-STEM image of a CdSe rod shell with a faceted PbSe core at the centre. Images **c**, **d**: courtesy of Yalcin et al. [3]. Image **a** is reprinted with permission from Ref. [4]. Copyright (2001) American Chemical Society. Image **e** is reprinted with permission from Ref. [5]. Copyright (2011) American Chemical Society

Everhart-Thornley detector). Alternatively, nanostructures can be imaged in transmission mode using ***Transmission Electron Microscopy*** (TEM), whereby the electrons travel through a very thin sample (usually called a *specimen*) and are collected by a detector at the rear side. The latter method requires that the specimen is very thin (it should be *electron-transparent*, typically less than 100 nm thick). Using SEM, one obtains an image of the *surface* of the nanomaterial. Using TEM, one obtains a *two-dimensional projection* of the nanomaterial. There are many other microscopy techniques such as scanning tunneling microscopy (STM, Chap. 8), atomic force microscopy (AFM, Chap. 8), electron probe microscopic analysis (EPMA), correlative light and electron microscopy (CLEM), and X-ray microscopy (XRM), which will not be discussed here. In the remainder of this chapter, we will discuss almost exclusively TEM, because of its superior resolution which allows extracting very detailed information from nanoscale samples.

7.2.1 Specimen Preparation Techniques

Many NPs are synthesized under wet chemistry conditions (see Chap. 6) and are therefore dispersed in solvents (colloidal suspensions). In case the NPs are stable without the solvent, no special sample preparation is required for TEM investigation. When the NPs are sufficiently diluted, dropcasting of one drop of the suspension onto a TEM support film such as a thin carbon foil, followed by evaporation of the liquid medium, is sufficient for basic imaging. Alternatively, the TEM grid may be dipped for a few seconds in the NP suspension. In general, 'washing' the suspended NPs (i.e., removing excess surfactants and other molecules) prior to dropcasting is highly recommended. This can be achieved by precipitating the NPs from the colloidal suspension by addition of a non-solvent, followed by centrifugation and redispersion of the NPs in a solvent (this purification process may be repeated several times). Sometimes high-quality imaging of the NPs is hampered by the presence of ligands at the surface, or by other molecules that were present in the colloidal suspension. In those cases, a fast 5–30 s plasma etch (the plasma typically consists of Ar and O ions) is applied to remove the molecules which were blurring the images. Much precaution should be taken not to modify the NPs in the process.

There are cases where a more extensive sample preparation is required. For example, in the case of catalytic NPs that are present in much larger three-dimensional porous supports, in the case of multilayer semiconductor quantum dot films (solar cell nanomaterials), and when studying three-dimensional self-ordered NP assemblies (Fig. 7.1b). In those cases, the conventional materials science techniques of grinding, polishing, and ion milling (i.e., sputtering atoms from the sample at a low incident angle using a 4 keV Ar^+ ion beam) can provide electron-transparent samples. On the other hand, most 3D nanoparticle materials are rather soft, and will not withstand conventional grinding and polishing. In those cases, a more advanced technique is FIB-SEM (focused ion beam inside the scanning

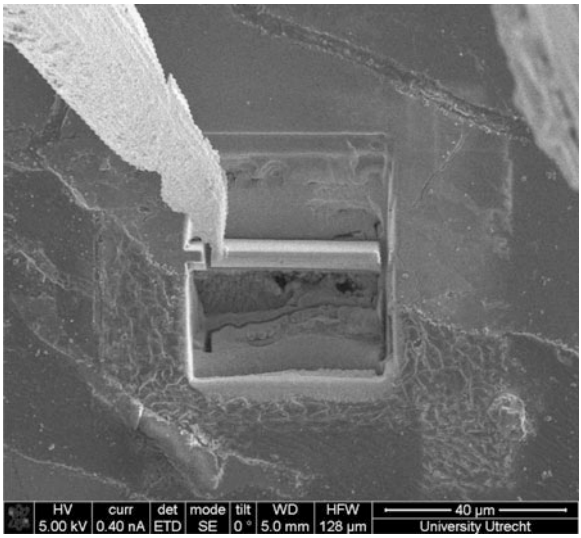

Fig. 7.2 Scanning electron microscope (SEM) image showing a trench in the surface of geological rock material, with at the center the lamella that has been cut out using a focused ion beam (FIB) of Ga^+ ions. The lamella is attached to a needle by ion-induced Pt deposition at the contact point, and is subsequently cut completely free from the trench and transported and deposited onto a TEM support using the needle (courtesy of C.T.W.M. Schneijdenberg, Utrecht University)

electron microscope), whereby a focused Ga^+ ion beam is used to cut out a very thin slice (called a 'lamella') out of a larger sample. An example is shown in Fig. 7.2. This slice (with a typical thickness of 20–50 nm) can then be further analyzed in the TEM.

7.3 Two Imaging Modes: TEM and STEM

There are two main imaging modes of the transmission electron microscope. When imaging in the regular TEM mode, a wide, homogeneous and parallel electron beam is incident on the sample as indicated schematically at the left-hand side of Fig. 7.3. Alternatively, the electron beam can be focused into a fine spot (50–1,000 pm wide, depending on the microscope) at the position of the specimen, whereby one speaks of an *electron probe*. This probe beam is then scanned over the surface of the specimen in a matrix of e.g. 1,000 × 1,000 points in X and Y direction, whereby the image is created point by point. Hence, this operational mode is called *scanning transmission electron microscopy* (STEM). Underneath the specimen, a ring-shaped detector is placed that collects only electrons that have undergone a scattering event, so that they do not proceed along the central optical axis, but are scattered at an angle large enough to hit the ring. By varying the angle of the edges

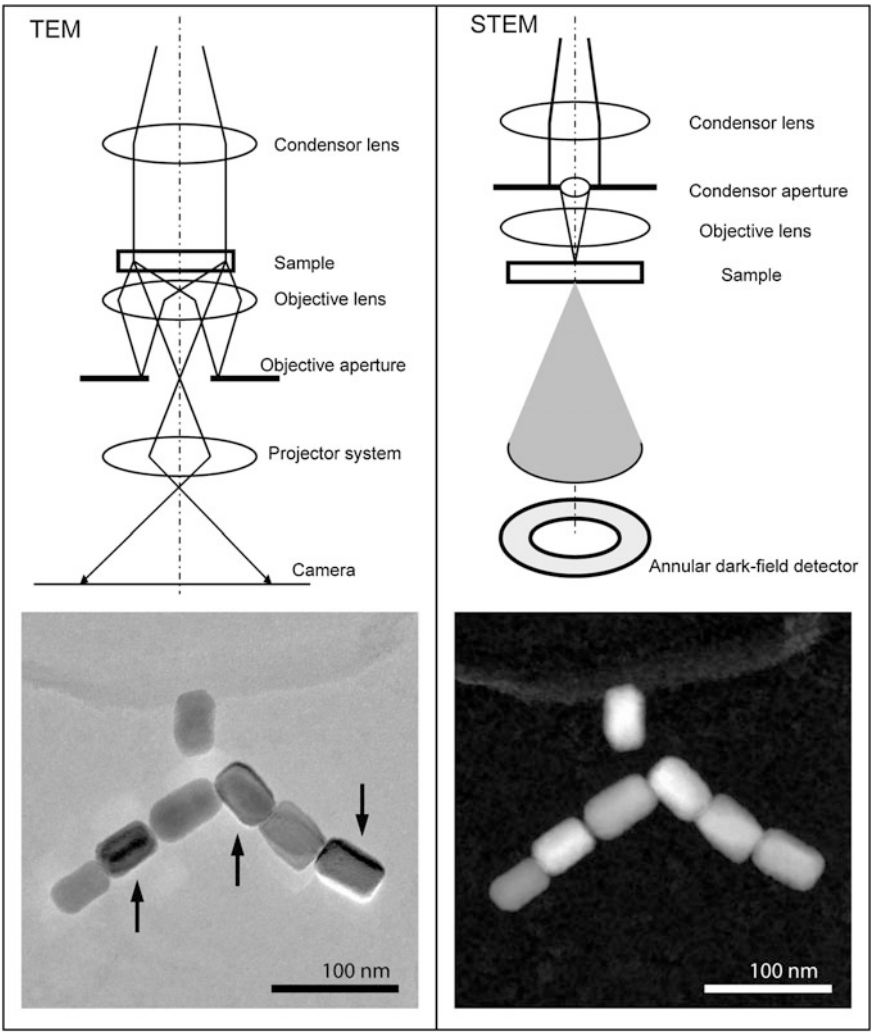

Fig. 7.3 Ray diagram for *bright-field* TEM and annular *dark-field* STEM mode with examples of Fe_3O_4 NPs imaged in the corresponding mode shown below. The *arrows* in the TEM image denote NPs that have their crystal lattice aligned with the electron beam resulting in bright 'ghosts'. The lenses consist of electromagnetic fields that control and focus the electron beam

of the ring with respect to the optical axis, electrons can be selected that have interacted with very heavy atoms (strong scattering, large scattering angle), or that have interacted with lighter atoms (smaller scattering angle).

Below the ray diagrams in Fig. 7.3 example images of the two imaging modes are given, in which Fe_3O_4 NPs on top of a thin carbon support membrane are imaged. In the TEM image the NPs appear darker than the support, because the heavier NPs will "stop" (scatter or diffract) a number of the incident electrons, so

that they are not detected on the camera behind the specimen. In annular dark field (ADF) STEM mode, the carbon support appears dark. Carbon is a very light element that hardly scatters electrons. The electrons that interact with the carbon atoms, will hardly be deflected and will thus proceed in a forward trajectory, passing through the center of the ring (right side in Fig. 7.3), so that they are not detected at all. The electrons that are detected on the ring-shaped ADF detector, almost all originate from interactions with the Fe_3O_4 NPs, which is why they appear bright in the ADF-STEM image.

One should always realize that in regular TEM mode with the wide parallel beam, all electrons that contribute to the image are collected in principle simultaneously (although there is always a finite exposure time). In STEM mode, the image is created sequentially, pixel by pixel, by scanning the electron probe across the sample, so that the acquisition of a STEM image takes more time (e.g., 5 s for STEM vs. 1 s for TEM). Therefore, STEM recording is more sensitive to drift of the specimen (due to, e.g., mechanical vibrations and temperature variations). The advantages and disadvantages of various viewing modes, and the underlying physical mechanisms, will be discussed more extensively in Sects. 7.4 and 7.5.

7.4 Electron Diffraction

When analyzing NPs and their assemblies it is in some cases desirable not to look at a magnified image of the sample, but instead, at the pattern generated in the back-focal plane (BFP) of the objective lens. The BFP of the objective lens is the plane in which the objective aperture (OA) is located. Note that in electron diffraction the OA is withdrawn from the beam path. For almost all specimens, and in particular for specimens made up of regularly spaced arrays of atoms, the intensity distribution in the BFP is inhomogeneous, often showing a pattern of spots or rings. These patterns, referred to as ***electron diffraction patterns***, arise from the interaction of a parallel and coherent beam of electrons with an ordered (e.g. polycrystalline) sample by interference of the refracted electron waves from neighboring atoms and lattice planes. The diffraction pattern (DP) generated in the BFP can be viewed magnified on screen or recorded on the CCD camera by suitably focused transfer and projection lenses. Since the DP is generated from the entire area that is illuminated by the electron beam, the information from many NPs is averaged. To differentiate between the DP generated in different regions or from different NPs an aperture, referred to as selected area electron diffraction (SAED) aperture can be inserted in the beam path (see Fig. 7.4).

The position of the rings or spots in a diffraction pattern (DP) with respect to the central beam gives information on the specimens atomic scale order, such as being amorphous, poly- or single- crystalline, including the respective lattice parameters and symmetry, grain morphology, grain-size distribution, or grain orientation. Nevertheless, a detailed analysis can be time consuming and often requires the combination of electron diffraction with atomic resolution images. In this context, it

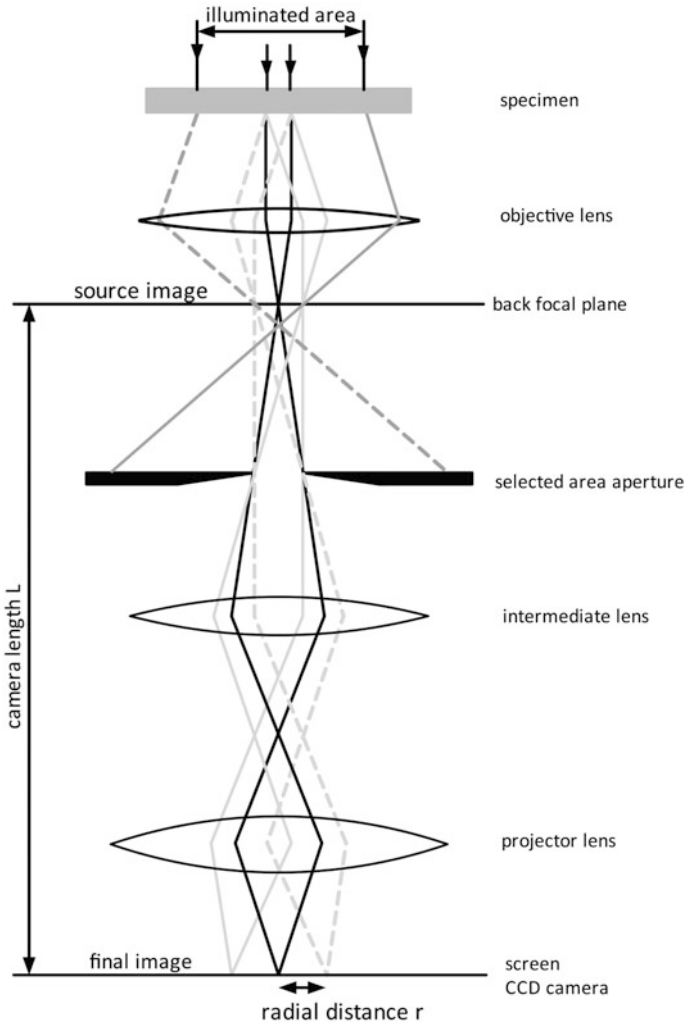

Fig. 7.4 Ray diagram for selected area electron diffraction (SAED)

suffices to say that the radial distance of the rings or spots can be evaluated in terms of lattice distances similar to X-ray diffraction. The *lattice distance* ($d = \lambda \cdot L/r$) is related to the radial distance (r in mm) by the wavelength of the electrons ($\lambda = 3.86$ pm for 100 kV and $\lambda = 2.54$ pm for 200 kV acceleration voltage) and the camera length (L in mm, distance between the scattering event and the recording plane).

An example illustrating electron diffraction without and with a selected area aperture on assemblies of magnetite NPs is shown in Fig. 7.5. Note that the illuminated area in Fig. 7.5a is much larger than the area of the image. Illuminating and, thus, averaging over a large number of NPs (Fig. 7.5a) leads to a DP consisting

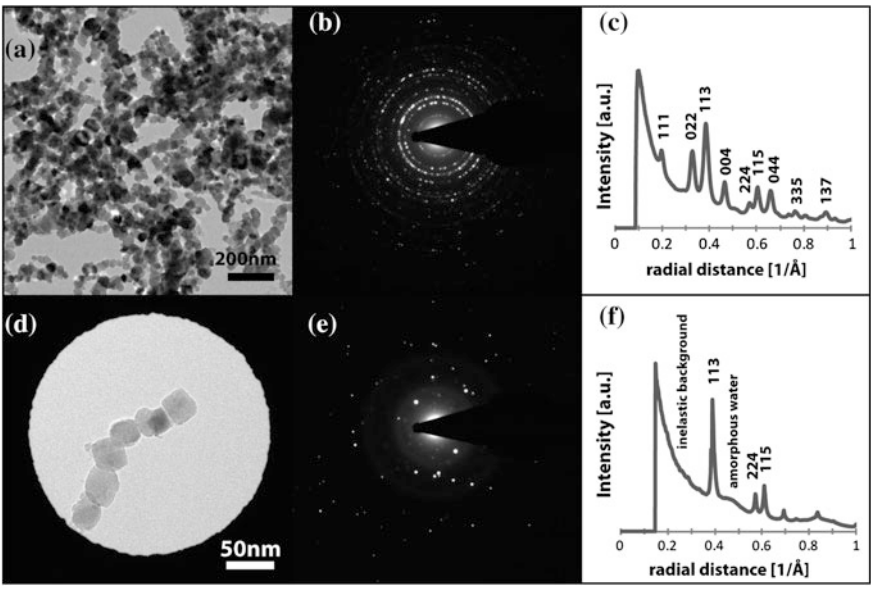

Fig. 7.5 Image (**a**, **d**), diffraction pattern (**b**, **e**) and radial average (**c**, **f**) of FeO_x NPs without (**a**–**c**) and with (**d**–**f**) selected area electron diffraction (SAED) aperture [6]

of rings (Fig. 7.5b) which is, if radially averaged (Fig. 7.5c), comparable in information to a powder X-ray diffraction pattern. In case a SAED aperture is inserted in the beam path (Fig. 7.5d) the information in the DP is limited to the magnetite NP within the field of view, thus, no rings but only diffraction spots (Fig. 7.5e) are visible. Henceforth, the radial average of the spot pattern plotted in (Fig. 7.5f) differs from the that shown in Fig. 7.5c and may indicate preferential orientation of the NPs on the TEM grid on account of e.g. shape anisotropy. The increase in background signal towards low radial distances results from inelastic interactions between electron beam and sample. In the limit of only one crystallite being present in the selected field of view its crystalline lattice and orientation with respect to the electron beam can be determined. If one carefully examines Fig. 7.5e, two diffuse rings are observed. The rings are caused by the fact that the NPs were imaged in a vitreous water layer, a technique referred to as Cryo-TEM which will be further discussed in Sect. 7.8. The position and breadth of the broad maximum at a radial distance of ~ 4.7 Å^{-1} corresponding to ~ 2.1 Å nearest neighbor distance is a characteristic of amorphous, i.e. vitreous, water.

To complete the discussion of electron diffraction, it needs to be added that it also can be carried out using a convergent (S)TEM probe. In convergent beam electron diffraction (CBED) the diffraction spots widen to discs containing additional bright and dark features. Henceforth, CBED provides beyond unit cell and associated lattice parameters, also quantitative data on specimen thickness, lattice-strain (key parameters for semiconductors and other multilayer nanostructures),

valence-electron distribution, or chemical bonding. However, this information can only be extracted aided by detailed CBED pattern simulations.

In summary, electron diffraction complements X-ray diffraction providing detailed crystallographic information of small volumes such as individual NPs (electron-matter interaction is about 1 million times stronger than x-ray-matter interactions) and with exposure times in the order of seconds (much longer exposures are needed for X-rays, except when using high brightness synchrotron sources).

7.5 Advanced Imaging—Contrast Modes

As explained in Sect. 7.3, electron microscopes are operated in two basic modes, TEM or STEM. To understand the information contained in the corresponding images it is worthwhile to look at the electron-sample interaction and how image contrast is generated. As shown in Fig. 7.6a, in TEM a parallel beam of electrons may be transmited through a sample consisting of a low and a high mass-density region. The high-density region will interact more strongly with the electron beam and, thus, scatter more of the incoming electrons. Electrons scattered towards the objective aperture are removed from the beam resulting in lower image intensity in the corresponding image region. This contrast mode is referred to as ***mass-contrast*** and occurs for homogeneously thick samples. It can be used to distinguish same-sized NPs with vastly different elemental compositions, e.g. carbon or metal NPs. It is also applied to image organic macromolecules by embedding them in a homogeneously thick film of a heavy metal stain. The stain creates a strongly scattering replica of the macromolecules outline, thus enhancing contrast.

Besides differences in mass-density, differences in thickness, as shown in Fig. 7.6b, also generate contrast. ***Thickness contrast*** results in a reduced image intensity of thick sample regions, thus providing information such as surface roughness, or object outline. Note that a (S)TEM image is in first approximation a two dimensional (2D) projection of a 3D object along the beam path. Henceforth, image intensities reflect the cumulative thickness of objects. The contrast effects discussed above are commonly combined into ***mass-thickness-contrast,*** which is quite similar to the well-known Lambert-Beer absorption contrast. However, it is only virtual absorption by the objective aperture creating TEM contrast, which is increasing with decreasing aperture size. The recorded image intensity $(I \sim I_0 e^{-\sigma t})$ scales with the total (in) elastic scattering cross-section (σ) and the sample thickness (t).

In case of crystalline NPs, image contrast will also depend on the orientation of the crystal lattice with respect to the electron beam. As illustrated in Fig. 7.6c, if lattice planes of a NP are parallel to the electron beam the diffraction pattern generated in the back focal plane of the objective lens will contain strong diffraction spots. If these spots are cut out by a suitably sized objective aperture the image intensity of the oriented NP will be significantly decreased, which is referred to as ***diffraction contrast***. All crystalline NPs with non-parallel orientation and all amorphous NPs will not show this behavior. Based on above contrast considerations

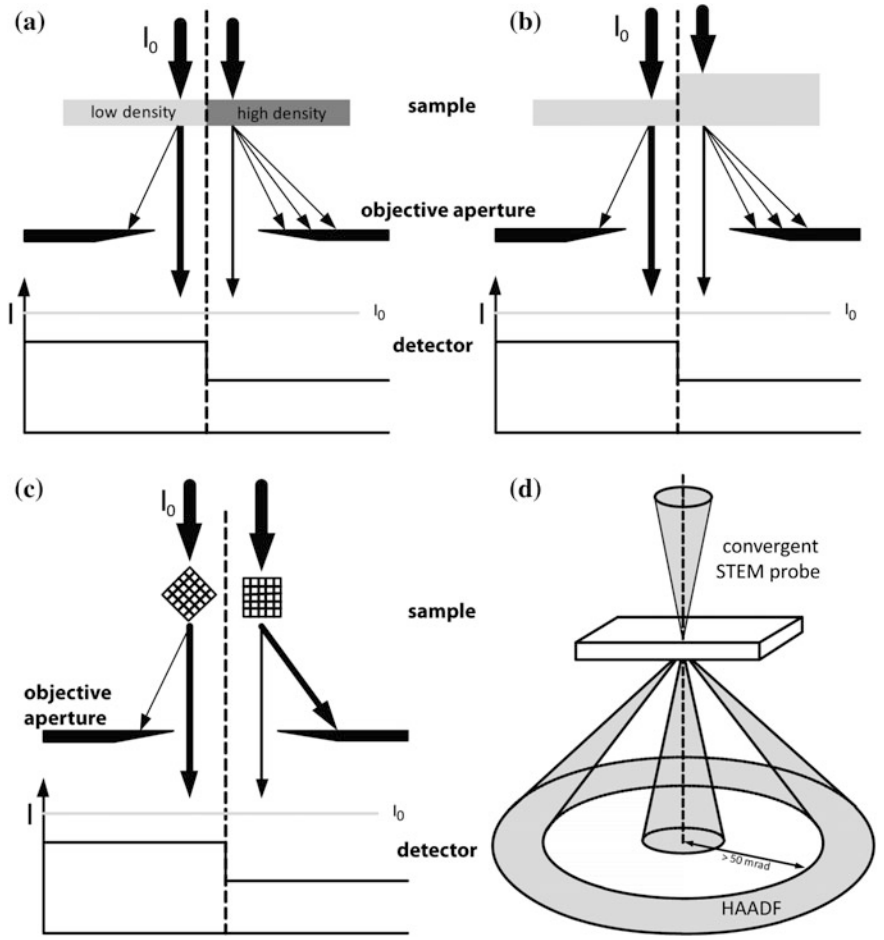

Fig. 7.6 Cartoon of contrast generation by mass-density (**a**); thickness (**b**); crystal orientation (**c**); and atomic number (**d**)

one can easily infer that in general it is difficult to distinguish between dense, thick or oriented crystalline NPs using a single TEM image.

To simplify the intricate contrast associated with the coherent nature of electron waves, i.e. the scattering of electrons into low angles, a technique called ***z-contrast imaging*** is utilized. It employs a convergent STEM probe that transverses the sample as sketched in Fig. 7.6d. The image is formed point by point using only electrons that are scattered into angles larger than 50 mrad onto a high-angle annular dark-field (HAADF) detector. In HAADF images the contrast is predominantly incoherent as electrons are scattered close to the atomic core which is governed by thermal vibrations. In more physical terms, the electron-matter interaction approaches the unscreened Rutherford scattering cross-section, which generates images with intensities that are proportional to the square of the atomic number of the element

($I \sim Z^2$). Note that the Rutherford limit is not reached and the exact dependence has many parameters. Overall, HAADF imaging is very little susceptible to lattice orientation effects. One significant limitation is that only a very small fraction of the impinging electrons are used for imaging, thus requiring a high initial dose. Henceforth, only beam-stable materials like e.g. (metal)oxide NPs on a carbon support film can be imaged by HAADF STEM without damage.

An example of a bright-field (BF) TEM image of biogenic magnetite (Fe_3O_4) NPs and a HAADF STEM image of the same chain of crystallites was displayed in Fig. 7.3 above. While the contrast of the NPs in the TEM image is strongly dependent on thickness, lattice orientation and defocus (see arrows in Fig. 7.3a for oriented crystallites), the STEM image more closely approximates a projection of the thickness along the electron trajectory.

The observation that the intensity in BF-TEM images depends on the defocus of the objective lens deserves a more detailed discussion. This requires that we leave the description of a particle beam that interacts with the sample behind and use the more general concept of electron waves that was also utilized in the previous section on electron diffraction. In wave optics the electron is described by its associated wave following de Broglie's equation, i.e. the electron wavelength ($\lambda = h/p$) is given by Planck's constant (h) divided by the momentum of the electron (p). This gives wavelengths of $\lambda = 3.86$ pm for electrons accelerated in an electric potential of 100 kV and $\lambda = 2.54$ pm for 200 kV. Furthermore, the electron wave is described not only by its wavelength but also by its amplitude (a) and phase (ϕ). The interaction of an electron wave with a sample and the magnifying objective lens is sketched in Fig. 7.7.

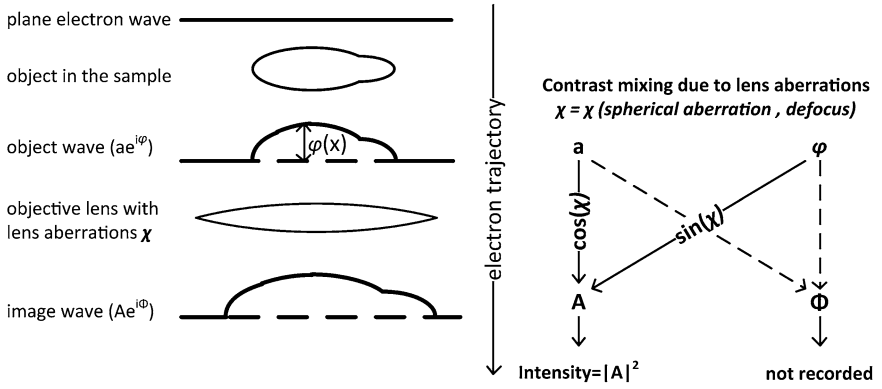

Fig. 7.7 Scheme of electron wave optics and contrast mixing

The imaging process starts with a plane electron wave ($a = 1$, $\phi = 0$ everywhere) whose phase is locally deformed or 'bent' by the sample's electromagnetic potential. This process is analogous to light travelling slower in a medium with higher refractive index, such as glass, leaving the object with a modulated wave front. Most importantly for atomic resolution TEM, the resulting object wave has a position dependent phase shift $\phi(x,y)$ imprinted on it. The amplitude and phase

information contained in the object wave is then transferred and mixed by the objective lens into the image wave. The mixing of object wave information occurs on account of the objective lens aberrations (χ) with spherical aberration and defocus being the main contributors. Since intensity ($I = |A|^2$) is only recorded in the final CCD image, tuning of the ***phase contrast transfer function*** (PCTF = sin (χ)) by choosing a suitable defocus determines the information content of the image.

Figure 7.8 further illustrates the relation between defocus and image contrast by showing images of gold and silica NPs on a carbon support film. In positive focus condition (Fig. 7.8b and light gray curve in Fig. 7.8a), phase contrast is bright (positive lobe at large feature sizes), thus competing with mass-thickness (amplitude) contrast. The modulations in the PCTF act like a filter resulting in the strange appearance of the image. When decreasing the defocus, phase contrast transfer becomes inverted (negative values equals dark objects) with the first curve minimum (−1) shifted to small feature sizes needed for atomic resolution imaging. Under such conditions objects such as the silica NP are often not seen (Fig. 7.8c) while for the gold NPs mass-thickness (amplitude) contrast dominates. Defocussing further to negative values shifts the transfer band (negative lobe at large feature sizes of black curve Fig. 7.8a) to increase the contrast of the silica NPs.

To experimentally obtain an estimate of the actual defocus, one starts by finding the focus producing minimum image contrast. To improve accuracy this should be

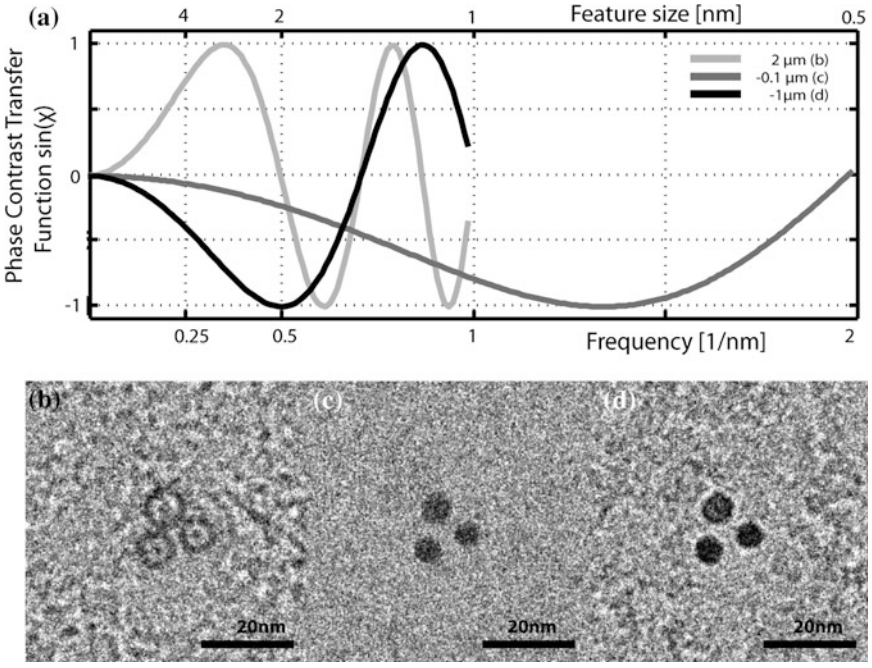

Fig. 7.8 **a** Plot of phase contrast transfer function (PCTF) for images of gold and silica NPs on a carbon film taken at, **b** 2 μm, **c** −0.1 μm, and **d** −1 μm defocus

carried out on the edge of a thin carbon film. Since minimum contrast is located within a few tens of nanometers to zero or Gaussian focus, one can reset defocus here. Decreasing focus further to negative values will then give a reasonable estimate of the applied defocus when recording images. It should be noted that at medium resolution (Fig. 7.8b, d) reducing the size of the objective aperture will increase amplitude contrast.

To conclude this section, a few comments on advanced methods using aberration correctors and monochromators. Similar to light optics, electron microscopes suffer from lens aberrations, namely spherical (Cs) and chromatic (Cc) aberration. Both aberrations can be alleviated using correctors which are classified as being either imaging correctors (TEM, placed below the sample) or probe correctors (STEM, placed above the sample). In TEM the corrector provides the flexibility to adjust both Cs and defocus for maximum information transfer from the object wave phase into the image wave amplitude. In STEM the corrector provides the flexibility to increase the probe convergence angle, thus forming focused electron beams with sub-atomic diameters. When combining an imaging and a probe corrector into a double corrected instrument even more sophisticated experiments become possible, such as confocal electron microscopy. Finally, monochromators are used to narrow the range of electron wavelengths, which is most useful for elemental analysis and is further discussed in Sect. 7.7.

7.6 Electron Tomography: 3-Dimensional Imaging

One significant feature of (S)TEM imaging is that it generates in first approximation two-dimensional (2D) images, i.e. projections, of the sample. Henceforth, sample features that overlap along the electron trajectory may not be distinguishable in 2D images since NPs and their assemblies are inherently three-dimensional (3D). To overcome these limitations ***Electron Tomography (ET)*** can be employed to determine the samples 3D morphology from a set of two-dimensional projections acquired from different directions. Tomography is a very general method that is probably best known from medical diagnostics, e.g. in CAT (computer aided tomography) scans employing 2D projections of transmitted X-rays.

The general principle underlying ET, i.e. 3D reconstruction from 2D electron micrographs, is sketched in Fig. 7.9. Starting from a 3D object, e.g. NPs or an assembly of NPs, a 2D projection is acquired using (S)TEM imaging. It is important to realize that the 2D Fourier Transform (FT) of this 2D projection is mathematically equivalent to a central 2D slice through the 3D Fourier space of the object (*note*: Fourier Transform is a coordinate transform relating real space and frequency space of an object). When combining multiple projections acquired from different directions, i.e. different tilt angles, one obtains information of the entire 3D Fourier space of the 3D object. Finally, a 3D Inverse Fourier Transform (IFT) provides us a 3D image (3D intensity map) of the object. Please note that 3D reconstruction from 2D projections does not need to be carried out in Fourier space. Actually, the most

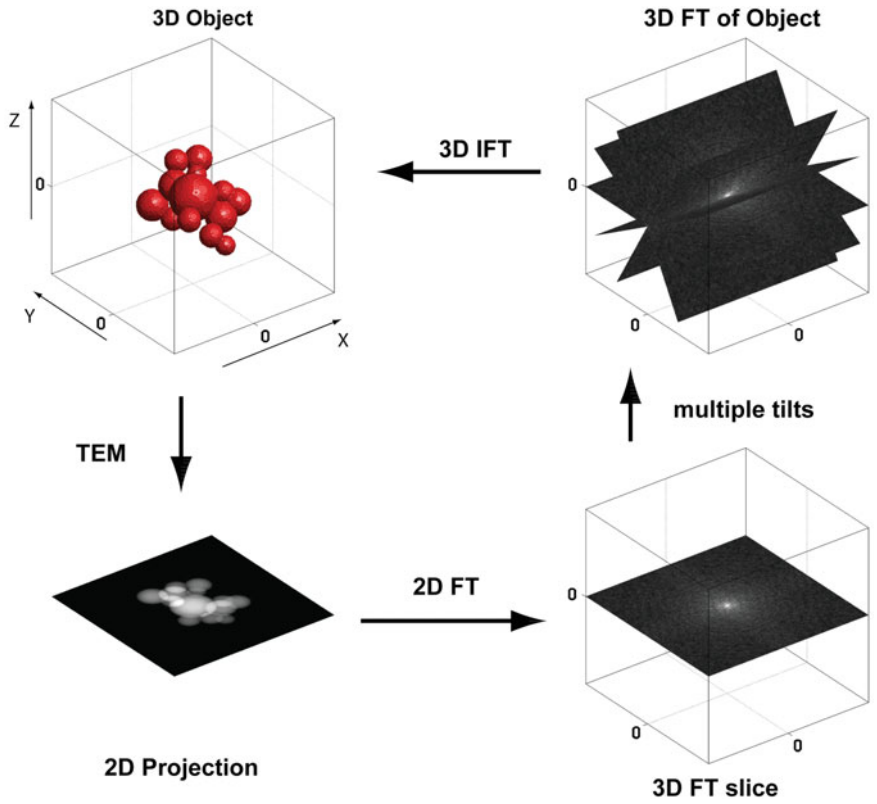

Fig. 7.9 Principle of electron tomography, i.e. 3D reconstruction from a tilt series of 2D projections. (FT stands for Fourier Transform, IFT stands for Inverse Fourier Transform.) Reprinted with permission from Ref. [7]. Copyright (2009) American Chemical Society

common reconstruction algorithms are real space algorithms namely ***back-projection*** and ***weighted back-projection***.

From an experimental point of view, one could ask how to maximize the '3D information' one can collect from a sample. Figure 7.9 clearly shows that to achieve this one should tilt to as high as possible angles with ±90° being the optimum and to tilt the sample at as small as possible increments. This intuitive relationship has been formalized into the ***Crowther criterion*** (R = πd/N) which relates the obtainable resolution (R) to the angular increment (π/Number of images) and diameter of the reconstructed volume (d). For practical reasons, such as sample damage by the electron beam, total acquisition time, and the available tilt range of the sample holder in the microscope stage, most data acquisition nowadays covers an angular range of approximately ±70° at 1° or 2° increments. The missing angular range is often referred to as "missing wedge" of information which degrades the attainable resolution in particular along the beam direction (z-axis). Sometimes, it is possible to circumvent the missing wedge, for example when using a needle-shaped specimen

pointing into free space (think of, e.g., a carbon nanotube) that can be tilted over its own axis by 360°. Another possibility is to tilt over two axes instead of one, e.g. first x-axis and then y-axis, which is frequently used in the biological sciences. Finally, images of the tilt-series require aligning with respect to each other prior to 3D reconstruction, which, if not properly done, may cause artifacts and a subsequent loss in resolution. To summarize, the resolution of a 3D reconstruction is anisotropic: the resolution along the rotation axis (x-axis) is roughly the image resolution, that along the y-axis is given by Crowthers criterion, and that along the beam direction (z-axis) is also given by Crowthers criterion with an additional factor, often referred to as elongation factor, introduced by the maximum tilt-range.

Figure 7.10 shows an example of the unique insight provided by ET. The 2D TEM image in the left side of the figure shows two NPs that have a cross-like or star-like shape, but the 3D morphology is unclear. After performing a tilt series and a 3D reconstruction (right side), the 3D shape is completely resolved, and can be viewed from any angle. It becomes then clear that the NPs are octapods, whereby 4 pods (branches) have pointy tips, while the other 4 branches have blunt tips.

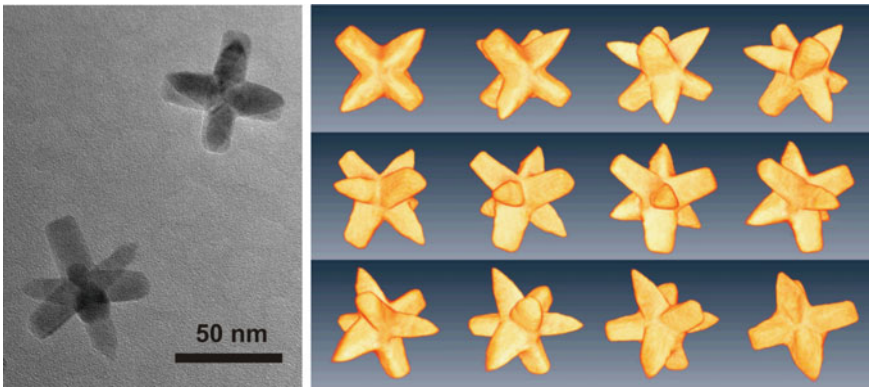

Fig. 7.10 Octapods consisting of a CdSe core and eight CdS branches (pods). In the projection into a regular TEM image (*left*), the morphology is unclear. However, after a tomographic 3D reconstruction of a single octapod (*right*), the structure can be viewed from any angle and the shape can be analyzed in detail. Adapted with permission from Ref. [8]. Copyright (2012) Wiley

A second example, shown in Fig. 7.11, illustrates the potential of ET for the analysis of assemblies of NPs. In this example, binary NP superlattices (ordered structures of two types of colloidal NPs) have been analyzed [9]. Such structures, also referred to as metamaterials, hold promise for a series of functional materials with novel collective properties. Using ET in combination with quantitative image analysis, ambiguous interpretations based on 2D TEM could be prevented, NP sizes and superlattice parameters accurately determined, individual crystallographic point and plane defects studied, and the order/disorder at the top and bottom surfaces imaged. Furthermore, the results suggested that superlattice nucleation and growth occurred at the suspension/air interface, and even that the unit cells of some lattices were anisotropically deformed upon drying. One can imagine such detailed and

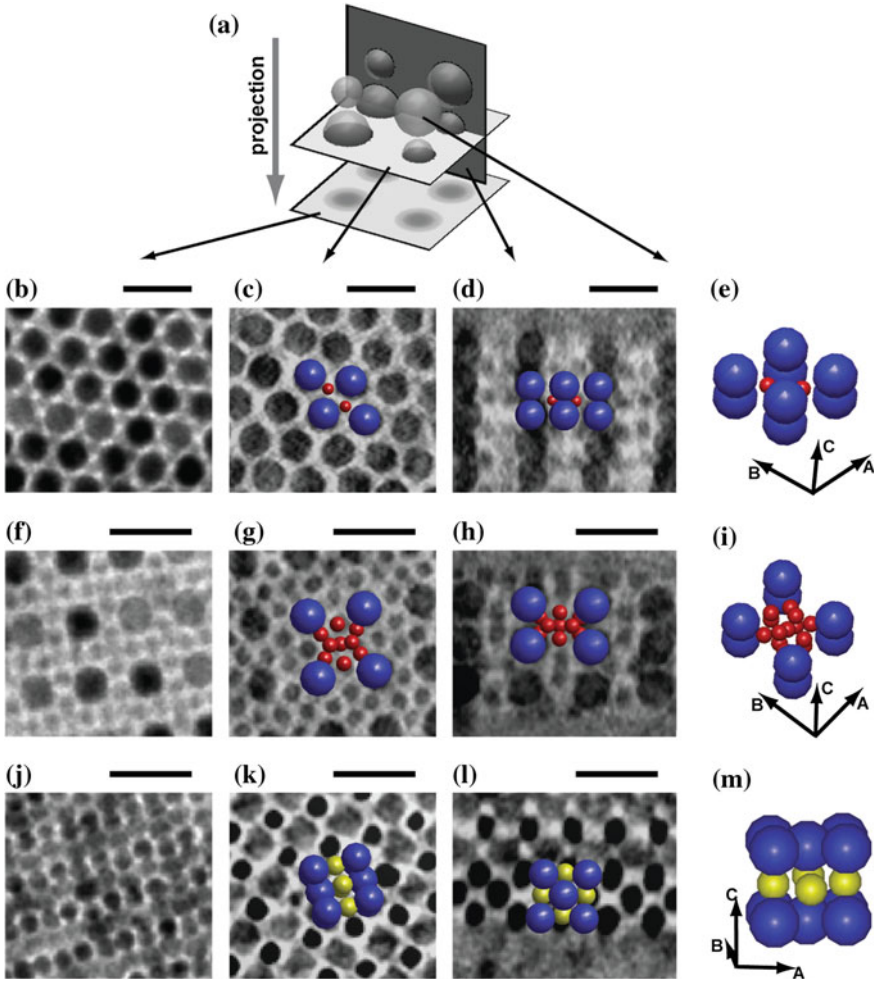

Fig. 7.11 Crystallographic analysis of binary NP superlattices with AB_2, AB_{13}, and AB stoichiometries. **a** Cartoon explaining the relationship between the panels below. TEM image (*left*), numerical cross section through 3D reconstruction (3D intensity map) parallel to imaging plane (*left center*), numerical cross section perpendicular to imaging plane (*right center*), and unit cell showing the nanocrystal cores with lattice vectors (*right*). **b–e** AB_2 superlattice of 9 nm PbSe (*blue*) and 3.4 nm CdSe NPs (*red*); **f–i** ico-AB_{13} superlattice of 8.8 nm PbSe (*blue*) and 3.8 nm CdSe (*red*) NPs (1/8th unit cell); **j–m** AB superlattice of 6.8 nm PbSe (*blue*) and 4.6 nm Au (*yellow*) NPs. Scale bars are 20 nm. Reprinted with permission from Ref. [9]. Copyright (2009) American Chemical Society

quantitative 3D information will be essential to understand and tune the emerging materials properties.

ET is also an essential technique for the analysis of catalytically active NPs inside porous carrier particles, e.g. to study the 3D distribution of the catalytic NPs

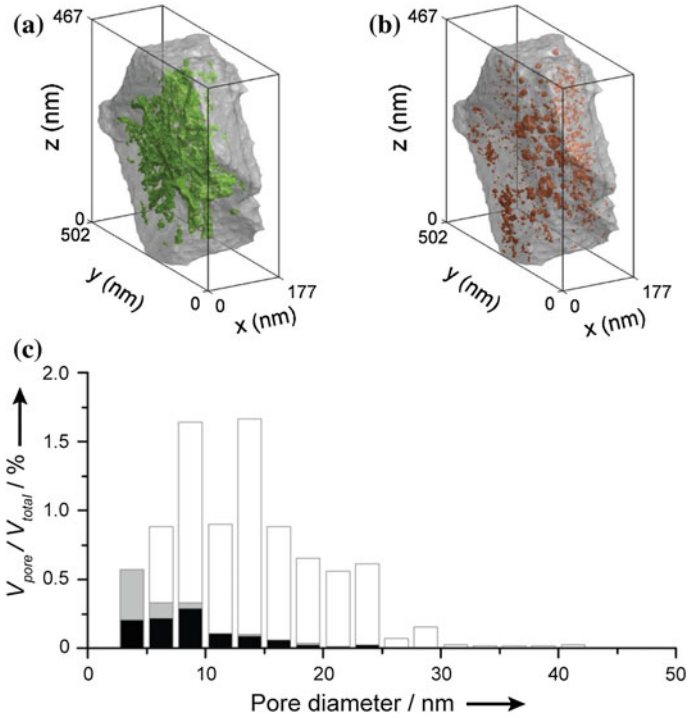

Fig. 7.12 ET analysis of porous zeolite-Y crystallite showing open mesopores in *green* (**a**), closed mesopores in *red* (**b**), and pore size distribution quantified using image processing with open mesopores (*white*), constricted mesopores (*gray*), and closed mesopores (*black*) (**c**). Reprinted with permission from Ref. [10]. Copyright (2012) Wiley-VCH

in terms of size and inter-particle spacing. Moreover, quantitative 3D analysis of the carrier particle can provide detailed information on the pore system, as illustrated in Fig. 7.12 for a zeolite-Y crystallite. This micro-porous crystallite contains mesopores that are 2–50 nm in diameter that provide 'highways' for efficient access of reaction gases or liquids to the catalytically active sites in the zeolite framework and to the catalytic NPs. Hence the morphology of the combined system needs to be known to optimize the catalysts that produce e.g. gasoline or diesel fuels.

Now that we have become acquainted with ET, it is worthwhile to discuss in more detail that (S)TEM images are only in first approximation 2D projections of a 3D structure. From a mathematical point of view ET requires ('projection requirement') that the intensity in the image is a measure of a physical parameter of the 3D object (such as the mass thickness, or the Z number), and that it does only depend on the transmitted thickness and *not* on the direction from which the image is acquired. As seen for TEM in Fig. 7.3, if the image contrast is dependent on the orientation of the magnetite crystallites with respect to the electron beam, a 3D reconstruction will contain some artifacts. Therefore, it is important to choose wisely the imaging mode wherein the 2D projections are recorded. For non-crystalline materials (most

biological materials, glasses, etc.) or for materials which do not display much diffraction contrast such as zeolites, TEM can readily be used. In contrast, for materials which display high diffraction contrast (most crystals, metals, semiconductors), HAADF-STEM is often the preferred imaging mode, as here diffraction contrast is almost eliminated and the signal depends mainly on the atomic number of the atoms in the sample (see Sect. 7.5). Nevertheless, above observation that orientation dependent diffraction contrast of NPs in TEM does not strongly effect the tomographic reconstruction (Figs. 7.10 and 7.11) can be rationalized by the fact that diffraction contrast is only present in a few images of the tilt series, while ET averages over a much larger number of images. For more details please consult Refs. [7, 11] on ET in materials science and Ref. [12] on a direct comparison of TEM and STEM ET of the magnetite NPs shown in Fig. 7.3.

Finally, we would like to note that the availability of advanced, aberration-corrected TEMs recently made it possible to perform ***atomic-resolution tomography***. Although there are currently only a few EM groups in the world who can achieve this, it is expected that this technique will be much more widely applied in the near future, enabling e.g. atomic-scale 3D reconstruction of semiconductor-semiconductor interfaces. Furthermore, it is also possible to combine tomography with chemical mapping, which will be discussed in the following Sect. 7.7. This technique requires much effort (generating chemical maps at many tilt angles, separating the chemical elements involved, followed by a 3D reconstruction per chemical element), but provides a real 3D distribution of the chemical elements. Lastly, in ET one needs to seriously consider the beam stability of the sample so that a large number of images can be acquired without damaging the object, a point that will be further discussed in Sect. 7.8 in the context of Cryo-TEM.

7.7 Analytical EM: Chemical Mapping, EDX and EELS

Amongst the many interactions whereby the high-energy electrons from the electron beam interact with the electrons in the sample, there are a number of processes that can provide chemical information about the atoms in the sample. Two of these are particularly important: the emission of characteristic *X*-rays (***energy-dispersive X-ray spectrometry*, EDX**) and the energy spectrum of electrons that have lost energy as a result of their interaction with the specimen (***electron energy loss spectrometry***, **EELS**). Two such spectra, obtained on the same material, are shown in Fig. 7.13. In general, it can be stated that EDX can be used for most chemical elements but is less sensitive to light elements (e.g., B, C, N, O).

EELS works well for a number of chemical elements, but in some cases the peaks are not distinguishable from the background. It is quite suitable for most light elements, though, and is thereby complementary to EDX analysis. In addition, EELS offers the opportunity to study plasmonic properties (whereby electrons lose their energy through interactions with plasmons) and is sometimes able to distinguish

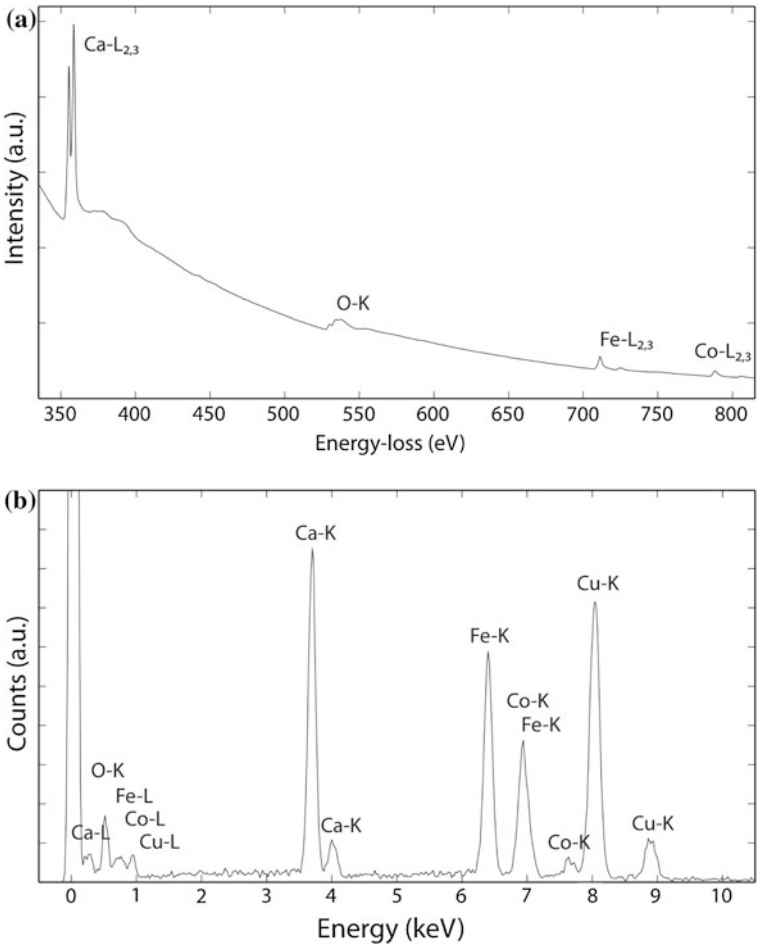

Fig. 7.13 **a** EELS spectrum and **b** EDX spectrum obtained on the same material: Ca_2FeCoO_5. There are clear differences in background and detectability of the peaks. Reprinted with permission from Ref. [13]. Copyright (2012) Wiley-VCH

between different electronic or magnetic states of the atoms (e.g., distinguishing between Fe^{2+} and Fe^{3+}, or Mn^{2+} and Mn^{3+}). Below, we will discuss EDX and EELS into more detail.

7.7.1 Energy-Dispersive X-ray Spectrometry (EDX)

Emission of a characteristic X-ray can occur after an electron from the electron beam has knocked out a core or semi-core electron from its orbit in one of the atoms in the specimen. When the vacant electronic level is filled by an electron from one

of the outer shells, the energy difference between these two electronic levels results in the emission of a photon with energies in the X-rays range. Therefore, the bombardment of target atoms with ~100 keV electrons results in the emission of many X-rays (K-, M- and L-edges in the spectra) corresponding to the filling of vacant electron levels in various electronic shells (K, L, and M shells). The energy of the X-rays is characteristic for each chemical element in the specimen. By using an electron probe (STEM mode, Sect. 7.3) and collecting an X-ray spectrum at every pixel of the image, a chemical map can be made of all atom species in the nanostructure. Such chemical maps (separate per element, and the overlapping image) are shown in Fig. 7.14 for a Au-CdSe-Au nanodumbbell and a AuS/Cd core/shell NP [14]. This technique is referred to as ***energy-dispersive X-ray spectrometry*** (abbreviated as either ***EDX*** or ***EDS***).

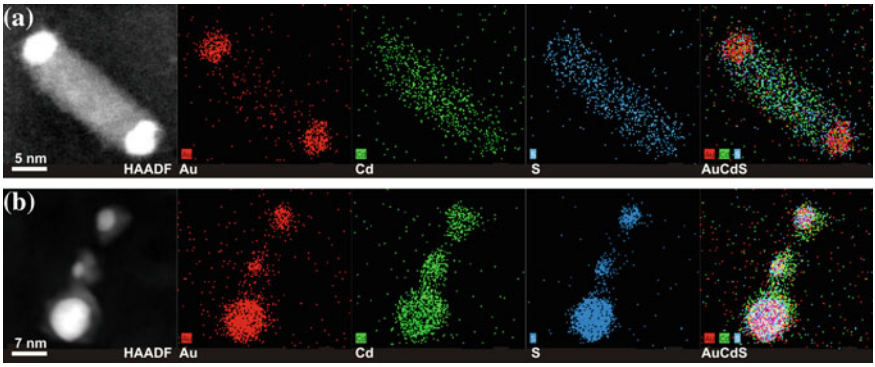

Fig. 7.14 HAADF-STEM image and EDX chemical maps (elements Au, Cd, and S) of **a** a CdSe nanorod with Au tips and **b** AuS/Cd core/shell NPs. Reprinted with permission from Ref. [14]. Copyright (2011) American Chemical Society

Please note that separate X-ray spectra such as shown in Fig. 7.13b are collected for every individual pixel of the image, and that all of these spectra have to be analyzed with X-ray spectra fitting software to translate them into the chemical composition at each pixel position. Only when fitting of the spectra has been performed for all pixels, chemical maps such as those shown in Fig. 7.14 can be obtained.

7.7.2 Electron Energy Loss Spectrometry (EELS)

While the majority of the electrons will go through the TEM specimen without having any interaction at all, a number of them will undergo elastic interactions (such a Bragg scattering, see Sect. 7.3) whereby no energy losses occur. Other electrons will undergo interactions with the target atoms whereby energy losses do occur. By analyzing the energy spectrum of the electrons that have lost energy,

certain atomic species can be identified because all atoms have a characteristic energy loss, a 'fingerprint'. This technique is referred to as ***electron energy loss spectrometry*** (**EELS**). Examples of characteristic energy loss peaks are shown in Fig. 7.13a. Please note that the peaks have a width of a few eV, which implies that an energy resolution of approximately 0.1 eV is required to resolve peaks that are in close vicinity. This is not a trivial issue, as the total energy of the electrons is typically 200,000 eV, so that the relative energy spread of the beam electrons should be approximately 10^{-6}. This is achieved with a monochromator, which is mounted directly underneath the electron source. The mono-energetic (*monochromatic*) electron beam then passes through the specimen, whereby a fraction of the electrons undergoes energy losses due to the interaction with atoms in the sample. The resulting energy spectrum at the end of the beam line is then analyzed with an EELS detector, which employs a magnetic prism. The higher the energy of the electrons, the less they are deflected in the magnetic field, which allows collecting spectra such as shown in Fig. 7.13a.

It should be mentioned that while EDX works for almost all elements, except the lightest ones, EELS only works well for particular atomic species that have a clear 'fingerprint'. Another difficulty often encountered with EELS is that the characteristic peaks of a number of elements are broad and overlapping, which makes it difficult to resolve the spectrum. Similar to the chemical mapping using EDX in STEM mode (Fig. 7.14), also chemical mapping can be performed using EELS in STEM mode (*EELS mapping*), now by analyzing the chemical composition by fitting the EELS spectra (Fig. 7.13a).

An alternative mode for chemical mapping using EELS is called ***energy-filtered TEM*** (**EFTEM**). Here the microscope is operated not in STEM mode, but in regular TEM mode, but with an energy filter somewhere in the beam line whereby only those electrons are selected that are within a certain energy window. For example, in Fig. 7.13a an energy window can be put over the Ca-L peak, so that an image is obtained that is built only from electrons that have interacted with Ca (obviously, this requires an advanced background correction which we will not discuss here).

An example of an EFTEM image is shown in Fig. 7.15. Panel (e) shows an image of an octapod whereby the energy window is set such that only electrons with zero loss (ZL) of energy are used to create the image. Panel (f) shows two overlapping images: in red the image obtained by selecting the Cu-L peak in the EELS spectrum, and in blue the image obtained by selecting the Cd-M peak in the EELS spectrum. In these octapods (NPs consisting of a CdSe core and eight CdS legs, similar to those shown in Fig. 7.10), the tips of the pods have been chemically modified to consist of a Cu-containing compound [15]. EFTEM provides direct chemical mapping of the result of these chemical modifications. EFTEM relies on the same physical principle as EELS mapping (recording EELS spectra at every pixel in STEM mode). Nonetheless, EFTEM is in general preferred over EELS mapping because it is faster in acquisition times, although this may change in the future as EELS detectors are becoming increasingly sensitive.

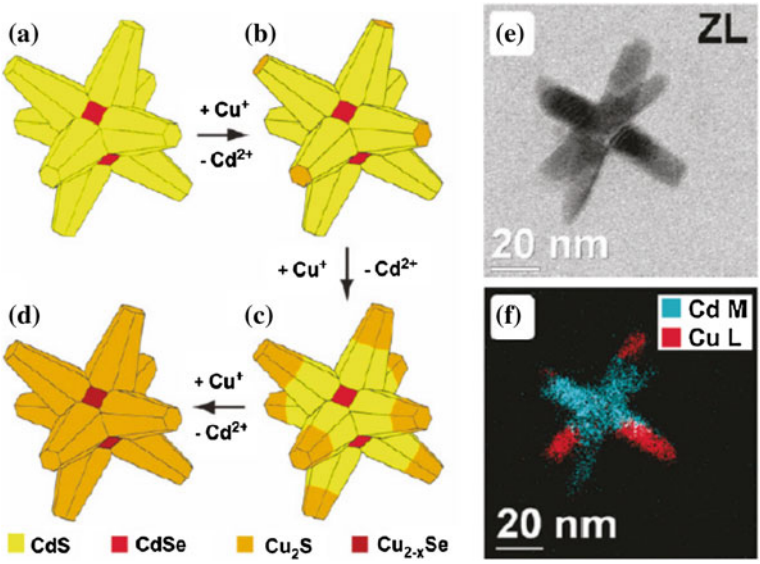

Fig. 7.15 **a–d** Schematic of the cation exchange process whereby the CdS pods of octapod-shaped particles are transformed into $Cu_{2-x}Se$. **e** EFTEM image showing the zero-loss electrons. **f** Overlapping EFTEM images showing the Cd-associated chemical map in *blue* and the Cu-associated chemical map in *red*. Reprinted with permission from Ref. [15]. Copyright (2011) American Chemical Society

7.8 Cryo-TEM: Frozen-in Nanoparticles and Their Assemblies

One topic that has not been discussed so far is the preservation state of the sample. For instance, a common preparation method for solid inorganic NPs involves the drying of suspension droplets atop an electron transparent carbon support film (Sect. 7.2.1 above). In case the NPs are stabilized and do not deform upon agglomeration, no adverse effects of the sample preparation are observed.

In case of drying of a colloidal suspension the concentration of the material will increase dramatically and may drive aggregation of existing assemblies along non-equilibrium pathways. Subsequently suspended structures will be exposed to the surface tension of the solvent, potentially leading to the collapse of aggregate structures. This may cause severe misinterpretation of actually existing NP populations. To circumvent such sample preparation artifacts, colloidal NPs should be observed in their native liquid environment. To enable observation of liquid samples inside a high vacuum electron column essentially two approaches are applied: (1) using an environmental cell holder (see the next section) or (2) cryogenic preservation of a thin film of the liquid sample.

Cryo-TEM images NPs within a solidified film of the native embedding liquid, thus preserving their respective temporal and spatial arrangement. The workflow of

Cryo-TEM sample preparation by *plunge freezing* is sketched in Fig. 7.16. First, a droplet of the solution, commonly ~ 3 μL, is applied to a perforated carbon film. The suspension not only fills the holes in the support but also covers one or both sides of the support film (panel a). Second, the support film is pressed (blotting) from both sides with filter paper which removes all excess liquid except the one contained in the holes (panel b). When the filter paper is withdrawn, some of the liquid in the holes is also removed creating slightly convex menisci. Such thin liquid films are very sensitive to drying, thus samples need to be prepared in an environmental chamber with a saturated solvent atmosphere to minimize evaporation. Third, the sample is plunged into a cryogen (panel c), e.g. liquid ethane, which very rapidly cools the sample, thus avoiding crystallization of the liquid embedding medium. Fourth, the sample is removed from the liquid ethane bath and kept at liquid nitrogen temperature during sample transfer to electron microscope and during observation (panel d). Note that blotting may induce shear stress in the liquid and, therefore, a waiting time (seconds to minutes) can be applied between blotting and vitrification, so that the film and dispersed objects can relax into their original organization. Moreover, good wettability of the carbon support film and inert filter paper are required.

While Cryo-TEM has the unique advantage of imaging NPs in their native environment, it is also prone to misinterpretation. Some of the artifacts that may

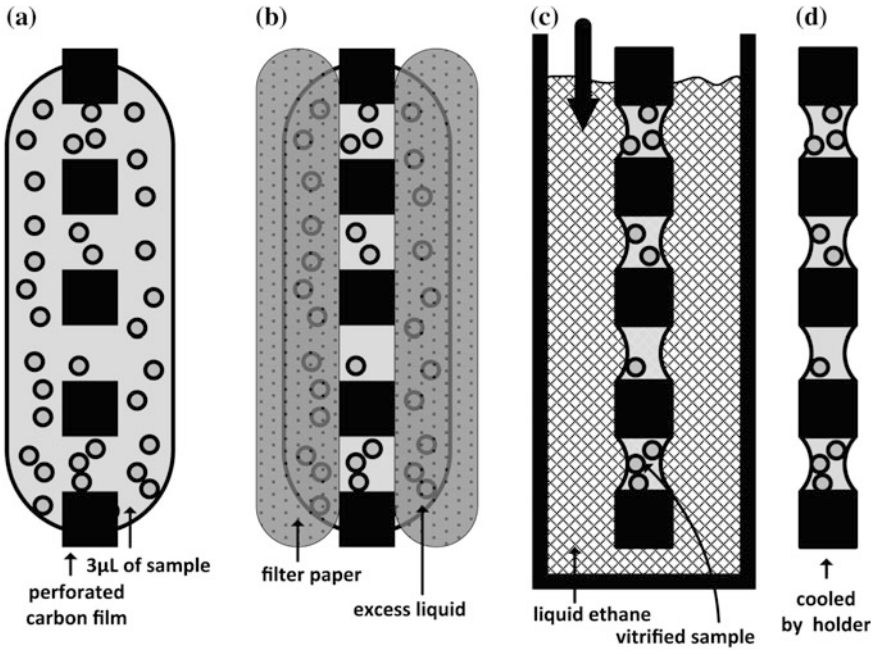

Fig. 7.16 Workflow of plunge freezing: apply sample (**a**), blotting of excess liquid (**b**), rapid cooling (**c**), cryo transfer and imaging (**d**)

arise when trying to vitrify aqueous suspensions are displayed in Fig. 7.17. Panel (a) shows a polymer aggregate that is embedded in hexagonal ice (indicative of too low cooling speed during vitrification) appearing as dark bands throughout the image. In the case of cubic ice, high contrast objects seemingly appear as illustrated in (panel b), which is indicative of a temperature increase above −140 °C (recrystallization temperature of cubic ice) during sample transfer. Moreover, ice particulates from ambient air or contamination from the liquid ethane (see panel c) may be deposited during sample transfer to the microscope column. Finally, the most important cause of artifacts and sometimes misinterpretation is electron-beam-induced radiation damage (panel d).

All organic specimens, and under high magnification most inorganic specimens, degrade as a result of the impact of the high-energy electrons. The dissipation of the electron energy gives rise to chemical reactions and rearrangements during image

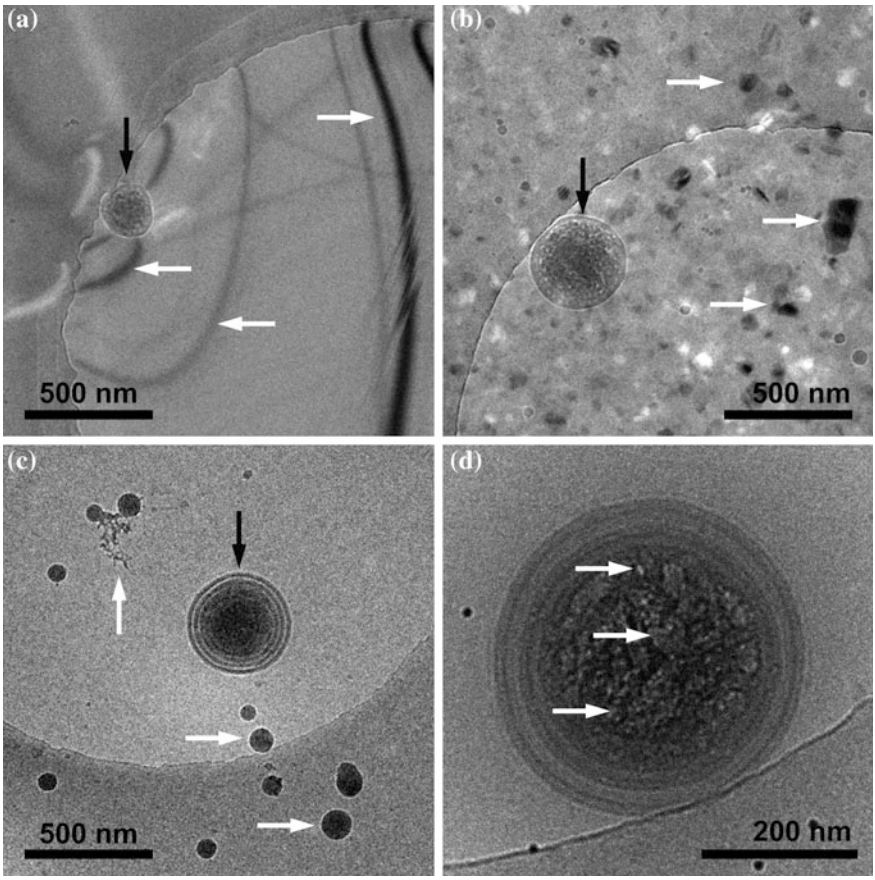

Fig. 7.17 Polymer aggregate (*black arrows*) and Cryo-TEM artifacts (*white arrows*) showing hexagonal ice (**a**), cubic ice (**b**), ethene and ice contamination (**c**), and beam damage (**d**)

acquisition. Therefore, low-dose imaging is mandatory which utilizes a "safe" predetermined electron dose (number of electrons per square nanometer) for each image so that the required information can be extracted before the specimen is altered. For cryo electron tomography even more stringent dose requirements apply.

To conclude this section, it is worth mentioning that Cryo-TEM is a rapidly growing field of materials science. One of the driving forces is that investigations of solution borne nanostructures are extendable to organic solvents. Note that organic solvents may be even more susceptible to beam damage than water or the embedded NPs. Finally, the conclusions drawn from the experiments fully depend on the careful interpretation of the data. Hence, complicated sample preparation and advanced imaging techniques may not be required if one can establish that the observed features are without doubt the result of the solution chemistry rather than of the procedures used to obtain the images. Further details can be found in two reviews of the subject [16, 17].

7.9 In situ TEM: Gas Exposure and Heating

One major challenge, and a fast developing sub-field of electron microscopy, is in situ TEM: performing physical and chemical experiments *inside* the electron microscope while watching. For example, long before "nanoscience" emerged as a research field, catalytic NPs were already used in the catalysis industry, e.g. to crack hydrocarbons in oil refineries. It is possible, of course, to let these particles do their work at high temperatures and high pressures, and examine them afterwards to investigate what happened to the samples. The issue at hand is that the NPs that are studied afterwards are no longer the same NPs that were catalytically active at high pressures and high temperatures. Therefore, what is really required is to replicate these conditions inside the electron microscope.

There are many possible experiments that can be performed in the EM, for example illumination with lasers, ion beam implantation, examination of particles in liquids and fluids, passing electrical current through the specimen, exposure to magnetic fields, mechanical testing such as bending and tensile testing, correlative light and electron microscopy (CLEM) whereby a light microscope and an electron microscope are combined in one apparatus, etc. As this chapter does not intend to be exhaustive, we selected two popular in situ methods for further discussion: gas exposure and heating experiments.

7.9.1 In Situ Gas Exposure

Studying NPs while being exposed to gases usually takes place in a specially designed microscope: the *environmental TEM (E-TEM)*. There is a low gas pressure ($\sim 10^{-3}$ bar) present at the position of the specimen. The presence of gas degrades

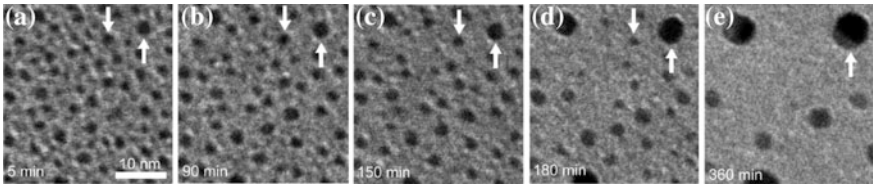

Fig. 7.18 Pt NPs on an Al_2O_3 support, ripening in time under the influence of an oxygen atmosphere (10 mbar air at 650 °C). Shrinkage and growth of NPs is indicated with *white arrows* to guide the eye. Adapted with permission from Ref. [18]. Copyright (2010) American Chemical Society

the resolution of the microscope, because the electrons have to travel through a long volume containing gas molecules, where they interact with gas molecules instead of the NP under investigation. Therefore, a differential pumping system is installed which maintains the pressure in the direct vicinity of the specimen, but restores the vacuum in the rest of the column so that at the top (where the electron source is), the vacuum is of very high quality. A nice demonstration of E-TEM is shown in Fig. 7.18. Here catalytic Pt NPs supported on alumina are ripening in the presence of an oxygen-rich gas (air). During heating at a temperature of 650 °C in this environment, bigger particles grow at the expense of smaller ones. The size distribution of the particles thus obtained depends on the particular gas atmosphere [18]. While in E-TEM pressures are limited to the mbar range, much higher pressures (~ 1 bar) can be obtained when using gas cells, whereby the gas is confined in a very thin volume between two membranes. In either case, there is always a risk that the electron beam creates ionizations in the gas which affect the experiments. Therefore, in E-TEM it is a standard procedure to vary the intensity of the electron beam in order to verify that it does not have a strong influence on the observations.

7.9.2 In Situ Heating

As many materials are processed and manipulated by means of heating, also this in situ method is very popular. Apart from conventional heating holders whereby the whole TEM support is heated by a surrounding ceramic oven, recently microhotplates based on MEMS (microelectromechanical systems) technology have emerged as a preferred means to perform in situ heating experiments. One major issue with heating is thermal drift. The heat that is produced in the sample area, spreads to the sample holder itself (typically 30–40 cm in length), which then thermally expands. While this is a very minimal effect from a macroscopic point of view (the linear thermal expansion coefficient of most metals is in the order of $10^{-6}\,K^{-1}$), when zooming into the nanoscale this means that the specimen is moving so fast that the image is completely blurred and that high resolution is not achievable. The miniaturization of the experiment is a solution to this problem: only the direct

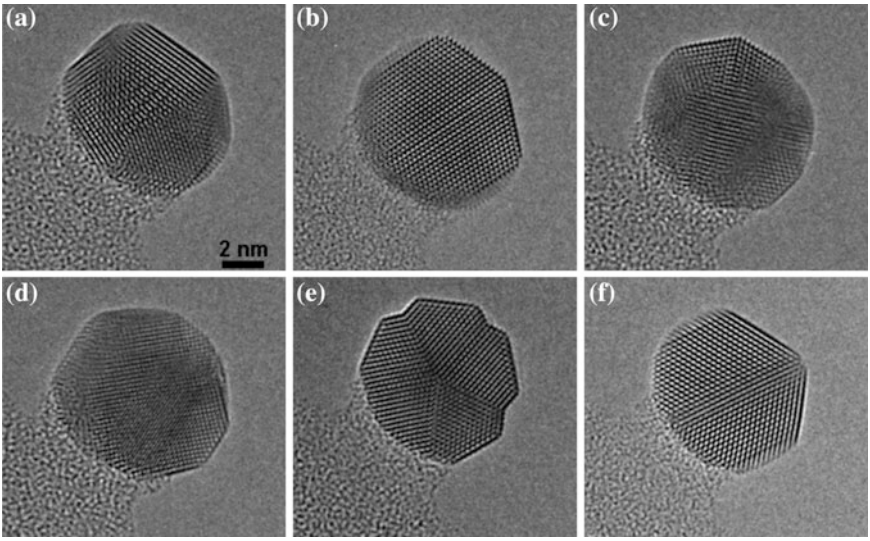

Fig. 7.19 Heating experiment performed in the TEM, whereby a 9-nm sized Au NP transforms from one morphology at elevated temperature: 415 °C in panels (**a**–**d**), 450 °C in panels (**e**, **f**). Reprinted with permission from Ref. [19]. Copyright (2010) Elsevier

environment of the NPs is heated to a certain temperature. The total heat dissipation of this microscale experiment is so small that the heating holder itself does not heat up significantly, thereby minimizing thermal drift issues.

Figure 7.19 shows a nice example of a gold NP at an elevated temperature of approximately 450 °C. It is clear that the NP swaps from one morphology to another. Sometimes the particle displays a single crystal (panel d), but is also found in multiply twinned particle (MTP) configurations (panels a, b, c, e, f). Usually NPs will not change their morphology at room temperature: there is an energy barrier that needs to be crossed. At elevated temperatures, however, there is sufficient kinetic energy available to cross these barrier and to 'hop on the morphology-dependent energy landscape'. The lower melting points of NPs with respect to the bulk materials can also be studied in detail with these in situ experiments.

7.10 Outlook: Quantitative and Dynamic EM

Recent developments in the field of EM now emphasize more and more the quantitative aspect of experimentation and analysis. This means that electron microscopes have evolved from powerful magnifying tools that provide images to extremely versatile measurement devices that provide structural, chemical, electronic, or magnetic information down to the atomic scale. For example, in Fig. 7.1e above bright spots are visible that represent columns of atoms. By analyzing the

intensity of the atomic columns the number of atoms in each column was estimated. By combining the information from just three such analyses, looking at the sample from different directions, an atomic resolution 3D reconstruction of the PbSe core within the CdSe rod-shaped shell was obtained [5]: an excellent example of quantitative EM (QEM). Also the analysis of the 3D inter-particle spacing and ordering in NP superlattices (Fig. 7.11, [9]); or the determination of the pore structure and connectivity (Fig. 7.12, [10]) are examples of QEM.

A second direction of EM development that now evolves rapidly is in situ experimentation, dynamic TEM (DTEM) and ultrafast electron diffraction (UED). This means that experiments that were previously performed outside the electron microscope (ex situ) are now redesigned to be performed inside the TEM, so that structural and chemical changes during materials assembly or operation, (e.g., catalysts) can be followed in real time and under realistic application conditions. The dynamic aspect of EM is introduced by using very short electron pulses for imaging (DTEM) or diffraction (UED). Both DTEM and UED allow observing the transient behavior during e.g. a chemical reaction or a phase transformation and will in the future bring significant advance in our conception of the basic phenomena of physics, chemistry, and biology.

Furthermore, a point that has been hardly addressed in this chapter on account of size limitations, the impact of calculation and simulation methods becomes increasingly important. For instance, to analyze EELS spectra it is often required to be guided by quantum mechanical calculations which predict the 'fingerprint' of the chemical elements. Also, imaging simulations are often required to fully understand and interpret the contrast in TEM images. Finally, as the field of nanoscience and nanotechnology continues to develop from *describing* to *understanding* to *designing* [13], also TEM will develop as indispensable characterization method; its contribution cannot be overestimated.

7.11 Exercises

1. What would you use for imaging of nanoparticles, layers or aggregates thereof, SEM or TEM? Explain your choice depending on size, composition, and state of the material.
2. Assume you have NPs present in suspension or as a composite, i.e. embedded in a matrix such as a polymer, how would you prepare your sample for TEM or SEM? Why?
3. What would be necessary requirements for a EM sample support film? Suggest commonly used examples.
4. What kind of samples would be sensitive to charging effects by the electron beam? What solutions can you propose to resolve this issue?
5. You are given a mixture of nanoparticles and have to determine which are crystalline and which are amorphous. How would you do it? Give two alternative approaches using EM.

6. In case you do not clearly see the nanoparticles in bright-field TEM images, what can you do to increase image contrast? Can you think of three alternatives? Would you think that annular dark-field STEM imaging can help?
7. For the octapods shown in Fig. 7.10, calculate the resolution defined by the Crowther criterion (Sect. 7.5) for 3D reconstructions based on tilt series over ±60° and ±80° with increments of 1°, 2°, and 5°.
8. What would be the best way to analyze Pt NPs inside a nanoporous zeolite support (consisting mainly of Si, Al and O)? TEM or STEM? EDX or EELS? Explain why and discuss advantages and disadvantages.
9. What problems can you expect when you put a liquid sample (contained by two thin sealing membranes) in the path of the electron beam in an EM?
10. What other experiments can you think of that can be performed in situ in the TEM? What are the challenges in those cases?
11. Assume you would like to carry out a time-resolved experiment in the EM. What limits your time resolution and how could you improve it?

References

1. Williams, D.B., Carter, C.B.: Transmission Electron Microscopy—A Textbook for Materials Science, 2nd edn. Springer, USA (2009)
2. van Tendeloo, G., van Dyck, D., Pennycook, S.J. (eds.): Handbook of Nanoscopy. Wiley-VCH, Weinheim (2012)
3. Yalcin, A.O., Fan, Z., de Nijs, B., Tichelaar, F.D., van Blaaderen, A., Vanmaekelbergh, D., van Huis, M.A., Zandbergen, H.W.: unpublished results
4. Velikov, K.P., van Blaaderen, A.: Synthesis and characterization of monodisperse core-shell colloidal spheres of Zinc Sulfide and Silica. Langmuir **17**, 4779–4786 (2001)
5. Bals, S., Casavola, M., van Huis, M.A., van Aert, S., Batenburg, K.J., van Tendeloo, G., Vanmaekelbergh, D.: 3D atomic imaging of colloidal core-shell nanocrystals. Nano Lett. **11**, 3420–3424 (2011)
6. Lenders, J., Dey, A., Friedrich, H., de With, G., Sommerdijk, N.: unpublished results
7. Friedrich, H., de Jongh, P.E., Verkleij, A.J., de Jong, K.P.: Electron tomography for heterogeneous catalysts and related nanostructured materials. Chem. Rev. **109**, 1613–1629 (2009)
8. Goris, B., van Huis, M.A., Bals, S., Zandbergen, H.W., Manna, L., Van Tendeloo, G.: Thermally induced structural and morphological changes of CdSe/CdS octapods. Small **8**, 937–942 (2012)
9. Friedrich, H., Gommes, C.J., Overgaag, K., Meeldijk, J.D., Evers, W.H., de Nijs, B., Boneschanscher, M.P., de Jongh, P.E., Verkleij, A.J., de Jong, K.P., van Blaaderen, A., Vanmaekelbergh, D.: Quantitative structural analysis of binary nanocrystal superlattices by electron tomography. Nano Lett. **9**, 2719–2724 (2009)
10. Zečević, J., Gommes, C.J., Friedrich, H., de Jongh, P.E., de Jong, K.P.: Mesoporosity of Zeolite Y: quantitative three-dimensional study by image analysis of electron tomograms. Angew. Chem. Int. Ed. **51**, 4213–4217 (2012)
11. Midgley, P.A., Dunin-Borkowski, R.E.: Electron tomography and holography in materials science. Nat. Mater. **8**, 271–280 (2009)

12. Friedrich, H., McCartney, M.R., Buseck, P.R.: Comparison of intensity distributions in tomograms from BF TEM, ADF STEM, HAADF STEM, and calculated tilt series. Ultramicroscopy **106**, 18–27 (2005)
13. Van Tendeloo, G., Bals, S., Van Aert, S., Verbeeck, J., Van Dyck, D.: Advanced electron microscopy for advanced materials. Adv. Mater. **24**, 5655–5675 (2012)
14. van Huis, M.A., Figuerola, A., Fang, C.M., Béché, A., Zandbergen, H.W., Manna, L.: Chemical transformation of Au-tipped CdS nanorods into AuS/Cd core/shell particles by electron beam irradiation. Nano Lett. **11**, 4555–4561 (2011)
15. Miszta, K., Dorfs, D., Genovese, Al, Kim, M.R., Manna, L.: Cation exchange reactions in colloidal branched nanocrystals. ACS Nano **5**, 7176–7183 (2011)
16. Friedrich, H., Frederik, P.M., de With, G., Sommerdijk, N.A.J.M.: Imaging self-assembled structures: the interpretation of TEM and cryo-TEM images. Angew. Chem. Int. Ed. **49**, 7850–7858 (2010)
17. Cui, H., Hodgdon, T.K., Kaler, E.W., Abezgauz, L., Danino, D., Lubovsky, M., Talmon, Y., Pochan, D.J.: Elucidating the assembled structure of amphiphiles in solution via cryogenic transmission electron microscopy. Soft Matter **3**, 945–955 (2007)
18. Simonsen, S.B., Chorkendorff, I., Dahl, S., Skoglundh, M., Sehested, J., Helveg, S.: Direct observations of oxygen-induced platinum nanoparticle ripening studied by in situ TEM. J. Am. Chem. Soc. **132**, 7968–7975 (2010)
19. Young, N.P., van Huis, M.A., Zandbergen, H.W., Xu, H., Kirkland, A.I.: Transformation of gold nanoparticles investigated using variable temperature high-resolution transmission electron microscopy. Ultramicroscopy **110**, 506–516 (2010)

Chapter 8
Scanning Probe Microscopy and Spectroscopy

Peter Liljeroth, Bruno Grandidier, Christophe Delerue and Daniël Vanmaekelbergh

Abstract This chapter shows how scanning tunneling microscopy and spectroscopy and atomic force microscopy can be used to measure the properties of individual nanocrystals, thereby circumventing the limitations of ensemble based measurements.

8.1 Introduction

Optical and electrical spectroscopies are typically used to explore the properties of colloidal semiconductor nanocrystals (NCs) and their self-assembled structures. Since these techniques have a limited spatial resolution, they provide sample-averaged results. Due to the inherent variation of size and shape of the nanocrystals and thus of their electronic spectrum, it would be desirable to measure the properties of individual nanocrystals as single quantum objects. This is made possible by advanced scanning probe techniques, in particular low-temperature scanning tunneling microscopy (STM) and spectroscopy (STS) and atomic force microscopy (AFM), as they measure the topography and electronic structure with sub-nanometer spatial resolution. We will show in this chapter how STM/STS can be used to carry out single-electron transport experiments on individual NCs enabling one to study the quantum confined energy levels of single nanocrystals. We will first

P. Liljeroth
Department of Applied Physics, Aalto University School of Science,
PO Box 15100, 00076 AALTO, Finland

P. Liljeroth · D. Vanmaekelbergh
Condensed Matter and Interfaces, Debye Institute for Nanomaterials Science,
PO Box 80000, 3508 TA Utrecht, The Netherlands

B. Grandidier (✉) · C. Delerue
Département ISEN, Institut d'Electronique, de Microélectronique et de Nanotechnologie
(IEMN), CNRS, UMR 8520, 41 Bd Vauban, 59046 Lille Cedex, France
e-mail: Bruno.Grandidier@isen.iemn.univ-lille1.fr

C. de Mello Donegá (ed.), *Nanoparticles*,
DOI 10.1007/978-3-662-44823-6_8

introduce the basic physical principles of STM and STS. Then, we will focus on a number of examples illustrating how the electronic properties of colloidal NCs and hetero-nanostructures have been measured, how quantum mechanical coupling between NCs has been detected, and how the addition of single charge carriers can be detected by AFM.

8.2 Basics of Scanning Probe Microscopy and Spectroscopy of Colloidal Quantum Dots

8.2.1 Why Perform Microscopy and Spectroscopy on Single Nanocrystals?

One of the long-term goals of nanoscience is to establish a direct relationship between the structure of a nano-object (molecule, nanocrystal) and its electronic properties and optical and electrical functions. In addition, in self-assembled superstructures, one would like to connect the properties of individual building blocks to the macroscopic, collective behavior of the entire structure. In the case that we consider here (colloidal nanocrystals, NCs), one would like to establish the relation between the structure (atomic lattice, surface chemistry, size and shape) of the NC and its energy levels and optical properties.

Considered on the atomic scale, colloidal semiconductor NCs are, in fact, large objects: they have a diameter between two and ten nanometers and contain about a thousand to a hundred thousand atoms. Due to the tremendous progress in wet chemical synthesis (see Chap. 6), it has become possible not only to control the size and shape of the colloidal nanoparticles, but also to synthesize nanoparticles that consist of two or more crystalline compounds joined by hetero-interfaces. The atomic landscape of such hetero-NCs can be quite complex. For instance, a core/shell system consists of a core NC surrounded by a second crystalline compound (the shell), which is itself covered with organic capping molecules (see Chap. 6). Such an organically capped core/shell system already contains two chemical types of interfaces.

In contrast to molecules, colloidal NCs are—considered on the atomic scale—all a little different. In the best cases, the size dispersion is about 5 % and small variations in the shape also occur. Since the energy levels are determined by quantum confinement (see Chap. 2), this size-dispersion translates into a variation in the energy levels of each NC. This means that optical and electrical spectroscopy on ensembles of NCs (dispersed or self-assembled in a superlattice) will provide results that are broadened by the intrinsic structural variations (inhomogeneous broadening).

A more direct relationship between the structure of a nanocrystalline quantum dot and its electronic properties can be obtained by performing spectroscopy on a single dot. In the case of single-dot optical spectroscopy, it means that the NCs are attached to a substrate in a very dilute form, such that luminescence from a single

NC can be optically resolved. The luminescence, however, provides only an indirect and incomplete picture of the energy levels (see below). Alternatively, colloidal NCs can be attached on a conducting substrate and investigated one-by-one in a scanning tunneling microscope set-up. Below, it will be shown how the (overall) shape and size of each NC can be determined by scanning tunneling microscopy and how measuring the tunneling current between the tip electrode (on top of a NC) and the substrate provides the energy levels of the NC under investigation in a very direct way.

8.2.2 Scanning Tunneling Microscopy and the Double-Barrier Tunnel Junction

In order to perform single-dot microscopy and spectroscopy, the NCs which are naturally present in a colloidal suspension have to be deposited as single NCs or a monolayer array on an atomically flat conducting substrate. This is commonly performed by either binding individual NCs onto the substrate using chemical linkers or by drop-casting the suspension on a clean surface resulting in a self-assembled close-packed NC monolayer array (see, Sect. 8.2.6). More experimental details and examples of these architectures will be shown below. Subsequently, the substrate is loaded in the ultra-high vacuum (UHV) system. Annealing at low temperatures (<150 °C) in UHV is used to evaporate undesired molecules and to obtain reasonably clean systems. After that, STM or AFM imaging can be performed to investigate the size and shape of the individual NCs, and their packing in NC assemblies. Finally, the energy levels are commonly measured by stabilizing the STM tip at a fixed position and height above the NC of interest and acquiring the tunneling current (I) as a function of the bias (V_b) between the tip and substrate electrodes. Below, we will discuss in detail what can be learned from the tunneling spectrum, $I(V_b)$ and $dI(V_b)/dV_b$.

Hence, during STM or AFM, the tip/NC/substrate system forms a double-barrier tunnel junction (DBTJ) geometry illustrated in Fig. 8.1a [1–5]. The same DBTJ is shown as an energy diagram in Fig. 8.1 b, c. When there is no or only a small applied bias, the Fermi levels of the tip and substrate are located in the energy gap between the HOMO (first valence hole level) and the LUMO (first conduction electron level) of the semiconductor NC. This means that current transport is not possible since, due to the distance, direct tunneling between the tip and substrate does not occur at an appreciable probability. When a sufficiently positive (negative) bias voltage is applied between the tip and the substrate, the Fermi level of the tip can become resonant with the LUMO (HOMO) of the NC as illustrated in Fig. 8.1b, c. This leads to the opening of a resonant tunneling channel resulting in a step increase in the measured current at a given bias V_b. Steps in the current correspond to peaks in the derivative dI/dV_b versus V_b. By applying a small AC bias, the derivative can also be directly measured, which enhances sensitivity to small features in the spectra.

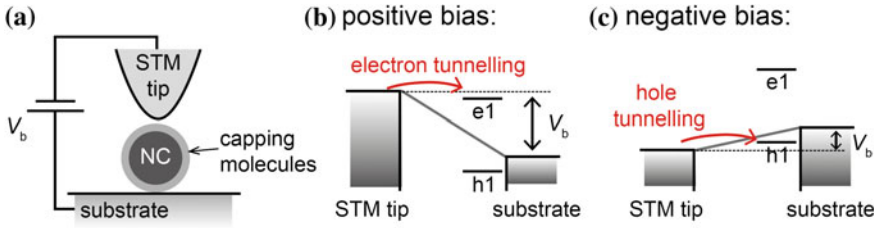

Fig. 8.1 **a** Schematic illustration of the double-barrier tunnel junction formed in the STM tip—NC—substrate junction. A bias voltage is applied between the sample and the tip. **b** Electron tunneling through the lowest conduction level e1 at positive bias polarity. **c** Hole tunneling through the highest valence level h1 at negative bias

Further increase in the bias voltage causes no changes in the current until the next quantum-confined energy level becomes resonant with the tip Fermi level. Consequently, the steps in the measured current versus the applied bias voltage, $I(V_b)$, or the peaks in the $dI(V_b)/dV_b$, can be used to deduce the positions of the quantum confined energy levels of the nanostructure under the STM tip [1, 2, 4, 5]. Below, we will focus in more detail on what kind of information can be obtained from the measurement of such conductance spectra on semiconductor NCs.

Electron transport from the STM tip into the substrate involves two steps: tunneling between the tip and the NC, and between the NC and the substrate. The intrinsic rates of these steps are denoted as Γ_{in} and Γ_{out}, respectively. In the STM configuration, the capacitance and tunneling rate between the NC and the substrate are fixed by the nature and width of the barrier. On the other hand, the tunneling rate between the tip and the NC can be modified by changing the width of the tip/dot tunneling barrier, i.e., moving the tip vertically. As a matter of fact, the double-barrier tunneling junction is typically rather asymmetric: the tip/dot barrier has the largest width and hence smallest capacitance resulting in most of the applied bias dropping between the tip and NC; this barrier also limits the current, i.e. $\Gamma_{in} << \Gamma_{out}$.

In the regime where $\Gamma_{in} << \Gamma_{out}$ [the shell-tunneling regime, Fig. 8.2a], a single electron tunnels from the tip to the NC and leaves the NC before a second electron arrives [2, 5]. This means that the number of added electrons in the NC at any given time is either 0 or 1 and repulsions between tunneling electrons are absent. In the opposite limit, where $\Gamma_{in} >> \Gamma_{out}$ [the shell-filling regime, Fig. 8.2b], electrons accumulate in the NC and the number of added electrons depends on the bias voltage. We remind that shell-tunneling conditions are common practice, while spectroscopy in the shell-filling regime requires that the tip is brought very close to the NC under investigation.

In the shell-tunneling regime, the first resonance is observed when the bias is sufficient to align the tip Fermi level with the first electron level of the NC:

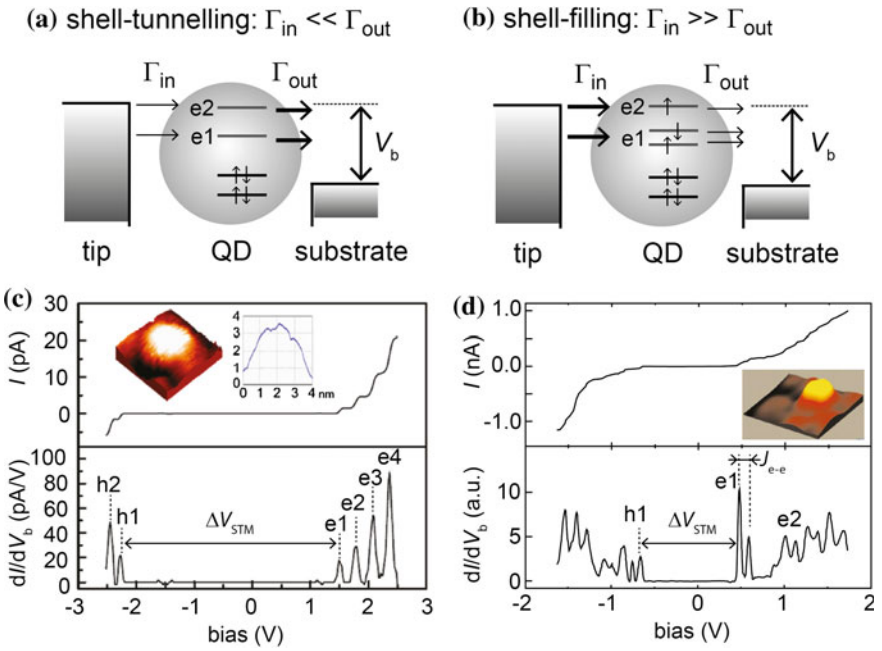

Fig. 8.2 Different limiting cases of tunneling spectroscopy on NCs. Schematics of (**a**) shell-tunneling and (**b**) shell-filling spectroscopy. Experimental spectra acquired (**c**) on a CdSe NC in shell-tunneling regime [6], and (**d**) on an InAs NC under shell-filling conditions [4]. Panel (**c**) is adapted with permission from [6], Copyright (2006) American Physical Society. Panel (**d**) is reprinted from [4] by permission from Macmillan Publishers Ltd., copyright (1999)

$$\eta e V_b = E_{e1} + \Sigma_{e1} - E_F \tag{8.1}$$

where E_{e1} is the energy of the lowest unoccupied electron level and the parameter η quantifies the potential distribution in the DBTJ. η is defined as the potential drop between the tip and the NC divided by the overall applied bias. We will discuss how to estimate this parameter in the following; for the moment it suffices to state that under shell-tunneling conditions η is close to 1. Σ_{e1} (>0) denotes the electrostatic polarization energy (charging energy) associated with adding one electronic charge to the NC (Sect. 8.2.3) [5, 7–9]. E_F is the energy of the substrate Fermi level. Analogously, the first hole will be added when:

$$\eta e V_b = E_{h1} - \Sigma_{h1} - E_F \tag{8.2}$$

where E_{h1} is the energy of the highest occupied hole level and the charging energy Σ_{h1} is positive as for the electron [5, 7–9].

The STM transport gap, i.e. the bias voltage range where no current flows, is given by:

$$\eta e \Delta V_{\mathrm{STM}} = E_{\mathrm{e1}} - E_{\mathrm{h1}} + \Sigma_{\mathrm{e1}} + \Sigma_{\mathrm{h1}} \approx E_{\mathrm{e1}} - E_{\mathrm{h1}} + 2\Sigma \tag{8.3}$$

where the approximation $\Sigma_{e1} + \Sigma_{h1} \approx 2\Sigma$ is good as the polarization energy is not sensitive to the exact shape of the wavefunction ($E_{e1} - E_{h1} + 2\Sigma$ is often referred to as the *quasi*-particle gap of the NC).

Tunneling into the second electron level will occur if the bias is increased to:

$$\eta e V_{\mathrm{b}} = E_{\mathrm{e2}} + \Sigma_{\mathrm{e2}} - E_F \tag{8.4}$$

The spacing between the first and the second peak at positive bias in the shell-tunneling regime then directly gives the energy separation (divided by the potential distribution factor), as the polarization energies Σ_{e1} and Σ_{e2} are equal to a good approximation [2, 7, 8]. These factors are all illustrated in the experimental spectra measured on a CdSe NC under shell-tunneling conditions shown in Fig. 8.2c. [6] Since repulsions are absent, the first and second resonances indicate fundamentally different sets of energy levels with S and P envelope functions. The peak positions are not affected by the (different) degeneracies of the levels.

What is the experimental signature of shell-tunneling? Changing the set-point (i.e., bringing the STM tip closer to the NC), does not cause major changes in the spectra, apart from increasing the intensity of all peaks in the same proportion. When the tip is brought closer, also the potential distribution is changed slightly, which means that the resonance peaks can be slightly shifted to higher bias values (see Sect. 8.3.4).

In the case of shell-filling, i.e. $\Gamma_{\mathrm{in}} >> \Gamma_{\mathrm{out}}$, the first electron addition occurs at the same energy as in the case of shell-tunneling. However, in contrast to shell-tunneling, as the bias is increased, a second electron is added to the level e1 (which is two-fold spin degenerate) if:

$$\eta e V_{\mathrm{b}} = E_{\mathrm{e1}} + \Sigma_{\mathrm{e1}} + J_{\mathrm{e-e}} - E_F \tag{8.5}$$

where $J_{e\text{-}e}$ is the electron-electron repulsion between the added electrons (we neglect spin-interactions since they are small) [3, 5, 7–9]. A third electron is added when:

$$\eta e V_{\mathrm{b}} = E_{\mathrm{e2}} + \Sigma_{\mathrm{e2}} + 2J_{\mathrm{e-e}} - E_F \tag{8.6}$$

These features are illustrated in Fig. 8.2d, which shows experimental results on an InAs NC obtained under shell-filling conditions [4]. The experimental signature of complete shell-filling would be that the current through the NC cannot be further increased by moving the tip closer as the tunneling rate between the NC and the substrate controls the overall current [10]. The spectra should show sets of resonances that reveal the degeneracy of the levels E_{e1} (two-fold), E_{e2} (two, four or six-fold depending on the NC shape). In practice, the shell-filling regime is difficult to reach and the spectra can be obscured by instabilities of the tunnel junction, strong

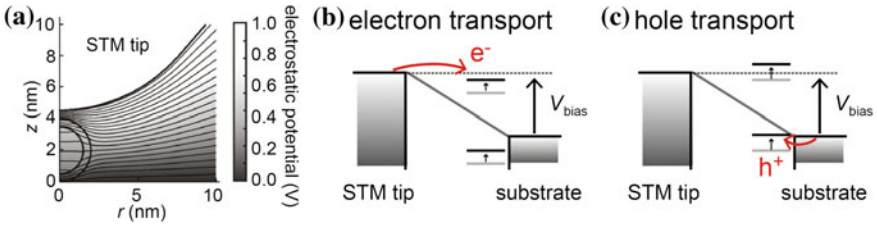

Fig. 8.3 **a** Calculated electrostatic potential distribution over a 3 nm diameter CdSe NC in the STM tip—NC—substrate junction. **b** Schematic illustration of the effect of the bias voltage on the energetic position of the NC energy levels at positive bias while still having electron tunneling through conduction levels. **c** Ambipolar transport caused by the shift of the energy levels due to the electrostatic potential distribution, where electron transport will occur through the conduction levels after hole transport is established through the valence level(s)

charge screening by the tip, and considerable decrease in η below 1 with the onset of more complicated tunneling processes, some of which are discussed below.

The parameter η is often referred to as the lever-arm. When a bias voltage is applied between the tip and the metallic substrate, there is a continuous potential distribution over the NC [Fig. 8.3a] [2, 6, 11]. This means that the quantum-confined levels shift with respect to their zero bias position. This effect is similar to the effect of the gate electrode in a three-terminal device. Effectively, it means that we have to apply a larger positive (negative) bias to reach tunneling through the first electron (hole) level, as illustrated in Fig. 8.3b.

A "symmetric" potential distribution (*η close to 0.5)* in the DBTJ can give rise to more complicated tunneling mechanisms. The most frequently observed one is ambipolar transport. Instead of separate tunneling through the electron (hole) levels at positive (negative) bias, tunneling through both levels may occur simultaneously at a given positive or negative bias [2, 11, 12]. A situation of hole transport through the h1 level together with electron tunneling through the e1 levels is illustrated in Fig. 8.3c. In this regime, the STM gap is no longer related to the HOMO-LUMO gap of the NC. For example, if hole transport takes place at both bias voltage polarities, the STM gap is given by [1, 2]:

$$e\Delta V_{\mathrm{STM}} = -1/\eta(1-\eta)\,(E_{\mathrm{h1}} - \Sigma_{\mathrm{h1}} - E_{\mathrm{F}}) \tag{8.7}$$

The other important consequence of ambipolar transport is the possibility of light emission in the DBTJ due to the recombination of electron-hole pairs [2, 13].

The intensity of the peaks in the $\mathrm{d}I(V_{\mathrm{b}})/\mathrm{d}V_{\mathrm{b}}$ spectra are related to the local density of states at the position of the STM tip [14]:

$$\mathrm{d}I(V_{\mathrm{b}})/\mathrm{d}V_{\mathrm{b}} \propto LDOS(eV_{\mathrm{b}}) = \sum_{\delta E} |\psi_i|^2 \tag{8.8}$$

where the sum is taken over the energy resolution of the instrument at the energy eV_b. This implies that certain levels lead to a very small current step if the amplitude of the wavefunction at the tip position is small, e.g., when the tip is positioned above a nodal plane. On the other hand, Eq. (8.8) implies that a spatial map of $dI(V_b)/dV_b$ at a bias V_b corresponding to a given resonance maps the squared amplitude of a given wavefunction. This will be discussed in more detail in Sect. 8.3.7.

8.2.3 Electron-Electron Interactions in Nanocrystals

In this section, we discuss the physical meaning of the terms Σ_e, Σ_h, $J_{e\text{-}e}$, $J_{h\text{-}h}$, and $J_{e\text{-}h}$, which were introduced in the previous sections. Further, simple expressions are provided for the particular cases of spherical NCs and cylindrical rods. These terms arise from screened electron-electron (or electron-hole) interactions which take place when carriers are injected into a NC from the STM tip or the substrate.

When an electron is injected into a NC, valence electrons respond *quasi*-instantaneously to the presence of this extra particle because the plasmon frequency (>10 eV) in semiconductors is high compared to the electron kinetic energy (in contrast to the situation in metals, see Chap. 3). Therefore, at each position **r** of the electron, electrostatics can be safely used to calculate the response of the valence electrons to the electron potential. After screening, the electron charge at the position **r** becomes $-e/\varepsilon_{in}$ where ε_{in} is the semiconductor dielectric constant. In bulk semiconductor, the remaining polarization charge $-e(1-1/\varepsilon_{in})$ is repelled to infinity whereas in nanostructures it builds up around the surfaces or the dielectric interfaces. It thus gives a non-zero contribution to the potential in NCs (sometimes referred to as the image potential).

The term Σ_e represents the self-energy of the injected electron. It comes from its interaction with the polarization charges induced by its own presence. The potential $V(\mathbf{r},\mathbf{r}')$ at the point $\mathbf{r}'$ due the electron at the position **r**, solution of the Poisson equation, can be written quite generally as the sum of the bulk term $-e/\varepsilon_{in}|\mathbf{r}-\mathbf{r}'|$ and a corrective term $V_s(\mathbf{r},\mathbf{r}')$ due to polarization charges at dielectric interfaces. If we put the additional electron in the lowest conduction state φ_c, Σ_e is thus given to the first order by $\Sigma_e = -e\int|\varphi_c(\mathbf{r})|^2 V_s(\mathbf{r},\mathbf{r})\,dv/2$. The factor ½ comes from the adiabatic building of the charge distribution. In the case of a spherical NC of radius R embedded in an homogeneous medium of dielectric constant ε_{out}, V_s can be derived analytically [1, 7, 8]. In the strong confinement regime φ_c can be approximated by $\sin(\pi r/R)/r$, where r is the distance to the center of the NC. The self-polarization energy is then given by [1, 8]:

$$\Sigma_e = \frac{1}{2}\left(\frac{1}{\varepsilon_{out}} - \frac{1}{\varepsilon_{in}}\right)\frac{e^2}{R} + 0.47\,\frac{e^2}{\varepsilon_{in}R}\left(\frac{\varepsilon_{in}-\varepsilon_{out}}{\varepsilon_{out}+\varepsilon_{in}}\right) \tag{8.9}$$

which is valid when $\varepsilon_{in} + \varepsilon_{out} > > 1$ (more general expressions are given in [1]). This approximate value of the self-polarization energy is quantitatively justified by more elaborated non perturbative Green's function methods such as the GW approximation, in which a screened potential is considered [15]. Σ_e gives the upward shift in energy of the extra electron in the lowest conduction state. Using the same approximations, similar expression is obtained for the self-energy Σ_h of a hole, giving the downward shift of the extra hole in the highest valence state.

The injection of a second electron into an already negatively-charged NC leads to an additional upward shift $J_{e\text{-}e}$ of the energy level. $J_{e\text{-}e}$ is given by the average repulsion with the other electron and its polarization charge:

$$J_{e-e} = -e \int |\varphi_{c2}(\mathbf{r})|^2 V_s(\mathbf{r}, \mathbf{r}') |\varphi_{c1}(\mathbf{r}')|^2 dv dv' \tag{8.10}$$

Here we assume that the second electron is injected into the same state φ_c but with opposite spin (approximation justified in the strong confinement regime). Using the same expression for φ_c, we obtain [7, 8]:

$$J_{e-e} = \left(\frac{1}{\varepsilon_{out}} + \frac{0.79}{\varepsilon_{in}} \right) \frac{e^2}{R} \tag{8.11}$$

$J_{h\text{-}h}$ is equal to $J_{e\text{-}e}$ in this approximation. It gives the additional downward shift of the highest valence level upon injection of a second hole. In addition, when $\varepsilon_{in} \to \infty$, we recover the case of a metallic island where $J = 2\Sigma$.

The case of an exciton in a NC can be treated similarly. The electron-hole attraction energy $J_{e\text{-}h}$ is also equal to $J_{e\text{-}e}$ in this simplified model. The exciton binding E_{BX} energy is given by $-(\Sigma_e + \Sigma_h - J_{e-h})$ where Σ_e and Σ_h account for the self-energy of the electron and the hole, respectively. The polarization term in the electron-hole attraction energy almost compensates the self-polarization terms. Using previous equations, the exciton binding energy becomes:

$$E_{BX} = 1.79 \frac{e^2}{\varepsilon_{in} R} - 0.94 \frac{e^2}{\varepsilon_{in} R} \left(\frac{\varepsilon_{in} - \varepsilon_{out}}{\varepsilon_{out} + \varepsilon_{in}} \right) \tag{8.12}$$

All the terms defined above scale like $1/R$ in spherical NCs, as expected for Coulomb interactions. However, the Σ and J terms do not vary with the NC shape in the same way. For example, in the case of a nanorod, if the electron wavefunction φ_c is extended over the whole system, it is clear that the electron-electron interaction $J_{e\text{-}e}$ tends to zero at increasing rod length, in the limit of a nanowire (viz., length $\gg$ diameter). On the contrary, the self-polarization term Σ_e does not vanish because, at each position of the electron, there are always polarization charges at the surfaces close to the electron. For a cylindrical nanowire of radius R and dielectric constant ε_{in} embedded in a material of dielectric constant ε_{out}, the self-energy of the electron (or hole) is approximately given by [16]:

$$\Sigma_e = \frac{e^2}{\varepsilon_{\text{in}} R}\left(\frac{\varepsilon_{\text{in}} - \varepsilon_{\text{out}}}{\varepsilon_{\text{out}} + \varepsilon_{\text{in}}}\right) F\left(\frac{\varepsilon_{\text{in}}}{\varepsilon_{\text{out}}}\right) \tag{8.13}$$

where

$$F(x) = \frac{0.0949x^3 + 17.395x^2 + 175.739x + 200.674}{x^2 + 50.841x + 219.091} \tag{8.14}$$

The magnitude of the self-energy shift in spherical NCs and in nanowires (or nanorods) is comparable. For example, for $R = 1.5$ nm, $\varepsilon_{\text{out}} = 3$, $\varepsilon_{\text{in}} = 10$, Σ_e is equal to 0.136 eV in the dot, 0.127 eV in the nanowire.

In actual STM experiments on NCs, the medium surrounding the NC is clearly not homogeneous. In particular, the metallic tip and substrate strongly screen the Coulomb potentials. Interestingly, it seems that many experimental results can be interpreted using previous equations with an effective dielectric constant ε_{out} of the order of 5–8 depending on the environment [2].

8.2.4 *Comparison Between Optical and Tunneling Spectroscopy*

Using the present terminology, the optical gap, i.e. the photon energy required to promote the electron from the highest valence to the lowest conduction level can be written as ($\Sigma_e \approx \Sigma_h \approx \Sigma$) [5, 7–9]:

$$\Delta E_{\text{opt}} = E_{\text{e1}} - E_{\text{h1}} + 2\Sigma - J_{\text{e-h}} \tag{8.15}$$

As shown in the previous section, the Coulomb terms 2Σ—$J_{\text{e-h}}$ nearly but not entirely compensate [5, 7–9]. The remaining value, the exciton binding energy E_{BX}, can be considerably larger than in the bulk semiconductor. In shell-tunneling spectroscopy, the STM gap (or *quasi*-particle gap) is given by $\eta\, e\Delta V_{\text{STM}} \approx E_{\text{e1}} - E_{\text{h1}} + 2\Sigma$ (Eq. 8.3), and hence the relation between the optical gap and STM gap is:

$$\Delta E_{\text{opt}} = \eta e \Delta V_{\text{STM}} - J_{\text{e-h}} \tag{8.16}$$

We conclude that the difference between the STM and optical gaps results from a fundamental difference in the experiments: the energy levels are probed in STM by adding either one electron or one hole from the tip to the NC. In optical spectroscopy, the energy levels are probed either by absorption of a resonant photon, which results in the formation of an exciton, or by emission of a photon due to exciton recombination (see Chap. 2). Since the exciton is an electron-hole pair, optically probing a NC will not change its charge state, in contrast with STM experiments.

The other main difference between the two types of spectroscopy (i.e., STM and optical) concerns the states that can be observed in the measured spectra. Optical spectroscopy probes transitions between two energy levels, while STS directly probes single energy levels. Optical transitions are subject to selection rules, and therefore not all transitions between valence and conduction levels can be observed (see Chap. 2). In STS, conservation of the electron linear momentum (k) should apply. However, there are enough electrons at the Fermi level with different k. Moreover, the linear momentum in the NC is not well defined. It is obvious from this—and supported by experiments—that the tunneling current is not constrained by momentum conservation rules and therefore all energy levels can in principle be detected.

8.2.5 Charge Sensing with Atomic Force Microscopy

We have seen in the previous paragraphs that the strengths of STM and STS lie in their ability to provide the energy and spatial symmetry of quantum confined energy levels in quantum dots (QDs). Atomic force microscopy (AFM) can also be used to study colloidal NCs with sub-nanometer spatial resolution. In particular, by measuring the force as a function of the applied bias voltage, the electrostatic component of the interaction between the NC and a biased metal tip can be measured (electrostatic force microscopy)[17–20].

The typical method of choice for experiments in ultra-high vacuum at low temperatures is non-contact frequency modulation AFM [21, 22]. The feedback parameter is the shift of the cantilever resonance frequency as the AFM tip scans over the sample. The frequency shift $\Delta f = f – f_0$ can be related to the tip-sample force F_{ts} as follows [22]:

$$\Delta f(z) = -\frac{f_0}{2k}\left\langle \frac{\partial F_{ts}(z)}{\partial z} \right\rangle \tag{8.17}$$

where z is the average tip-sample distance, f_0 the frequency of the freely oscillating cantilever ($z \rightarrow \infty$) and $< \partial F_{ts}(z)/\partial z >$ is the average force gradient over the tip oscillation cycle:

$$\left\langle \frac{\partial F_{ts}(z)}{\partial z} \right\rangle = \frac{2}{\pi A^2}\int_{-A}^{A} \frac{\partial F_{ts}(z-q)}{\partial z}\left(A^2 - q^2\right)^{1/2} dq \tag{8.18}$$

where A is the tip oscillation amplitude. For small oscillation amplitudes, the frequency shift can be approximated as:

$$\Delta f(z) = -\frac{f_0}{2k}\frac{\partial F_{ts}(z)}{\partial z} \tag{8.19}$$

There are several contributions to the total tip-sample force. At small tip-sample distances, the Pauli exclusion principle results in a strong repulsive interaction as the electron clouds of the last tip atom and first sample atom overlap. At larger distances, the van der Waals attraction is important, as well as electrostatic and, possibly, magnetic interactions.

The electrostatic force at a certain position and height z can be measured by acquiring the frequency shift as a function of the tip-sample bias. For an isolated charge q in the tip-substrate junction (in a double-barrier geometry), the electrostatic force F_{es} is given by [17–20]:

$$F_{es} = -\frac{\partial W}{\partial z} = \frac{1}{C_T^2}\frac{\partial C_1}{\partial z}\left(\frac{q^2}{2} + C_2 q V_b + \frac{C_2^2 V_b^2}{2}\right) + \frac{1}{2}\frac{\partial C_0}{\partial z}V_b^2 \tag{8.20}$$

where C_1 and C_2 are the capacitances of the tip-charge and charge-substrate junctions, $C_T = C_1 + C_2$ and C_0 the background capacitance. The extreme of the parabola F_{es} versus V_b (or parabola Δf versus V_b) shifts depending on the absolute value and sign of the charge q. In addition, if the charge state of the NC under the tip changes as a function of the bias voltage, there will be discrete changes in the force as well. This allows charge spectroscopy to be performed using AFM. This is illustrated in Fig. 8.4, which shows experiments carried out on gold NCs. These NCs are essentially metallic and the energy spacing of the charging events is thus dictated only by the charging energy (energy-levels spacing is very small in metallic NCs and is not significantly affected by confinement effects, see Chaps. 2 and 3).

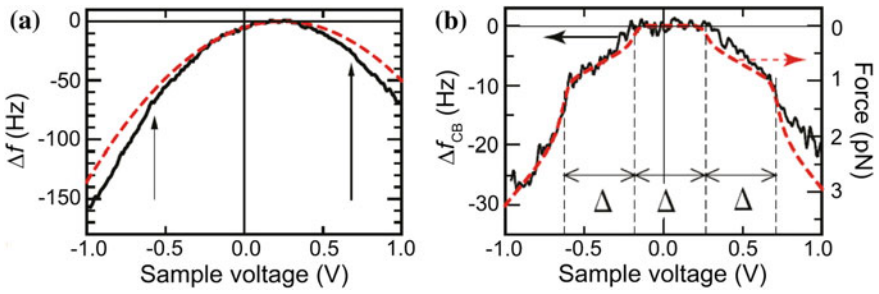

Fig. 8.4 Charge sensing with AFM. **a** Frequency shift vs. bias voltage recorded over a gold NC. Sudden changes of slope (*marked with arrows*) indicate discrete charging of the NC under the AFM tip. **b** The same data after subtraction of a parabolic background. Adapted with permission from [19]. Copyright (2006) American Physical Society

8.2.6 Sample Preparation

Sample preparation is of crucial importance for reproducible STM and STS experiments on colloidal NCs. The NCs must be immobilized on the substrate surface. This can be done by two different approaches: either covalent linkage between the NCs and the substrate by bifunctional molecules [4, 5, 23, 24], or stabilization in an array of NCs [25–27]. These approaches are illustrated in Fig. 8.5. A stereotypical example of the covalent linkage approach is to use a self-assembled alkane dithiol monolayer on a gold substrate followed by exposure to a NC suspension. The surface of the NCs is passivated by organic ligands (see Chap. 6). Therefore, prior to the STM sample preparation, the native ligand shell of the as-synthesized NCs should be exchanged to shorter, more labile molecules such as hexylamine or pyridine (see Chap. 6). This greatly enhances the stability of the NCs under STM imaging. Typically, exposure for a couple of minutes (for NC concentration in the μM range) is sufficient for suitable NC coverage on the surface [Fig. 8.5a]. The NC coverage on the substrate can naturally be controlled by the NC concentration in the solution and/or the immersion time. The covalent attachment should be used if individual, well-separated NCs on the substrate are desired [4, 5, 23, 24]. NC height extracted from the cross-sectional scans (Fig. 8.5a) can be used to estimate the NC core diameter (see Sect. 8.3.2) [28].

The other method to stabilize NCs on the substrate relies on assembling a NC superlattice by deposition from a NC suspension, i.e. drop-casting, see Fig. 8.5c. This means applying some drops of monodisperse NCs dissolved in a suitable solvent onto a desired substrate, followed by solvent evaporation. The amount of particles determines the resulting NC coverage. The interparticle spacing in these assemblies is initially determined by the length of the capping molecules. However, this can be modified by heating the film under vacuum, which results in partial or complete desorption of the capping molecules. Gentle annealing in vacuum is also very beneficial in terms of the resulting film stability under STM imaging [25–27]. Another way to obtain a compact array of NCs on a substrate consists in forming a Langmuir-Blodgett monolayer. For that purpose, suspended NCs in $CHCl_3$ are deposited on the surface in a Langmuir trough, followed by a single-stroke compression of the Langmuir film. Transfer to the substrate is typically achieved at a controlled surface pressure (25 mN/m for a flame-annealed Au(111) substrate, for example) [29]. In the case of almost spherical NCs, the interparticle distance is usually smaller than the separation found between NCs that are deposited by the drop-casting method [30]. The mechanical stability of extended arrays under STM imaging makes them very attractive in general for STM experiments. For instance, in an array of PbSe NCs, the electronic coupling between the NCs has been investigated. On the other hand, the NCs of interest can be randomly incorporated as single dots, dimers and trimers in an array of other NCs with a larger band gap that act as an insulating matrix [27]. In such a way, the energy levels of individual NCs, NC dimer molecules, etc. can be measured under mechanically stable conditions.

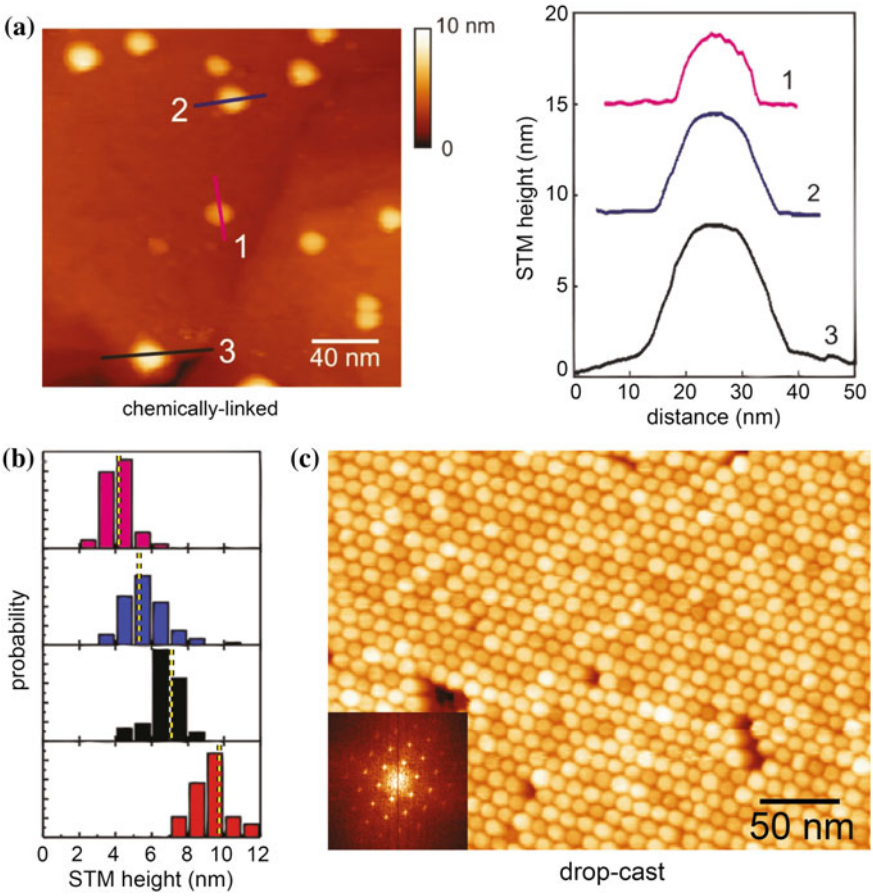

Fig. 8.5 Sample preparation either by chemical linking or drop-casting. **a** STM image of a sample of PbSe NCs chemically bond to a Au(111) surface by hexanedithiol molecules. The NC diameter can be obtained by the cross-sectional profiles along the indicated lines [28]. Imaging parameters: bias voltage $V_b = 2.5$ V and set-point current of $I = 20$ pA. **b** Histograms of the STM heights of several NCs on four different samples with different nominal NC diameters. The average NC core diameter of each sample measured by TEM is indicated by the *dotted lines* (4.1, 5.3, 7.1, and 9.8 nm). **c** STM image of an array of PbSe NCs capped with oleic acids and assembled on a highly oriented pyrolytic graphite (HOPG) surface by drop-casting from $CHCl_3$. Imaging parameters: bias voltage $V_b = 2.5$ V and set-point current of $I = 30$ pA. Inset: Fourier transform of the STM image. Panels (a) and (b) are adapted with permission from [28]. Copyright (2009) American Institute of Physics

8.3 Examples of Typical STM experiments with Nanocrystals

The energy levels of proto-typical nanocrystalline quantum dots such as CdSe, PbSe, PbS and InAs and NC hetero-structures have been studied extensively with STM/STS [4–6, 24, 26, 31–38]. The energy levels were measured as a function of the size and shape of the NCs revealing the effects of quantum confinement. The energy level spectra were also compared with the results of optical spectroscopy and tight-binding and pseudo-potential theory. In some cases, shell-filling spectroscopy could be applied to reveal the electron-electron repulsion. Recently, also the interaction between tunneling electrons and LO phonons in CdSe quantum dots could be studied.

In the following subsections we will focus on PbSe quantum dots. Not only the electronic structure and the electron-electron repulsion energy could be assessed, but also the electronic coupling between NCs in a monolayer array could be determined. Starting with an accurate description of the electronic structure of PbSe NCs (8.3.1) will be quite insightful for the subsequent interpretation of the peaks and their line widths measured in the tunneling spectra (8.3.3–8.3.6).

We will then discuss three features that have not yet been clearly revealed on PbSe NCs: the spatial extent of electron states and the direct observation of their symmetry (8.3.7), the signature of the electron-phonon coupling in tunneling spectra (8.3.8), and the location of a core embedded in a rod (8.3.9). For that purpose, we will choose examples related to CdSe-based NCs.

8.3.1 Electronic Structure of PbSe Nanocrystals

In contrast to common direct-gap semiconductors with zinc-blende or wurtzite lattice like CdSe or InAs, PbSe has a rock-salt lattice and an eightfold-degenerate conduction-band minima and valence-band minima at the L-point of the Brillouin zone (see Chap. 2). PbSe is also characterized by a small bandgap (0.28 eV at room temperature). Owing to its small electron and hole effective masses (<0.1 m_0), the gap of PbSe NCs can be tuned with size from the bulk value to about 2.0 eV. The evolution of the conduction-band and valence-band levels in spherical PbSe NCs calculated in tight-binding is presented in Fig. 8.6a, b [30, 39]. As a consequence of the degeneracy of the valleys, the electronic structure of the NCs is characterized by multiplets of states, but their degeneracies are lifted by inter-valley couplings, which are strongly size-dependent. Figure 8.6c shows the evolution of the electron-electron (or hole-hole) repulsion energy $J_{e\text{-}e}$ (or $J_{h\text{-}h}$) as a function of the size. $J_{e\text{-}e}$ takes substantial values due to the dielectric contrast at the surface (ε_{in} = 23).

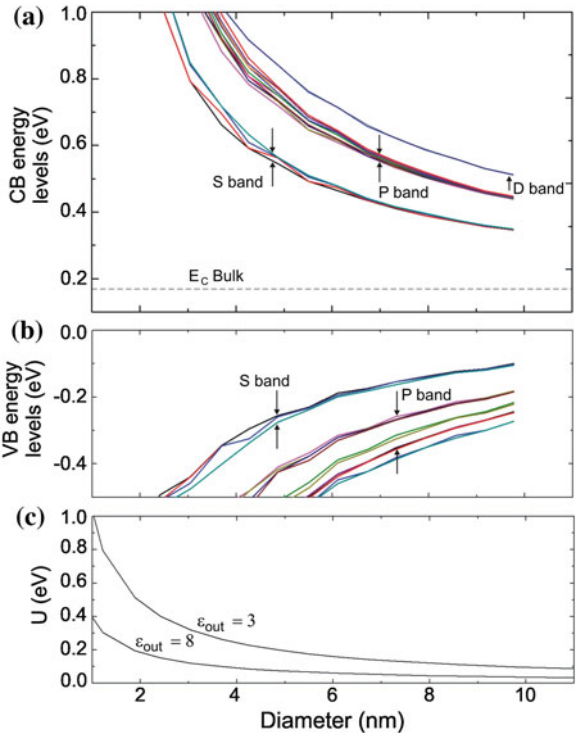

Fig. 8.6 **a** Energy of the electron levels in the conduction band as a function of the NC size. The horizontal dashed line indicates the position of the conduction band edge E_c for PbSe bulk at 0 K. **b** Energy of the hole levels in the valence band as a function of the NC size. The levels are grouped in bands of four S-type levels and twelve P-type levels. The first D level is also shown. The zero in energy corresponds to the top of the valence band for bulk PbSe. **c** Electron-electron interaction energy $J_{e\text{-}e}$ (Eq. 8.11) for two electrons on a S-level as a function of PbSe core size, in NCs that are embedded in a medium with two different static dielectric constant ε_{out}, corresponding to an organic capping layer (low ε_{out}) and a CdSe shell (high ε_{out})

8.3.2 Measuring the Size of a Nanocrystal

As the most pronounced effect of quantum confinement is an increase of the energy gap with decreasing NC size (Chap. 2), it is important to correlate the apparent band gap that is measured in tunneling spectroscopy, to the size of the NC. When an ensemble of NCs is synthesized, the mean size of the NCs is generally characterized by optical spectroscopy and high resolution transmission electron microscopy (TEM). This mean size can be compared with the average size measured by STM on an ensemble of NCs.

Depending on the method used to deposit NCs onto the substrate, two different ways exist to accurately determine their size based on STM imaging. In the case of a sample with individual, well-separated NCs, the size is obtained from the vertical height measured by the STM tip that scans over an isolated NC. Typical height profiles

are presented in Fig. 8.5a for the PbSe NCs seen in the STM image on the left [28]. Figure 8.5b shows that the maximum of the STM height histograms measured on different samples compares well with the average NC core diameter measured by TEM. Although the PbSe NCs used in these experiments were passivated with hexylamine, we never found a significant contribution of the ligands to the STM height in comparison with the size measured by TEM. Three reasons can be invoked to explain this observation: (1) heating the sample to 120 °C before imaging it at low temperature causes a partial desorption of the ligands; (2) the attached ligands can change their conformation when the tip scans over the NC; (3) a high barrier height induced by ligands with large gap. Therefore, the STM height of an individual NC gives a rather good indication of its size. While the NC should have a rather spherical shape, it is worth noting that the width of the NC observed in the STM profile is always larger than the height. This discrepancy arises because the tip has an effective radius of curvature that broadens the lateral size of the NCs due to the tip convolution effect.

On samples formed by drop-casting, where the NCs are arranged in a close-packed layer, the lateral broadening is minimized, because the tip cannot reach the surface anymore. In this situation, the mean size of the NCs is obtained from the Fourier transform of the topographic image. Figure 8.5c shows a typical example for an array of PbSe NCs, where the hexagonal reciprocal lattice with six bright spots in the Fourier transform image reveals the *quasi*-hexagonal order of the NCs seen in the real-space topographic image. From the reciprocal length measured between the centre of the Fourier transform image and the six bright spots, a lattice parameter of 11.8 nm is found. Such lattice parameter is larger by 2.0 nm than the mean size of the NCs that was measured by TEM and is caused by the steric hindrance of interdigitated ligands. Therefore, the size of a NC in an array is measured by inscribing the NC into a circle, determining the diameter of the circle and subtracting the average spacing that is related to the presence of ligands.

8.3.3 Acquisition and Processing of Spectroscopic Measurements

When the NC size has been determined, the tip can be positioned above the centre of the NC. By opening the feedback loop, the distance between the tip and the NC is kept constant and sweeping the voltage across the DBTJ allows to acquire an $I(V_b)$ characteristic. The current is obtained from the integration of states within the energy range for which tunneling can occur. Thus, the acquisition of the derivative of the current, that is proportional to the NC density of states, is preferable. Although the differential conductance dI/dV_b can be obtained by the numerical differentiation of the current, a better resolved signal is usually acquired with a lock-in amplifier. In this case, the parasitical AC current, resulting from the electrical setup and tip-sample geometry, that is phase shifted by 90° with respect to the modulation of the tunneling current, has to be cancelled to increase the sensitivity of the measurements. Care has also to be taken regarding the amplitude of the

modulation V_m, which has to be kept smaller than the spacing of the characteristic spectral features. The broadening caused by the modulation amplitude is 2 eV_m and it has to be added to the thermal broadening of 3.2 k_BT [40].

Typically, a large number of curves is acquired above a single NC under identical feedback conditions, so that sets of reproducible curves are averaged to increase the signal-to-noise ratio. Figure 8.7a shows ten successive curves that were acquired among a set of one hundred curves. In order to select curves with a high reproducibility, we zoom into the lowest peak at positive and/or negative bias. Discrete shifts between the peak position or fluctuations in the linewidth are observed and we generally limit the shift and full width at half maximum to a few meV with respect to the average result. For example in the inset of Fig. 8.7a, only the curves that show a peak positioned within ± 4 meV from the peak position of the differential conductance dI/dV_b, displayed as the lowest curve, have been selected. For that reason, curves 38, 40 and 45 were discarded.

The differential conductance dI/dV_b has then to be compared to the numerical differentiation of the current in order to remove the bias offset due to the time constant of the lock-in, and normalize the intensity of the peaks, since the sensitivity of the lock-in and the amplification of the converter may not be accurately known. In Fig. 8.7b, the intensity of the differential conductance dI/dV_b has been normalized, but the bias offset has still to be adjusted. Such an offset is better seen in the inset of Fig. 8.7b: the 20 meV shift towards smaller voltages is caused by the 10 ms integration time of the lock-in, the voltage sweep starting at V_b = 1.2 V.

8.3.4 Identification of the Transport Regime

As discussed in Sect. 8.2.2, when a NC is weakly coupled to two leads in a double barrier tunnel junction (DBTJ), the potential distribution in such a system is usually characterized by the lever arm η. Defining the capacitance between the NC and the substrate as C_1 and the capacitance between the tip and the NC as C_2, the lever arm is given by the ratio between the capacitance C_1 and the sum of the capacitances C_1 and C_2: $\eta = C_1 / C_1 + C_2$).

When the tip is far from the NC, C_2 is usually much smaller than C_1 and the lever arm is close to 1. In this case, the transmission probability across the second potential barrier is much smaller than the transmission probability across the first potential barrier, and the peaks in the tunneling spectra correspond to single-electron energy levels. In this situation, a transition level observed in the tunneling spectrum at positive sample bias involves the filling of a discrete energy level in the conduction band. Conversely, at negative sample bias, a transition level corresponds to the removal of one charge carrier from the occupied quantized levels of the valence band.

An alternative tunneling regime may occur, when C_2 becomes comparable to C_1, which means that the lever arm approaches 0.5. In the simplified capacitance model, this can arise when the thickness of both tunnel barriers are similar. In this case, the transmission probability across both potential barriers becomes comparable, and, if

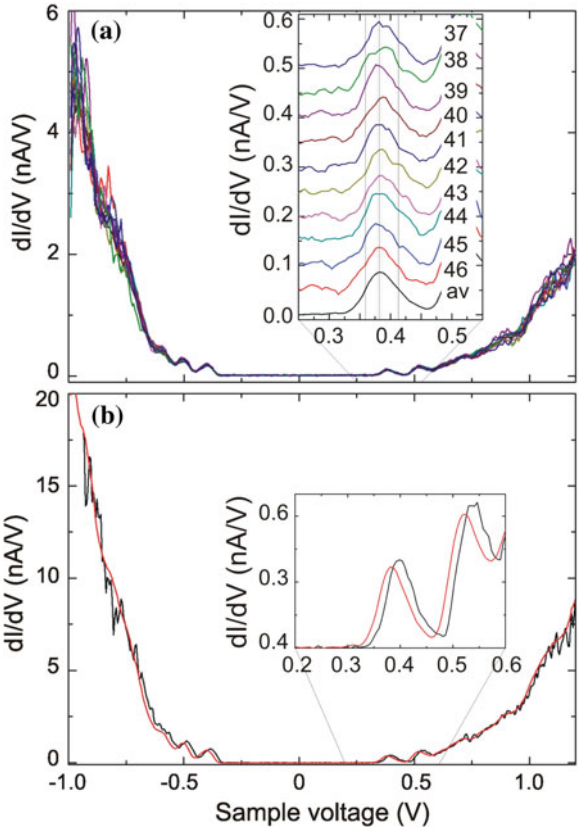

Fig. 8.7 **a** Set of ten successive differential conductance dI/dV_b curves acquired with a lock-in amplifier on a PbSe/CdSe core-shell NC. STM parameters: V_b = 1.2 V, modulation amplitude V_m = 9 mV, modulation frequency f_m = 480 Hz, I = 30 pA, T = 5 K. Inset: Zoom into the energy range corresponding to the lowest peak observed at positive bias. The curves are labeled with respect to their acquisition. The average differential conductance dI/dV_b spectrum is labeled av. The thick, *dotted* and *thin vertical lines* indicate the peak position of the average spectrum, the boundaries of the bias range within ± 4 mV with respect to this peak, the full width at half maximum of this peak. **b** Comparison of the average differential conductance dI/dV_b spectrum (*red*) normalized in intensity with the numerical differentiation of the current (*black*). Inset: Zoom into the energy range corresponding to the lowest peak observed at positive bias in order to show the bias offset that is caused by the lock-in time constant

the Fermi level in the NC is not positioned mid-gap, the same state can contribute to the tunneling current on each side of the zero-conductance region, leading to unipolar transport (Sect. 8.2.2 and Fig. 8.3) [2].

A proper identification of the peaks at positive and negative bias as corresponding to electron or hole tunneling is possible by looking at the change in the peak voltage as a function of the lever arm. For that purpose, the use of core/shell NCs, such as PbSe/CdSe core/shell NCs, is quite helpful, because it makes it easier to probe the transport

regime, where the tunnel barriers on both sides of the NCs are similar. Figure 8.8 shows two tunneling spectra that were obtained with an asymmetric (a) and a more symmetric (b) DBTJs. In Fig. 8.8a, the peaks V^+ and V^- measured at positive/negative bias shift away from the Fermi level as the set-point current increases, indicating that the levels probed at, respectively, positive/negative sample voltages correspond to conduction/valence band states. In this case, the relation between the zero-conductance region ($V^+ - V^-$) and the *quasi*-particle gap is given by:

$$e(V_e^+ - V_h^-) = \frac{E_{Gap}^{qp}}{\eta} \tag{8.21}$$

As the hole and electron ground states are respectively measured at negative and positive voltages, V^- and V^+ are respectively labeled V_h^- and V_e^+. E_{Gap}^{qp} corresponds to the *quasi*-particle gap (or STM gap), that is defined by the sum of NC band gap and twice the polarization energy (Eq. 8.3).

Conversely, in Fig. 8.8b, both V^- and V^+ shift towards lower energies, when the set-point current increases, corresponding to a unipolar hole transport. In this situation, the measurement of the zero-conductance region provides the determination of the lever arm η as follows [2]:

$$\eta = \frac{V_h^+}{V_h^+ - V_h^-} \tag{8.22}$$

8.3.5 Quantum Mechanical Coupling

According to Fig. 8.6 above, the energy separation between the first excited state and the ground state in the conduction and valence bands is of the order of 100 meV or more, for NC sizes below 8 nm. Thus, the states are well separated in energy. As the electron and hole Bohr radii are known to be much larger than the NC size in a PbSe, [41] these properties make PbSe NCs quite attractive to study the electronic coupling between adjacent NCs arranged in a 2-dimensional array. As an example, Fig. 8.9 shows the changes observed in the tunneling spectra measured on similar sized PbSe NCs, that are either isolated on a surface or inside an array with variable degree of ordering. When an isolated NC is probed in the shell-tunneling regime, the hole first excited state, hole ground state, electron ground state and electron first excited state are well resolved at the corresponding voltages $V_{h_2}^-$, $V_{h_1}^-$,$V_{e_1}^+$, $V_{e_2}^+$.

In contrast, when the NC is surrounded by similar NCs, a reduction of the zero-conductance region is clearly seen and some of the peaks are no longer observable. While a change of the lever arm only affects the spacing between the peaks, it cannot explain the disappearance of the discrete levels. This effect is related to a reduction of the quantum confinement, due to electronic coupling between the same

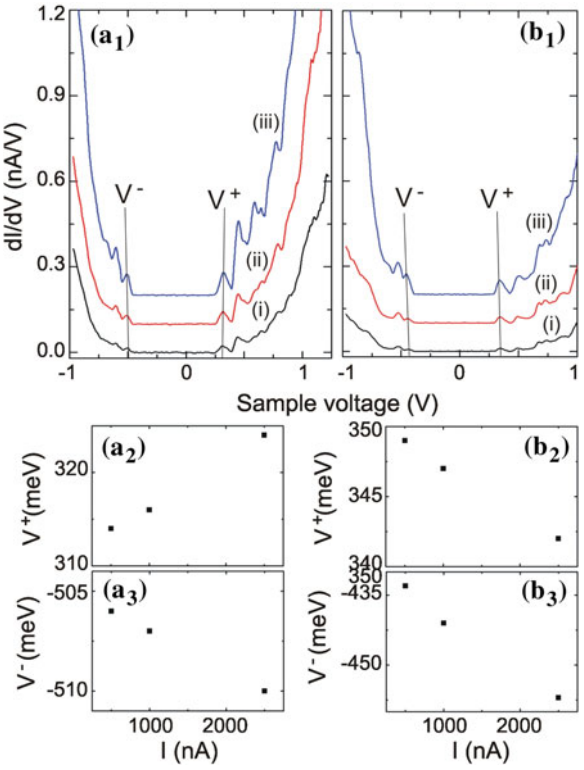

Fig. 8.8 Evolution of the highest/lowest peak measured at a negative/positive bias as a function of the set-point current for two different PbSe/CdSe core-shell NCs (**a**) and (**b**). The peaks are respectively labelled V^- and V^+. STM parameters: V_b = 1.2 V, I = 500 pA (*i*), 1000 pA (*ii*), 2500 pA (*iii*), T = 5 K

energy levels of several NCs within the array. Such result is obtained due to the small size distribution of the NCs.

The system can be modeled by an array consisting of potential wells separated by tunnel barriers with finite height [25]. The degree of coupling depends on the local ordering, since the ordering directly affects the barrier width. As to the barrier height, it might be lowered by the non-resonant orbitals of the capping molecules [39] and this lowering could lead to different exchange energy couplings between electron levels and hole levels. Therefore, fluctuations in the degree of coupling are generally found in a given array. As highlighted in Fig. 8.9, spectrum (ii) reveals a band selective coupling, where only the electron levels coupled, whereas spectrum (iii) shows the formation of bands of states for both the valence hole and the conduction electron levels. The highest and lowest bands observed at negative and positive voltages are respectively labeled $V^-_{VB_1}$ and $V^+_{CB_1}$.

Interestingly, we have never been able to detect such a degree of broadening for the measured energy levels in arrays of CdSe NCs [27]. On the other hand, electronic coupling was demonstrated in the case of InAs NCs [42]. These results are in line with the increase of the Bohr radii of the electron and hole as the effective mass of the carriers in the semiconductor material decreases.

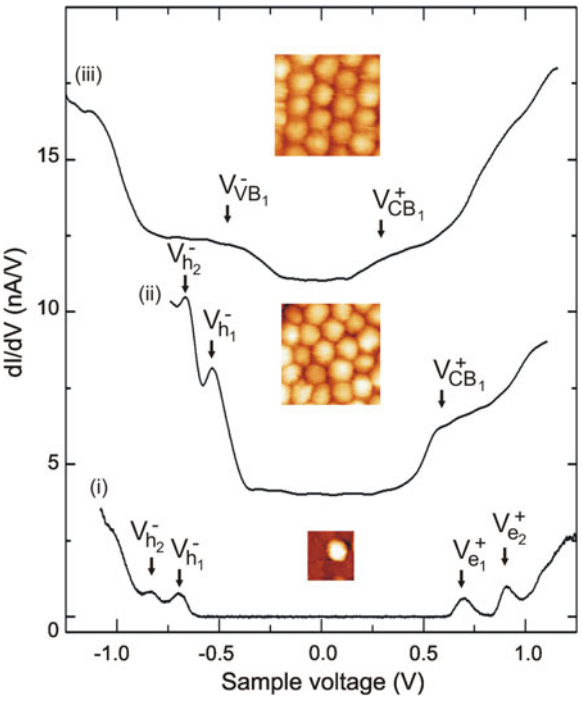

Fig. 8.9 Differential conductance spectra measured on (*i*) an isolated PbSe NC, (*ii*) a PbSe NC in the center of a disordered array, (*iii*) a PbSe NC in the center of an ordered array. The peaks labeled $V^-_{h_2}$, $V^-_{h_1}$,$V^+_{e_1}$, $V^+_{e_2}$ correspond to the hole first excited state, hole ground state, electron ground state and electron first excited state respectively. The bands labeled $V^-_{VB_1}$, $V^+_{CB_1}$ correspond to the valence band and conduction band of the array, that are probed at negative/positive voltages respectively. Feedback parameters: (*i*) V_b = +1.25 V and I = 100 pA, (*ii*) V_b = +1.2 V and I = 100 pA, (*iii*) V_b = −1.2 V and I = 50 pA, T = 5 K

8.3.6 Charge Sensing

So far, most of the electronic spectra shown above for PbSe NCs have been investigated in the shell-tunneling regime (i.e., $\Gamma_{in} << \Gamma_{out}$, Sect. 8.2.2). The occupation probability of the NCs is thus on average much lower than one. In contrast, when the potential distribution across the DBTJ becomes more symmetric, the transmission probabilities across both potential barriers become comparable. Indeed, with the addition of a shell around the core, the NC-substrate distance increases. The transmission probability across the DBTJ gets smaller and working at tunneling current set-points that are commonly used for PbSe NCs, requires a decrease of the tip-NC distance. This situation favors charging effects and can be encountered with the use of core-shell NCs where the electron and hole are both confined in the core (heterostructure with a type-I band alignment, see Chap. 2).

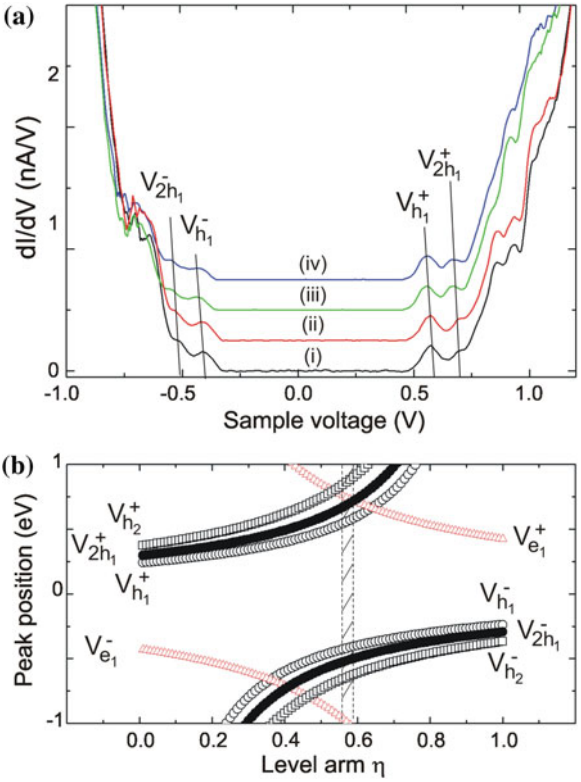

Fig. 8.10 **a** Set of differential conductance spectra measured on a PbSe/CdSe NC with a diameter of 7.5 nm. The peaks labeled $V_{h_1}^-$, $V_{2h_1}^-$, $V_{h_1}^+$, $V_{2h_1}^+$ correspond to tunneling through the hole ground state with zero and one hole at negative and positive bias. The oblique segments are used as eye guide to highlight the shift of the peak positions with increasing set-point currents. Feedback parameters: $V_b = +1.2$ V and $I = 0.5$ nA (*i*), 1.0 nA (*ii*), 2.5 nA (*iii*), 3.0 nA (*iv*). **b** Variation of the peak position as a function of the lever arm η. The hole first excited and electron ground states measured at negative and positive voltages are respectively labeled $V_{h_2}^-$, $V_{h_2}^+$, $V_{e_1}^-$, $V_{e_1}^+$. The shaded region corresponds to the range of lever arms measured in (**a**)

Figure 8.10 shows set of differential conductance dI/dV_b curves obtained on a PbSe/CdSe core/shell NC, where the peaks on each side of the zero-conductance gap shift towards smaller voltages as the set-point current increases. The observed shift for the peaks measured at positive voltages is opposite to the expected shift that should occur if electrons were tunneling through the conduction band ground state for smaller and smaller lever arms [2]. Therefore, the shifts result from the contribution of the hole ground state h_1 to the tunneling current.

From the position of the lowest peak $V_{h_1}^+$ at positive voltages and the separation between $V_{h_1}^+$ and $V_{h_1}^-$, we can deduce the lever arm, based on Eq. (8.22). At low set-point current, a lever arm of 0.58 is found. Then, the lever arm monotonously

decreases to 0.56 as the set-point current increases. Knowing the diameter of the NC from the topographic STM image (7.5 nm), and assuming that the very thin layer of CdSe (0.4 nm) does not significantly affect the confinement of the electron and hole ground states in the core, we can determine the *quasi*-particle gap of the NC from Fig. 8.6. For a core diameter of 6.7 nm, the band gap E_{e1}–E_{h1} and the polarization energy Σ are 609 meV and 27 meV respectively. As a result, the position of the hole ground state h_1 with respect to the Fermi level E_F is given by:

$$E_{h_1} - E_F = \eta e V_{h_1}^- + \Sigma = -((1-\eta) e V_{h_1}^+ - \Sigma) \tag{8.23}$$

and we find $E_{h_1} - E_F = -212$ meV.

The theoretical knowledge of the band gap then yields $E_{e_1} = 397$ meV. Although the peaks $V_{e_1}^+$, $V_{e_1}^-$, that correspond to the tunneling of electrons from the conduction band ground state at positive and negative voltages respectively, are not provided by the spectroscopic experiments, they can be deduced from the knowledge of E_{e_1}:

$$e V_{e_1}^+ = \frac{(E_{e_1} - E_F) + \Sigma}{\eta} \tag{8.24}$$

and

$$e V_{e_1}^- = -\frac{(E_{e_1} - E_F) + \Sigma}{1-\eta} \tag{8.25}$$

Based on Eqs. (8.23)–(8.25), the position of the peaks $V_{h_1}^-$, $V_{h_1}^+$, $V_{e_1}^+$ and $V_{e_1}^-$ can be plotted as a function of the lever arm, as shown in Fig. 8.10b. In the shaded area of Fig. 8.10b, that corresponds to the range of lever arms deduced from Fig. 8.10a, $V_{e_1}^+$ and $V_{e_1}^-$ are clearly higher and lower than $V_{h_1}^+$ and $V_{h_1}^-$ respectively, demonstrating that only holes are allowed to tunnel on both sides of the zero-conductance region.

The second peak observed at positive and negative voltages shifts in the same way as the set-point current increases. This peak could arise from the contribution of the first hole excited state to the tunneling current, or the charging of the hole ground state, that can accommodate up to 8 holes due to its spin degeneracy. In the first case, it is labeled $V_{h_2}^-$, and in the second case, $V_{2h_1}^-$. In order to discriminate between the first excited state and a charging effect, the expected separations between the different transition levels are deduced from Fig. 8.6. For a lever arm around 0.58, the spectral separation between $V_{h_2}^-$ and $V_{h_1}^-$ is 224 mV, whereas the spectral separation between $V_{2h_1}^-$ and $V_{h_1}^-$ is 95 mV. As the measured separation between the first and second peaks at negative voltages is around 105 mV, the second peak can be ascribed to the charging of the hole ground state.

Similarly, replacing the lever arm η by (1–η) yields a separation of 131 mV for the charging of the hole ground state, that is consistent with the measured

separation of 125 mV. Therefore the differential conductance *dI/dV* curve of Fig. 8.10 corresponds to a shell-filling regime, where the NC hole ground state is charged at positive and negative voltages.

8.3.7 Symmetry of the Energy Levels

Figure 8.11a shows a normalized differential conductance dI/dV_b spectrum that was measured on the CdSe nanorod shown in Fig. 8.11b. Based on the analysis of the peak position as a function of the set-point current, it was found that the peaks correspond to single-electron energy levels (shell-tunneling regime), where the conduction band states are probed at positive sample voltages. The peaks at positive bias are labeled according to the expected envelope wavefunction symmetries, where the first peak corresponds to the ground state with S envelope symmetry. Interestingly, this peak is followed by a series of progressively weaker peaks, which can be ascribed to replicas due electron-phonon coupling (see Sect. 8.3.8). The P states are non-degenerate in a nanorod due to the breaking of the spherical symmetry. The P_x state (oriented along the long axis of the nanorod) will be lowered in energy due to reduced quantum confinement compared to the P_y and P_z states.

In order to verify that the peaks in the measured dI/dV_b spectrum correspond to the different discrete single particle levels of the NC, spatial mapping of the differential conductance as a function of the voltage was performed. This involves recording dI/dV_b spectra at each point of the topographic scan, and then looking at the spatially-resolved dI/dV_b signal at a given energy. The tip-sample distance is controlled by the feedback set point. Plotting the intensity of the differential conductance for each point of the map at a given voltage (Fig. 8.11c) reveals that the lowest peak (labeled S in the spectrum shown in Fig. 8.11a at a bias of 0.82 V) is spatially delocalized over the nanorod and has no nodal planes. In contrast, the second peak (P_x at a bias of 0.99 V) corresponds to an orbital that has a nodal plane in the center of the nanorod, consistent with the expected shape of the P_x envelope wavefunction.

8.3.8 Elastic or Inelastic Charge Transfer

When an electron is transferred to a NC, its charge interacts with the ions of the crystal and leads to a local lattice distortion. As the dimensions of the crystals shrink, the lattice distortion is enhanced and the energy of the electrons transferred to the lattice, as lattice vibrations, might become significant. In STS, the signature of a strong coupling between the electron and the lattice appears as peak replicas or a broadening of the resonance line width, if the replicas are not sufficiently separated in comparison with the spectral resolution of the microscope or if there is coupling to a *quasi*-continuum of acoustic modes [12, 42–45].

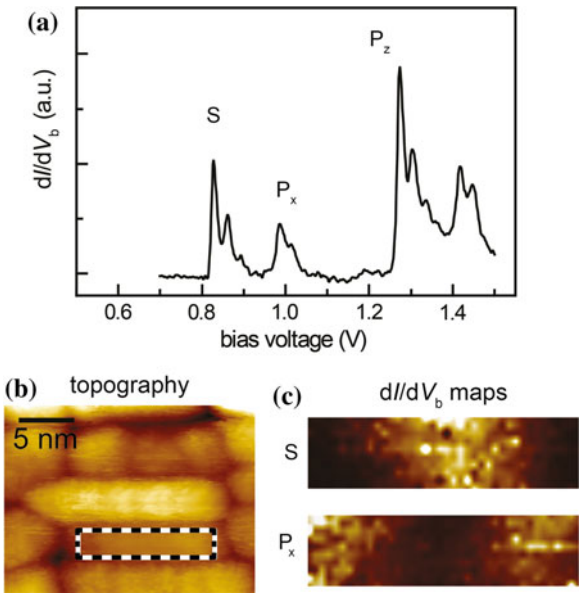

Fig. 8.11 Imaging electron wavefunctions with STM. **a** dI/dV_b spectrum recorded on the nanorod shown in panel (**b**). The different resonances have been labeled according to the wavefunction envelope symmetries. **b** STM image of a close-packed layer of CdSe nanorods at $V_b = 2.5$ V and $I = 10$ pA **c** Spatial maps of the dI/dV_b signal at the bias voltages corresponding to the first (S) and second (P_x) resonances. The maps show the spatial shape of the electron wavefunctions

For polar materials, the dominant coupling is the Fröhlich interaction between the polarization field induced by the vibrational motion and the electronic charge density. The polarization field is carried out by the longitudinal optical (LO) phonons. In PbSe, the energy of LO modes is around 17 meV [45, 46]. However, in PbSe NCs, the intervalley coupling splits the lowest L states (Sect. 8.3.1). The magnitude of the splitting may become of the order of the measured linewidth corresponding to tens of meV, as seen in Fig. 8.6. This effect prevents the discrimination between phonon replicas and intervalley splitting [28].

In contrast, the LO phonon mode in CdSe has an energy of 26 meV [47, 48] and the ground state is only spin-degenerate. As a result, a CdSe NC is a better candidate to resolve vibronic peaks in STS. Figure 8.12 shows a typical differential conductance dI/dV_b curve obtained on a CdSe NC of 5 nm diameter. The spectrum was acquired at a low set-point current and the series of peaks observed on both sides of the zero-conductance region correspond to the transfer of an electron through the single-particle discrete energy levels of the NC. Each transition level is labeled by the symmetry of the wave functions (see 8.3.7). The lowest S_e peak has a full width at half maximum of 91 mV, that is partly caused by the coupling of the electron with the LO phonons [45]. For some sets of CdSe NCs, the broad peaks turn into a progression of equally spaced narrower peaks, as seen in the inset of the

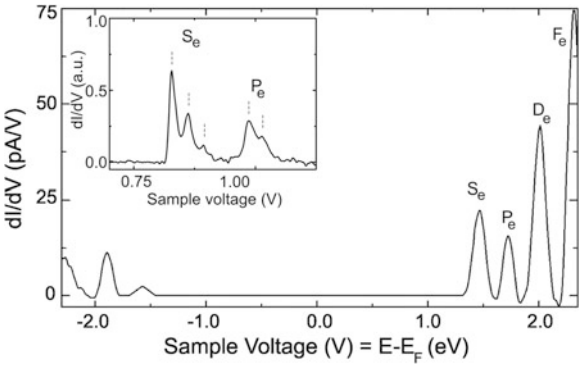

Fig. 8.12 Differential conductance spectrum measured on a CdSe NC with a diameter of 5 nm. The peaks in the conduction band are labeled as a function of the symmetry of the quantized levels. Feedback parameters: V_b = +2.5 V and I = 20 pA. Inset: Enlarged view of the S_e and P_e peaks measured on a CdSe nanorod. The position of the vibronic peaks is indicated by vertical dashed segments

Fig. 8.12 for the S_e and P_e levels. In this example obtained on a CdSe nanorod deposited on a HOPG (highly oriented pyrolithic graphite) surface, the peak spacing is 31 mV. To convert this number to the true energy scale, the potential distribution in the DBTJ was calculated by solving the Poisson equation for a realistic tip-NC-substrate geometry [49]. A lever arm of 0.85 was found, yielding an energy spacing of 26 meV, consistent with the energy of the LO phonon mode in CdSe.

Measuring the polaronic density of states, where each one-electron configuration is characterized by a ground and several vibrationally excited states requires to place the NC in a low temperature environment. If the internal temperature of the NC does not rise significantly due to the heating from lattice vibrations, then the number of vibronic peaks in the progression and their intensity depend on the electron-vibration coupling strength [45]. Three vibronic peaks are seen for the S_e transition levels, the first peak having the strongest intensity. In such a case, the electron-phonon coupling was estimated to be 0.35 [49].

8.3.9 Dot-in-Rod Heteronanocrystals

NCs consisting of two different materials grown with a strongly asymmetric shape are a very interesting system for studying the localization or delocalization of the charge carriers in the heteronanocrystal. CdSe/CdS dot core/rod shell nanorods belong to this type of heterostructures. The nanorods can be seen in the STM image of Fig. 8.13. The CdSe core has a diameter of 3.5 nm, consistent with the energy of the onset measured at 2.1 eV by optical absorption spectroscopy. The thickness of

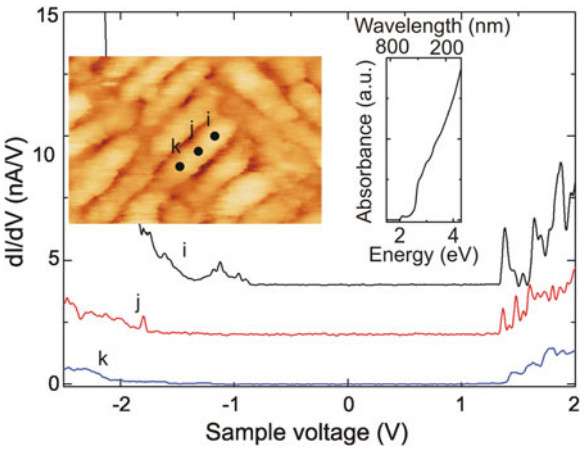

Fig. 8.13 Spatially-resolved differential conductance spectra measured at the location (*i*), (*j*) and (*k*) on the CdSe/CdS dot-in-rod NC seen in the STM image. Feedback parameters: V_b = +2.0 V, I = 2.0 nA, T = 4.8 K. Inset: Absorption spectrum measured at room temperature on an ensemble of CdSe/CdS nanorods dissolved in toluene

the CdS shell was estimated to be between 0.3 and 0.4 nm around the dot core and the average length of the rod was 20.1 nm.

Typical spatially resolved differential conductance spectra acquired on a single nanorod are shown in Fig. 8.13. While a zero—conductivity gap is observed for all three spectra, the width of this gap is found to vary along the length of the rod. At one end of the nanorod, region (i), it extends over 2.27 eV. Then, for the two others positions, it is much larger. It reaches 3.16 eV in the middle of the rod, region (j), and 3.06 eV at the other end, region (k). Such a result clearly shows that STS allows to locate the CdSe core region, while it is embedded in a CdS shell, consistent with similar studies [50].

8.4 Exercises

1. Figure 8.14 shows differential conductance spectra acquired on single PbSe NCs with different sizes. Assuming a lever arm of 0.75 and a dielectric constant of 3 for the NC surroundings, find out the size of the three NCs based on the electronic structure and the polarization energy plotted in Fig. 8.6. What is the maximum modulation amplitude that can be applied to the DC sample bias to detect the energy separation between the levels e_1 and e_2 for each NC?
2. Figure 8.15 shows differential conductance dI/dV_b spectra that were measured on a PbSe/CdSe core/shell NC with different set-point currents. The diameter of the NC was 8.5 nm and the estimated CdSe shell thickness 0.4 nm.

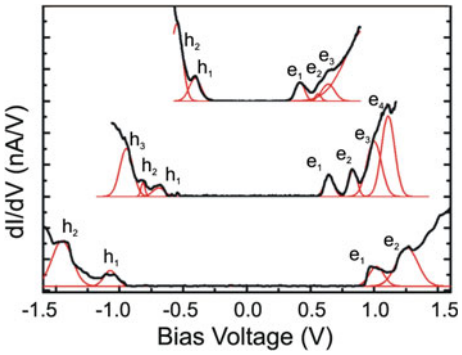

Fig. 8.14 Differential conductance dI/dV_b curves acquired on PbSe NCs with different sizes. T = 5 K. The spectra are fitted to distributions of Gaussian functions and the resonances are denoted h_1 to h_4 for the valence levels and e_1–e_4 for the conduction levels

Fig. 8.15 Set of differential conductance spectra measured on a PbSe/CdSe NC with a diameter of 8.5 nm. The feedback parameters were V_b = +1.2 V and I = 0.5 nA (*i*), 1.0 nA (*ii*), 2.0 nA (*iii*), 2.5 nA (*iv*), 3.0 nA (*v*)

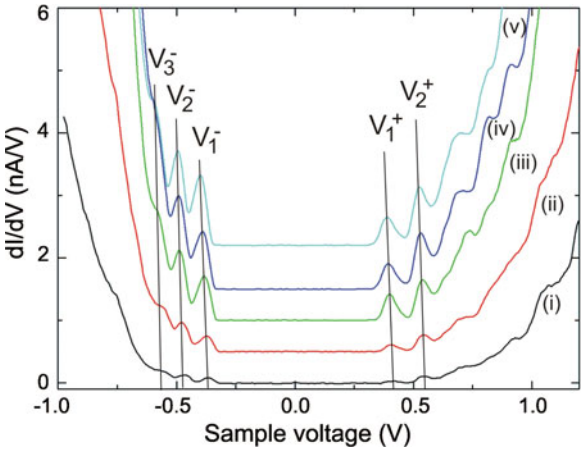

a. Identify the nature of the charge carriers that are transferred at voltages V_1^- and V_1^+.
b. Determine the lever arm as a function of the set-point current. Compare the potential drop in both tunnel barriers.
c. Based on the electronic structure and the charging energy provided in Fig. 8.6, determine whether the peaks observed at sample voltages V_2^-, V_3^- and V_2^+ correspond to single particle energy levels or are caused by charging effects.

3. Figure 8.16 shows a differential conductance dI/dV_b curve obtained on a CdSe NC, where the progression of equidistant peaks is observed for the lowest electron level. The peak spacing is 36 meV.

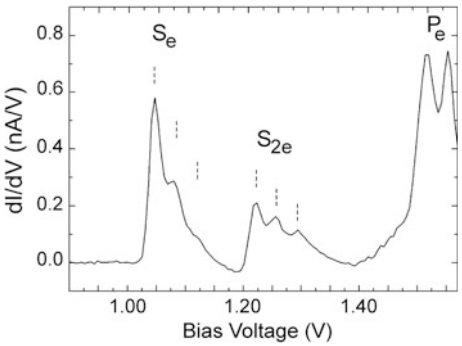

Fig. 8.16 Differential conductance curve measured on a CdSe NC that was deposited on a HOPG surface. The curve was obtained in the shell filling regime (V_b = 2.8 V, I = 1.6 nA, T = 5 K). The peaks are labeled by S, P, depending on the symmetry of the envelope wave function of the levels. The subscripts refer to electron states and the number of electrons in a level

a. Determine the lever arm.
b. Determine the electron-electron interaction of the S_e level.
c. Taking ε_{in} = 8 and ε_{out} = 2, calculate the diameter of the NC.

Acknowledgments We acknowledge financial support from the European Community ("HERODOT" project-grant PITN-GA-2008-214954 and ERC-2011-StG No. 278698 "PRECISE-NANO") and the Academy of Finland (Centre of Excellence in Low Temperature Quantum Phenomena and Devices No. 250280).

References

1. Delerue, C., Lannoo, M.: Nanostructures. Theory and Modelling. Springer, Berlin (2004)
2. Niquet, Y.M., Delerue, C., Allan, G., Lannoo, M.: Interpretation and theory of tunneling experiments on single nanostructures. Phys. Rev. B **65**(16), 165334 (2002)
3. Averin, D.V., Korotkov, A.N., Likharev, K.K.: Theory of single-electron charging of quantum wells and dots. Phys. Rev. B **44**(12), 6199 (1991)
4. Banin, U., Cao, Y.W., Katz, D., Millo, O.: Identification of atomic-like electronic states in indium arsenide nanocrystal quantum dots. Nature **400**(6744), 542–544 (1999)
5. Bakkers, E.P.A.M., Hens, Z., Zunger, A., Franceschetti, A., Kouwenhoven, L.P., Gurevich, L., Vanmaekelbergh, D.: Shell-tunneling Spectroscopy of the single-particle energy levels of insulating quantum dots. Nano Lett. **1**(10), 551–556 (2001)
6. Jdira, L., Liljeroth, P., Stoffels, E., Vanmaekelbergh, D., Speller, S.: Size-dependent single-particle energy levels and interparticle Coulomb interactions in CdSe quantum dots measured by scanning tunneling spectroscopy. Phys. Rev. B **73**(11), 115305–115306 (2006)
7. Brus, L.E.: Electron-electron and electron-hole interactions in small semiconductor nanocrystallites: The size dependence of the lowest excited electronic states. J. Chem. Phys. **80**(9), 4403–4409 (1984)

8. Lannoo, M., Delerue, C., Allan, G.: Screening in semiconductor nanocrystallites and its consequences for porous silicon. Phys. Rev. Lett. **74**(17), 3415–3418 (1995)
9. Franceschetti, A., Williamson, A., Zunger, A.: Addition spectra of quantum dots: the role of dielectric mismatch. J. Phys. Chem. B **104**(15), 3398–3401 (2000)
10. Berthe, M., Stiufiuc, R., Grandidier, B., Deresmes, D., Delerue, C., Stiévenard, D.: Probing the carrier capture rate of a single quantum level. Science **319**(5862), 436 (2008)
11. Liljeroth, P., Jdira, L., Overgaag, K., Grandidier, B., Speller, S., Vanmaekelbergh, D.: Can scanning tunnelling spectroscopy measure the density of states of semiconductor quantum dots? Phys. Chem. Chem. Phys. **8**(33), 3845–3850 (2006)
12. Wu, S.W., Nazin, G.V., Chen, X., Qiu, X.H., Ho, W.: Control of relative tunneling rates in single molecule bipolar electron transport. Phys. Rev. Lett. **93**(23), 236802 (2004)
13. Swart, I., Sun, Z., Vanmaekelbergh, D., Liljeroth, P.: Hole-induced electron transport through core-shell quantum dots: a direct measurement of the electron-hole interaction. Nano Lett. **10**, 1931–1935 (2010)
14. Tersoff, J., Hamann, D.R.: Theory of the scanning tunneling microscope. Phys. Rev. B **31**(2), 805 (1985)
15. Delerue, C., Lannoo, M., Allan, G.: Excitonic and quasiparticle gaps in Si nanocrystals. Phys. Rev. Lett. **84**(11), 2457–2460 (2000)
16. Niquet, Y.M., Lherbier, A., Fernandez-Serra, M.V., Blase, X., Delerue, C.: Electronic structure of semiconductor nanowires. Phys. Rev. B **73**(16), 165319 (2006)
17. Stomp, R., Miyahara, Y., Schaer, S., Sun, Q., Guo, H., Grutter, P., Studenikin, S., Poole, P., Sachrajda, A.: Detection of single-electron charging in an individual in as quantum dot by noncontact atomic-force microscopy. Phys. Rev. Lett. **94**(5), 056802 (2005)
18. Uchida, K.: In: Waser, R. (ed.) Nanoelectronics and Information Technology: Advanced Electronic Materials and Novel Devices. Wiley, New York (2003)
19. Azuma, Y., Kanehara, M., Teranishi, T., Majima, Y.: Single electron on a nanodot in a double-barrier tunneling structure observed by noncontact atomic-force spectroscopy. Phys. Rev. Lett. **96**(1), 016108 (2006)
20. Gross, L., Mohn, F., Liljeroth, P., Repp, J., Giessibl, F.J., Meyer, G.: Measuring the charge state of an adatom with noncontact atomic force microscopy. Science **324**(5933), 1428–1431 (2009)
21. Morita, S., Giessibl, F.J., Wiesendanger, R. (eds.): Noncontact Atomic Force Microscopy. Springer, Berlin (2009)
22. Giessibl, F.J.: Advances in atomic force microscopy. Rev. Mod. Phys. **75**(3), 949–983 (2003)
23. Liljeroth, P.: Zeijlmans van Emmichoven, P.A., Hickey, S.G., Weller, H., Grandidier, B., Allan, G., Vanmaekelbergh, D.: Density of states measured by scanning-tunneling spectroscopy sheds new light on the optical transitions in PbSe nanocrystals. Phys. Rev. Lett. **95**(8), 086801 (2005)
24. Millo, O., Katz, D., Cao, Y.W., Banin, U.: Imaging and spectroscopy of artificial-atom states in core/shell nanocrystal quantum dots. Phys. Rev. Lett. **86**(25), 5751–5754 (2001)
25. Liljeroth, P., Overgaag, K., Urbieta, A., Grandidier, B., Hickey, S.G., Vanmaekelbergh, D.: Variable orbital coupling in a two-dimensional quantum-dot solid probed on a local scale. Phys. Rev. Lett. **97**(9), 096803 (2006)
26. Jdira, L., Overgaag, K., Gerritsen, J.: Vanmaekelbergh, D.l., Liljeroth, P., Speller, S.: Scanning tunnelling spectroscopy on arrays of CdSe quantum dots: response of wave functions to local electric fields. Nano Lett. **8**(11), 4014–4019 (2008)
27. Overgaag, K., Liljeroth, P., Grandidier, B., Vanmaekelbergh, D.: Scanning tunneling spectroscopy of individual PbSe quantum dots and molecular aggregates stabilized in an inert nanocrystal matrix. ACS Nano **2**(3), 600–606 (2008)
28. Overgaag, K., Vanmaekelbergh, D., Liljeroth, P., Mahieu, G., Grandidier, B., Delerue, C., Allan, G.: Electron-phonon coupling and intervalley splitting determine the linewidth of single-electron transport through PbSe nanocrystals. J. Chem. Phys. **131**, 224510 (2009)

29. Justo, Y., Moreels, I., Lambert, K., Hens, Z.: Langmuir-Blodgett monolayers of colloidal lead chalcogenide quantum dots: morphology and photoluminescence. Nanotechnol. **21**, 295606 (2010)
30. Nguyen, T.H., Habinshuti, J., Justo, Y., Gomes, R., Mahieu, G., Godey, S., Nys, J.P., Carillo, S., Hens, Z., Robbe, O., Turrell, S., Grandidier, B.: Charge carrier identification in tunneling spectroscopy of core-shell nanocrystals. Phys. Rev. B **84**(19), 195133 (2011)
31. Alperson, B., Rubinstein, I., Hodes, G., Porath, D., Millo, O.: Energy level tunneling spectroscopy and single electron charging in individual CdSe quantum dots. Appl. Phys. Lett. **75**, 1751–1753 (1999)
32. Millo, O., Katz, D., Cao, Y.W., Banin, U.: Scanning tunneling spectroscopy of InAs nanocrystal quantum dots. Phys. Rev. B **61**(24), 16773–16777 (2000)
33. Katz, D., Millo, O., Kan, S.-H., Banin, U.: Control of charging in resonant tunneling through InAs nanocrystal quantum dots. Appl. Phys. Lett. **79**(1), 117–119 (2001)
34. Katz, D., Wizansky, T., Millo, O., Rothenberg, E., Mokari, T., Banin, U.: Size-dependent tunneling and optical spectroscopy of CdSe quantum rods. Phys. Rev. Lett. **89**(8), 086801 (2002)
35. Steiner, D., Katz, D., Millo, O., Aharoni, A., Kan, S., Mokari, T., Banin, U.: Zero-dimensional and quasi one-dimensional effects in semiconductor nanorods. Nano Lett. **4**(6), 1073–1077 (2004)
36. Bernard, R., Comtet, G., Dujardin, G., Huc, V., Mayne, A.J.: Imaging and spectroscopy of individual CdSe nanocrystals on atomically resolved surfaces. Appl. Phys. Lett. **87**(5), 053114 (2005)
37. Ou, Y.C., Cheng, S.F., Jian, W.B.: Size dependence in tunneling spectra of PbSe quantum-dot arrays. Nanotechnology **20**(28), 285401 (2009)
38. Ou, Y.-C., Wu, J.-J., Fang, J., Jian, W.-B.: Probing capacitive coupling and collective transport in PbSe quantum-dot arrays using scanning tunneling spectroscopy. J. Phys. Chem. C **113**(18), 7887–7891 (2009)
39. Allan, G., Delerue, C.: Confinement effects in PbSe quantum wells and nanocrystals. Phys. Rev. B **70**(24), 245321 (2004)
40. Klein, J., Léger, A., Belin, M., Défourneau, D., Sangster, M.J.L.: Inelastic-electron-tunneling spectroscopy of metal-insulator-metal junctions. Phys. Rev. B **7**(6), 2336–2348 (1973)
41. Wise, F.W.: Lead salt quantum dots: the limit of strong quantum confinement. Acc. Chem. Res. **33**(11), 773–780 (2000)
42. Steiner, D., Aharoni, A., Banin, U., Millo, O.: Level structure of InAs quantum dots in two-dimensional assemblies. Nano Lett. **6**(10), 2201–2205 (2006)
43. Repp, J., Meyer, G., Paavilainen, S., Olsson, F.E., Persson, M.: Scanning tunneling spectroscopy of Cl vacancies in NaCl films: strong electron-phonon coupling in double-barrier tunneling junctions. Phys. Rev. Lett. **95**(22), 225503 (2005)
44. Berthe, M., Urbieta, A., Perdigao, L., Grandidier, B., Deresmes, D., Delerue, C., Stievenard, D., Rurali, R., Lorente, N., Magaud, L., Ordejon, P.: Electron transport via local polarons at interface atoms. Phys. Rev. Lett. **97**(20), 206801 (2006)
45. Jdira, L., Overgaag, K., Stiufiuc, R., Grandidier, B., Delerue, C., Speller, S., Vanmaekelbergh, D.: Linewidth of resonances in scanning tunneling spectroscopy. Phys. Rev. B **77**(20), 205308 (2008)
46. Yang, A.L., Wu, H.Z., Li, Z.F., Qiu, D.J., Chang, Y., Li, J.F., McCann, P.J., Fang, X.M.: Raman scattering study of PbSe grown on (111) BaF2 substrate. Chin. Phys. Lett. **17**(8), 606–608 (2000)
47. Klein, M.C., Hache, F., Ricard, D., Flytzanis, C.: Size dependence of electron-phonon coupling in semiconductor nanospheres: the case of CdSe. Phys. Rev. B **42**(17), 11123–11132 (1990)
48. Saviot, L., Champagnon, B., Duval, E., Kudriavtsev, I.A., Ekimov, A.I.: Size dependence of acoustic and optical vibrational modes of CdSe nanocrystals in glasses. J. Non-Cryst. Sol. **197**, 238–246 (1996)

49. Sun, Z., Swart, I., Delerue, C., Vanmaekelbergh, D., Liljeroth, P.: Orbital and charge-resolved polaron states in CdSe dots and rods probed by scanning tunneling spectroscopy. Phys. Rev. Lett. **102**(19), 196401 (2009)
50. Rainò, G., Stöferle, T., Moreels, I., Gomes, R., Kamal, J.S., Hens, Z., Mahrt, R.F.: Probing the wave function delocalization in CdSe/CdS dot-in-rod nanocrystals by time- and temperature-resolved spectroscopy. ACS Nano **5**(5), 4031–4036 (2011)

Chapter 9
Electron Paramagnetic Resonance Based Spectroscopic Techniques

Pavel G. Baranov, Nikolai G. Romanov, Celso de Mello Donegá, Sergei B. Orlinskii and Jan Schmidt

Abstract This chapter addresses the use of electron paramagnetic resonance based spectroscopic techniques to study nanostructures. Particular attention is given to high frequency electron spin echo, electron-nuclear double resonance and optically detected magnetic resonance spectroscopy.

9.1 Fundamentals

Magnetic resonance methods are the basic techniques for studying spin phenomena in condensed matter and biological systems. Spin is a purely quantum-mechanical object and spin phenomena are beginning to play a crucial role in the development of devices based on nanostructures. As a result, magnetic resonance techniques have attracted increasing interest in the last few decades.

Electron paramagnetic resonance (EPR) was discovered by Zavoisky in 1944 [1, 2]. Since then, EPR based spectroscopic techniques have evolved into one of the most informative tools for investigating defects and dopants in solids. These techniques offer a uniquely sensitive probe of the chemical identity, local structural order, atomic-scale environment, and electron density distributions of defects and impurities, and have thus been used to unravel the microscopic structure of many intrinsic and impurity defects in solids [3–7].

P.G. Baranov (✉) · N.G. Romanov
Ioffe Physical-Technical Institute, St. Petersburg 194021, Russia
e-mail: pavel.baranov@mail.ioffe.ru

C. de Mello Donegá
Debye Institute for Nanomaterials Science, Utrecht University, Utrecht, The Netherlands

S.B. Orlinskii
Federal Center of Shared Facilities, Kazan State University, Kazan 420008, Russia

J. Schmidt
Huygens Laboratory, Leiden University, 2300 RA Leiden, The Netherlands

C. de Mello Donegá (ed.), *Nanoparticles*,
DOI 10.1007/978-3-662-44823-6_9

There are a variety of elegant techniques in which higher sensitivity and resolution are obtained by exciting two resonance transitions in the sample (double-resonance techniques). The great advantages of these techniques are that, in contrast to optical methods, they allow the identification of the dopants and provide information about the spatial distribution of the electronic wave function. This latter aspect is particularly attractive because it allows for a quantitative measurement of the effect of confinement on the shape and properties of the electron or hole wave function. In the following sections, we briefly address the fundamentals of three important EPR based spectroscopic techniques. The application of these techniques to nanomaterials is illustrated in Sect. 9.2.

9.1.1 Electron Spin Echo Detected Electron Paramagnetic Resonance (ESE-EPR)

In a conventional EPR experiment, the sample is placed in a microwave cavity and a magnetic field is applied to the sample such that the microwave magnetic field is normal to the static magnetic field. The ground state is normally in thermal equilibrium and so, when the microwave energy equals the separation between the magnetically split spin sublevels of the magnetic ion or defect, resonant absorption of microwave power occurs and is detected [2].

The spin echo experiment is based on the concept of an inhomogeneous broadened EPR line, which can be considered as composed of "homogeneous spin packets" (Fig. 9.1a). Microwave radiation is applied with a frequency ω_0 and polarized in the *xy*-plane. The oscillating B_1 field of this radiation can be decomposed into two counter-rotating components, one of which is rotating in the same direction as the Larmor precession of spins in magnetic field. Hence, in the rotating frame, B_1 is a stationary field, defined along *x*' [Fig. 9.1a (i)]. If the microwave field is strong, the resulting magnetic field is oriented along B_1 for every spin packet. During the presence of the microwave field the magnetization of the various spin packets, M_i, will precess around B_1 with a frequency $\omega_1 = \gamma_e B_1$, where γ_e is the giromagnetic ratio. When the duration of the microwave radiation is just enough to flip the magnetization M_i into the *xy*-plane, the pulse is defined as a $\pi/2$ pulse. Since the different spin packets have different offset frequencies ω_i', they start to dephase immediately after the pulse [Fig. 9.1a (ii)]. This process is called the Free Induction Decay (FID). From this FID, however, an echo can be generated by a second microwave pulse, applied at a time τ after the first pulse, which rotates the spins over π [Fig. 9.1a (iii)]. This π pulse is equivalent to a reflection of the dephased pattern in the x'z-plane. The original precession frequencies and the precession direction, however, remain unaltered. The result is that the spin packets refocus after the same time τ, into a macroscopic magnetic moment which produces the echo [Fig. 9.1a (iv)]. As an illustrative example, the ESE-detected EPR spectrum of Li-doped ZnO nanocrystals (NCs) is shown in Fig. 9.1b. This spectrum will be discussed in more detail below (9.2.1.1).

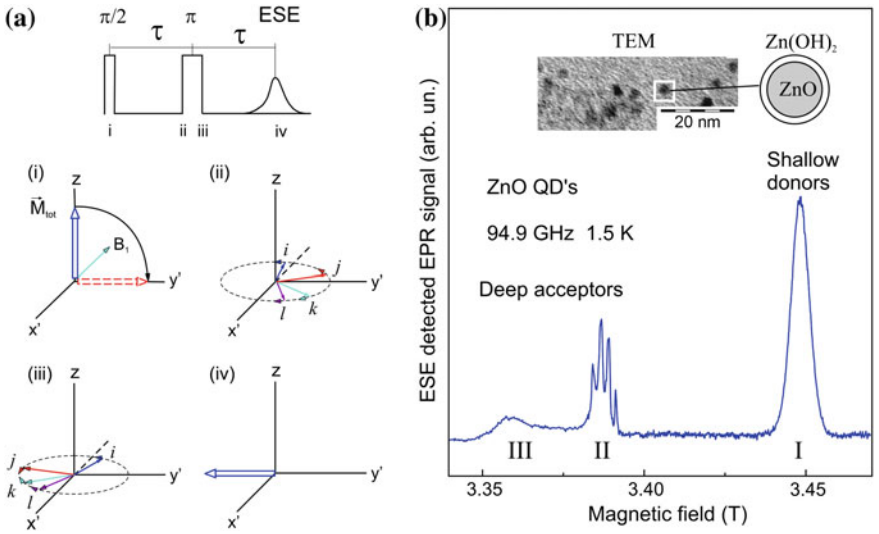

Fig. 9.1 **a** Illustration of two pulse electron spin echo (ESE) experiment: (*i*) magnetization of spin packets l,j,k, and l during the π/2 pulse, (*ii*) during the waiting time τ, (*iii*) after a pulse π, (*iv*) at the time after echo (time τ after the pulse). **b** ESE-detected EPR spectrum at 94.9 GHz and T = 1.5 K of a dry powder sample of Li-doped ZnO nanocrystals with an average diameter of 3.4 nm after 30 min UV irradiation. The inset in the top part of the figure shows a Transmission Electron Microscopy (TEM) image of the nanocrystals (*left*) and a model depicting its ZnO/Zn(OH)$_2$ core–shell structure (*right*)

9.1.2 Electron-Nuclear Double Resonance (ENDOR)

Electron-nuclear double resonance (ENDOR) is a magnetic resonance spectroscopic technique for the determination of hyperfine interactions between electrons and nuclear spins [2]. ENDOR can be considered as a method for increasing the resolution of EPR spectra and as a technique for improving NMR sensitivity for a limited number of nuclei that are located near the paramagnetic defect. There are two principal techniques. In continuous-wave ENDOR the intensity of an electron paramagnetic resonance signal, partially saturated with microwave power, is measured as radiofrequency is applied. In pulsed ENDOR the radiofrequency is applied as pulses and the EPR signal is detected as a spin-echo. In each case an enhancement of the EPR signal is observed when the radiofrequency is in resonance with the coupled nuclei and the nuclear-spin transitions are detected as changes in the EPR signal.

9.1.3 Optically Detected Magnetic Resonance (ODMR)

In optically detected magnetic resonance (ODMR), the population redistribution among magnetic sub-states, in passage through magnetic resonance in the ground or

excited state of a paramagnetic centre, produces a change in some aspect of either emitted or absorbed light associated with the centre [3]. The scaling up of the EPR detection from the microwave to the optical region renders these optical EPR methods extremely sensitive.

The resonance conditions are created in the same way as in conventional EPR experiment but instead of direct measurements of microwave resonant absorption, microwave induced changes in optical processes (viz., luminescence intensity or polarization, magnetic circular dichroism in optical absorption) are detected. Optical absorption or emission transitions are in some degree dependent on the population of the magnetic (spin) sublevels of the system under investigation. Therefore, magnetic resonance, by changing the populations of the spin sublevels, can induce changes in optical absorption and/or emission transitions (intensity or polarization). ODMR is thus a kind of a "trigger" detection since absorption of a microwave quantum results in additional emission (or absorption) of an optical photon with several orders of magnitude higher energy. This results in a huge increase in sensitivity, making it possible to detect a very small number of spins, down to the single spin level. In addition, ODMR provides spatial selectivity since, opposite to conventional EPR, magnetic resonance is measured only in optically active regions of the sample. Another selectivity channel is provided by appropriate selection of an optical spectral range in which ODMR is measured. Due to these advantages ODMR can be effectively applied for a study of nanostructures (see [6, 7] and references therein).

9.2 Applications to Nanomaterials

Understanding the structure and constituents of defects in nanostructures is crucially important since defects and impurities can greatly affect the properties of nanomaterials. EPR spectroscopy has been widely applied to characterize paramagnetic ions (*e.g.*, Mn^{2+}) in nanocrystals (NCs), as it allows dopants at the surface to be distinguished from those in the interior of the NC [8]. During the last two decades high-frequency (high-field) EPR and in particular pulse EPR and pulse ENDOR spectroscopy developed to a new fast advancing field in magnetic resonance spectroscopy [4]. These techniques were shown to be excellent tools for the investigation of the electronic properties of semiconductor NCs, allowing the interaction between the exciton and paramagnetic impurities to be probed, as well as the observation of photoexcited carriers bound to impurities (i.e., donor and acceptor centers) [5, 6]. In combination with optical excitation, EPR (photo-EPR) can also yield information regarding optical transitions and energy-level positions, thus providing a bridge between optical and magnetic resonance spectroscopy. Direct measurements of EPR and ENDOR in nanostructures are often difficult because of the small total number of spins, therefore ODMR is much better suited for such systems [6, 7]. Electron paramagnetic resonance based spectroscopic techniques have been successfully applied to a variety of nanocrystalline materials

(e.g., colloidal InP and CdTe NCs [7], silver halide NCs embedded in an alkali halide matrix [9], free-standing diamond NCs [10–12], etc.). One selected case (viz., ZnO nanocrystals) will be addressed below as an illustrative example.

9.2.1 ZnO Nanocrystals

ZnO offers a unique combination of high band gap energies, cohesion and exciton stability. ZnO quantum dots (QDs) are particularly attractive since the confinement of the electronic wave function allows the optical and electronic properties to be tuned. Doped ZnO nanocrystals (NCs), which can be easily processed at temperatures much lower than those for bulk ZnO crystals, are of particular interest due to their potential use in light-emitting and photovoltaic devices. In the next sections we will discuss experimental results obtained on powder samples of free-standing hydroxyl-capped ZnO NCs with average diameter ranging from 2.2 to 6 nm. These NCs were prepared by using a colloidal synthesis method based on the hydrolysis of Zn^{2+} ions in absolute alcohols [5]. A transmission electron microscopy (TEM) image of a representative sample and a model of the $ZnO/Zn(OH)_2$ core–shell structure are shown in Fig. 9.1b above.

9.2.1.1 The Identification of the Binding Core of Shallow Donors and Deep Acceptors in ZnO Nanocrystals by EPR and ENDOR

Figure 9.1b shows the ESE-detected EPR spectrum of a dry powder sample of Li-doped ZnO NCs with an average diameter of 3.4 nm. The EPR spectrum appears after illumination with above-band-gap light during 30 min at 1.6 K and persists at low temperature after switching off the light. The signal I is assigned to a shallow donor. Its average g-value $g_{av} = 1.9666$ differs somewhat from the $g_{\|} = 1.9569$ and $g_{\perp} = 1.9552$ values obtained for the interstitial-hydrogen donor in a single crystal of ZnO. The EPR signals labelled (II) and (III) are assigned to deep acceptors. A prerequisite for the observation of the EPR signal of the unpaired spin of shallow donors at liquid-helium temperatures is that the ZnO NCs are first illuminated with above-band-gap light. This observation shows that there must be deep acceptors present in the nanocrystals that capture the thermally excited donor electrons at room temperature. Apparently these electrons remain frozen at the acceptor when the material is cooled in the dark to low temperature. The above-band-gap light transfers the electron from the acceptor to the donor and makes both sites paramagnetic. The spectrum disappears when the temperature is increased above 200 K.

We will focus on the EPR signal I assigned to the shallow donor. The signal is ascribed to a donor because g_{av} is smaller than the g-value of a free electron.The shallow character becomes clear from the dependence of g_{av} on the size of the NCs, as will be discussed in Sect. 9.2.1.2. This shift towards the free-electron g_e-value with decrease of the NC size is caused by the confinement of the hydrogen-like

1s-type wave function of shallow donors when their Bohr radius becomes comparable to the size of the NC.

The EPR spectrum in Fig. 9.1b does not provide information on the chemical nature of the donor since no resolved hyperfine (HF) structure is observed, as is the case for the In and Ga shallow donors in ZnO bulk crystals. To identify the binding core, ENDOR experiments were performed. Figure 9.2 shows the ESE-detected ENDOR transitions observed on the EPR signal I (Fig. 9.1) of the shallow donor in Li-doped ZnO NCs with radius of 1.7 nm. Similar experiments were carried out on the EPR signal of the shallow donors in Na-doped ZnO NCs with radius of 1.7 nm and in Al-doped ZnO NCs with radius of 2.5 nm (Fig. 9.3). The pulse sequence for the ENDOR experiments is shown in the top panels of Figs. 9.2 and 9.3. In the pulsed ENDOR experiment, a Mims-type pulse sequence was used. It consists of three $\pi/2$ microwave pulses with separation τ and T between the first and the second and the second and the third pulse, respectively, and creates a stimulated echo at a time τ after the last pulse. A radio-frequency (RF) pulse, which is applied between the second and the third microwave pulse, induces a change in the intensity of the stimulated echo when this RF pulse is resonant with a nuclear magnetic resonance (NMR) transition. The ENDOR spectra are obtained by monitoring the stimulated echo intensity as a function of the frequency of the RF field.

To understand these results we consider the isotropic HF interaction or Fermi contact term a_i which reflects the spin density of the donor electron wave function at the site of the nucleus (r_i)

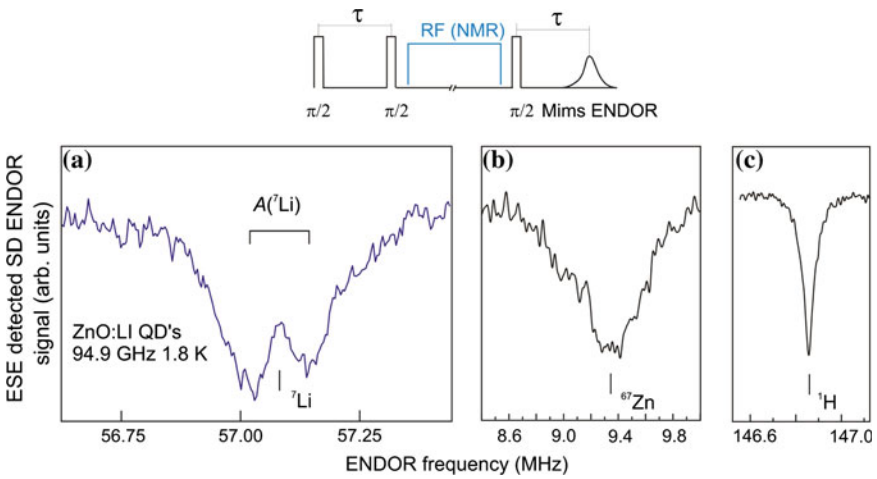

Fig. 9.2 ESE-detected ENDOR transitions of the ^{7}Li (**a**), ^{67}Zn (**b**), and ^{1}H (**c**) nuclear spins as observed in the EPR signal I (see Fig. 9.1) of the shallow donors in Li-doped ZnO nanocrystals with an average size of 3.4 nm. The Zeeman frequency of ^{7}Li, ^{67}Zn, and ^{1}H are marked by bars. The pulse sequence for the ENDOR experiments is shown in the top panel

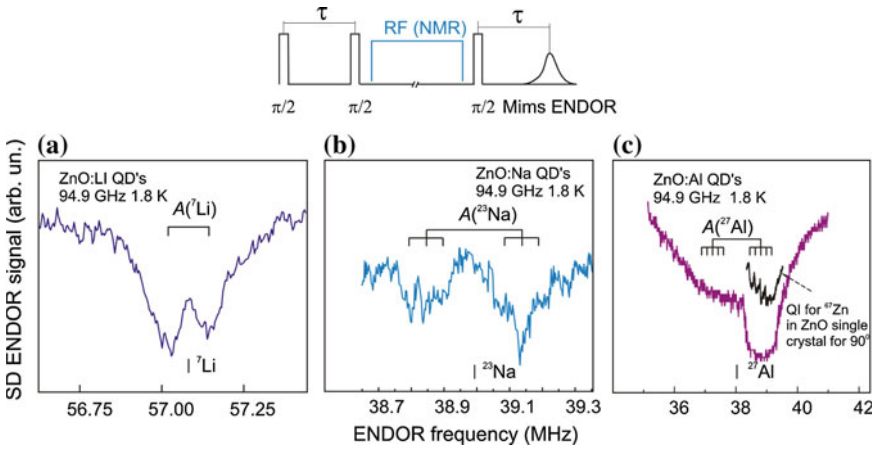

Fig. 9.3 ESE-detected ENDOR transitions as observed in the EPR signal I (see Fig. 9.1b) of the shallow donors in Li-doped ZnO NCs (**a**) and Na-doped ZnO NCs (**b**) with an average size of 3.4 nm, and Al-doped ZnO NCs with an average size of 5 nm **c** recorded at 94.9 GHz and T = 1.8 K. The ENDOR transitions are symmetrically placed around the Zeeman frequency of ^{7}Li, ^{23}Na, and ^{27}Al, respectively (marked by bars). The pulse sequence for the ENDOR experiments is shown in the top panel

$$a_i = (8\pi/3) g_e \beta_e g_{ni} \beta_n |\Psi(r_i)|^2 \tag{9.1}$$

where g_e is the electronic g-factor, β_e is the electronic Bohr magneton, g_{ni} is the g-factor of nucleus i, and β_n is the nuclear magneton. The related ENDOR transition frequencies are

$$\nu_{ENDOR} = h^{-1} |g_{ni} \beta_n B_0 \pm a_i/2| \tag{9.2}$$

Equation (9.2) predicts that each nucleus i gives rise to two ENDOR transitions symmetrically placed around its nuclear Zeeman frequency $g_{ni}\ \beta_n B_0/h$ when the quadrupole interaction is neglected and when $a_i < g_{ni}\ \beta_n B_0$. The ENDOR signals in Figs. 9.2 and 9.3 are symmetrically placed around the Zeeman frequencies of ^{7}Li, ^{23}Na, and ^{27}Al, respectively, which gives an unambiguous identification of the shallow donor core as Li-, Na-, or Al-related centres. Moreover, the observed HF splitting gives direct information about the density of unpaired electron spin of the shallow donor at the Li, Na and Al nuclei since the isotropic HF splitting is proportional to the wavefunction density. Further, it is seen in Fig. 9.2b that symmetrically around the Zeeman frequency of ^{67}Zn (I = 5/2, abundance 4.1 %) at 9.2 MHz a broad, unresolved set of ENDOR lines of ^{67}Zn spins is present. From the multitude of lines it is clear that we are indeed dealing with a delocalised electron of a shallow donor that interacts with a large number (tens) of ^{67}Zn nuclei [5]. The box-like form of the ENDOR spectra in Figs. 9.3b, c is explained by the quadrupole interaction of the ^{23}Na and ^{27}Al nuclei, which gives rise to three and five unresolved

ENDOR lines, respectively. In addition, ENDOR lines exactly at the Zeeman frequency of ^{1}H were found in these ZnO NCs (Fig. 9.2c). From the width of the line a ^{1}H HF interaction smaller than 60 kHz can be deduced. This should be compared to the hyperfine splitting of 1.4 MHz between the two ENDOR lines previously observed on the hydrogen-related shallow donor in bulk ZnO crystals [5]. This shows that the observed ENDOR lines originate in the hydrogen atoms present in the $Zn(OH)_2$ capping layer where the density of the electronic wave function is very small.

The EPR signal (II) in Fig. 9.1 exhibits a nearly isotropic hyperfine splitting that suggests a hyperfine interaction with a nucleus of spin $I = 3/2$ with an almost 100 % abundance. This observation favours a Na-related centre and indeed the ENDOR spectrum confirms this assignment. The conclusion that this deep Na-related centre is located close to or at the $ZnO/Zn(OH)_2$ interface is drawn from the observation that the ENDOR signals of both the ^{23}Na ($I = 3/2$) and the ^{1}H ($I = 1/2$) nuclei can be observed in the EPR signal II. The line width of 1.0 MHz is about 8 times larger than that of the ^{1}H ENDOR signals observed in the ESE-detected EPR signal of the Li-related donor (Fig. 9.2c). This shows that the density of the electronic wave function of the Na-related acceptor is relatively large in the $Zn(OH)_2$ capping layer. The main contribution to the EPR signal III (Fig. 9.1) comes from deep zinc vacancy acceptors. Zinc vacancies may be introduced during the growth of the NCs. This conclusion is supported by the results of ODMR measurements (see 9.2.1.4 below).

Figure 9.4a shows the ^{67}Zn ENDOR spectra in ZnO NCs of various sizes. The remarkable observation in Fig. 9.4 is that upon reduction of the size of the ZnO NCs the distribution of ENDOR lines broadens and a dip develops around the Zeeman frequency of the ^{67}Zn nuclear spins. The dip becomes more prominent and broader

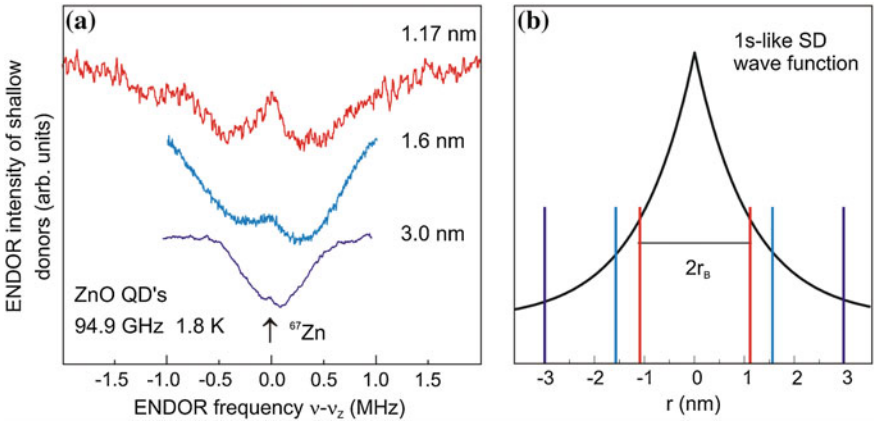

Fig. 9.4 **a** ENDOR spectra of the ^{67}Zn nuclear spins in ZnO NCs with radii of 1.17, 1.6 and 3.0 nm recorded at 94.9 GHz and T = 1.8 K. Each spectrum consists of many unresolved lines placed symmetrically around the Zeeman frequency (*marked by arrows*) of the ^{67}Zn nuclear spins. **b** Schematic representation of the 1 s-like wave function density for shallow donors

when the radius of the ZnO core is reduced from 3.0 to 1.6–1.17 nm. The broadening of the ENDOR signal indicates that the maximum density of the electronic wave function increases when reducing the size of the NCs. The disappearance of the ENDOR signals close to the ^{67}Zn Zeeman frequency shows that remote shells are missing in the small NCs as illustrated by bars in Fig. 9.4b.

9.2.1.2 Probing the Wave Function of Shallow Donors in ZnO Nanocrystals and Confinement Effects

The ENDOR studies allow the effects of confinement on the spatially extended wave function of the shallow donor to be probed by measuring the isotropic hyperfine (HF) interaction, which reflects the spin density at the site of the nucleus, and by varying the particle size in the quantum-size regime [5]. The ^{7}Li ENDOR signals are excellently suited for this purpose. Figure 9.5 shows the values of the isotropic HF interaction A of the ^{7}Li nuclear spin (a) and the wavefunction density of the shallow Li-related donor at the interface of the ZnO core (b) as a function of the NC size. The error bars in the values of A are estimated from the noise in the ENDOR spectra and the size distribution of the particles derived from TEM and powder X-ray diffraction measurements. The dashed line is a fit to the measured

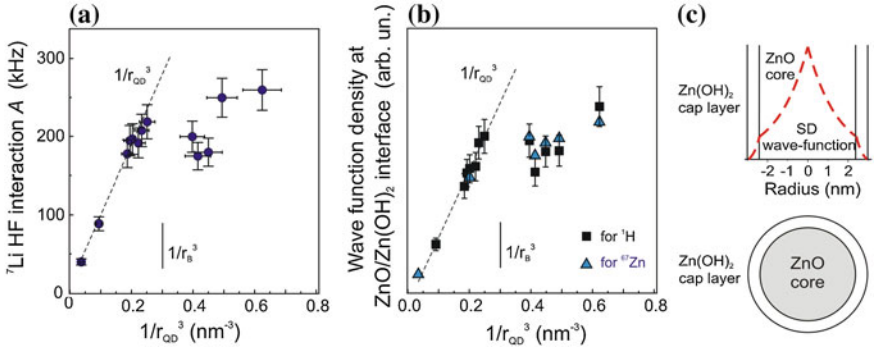

Fig. 9.5 **a** Isotropic hyperfine interaction A of the ^{7}Li nuclear spin of the shallow Li-related donors in ZnO NCs with radii between 3.0 and 1.1 nm. The *black circles* indicate the hyperfine splitting as observed in the ENDOR spectra at T = 1.2 K. The error bar in the values of A_{iso} is estimated from the noise in the ENDOR spectra. The variation in the size of the NCs is derived from Transmission Electron Microscopy and powder X-Ray Diffraction measurements. The *dashed line* is a fit to the measured values of A for NCs with radii between 3.0 and 1.5 nm using the function R^{-3}. **b** Variation of the wave function density at the interface of the ZnO core and the $Zn(OH)_2$ capping layer for the NCs as calculated from the dip in ENDOR of the ^{7}Li nuclear spin (*core side, squares*) and from the width of the ENDOR line of the ^{1}H nuclear spins in the $Zn(OH)_2$ capping layer (*triangles*). The dashed line is a fit to the measured values for NCs with radii between 3.0 and 1.5 nm using the function $*R^{-3}$. **c** Sketch of the wave function of the shallow donor in a ZnO quantum dot capped by a $Zn(OH)_2$ layer and a model of the ZnO/$Zn(OH)_2$ core–shell structure

values for NCs with radii between 3.0 and 1.5 nm using a function proportional to r^{-3}. The experimental results follow quite closely this dependence down to R = 1.5 nm, a value which is equal to the Bohr radius of the shallow donor, while for smaller radii a considerable deviation is observed. A sketch of the hydrogen-like wave function in ZnO quantum dots together with a model of the ZnO/$Zn(OH)_2$ core–shell structure are shown in Fig. 9.5c. It is thus clear that the model based on the effective-mass approximation does not yield an appropriate description of the electronic wave function when the NC radius is reduced below the Bohr radius. We suggest that molecular, cluster-type calculations should be carried out to describe the observed behaviour.

The shallow character of the Li-related donor is also visible in the dependence of the g-factor on the size of the ZnO NC (Fig. 9.6). The shift of the g-factor towards the free-electron value upon size reduction is caused by the spatial confinement of the shallow donors when the NC size becomes comparable to the Bohr radius of their hydrogen-like 1s-type wave functions. The effect is explained by the reduction of the admixture of valence-band states and higher-lying conduction bands into the

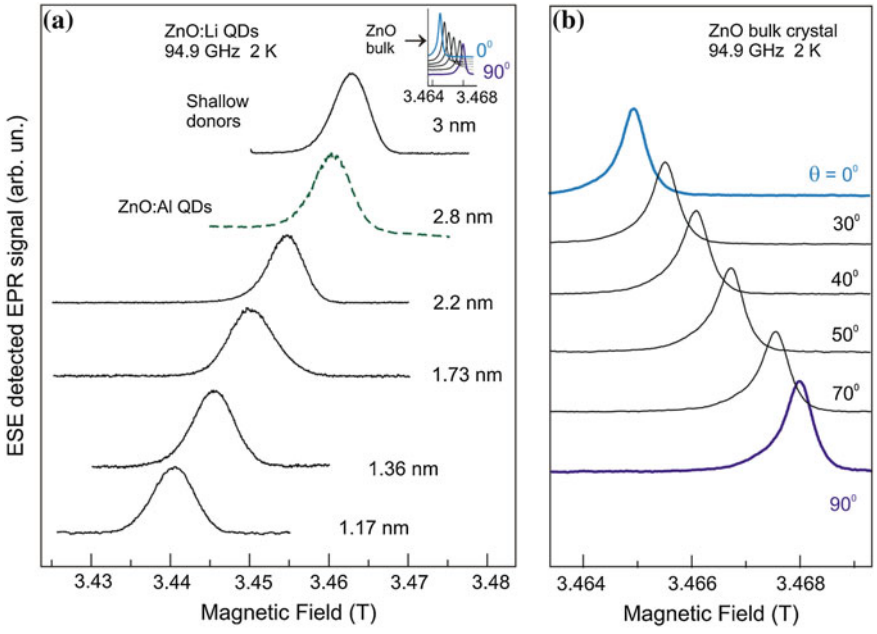

Fig. 9.6 **a** ESE-detected EPR spectra of shallow donors (SDs) in ZnO NCs with radii of 1.17, 1.36, 1.73, 2.2, 2.8 and 3 nm recorded at 94.9 GHz and T = 2 K. The solid lines are the ESE-detected EPR spectra of ZnO:Li NCs. The *dashed line* is the ESE-detected EPR spectra of ZnO:Al NCs. The inset shows the angular dependence of the ESE-detected EPR spectra of H-related SDs in ZnO bulk crystal presented on the same magnetic-field scale. This dependence in larger magnetic-field scale is presented in **b**, θ is the angle between the magnetic field direction and the c-axis of ZnO crystal

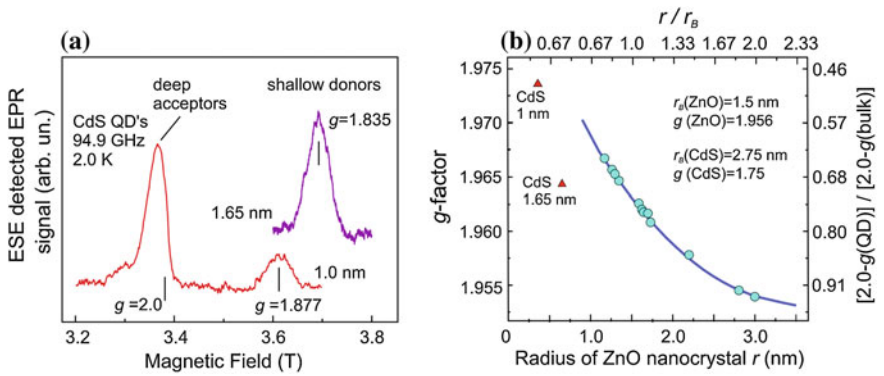

Fig. 9.7 **a** ESE-detected EPR spectra of SDs in CdS NCs with radii of 1.65 and 1.0 nm recorded at 94.9 GHz and T = 2.0 K. **b** Dependence of the *g*-factor of the shallow donor on the size of the ZnO NC. The upper scale gives the NC radius normalized to the Bohr radius r_B of the SD in the related bulk semiconductor. The right scale gives a *g*-factor shift of the SD in NC from $g = 2.0$ normalized to that for the bulk material. The filled tringles indicate the *g*-factor shift in CdS NCs on the normalized scale

lowest conduction band by the increase of the band-gap energy and the energy of higher-lying conduction bands upon the reduction of the NC size. For comparison, the anisotropic EPR spectra of the shallow hydrogen-related donors in a bulk ZnO crystal are presented in the top of Fig. 9.6 for several orientations of the magnetic field with respect to the *c*-axis. A line width close to that in ZnO NCs is obtained by averaging of the signal, under the assumption that the ZnO NCs are randomly oriented. A similar effect is observed in free-standing polyphosphate-capped CdS NCs with diameters of 2 and 3.3 nm (Fig. 9.7). The influence of the confinement effect on the *g*-factor of these shallow donors is visible in Fig. 9.7. The dependence of the *g*-factor of the shallow Li-related donor on the size of the ZnO NCs is also displayed for comparison. It is clear that the data on ZnO and CdS NCs cannot be fitted with the same dependence. It remains for theoreticians to explain these different behaviours.

9.2.1.3 Dynamic Nuclear Polarization of Nuclear Spins in ZnO Nanocrystals

Dynamic nuclear polarization (DNP) is a general method of enhancing by several orders the polarization of a nuclear spin system in interaction with an electron spin system by saturation of a suitable resonance of the combined system. The nuclear spins in a QD become polarized by the Overhauser effect when the EPR transitions of the shallow donor are excited by microwave irradiation [5]. These polarized nuclear spins create an internal magnetic field and, as a result, the resonance line of the electron spins, subjected to the microwave irradiation, shifts to a lower external field value resulting in a hole and an antihole in the inhomogeneously broadened

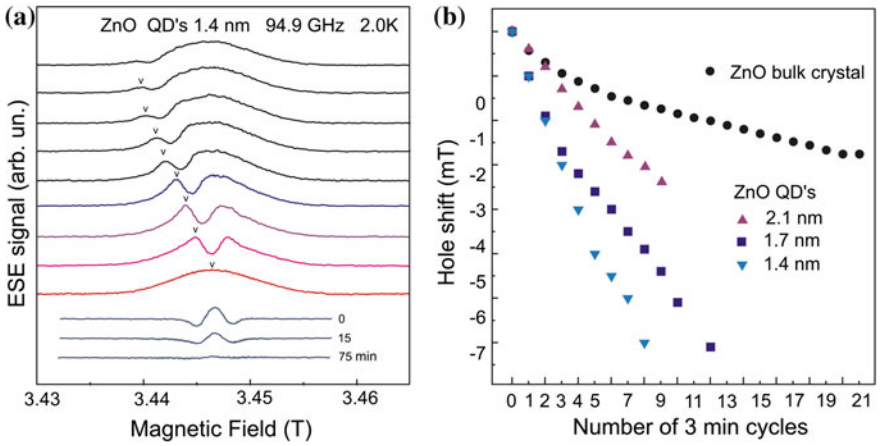

Fig. 9.8 **a** Shift of the hole in the EPR transition of the shallow Li donor in ZnO NCs with radius of 1.4 nm induced by cw microwave irradiation at 94.9 GHz and T = 2 K. The *lowest* EPR line is recorded without pre-irradiation. The second recording from the *bottom* is obtained after cw microwave irradiation during 3 min at the centre of the unperturbed line. The next curves are observed after cw microwave irradiation during 3 min at the maximum of the antihole of the previous recording. Finally, the antihole stabilizes at a position shifted by 7 mT with respect to the original position. The spectrum labelled by (0) represents the difference between two *upper curves*. Curves (15) and (75) are recorded 15 and 75 min after the pre-irradiation, respectively (the upper unperturbed line was subtracted from each spectrum). **b** Shift of the hole and the antihole versus the number of 3-min cycles of cw microwave irradiation in the 94.9 GHz EPR line of shallow Li-related donors in ZnO NCs with radii of 1.4, 1.7 and 2.1 nm, and that of the shallow H donors in a ZnO single crystal. $T = 2$ K

EPR line. Figure 9.8a shows the shift of the hole in the EPR transition of the shallow Li donor in ZnO NCs with a radius of 1.4 nm induced by exposing the samples to subsequent pre-irradiations with continuous wave (cw) microwaves. It is seen that slowly the hole and the "antihole" decrease and the EPR spectrum recovers its initial unperturbed form. The maximum shift of the antihole depends on the NC size (see Fig. 9.8b).

The creation of the hole and antihole in the EPR line of shallow donors in ZnO NCs is caused by dynamic nuclear polarization (DNP) of the ^{67}Zn ($I = 5/2$) nuclear spins and of the ^{1}H ($I = 1/2$) nuclear spins in the $Zn(OH)_2$ capping layer. Since the line width of the Li donor in a sample of randomly oriented ZnO NCs depends to a large extent on the anisotropy of the g-tensor, the hole in the line corresponds to electron spins of Li donors in ZnO NCs with a given orientation of their hexagonal crystal axis with respect to the external magnetic field. The striking result is that the intensity of the induced hole depends on the orientation of dry powder sample. The hole was observed to disappear after a rotation by 90° and to reappear at the same position after the reverse rotation or a rotation by 180°. This shows that one can select a particular orientation in a sample of randomly oriented NCs.

9.2.1.4 ODMR via Tunnelling Afterglow in ZnO Nanocrystals

In this subsection, we will consider one of the ODMR techniques which is based on EPR detection via tunnelling afterglow. This afterglow can be observed after X-ray or UV irradiation and in some cases persists for a long time after the irradiation. This technique was first applied for ionic crystals and proved to be very useful to study colloidal ZnO NCs.

The tunnelling afterglow is determined by the recombination of electron and hole centres that were created during irradiation. The recombination is forbidden for electrons and holes with parallel spins. Therefore, in the magnetic field at a low temperature, when all spins tend to orient along the field as a result of the Boltzmann polarization, the afterglow intensity decreases. The magnetic quenching of the afterglow can be described by the relationship

$$I(B,t) = I_0(t)(1 - P_e P_h) \tag{9.3}$$

where I_0(t) is the afterglow intensity in zero field, which decreases slowly with time according to a hyperbolic law, and P_e and P_h are the spin polarizations of the electron and hole centres, respectively. For centres with the electron spin $S = 1/2$, the spin polarization can be calculated from

$$P_{e,h} = \tanh(g_{e,h}\mu_B B/2\kappa T) \tag{9.4}$$

where $g_\mathrm{e,h}$ is the electron g factor of an electron (e) or a hole (h) centres and μ_B is the Bohr magneton. The spin polarization $P_\mathrm{e,h}$ increases with an increase in the magnetic field and with a decrease in the temperature and tends to zero in high magnetic fields. At saturation of the EPR transition $P_{e,h}$ tends to zero, since the populations of the levels with spin up and down become equal, and a resonance increase in the emission intensity appears. For a distant pair of an electron and a hole centres the overlap of their wave functions is weak and the exchange interaction can be neglected. Therefore the ODMR spectrum consists of the individual EPR signals of the electron centre and the hole centre. The sensitivity and resolution of the afterglow-detected ODMR can be considerably increased with an increase in the ODMR operating frequency, as shown in Fig. 9.9a.

The photoluminescence (PL) and afterglow spectra of ZnO NCs are shown in Fig. 9.9b. Two emission bands are observed in the PL spectra: a relatively weak and narrow UV exciton emission and a much stronger and broader emission band in the green part of the visible spectrum, which is ascribed to recombination of a shallowly trapped electron with a deeply trapped hole [13]. In contrast, in the afterglow spectrum only the broad emission band is observed. Long-lasting afterglow (up to 3 h after switching off the UV excitation) was observed in Li-, Na- and Al-doped ZnO NCs. The afterglow intensity did not depend on temperature in the range 2–10 K, and was therefore assigned to tunnelling recombination of donor and acceptor centres that had been created by a short term UV excitation.

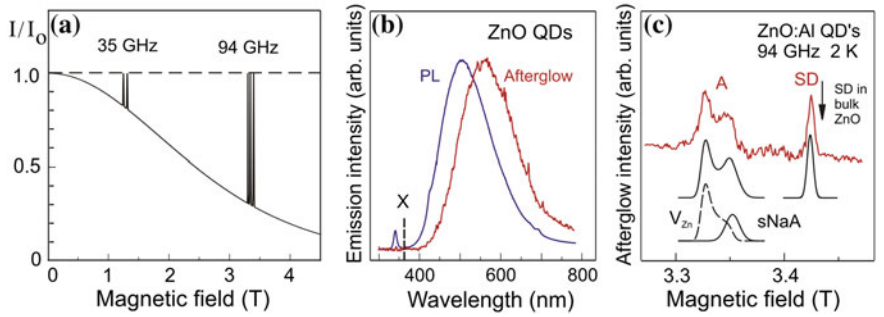

Fig. 9.9 **a** Dependence of the tunnelling afterglow intensity on the magnetic field at T = 2 K for two recombination centres with S = 1/2 and different *g*-factors according to the calculations from Eqs. (9.3) and (9.4), with the ODMR signals of these centres at frequencies of 35 and 94 GHz that correspond to a complete saturation of EPR transitions. **b** Photoluminescence (PL) and afterglow spectra of a diluted suspension of colloidal ZnO NCs (3.5 nm diameter) in ethanol. The temperature was maintained at 2 K in both cases. The afterglow spectrum was recorded 1 h after switching off UV irradiation. The *dashed line* marked with X indicates the position of the exciton luminescence line for bulk ZnO. **c** ODMR spectrum recorded in the W band (94 GHz) from the afterglow intensity for the same NCs at a temperature of 2 K. The arrow indicates the position of the EPR line of shallow donors in the bulk ZnO crystals for the magnetic field orientation perpendicular to the c crystal axis. The EPR spectra simulated for shallow donors and deep acceptors of two types, i.e., the zinc vacancies (V_{Zn}) and surface Na-related acceptors (sNaA), are shown at the *bottom*

The ODMR spectrum of ZnO:Al NCs recorded at 94 GHz on the afterglow intensity is shown in Fig. 9.9c. Shallow donors and two types of acceptors were resolved. The acceptors were identified as the zinc vacancy acceptors and the surface Na acceptors since the shape of the experimental spectrum is in good agreement with the spectrum simulated with the known parameters of these centres.

ODMR detected via afterglow of UV irradiated ZnO NCs can be used to estimate the NC size from the experimental values of the shallow donor *g*-factor and the magnitude of *g*-factor shown in Fig. 9.7b. It should be pointed out that the higher sensitivity of ODMR allows its application in the characterization of ZnO NCs dispersed in transparent media (such as polymers and frozen solvents), which cannot be studied by conventional EPR and ESE. This is an important advantage, since these systems are more relevant for a number of practical applications.

9.3 Outlook

EPR based spectroscopic techniques have developed into of the most powerful tools to investigate dopants and defects in condensed matter, and also provide essential information on the fate of photoexcited charge carriers in solids. These techniques have greatly contributed towards a deeper understanding of spin phenomena in

dopants and defects in nanostructures, which has important consequences for a number of potential applications in electronic, photovoltaic and spintronic devices.

In this chapter, the fundamentals of three important EPR based spectroscopic techniques were addressed. Further, the application of these techniques to nanomaterials was discussed, using ZnO nanocrystals as an illustrative example. EPR and ENDOR experiments on ZnO nanocrystals having ZnO/$(ZnOH)_2$ core/shell structures reveal the presence of shallow donors related to interstitial lithium and sodium atoms, and substitutional aluminium, in ZnO:Li, ZnO:Na and ZnO:Al nanocrystals, respectively. The shallow character of the shallow donor wave function is evidenced by the multitude of ^{67}Zn ENDOR lines and further by the hyperfine interaction s with the ^{7}Li, ^{23}Na and ^{27}Al nuclei that are much smaller than for atomic lithium, sodium and aluminium. The results show that one can monitor the change of the electronic wave function of a shallow donor in a ZnO nanocrystal when entering the regime of quantum confinement by using the nuclear spins in the semiconductor nanocrystals as probes. The ENDOR measurements show that the model based on the effective-mass approximation does not yield an appropriate description of the electronic wave function when the radius of the nanocrystal is reduced below the Bohr radius. The influence of confinement effects on the value of the *g*-factor of shallow donors has been observed for both ZnO and CdS nanocrystals. Long lasting tunnelling afterglow was found in ZnO nanocrystals and shallow donors centres and deep acceptors were identified by ODMR.

A future prospect for the technique seems to be connected with its application for the study and characterization of a wide range of nanostructures, including quantum dots doped with magnetic ions, self-organized nanostructured systems such as semiconductor nanocrystals embedded in glass and ionic crystal matrices, diamond nanocrystals, and organic-nanoinorganic photovoltaic structures, which aim to integrate the inexpensive processing properties of polymers with the superior optical, electrical, and carrier transport properties of nanoscale inorganic semiconductors.

9.4 Exercises

1. How can EPR spectroscopy be used to assess the average size of an ensemble of ZnO nanocrystals?
2. How does the size distribution of nanocrystals affect the width of the EPR line of shallow donors?
3. What are advantages of high frequency EPR in investigations of nanocrystals?
4. Estimate the shift of the EPR line of shallow donors in ZnO nanocrystals in X-band (9.3 GHz) and W-band (94 GHz) for nanocrystal radii changing from 2 to 3 nm.

Acknowledgments The work described in this chapter has been supported by the Russian Science Foundation under Agreement #14-12-00859.

References

1. Zavoisky, E.: The paramagnetic absorption of a solution in parallel fields. J. Phys. **8**, 377–380 (1944)
2. Abragam, A., Bleaney, B.: Electron Paramagnetic Resonance of Transition Ions. Oxford University Press, London (1970)
3. Geschwind, S.: Optical techniques in EPR in solids. In: Geshwind, S. (ed.) Electron Paramagnetic Resonance, pp. 353–425. New York, Plenum (1972)
4. Schweiger, A., Jeschke, G.: Principles of Pulse Electron Paramagnetic Resonance. Oxford University Press, London (2001)
5. Baranov, P.G., Orlinskii, S.B., Donega, C. d. M., Schmidt, J.: High-Frequency EPR and ENDOR spectroscopy on semiconductor quantum dots. Appl. Magn. Reson. **39**, 151–183 (2010) (and references therein)
6. Baranov, P.G., Romanov, N.G.: Magnetic resonance in micro- and nanostructures. Appl. Magn. Reson. **21**, 165–193 (2001). (and references therein)
7. Lifshitz, E., Fradkin, L., Glozman, A., Langof, L.: Optically detected magnetic resonance studies of colloidal semiconductor nanocrystals. Annu. Rev. Phys. Chem. **55**, 509–557 (2004). (and references therein)
8. Synthesis and properties of colloidal heteronanocrystals: Donega, C. d. M. Chem. Soc. Rev. **40**, 1512–1546 (2011)
9. Baranov, P.G., Romanov, N.G., Poluektov, O.G., Schmidt, J.: Self-Trapped excitons in ionic-covalent silver halide crystals and nanostructures: High-frequency EPR, ESE, ENDOR and ODMR studies. Appl. Magn. Reson. **39**, 453–486 (2010)
10. Fang, X.W., Mao, J.D., Levin, E.M., Schmidt-Rohr, K.: Non-aromatic core-shell structure of nanodiamond from solid-state NMR spectroscopy. J. Am. Chem. Soc. **131**, 1426–1435 (2009)
11. Bradac, C., Gaebel, T., Naidoo, N., Sellars, M.J., Twamley, J., Brown, L.J., Barnard, A.S., Plakhotnik, T., Zvyagin, A.V., Rabeau, J.R.: Observation and control of blinking nitrogen-vacancy centres in discrete nanodiamonds. Nat. Nanotechnol. **5**, 345–349 (2010)
12. Baranov, P.G., Soltamova, A.A., Tolmachev, D.O., Romanov, N.G., Babunts, R.A., Shakhov, F.M., Kidalov, S.V., Vul', A.Ya., Mamin, G.V., Orlinskii, S.B., Silkin, N.I.: Enormously high concentrations of fluorescent nitrogen-vacancy centers fabricated by sintering of detonation nanodiamonds. Small **7**, 1533–1537 (2011)
13. Orlinskii, S.B., Blok, H., Schmidt, J., Baranov, P.G., de Mello Donegá, C., Meijerink, A.: Donor-acceptor pairs in the confined structure of ZnO nanocrystals. Phys. Rev. B **74**, 045204 (2006)

Chapter 10
Solution NMR Toolbox for Colloidal Nanoparticles

Antti Hassinen, José C. Martins and Zeger Hens

Abstract In this chapter, solution nuclear magnetic resonance (NMR) spectroscopy is introduced and shown to be a powerful tool to analyze in situ the surface chemistry of colloidal nanoparticles. It is not that the questions that are asked are difficult ones, but the answers are very hard to get by, and it is in this respect that NMR makes a difference.

10.1 Introduction

While solution **Nuclear Magnetic Resonance** (**NMR**) **spectroscopy** has been applied to colloidal suspensions of nanoparticles (NPs) for over 20 years [1–3], it is only through more recent efforts that its full potential as a powerful in situ method to study NP systems has been appreciated. These recent efforts have expanded solution NMR from one-dimensional (1D) ^{1}H NMR to something that we have started calling the *solution NMR toolbox*. This toolbox consists of 1D ^{1}H NMR and a set of 1D and 2D NMR techniques which, when combined, can be used to study the surface chemistry of colloidal NPs dispersed in a liquid sample. The application of these NMR spectroscopic techniques has been very successful, and we have demonstrated that they enable the distinction between bound and free ligands [4], the identification and quantification of bound ligands [5–7], the analysis of

A. Hassinen (✉) · Z. Hens
Physics and Chemistry of Nanostructures, Ghent, Belgium
e-mail: Antti.Hassinen@UGent.be

Z. Hens
e-mail: Zeger.Hens@UGent.be

A. Hassinen · Z. Hens
Center for Nano and Biophotonics, Ghent, Belgium

J.C. Martins
NMR and Structural Analysis Unit, Ghent University, Ghent, Belgium
e-mail: Jose.Martins@UGent.be

C. de Mello Donegá (ed.), *Nanoparticles*,
DOI 10.1007/978-3-662-44823-6_10

adsorption isotherms [8, 9], and the study of the ligand exchange kinetics and mechanisms [10–12]. Solution NMR has also been used to study the synthesis of NPs, thereby unveiling the formation mechanism of monomers [13, 14] (see Sect. 6.3.3.1, Chap. 6, for details). On top of the techniques integrated into the solution NMR toolbox, NMR additionally provides a well-established set of methods that can be used for structure determination. These methods include correlation spectroscopy (COSY), heteronuclear single-quantum correlation spectroscopy (HSQC), and heteronuclear multiple-bond correlation spectroscopy (HMBC), which in combination with the NMR toolbox allow the assignment of the resonances of the ligands bound to the surface of the NPs. In this chapter, we only focus on the techniques of NMR toolbox and not on those used for structure determination, as the latter correspond to routine NMR methods.

10.2 One-Dimensional NMR Spectroscopy (1D NMR)

10.2.1 Exciting Spins

In solution ^{1}H NMR, the sample is placed in a coil and exposed to an *external magnetic field* B_0. This has two effects on nuclei that possess a spin, and therefore an associated magnetic field. First, the magnetic field of each nucleus will precess around the external magnetic field with an angular frequency $\omega_0 = \gamma B_0$, also known as the ***Larmor frequency*** (Fig. 10.1a). The term γ is the gyromagnetic ratio and is a natural constant for each NMR active isotope, protons in this case. Second, the external magnetic field lifts the spin degeneracy of the up and down spin states of the proton, which now correspond to the ground (spin up) and excited (spin down) state, respectively. In contrast to other spectroscopic techniques, such as fourier transform infrared spectroscopy (FTIR) or ultraviolet–visible spectroscopy (UV-Vis), the energy difference between these two states is very small in NMR ($\sim 10^{-25}$ J for

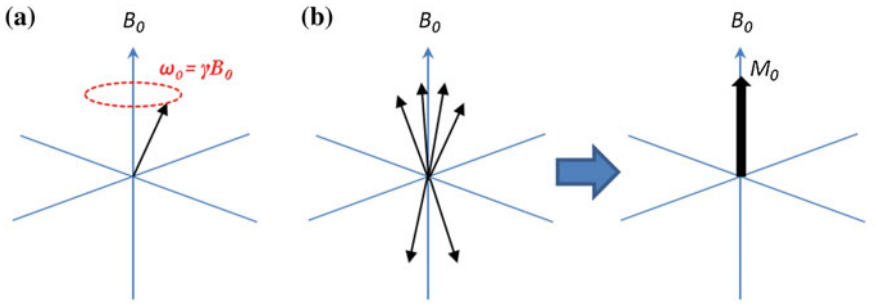

Fig. 10.1 Schematic representation of **a** the magnetic moment of a nucleus precessing around the applied external magnetic field B_0 with Larmor frequency ω_0 and **b** a collection of magnetic moments in B_0 which generates the bulk magnetization M_0 parallel to B_0

proton in 500 MHz field). Nevertheless, when a large number of spins are considered ($>10^{16}$ in this work), these still generate a tiny excess population of spin up states. This excess population can be calculated from a Boltzmann distribution which gives, by using the energy difference mentioned above, that for every 1,000,000 spins in the excited state there are ≈1,000,080 spins in the ground state. The combined nuclear magnetic fields of the spin up states gives rise to a macroscopic *bulk magnetization* M_0 (in thermal equilibrium) along the magnetic field axis defined by B_0 (Fig. 10.1b). In other words, the magnetic fields of a large collection of spins may be seen as precessing with randomized phase in the transverse plane (net contribution is zero) and a small net contribution (M_0) along the longitudinal axis defined by B_0.

Next, a pulse of radio frequency (rf) radiation, with magnetic field amplitude B_1 is used to rotate M_0 by 90°. If we consider that M_0 is along the z-axis, parallel to B_0, the B_1 field is applied perpendicular to B_0, for instance along the x-axis. Provided the frequency of the rf field matches that of the precessing spins generating the bulk magnetization (resonance condition), a bulk magnetization no longer in thermal equilibrium (M) is obtained through rotation to the y-axis when using a 90° pulse (Fig. 10.2a). After the 90° pulse, the population difference is zero and a coherent state is created in the transverse xy-plane. Since the bulk magnetization M is now at right angle with B_0, it will precess around B_0 with the Larmor frequency $\omega_0 = \gamma B_0$ (Fig. 10.2b). This precessing magnetization generates an oscillating field inside the coil, resulting in an alternating current with the same frequency, which can be measured to extract the precession frequency of the signal of interest.

Importantly, different local chemical environments produce electronic shielding effects of the spins, which lead to slightly different ***local magnetic fields B*** ($\neq B_0$). The frequency $\omega = \gamma B$ of a certain spin thus depends on its local chemical environment, generating a superposition of oscillating signals with slightly different frequencies in the coil. The complex signal measured in the time domain can then be converted into a spectrum in the frequency domain through *Fourier transformation*.

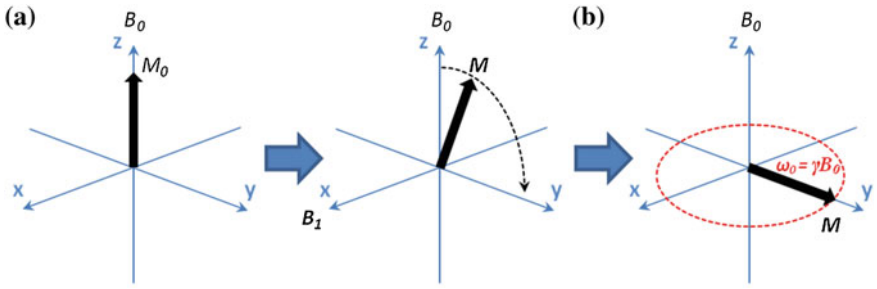

Fig. 10.2 Schematic representation of the effect of a radio frequency (rf) pulse on the bulk magnetization M_0 in a xyz-coordinate system. **a** The rf pulse generates a magnetic field B_1 that rotates M_0 over 90° pulse into the xy-plane. **b** The resulting bulk magnetization M (not in thermal equilibrium) starts to precess around B_0 with the Larmor frequency ω_0 after the 90° pulse

10.2.2 Spin Relaxation

The relaxation of nuclear spin states following excitation with an rf pulse is affected by several processes, which depend on molecular size and internal molecular motions. As we are interested in studying organic ligands interacting with NPs, it is clear that the relaxation will change considerably when going from free small organic molecules to big Np/ligand complexes. In the latter case, the motion of the ligands is restricted because of the slower overall tumbling of the larger NPs to which the ligands bind, and also because of the packing of the ligand shell (see Sect. 6.2.2, Chap. 6, for details), resulting in reduced local rotational freedom. Hence, to study bound ligands by NMR, it is important to be aware of relaxation when setting up measurements or during the interpretation of acquired data. We will now look more closely at the two main relaxation mechanisms and their behavior when studying NP/ligand complexes. A more detailed description can be found in reference [15].

Longitudinal relaxation (Fig. 10.3) is the recovery of M to its equilibrium value M_0 along B_0 and can be described by:

$$M = M_0\left(1 - ne^{-t/T_1}\right) \tag{10.1}$$

Here, T_1 denotes the longitudinal relaxation time constant (first-order) and depends on the rotational and internal motion of the spins in a molecule, and $n = 1 - \cos\beta$ is a factor that depends on the pulse angle β. For a 90° pulse $n = 1$, while for inversion (180°), $n = 2$. In the longitudinal relaxation process, the energy absorbed from the rf waves is released as heat to the surroundings. Since Eq. (10.1) describes an exponential recovery process, one should wait $> 5T_{1,max}$ between rf pulses, where $T_{1,max}$ refers to the longest T_1 time in the sample, to ensure quantitative measurements.

The second main mechanism for relaxation is ***transverse relaxation***. After a 90° pulse along the x-axis, the phase of the spins is no longer randomly distributed in the transverse plane, but is bunched up along the y-axis as described above. As the local magnetic field sensed by each spin fluctuates over time, and this fluctuation is different from molecule to molecule, each spin will have a different precession

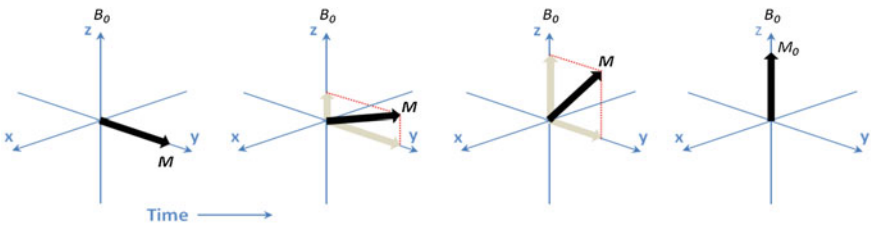

Fig. 10.3 Schematic representation of longitudinal relaxation where M returns to thermal equilibrium

history, causing the spins to fan-out in the *xy*-plane (Fig. 10.4). As a result, the phase alignment (coherence) is lost and the net magnetization in the transverse plain decays to zero. This exponential decay process is referred to as **transverse relaxation** and is characterized by a decay time constant T_2. This decay constant is correlated with the line width F of a resonance according to:

$$F = \frac{1}{\pi T_2} \tag{10.2}$$

T_2 scales ≈ linearly on molecular size, where small fast tumbling molecules have long T_2 compared to large slowly tumbling molecules. Consequently NP/ligand complexes tend to have broader resonances (short T_2). It should be noted that the principles described above are not limited to the ^{1}H nucleus, but can also be applied to other NMR active nuclei, such as ^{13}C and ^{31}P.

10.2.3 Quantification

^{1}H NMR enables the identification of molecules (molecular fingerprinting), as different environments of nuclei produce different chemical shifts. The resulting collection of resonances is thus characteristic for the molecule under investigation in a given solvent. Due to its dependence on the molecular size, the relaxation time T_2 of ligands bound tightly to the NP surface is expected to be short, which leads to broad resonances as shown in Fig. 10.5. When studying NP suspensions, one can also expect solvent induced shifts of the resonance frequency due to the different solvation of the ligand chains. Especially in the case of an aromatic solvent, ligands packed closely at the surface of the NPs experience a more aliphatic environment than free ligands in solution. As a result, bound and free ligands may demonstrate different chemical shifts (Fig. 10.5). Importantly, the broadening and shifting of ligand resonances when ligands are bound to NPs has no effect on quantification. As long as one waits for a sufficient time between the rf pulses (>5$T_{1,max}$), and uses well-defined experimental conditions [15], the bound ligands can be identified and

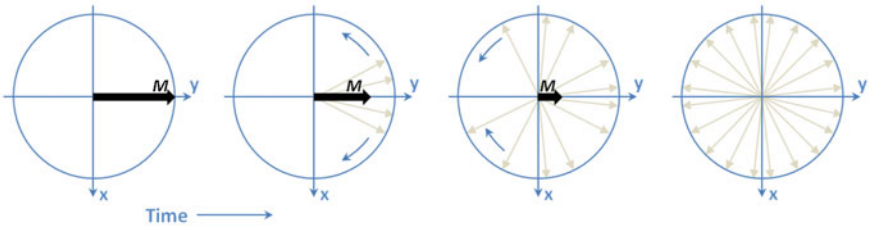

Fig. 10.4 Schematic representation of transverse relaxation where the magnetization in the xy-plane decays to zero due to the fanning-out of the phase of the individual magnetic moments of different nuclei

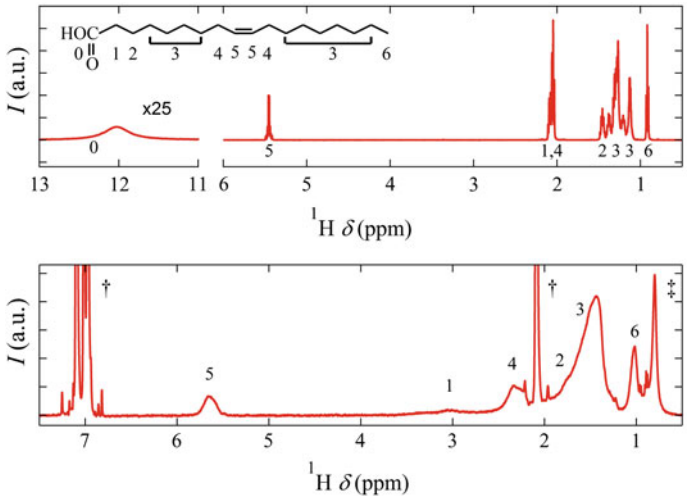

Fig. 10.5 ^{1}H NMR spectra of oleic acid (*top trace*, reprinted with permission from [7], Copyright (2008) American Chemical Society) and a CdSe NP suspension (*bottom trace*, reprinted with permission from [11], Copyright (2010) American Chemical Society) in toluene-d_8. Binding of oleic acid moieties to the NP surface leads to broad and shifted resonances. Numbered resonances are attributed to oleic acid and resonances with symbols to toluene-d_8 and to a proton pool related to H_2O contamination

quantified [5–7]. Hence, as soon as the sample volume, the concentration of NPs and the NP size are known, the surface density of bound ligands can be determined from quantitative NMR measurements. This helps us to build a complete structural model of the NP and the organic ligands. The model can then be used, for example, to better understand the connection between synthesis parameters and the final NP product [7].

Technically, quantification can be achieved by several methods, which include using internal standards or artificial resonances which are added to the acquired NMR spectrum. Internal standards have to fulfill several parameters before they can be used for quantification. First of all, the standard has to be soluble in the same solvent as the analyte and be chemically inert. Relaxation should preferably be similar to that of the solute, and the resonance(s) of the standard should not overlap with those of the solute. These points can make the use of an internal standard undesirable. An alternative way for quantification is to use an artificial resonance, with an intensity that is calibrated against a reference sample with known concentration. In this way, the integral value of the calibrated artificial resonance can be compared to that of a resonance of the solute, the concentration of which is unknown at this point.

Originally, we used a method by which the artificial resonance was added by physically generating a second low energy rf pulse which was then picked up by the coil during the acquisition [16–18]. The drawback of this so-called ***Electronic***

REference To access In Vivo Concentrations (**ERETIC**) method is that it needs changes in the spectrometer hardware, special experiments, and special processing. Wider et al. [19] introduced the next generation of artificial referencing which is based on the pulse length ***PULse Length based COncentration Determination*** (**PULCON**) and does not require any special hardware or software. PULCON uses the principle of reciprocity [20] and correlates the absolute intensities of two spectra measured in different solution conditions by using the fact that the NMR signal strength is inversely proportional to the 90° pulse length. By using the same NMR probe, which was tuned and matched to the same amplifier, delivering the same power for standard and unknown concentration sample with optimized 90° pulse lengths for each sample, the method was shown to be very robust and give accurate concentrations. Digital ERETIC (Bruker BioSpin software) and QUANTAS [21] refer to software packages representing practical implementations of the PULCON method where the artificial resonance is added in a post-processing fashion and can be used to compare the integrals of unknown concentration resonances to this artificial resonance.

10.3 Diffusion Ordered Spectroscopy (DOSY)

10.3.1 The Basics

In **DOSY** we apply field gradient pulses to obtain information regarding the self-diffusion rate of a molecule or complex in solution. This random translational (Brownian) motion can be described by a diffusion coefficient, D, which has units m^2s^{-1}. Therefore, D is a measure for the mean square displacement of a molecule or complex over a given time span. The principle of DOSY can be understood by imagining that the NMR sample at hand is sliced into separate volume elements and each of these elements are affected by different values of the magnetic field pulses (Fig. 10.6a). If a collection of molecules or complexes does not move between the two pulses, it will experience the same field and produce an unchanged response in the ^{1}H NMR spectrum. However, if part of the collection diffuses to a different position it will experience a slightly different magnetic field and, as a result, the overall signal intensity in the spectrum will have decayed to an extent characterized by D. The faster the molecule diffuses in solution, the larger the diffusion coefficient and the faster its signal decays in intensity. The intensity decay is given by the Stejskal-Tanner expression which, for the case of the pulsed field double stimulated echo using bipolar pulses and convection compensation, is:

$$I = I_0 \exp\left\{-D\gamma^2\delta^2G^2\frac{4}{\pi^2}\left(\Delta - \frac{5\delta}{8} - \frac{\tau_1}{2} - \frac{\tau_2}{2}\right)\right\} \tag{10.3}$$

Here, G is the gradient strength, τ_1 and τ_2 are the intergradient delays within the bipolar gradient pulses, Δ is the delay between pulses and δ the length of gradient

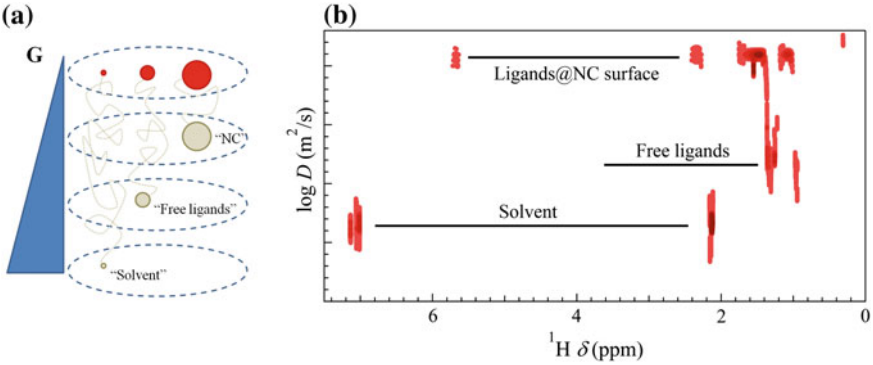

Fig. 10.6 **a** Molecules diffuse during the delay Δ and experience different local fields. Smaller molecules diffuse faster and experience bigger differences in local fields between the gradient pulses. Dotted lines represent the Brownian motion of the molecules in solution (figure adapted from Ref. [15]). **b** 2D DOSY presentation of CdSe NPs stabilized by oleic acid in toluene-d_8. Logarithmic diffusion dimension clearly demonstrates how the resonances are separated from each other if molecules diffuse with different rates in solution

pulses. The Stejskal-Tanner expression, as written above, is valid in the case of sine-shape gradient pulses. If different gradient shapes are used, the factors $4/\pi^2$ and $5\delta/8$ change depending on the selected gradient shape [22]. From the diffusion measurement D can be extracted for each frequency data point of the ^{1}H NMR spectrum. If we now plot the chemical shifts in one dimension and the D's of each component in the other dimension, we get a 2D contour plot. In other words, we have separated the proton spectrum along a second dimension, diffusion, creating a DOSY presentation (Fig. 10.6b).

In a DOSY spectrum, the center point of a cross-peak corresponds to the value of D itself and the width of the peak to the fitting error, both in the diffusion dimension. The diffusion coefficient values themselves are generated by exponential fitting of the decay intensities. The Bruker software (available for Bruker users) can be used to create a 2D DOSY presentation by fitting the decay intensities using either a mono- or biexponential function. This standard NMR processing is considered satisfactory for routine work and produces excellent results, especially in the case of single-exponential fits of high quality data. Biexponential fitting becomes necessary when two components overlap in the proton spectrum, and may give problems when there is only a slight difference in D values. In these cases, a more precise value for D can be obtained for the overlapping components through the use of other softwares (i.e, MatLab [23], DOSYm [24], DOSY toolbox [25]). To obtain high quality data from NP systems the delays (Δ and δ) should always be optimized to have ≈90 % signal decay with high G. The acquisition parameters should also be optimized to ensure adequate sampling of the decay. An example of adequate sampling is a series of minimum 32 1D spectra, each consisting of minimum 16 scans of 32,768 sampled points, covering the gradient induced gaussian intensity decay resulting from molecular diffusion.

10.3.2 Hydrodynamic Radius

Since we are exploiting diffusion in solution, the molecular size of the diffusing species will play a critical role in defining D. For rigid spherical objects, this is defined by the Stokes-Einstein equation:

$$d_H = \frac{k_B T}{3\pi\eta D} \tag{10.4}$$

Here, η denotes the solvent viscosity, k_B is Boltzmann's constant and T the absolute temperature. From this equation the hydrodynamic radius d_H may be obtained. As we are investigating organically capped NPs diffusing in solution, the obtained d_H corresponds to the sum of the NP diameter and the thickness of the ligand shell (Fig. 10.7). The NP diameter can be obtained directly by Transmission Electron Microscopy (Chap. 7), or, in the case of semiconductor nanocrystals in the quantum confinement regime (Chap. 2), by UV-Vis absorption spectroscopy and calibration curves correlating the observed band-gap (i.e., the lowest energy absorption peak) and the NP size.

When a ligand shows slow diffusion with an apparent d_H corresponding to the expected NP size, we consider the ligands to be tightly bound. However, as discussed in Chap. 6 (Sect. 6.2.3), the ligand shell may be very dynamic and therefore the ligands may spend part of the time of the measurement bound to the NP surface and be free in solution for the rest of the time. This exchange between bound and free ligands can be described as slow, fast or intermediate relative to the timescale of the NMR measurements. In DOSY the NMR timescale is determined by the delay between pulses Δ, and, depending on the exchange regime, the results can be drastically different between NP systems. As highlighted in Chap. 6 (Sect. 6.2), the importance of the inorganic/organic interface for colloidal NPs can be hardly overemphasized. For this reason, we will consider the use of DOSY to investigate different exchange regimes in more detail below.

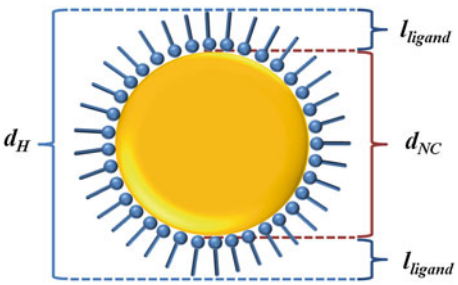

Fig. 10.7 Schematic representation of an NP coated with an organic ligand shell. The hydrodynamic radius d_H can be obtained from diffusion measurements and is the sum of the NP diameter and the thickness of the ligand shell

10.3.3 Ligand Dynamics in DOSY

The exchange regimes are defined by the relevant NMR timescales, which in diffusion are determined by Δ and in the frequency dimension by the frequency difference $\Delta\nu$ between the bound and free ligand states. If we consider that the exchange rate between free and bound ligands is k_{ex} and the relevant NMR timescale is τ_{NMR} [26–28], then the slow and fast exchange regimes are:

$$k_{ex} \ll \frac{1}{\tau_{NMR}} (slow) \tag{10.5}$$

$$k_{ex} \gg \frac{1}{\tau_{NMR}} (fast) \tag{10.6}$$

In the absence of exchange, two opposite situations concerning the interaction of the ligand with the NP are possible: either it is tightly bound to the surface or it does not interact at all with the NP. These two extreme cases can be distinguished on the basis of the observed diffusion behavior. Ligands that are tightly bound will show slow diffusion, with a d_H that corresponds to the expected diameter of the NP plus the ligand shell. On the other hand, ligands that do not at all interact with the NP surface will show fast diffusion, with the same characteristics of the free ligands. Between these two extremes, a number of other possibilities exist, depending on the strength of the interaction between the ligand and the NP surface and the partitioning between bound and free ligands.

When ligands are in ***slow exchange*** with respect to τ_{NMR} the bound and free ligands yield **two separate diffusion coefficients**, each corresponding to the value expected for free and bound (Fig. 10.8a). A slightly reduced value may be seen in cases where concentrated solutions are used causing solvent exclusion effects [6]. In diffusion measurements on NP systems, Δ values up to 500 ms have been used enabling to probe slow exchange on the second timescale [12]. When ***fast exchange*** conditions occur, **a single exchange averaged diffusion coefficient** may be obtained, according to:

$$D = x_{free} D_{free} + x_{bound} D_{bound} \tag{10.7}$$

Typically, in fast exchange conditions the observed D value is only a few percent lower than that obtained for the free ligands and the resonance lines are also only slightly broadened when compared to those of the free ligands (Fig. 10.8b). Even though the average diffusion coefficient and line-width are concentration sensitive, changing the concentration in this case will hardly change the diffusion coefficient, since due to the fast dynamics of the system the value of D is already within a few percent of the value for completely free ligands. As a result, it can be difficult to conclude using solely DOSY, that ligands are in exchange between solution and NP surface. The solution NMR toolbox provides tools to also distinguish such fast exchanging ligands from completely free and non-interacting ones. This point will be

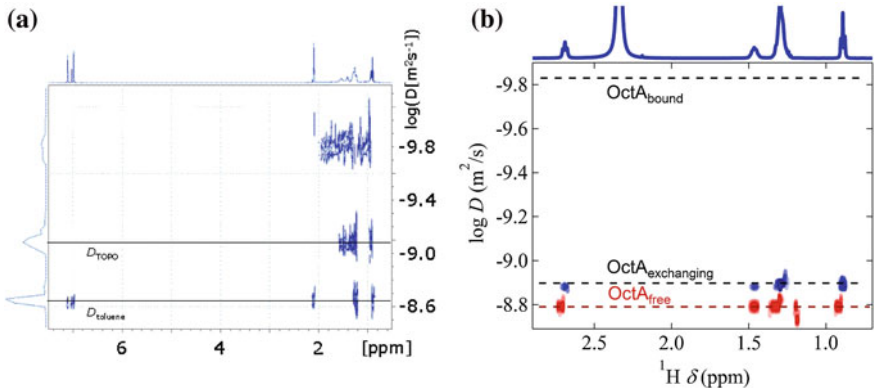

Fig. 10.8 **a** Diffusion-ordered spectrum for a colloidal suspension of TOPO-capped InP NPs in toluene-d_8. The solid lines correspond to the diffusion coefficient of free TOPO (D_{TOPO}) and free toluene ($D_{toluene}$). Set of subsequent dilutions of InP NP/TOPO suspension reveals slow exchange between free and bound TOPO [9]. Adapted with permission from Ref. [4]. Copyright (2005) WILEY-VCH Verlag GmbH & Co. KGaA, Weinheim. **b** In the presence of fast exchange dynamics a single exchange averaged resonance line and diffusion coefficient is obtained (*blue traces*). Samples: Octylamine (OctA) in $CDCl_3$ (*red traces*) and CdSe NP (4.4 nm) suspension stabilized by OctA in $CDCl_3$ (*blue traces*). Resonance at ≈2.3 ppm is attributed to a proton pool

discussed in the next section. Using diffusion measurements it is possible to probe fast exchange until ≈50–100 s^{-1} (Δ = 20–10 ms). Ligands in ***intermediate exchange*** result in two diffusion coefficients that no longer correspond to the respective bound and free values.

10.4 Nuclear Overhauser Effect Spectroscopy (NOESY)

10.4.1 Screening for Ligands

In **NOESY**, through-space interactions, known as dipolar couplings, between nearby ^{1}H nuclei give rise to the ***nuclear Overhauser enhancement*** or **NOE** effect. If we consider a system comprised of two homonuclear nuclei (i.e. two protons) with a magnetic dipolar coupling, we can draw an energy diagram describing the possible relaxation pathways available to the nuclei of the coupled spin system (Fig. 10.9a, spins I and S). Importantly, if these two nuclei are close enough in space, spin polarization can be transferred from one proton to the other by additional relaxation pathways (W_2 and W_0, Fig. 10.9a). The existence of these transitions gives rise to cross-relaxation, which effectively causes the transfer of magnetization (spin polarization). The W_2 and W_0 cross-relaxation processes compete with one another, with the dominant pathway dictating the sign and the rate at which the NOE develops. Relaxation via the W_2 process increases the population of spins in the lower energy state, thus increasing the population

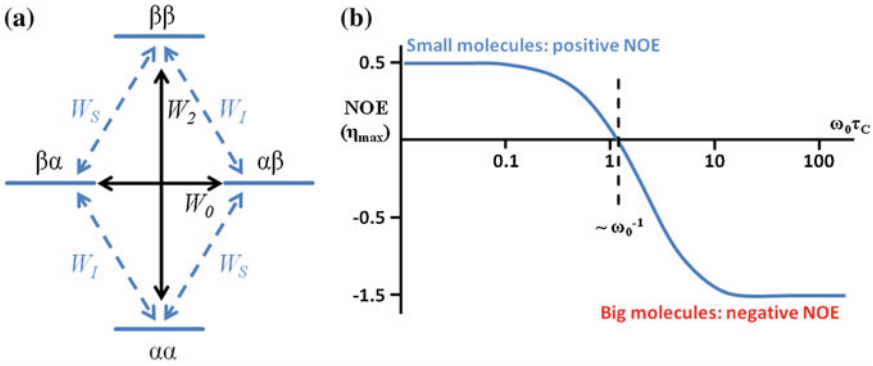

Fig. 10.9 **a** The six possible transitions in a two spin system, where the spins are labeled I and S. The double quantum transition (W_2) and the zero quantum transition (W_0) gives rise to cross-relaxation, whereas single quantum transitions (W_I or W_S) equals to longitudinal relaxation (T_1) of the spin. **b** The maximum ^{1}H-^{1}H NOE as a function of molecular tumbling rates as defined by $\omega_0\tau_c$ [15]. The actual zero cross-over point occurs when the molecular tumbling rate approximately matches the spectrometer observation frequency (figures adapted from Ref. [15])

difference across the single spin transitions, thereby resulting in increased resonance intensity (positive NOE). Relaxation via the W_2 process, which corresponds to the selective polarization perturbation of spin *I*, will also result in an increase of the polarization (and thus signal intensity after excitation) of spin *S*. On the other hand, relaxation via a W_0 process has a decreasing effect on the population difference, resulting in a decrease in resonance intensity and a negative NOE. In other words, if we selectively excite spin *I*, W_0 increases the polarization of spin *I*, but the polarization is decreased for spin *S*. The NOE effect is then defined as the change in relative signal intensity caused by the cross-relaxation pathways, normalized against the original intensity. Like the common relaxation processes, the NOE effect is modulated by molecular rotations.

We can plot the maximum ^{1}H-^{1}H NOE as a function of molecular tumbling rates to see the dependence of the NOE on molecular size (Fig. 10.9b). For small molecules, the rotational tumbling rate is high and characterized by a small value for the rotational correlation time constant τ_c and the positive NOE effect dominates. For large molecules or complexes, τ_c is large and the negative NOE effect dominates. The magnitude of the NOE effect is also dependent on the interproton distance ("r^{-6}" dependence). In practice, protons that are separated by a distance shorter than 0.5 nm can generate detectable NOE intensities. Being a source of interproton distances, the NOE is exploited widely in the last steps of structure determination of molecules and provides unique information on the 3D molecular geometry. We can observe the NOE as a cross-peak in a 2D NOESY spectrum which gives the NOE data plotted in a space defined by two frequency axes. Both of the axes have the same 1D proton spectrum originating both diagonal peaks and cross-peaks. The diagonal peaks connect the equivalent resonances in the ^{1}H spectrum and provide the starting points to look for *NOE cross-peaks*.

In our case, the property that is most of interest is the dependence of the NOE's sign on molecular size. For free ligands (small molecules), the rotational correlation time constant τ_c is typically on the order of ps (Fig. 10.10a). For large complexes, such as a ligand bound to a NP, τ_c is large and reorientation is slow (Fig. 10.10b). Thus, depending on whether a ligand molecule is bound or not, it will be characterized by either strong negative or weaker positive NOE cross-peaks in 2D NOESY spectra. The cross-over point, where positive and negative NOE's cancel each other out, is dependent on the spectrometer frequency and given by $\tau_c \approx \omega_0^{-1}$ (Fig. 10.9b). Of interest here, is the Stokes-Einstein relation which connects the τ_c to the radius r of a rigid spherical particle:

$$\tau_c = \frac{4\pi\eta r^3}{3k_B T} \tag{10.8}$$

Calculating τ_c for particles in toluene ($\eta_{toluene}$ = 0.556 MPa s) at 298 K, a 3 nm NP results in a τ_c of 1.9 ns while a 1.0 nm NP results in a τ_c of 70 ps. If we now compare these values to the inverse of the spectrometer's frequency ω_0, for instance 500 MHz, the condition $\tau_c \approx \omega_0^{-1}$ indicates that this is reached for $\tau_c \approx 0.3$ ns. We

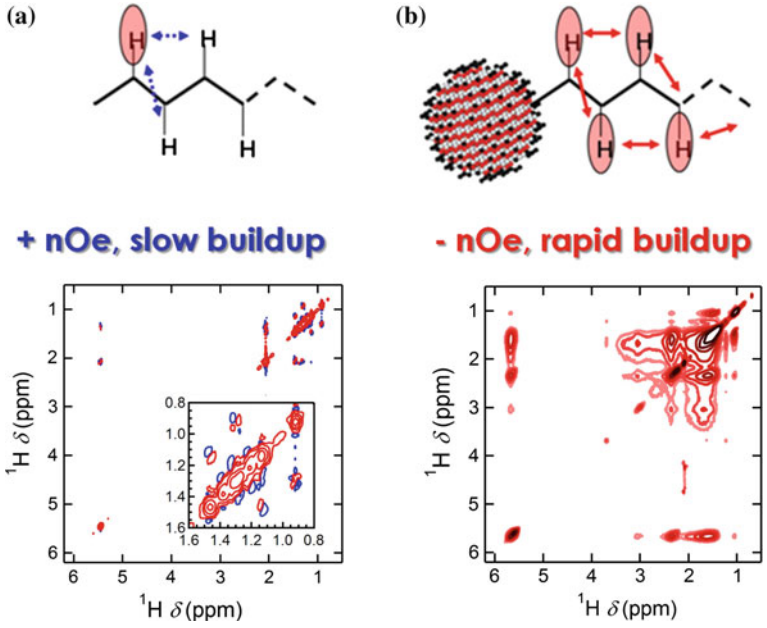

Fig. 10.10 **a** Small molecules tumble fast in solution and exhibit short rotational correlation time constants τ_c. This gives rise to positive NOE's and slow build-up of the cross-peak intensity. 2D NOESY spectrum of oleic acid in toluene-d_8 (figure adapted with permission from [7]). **b** Ligands bound to NCs tumble much slower and have long τ_c values. This gives rise now to rapidly negative NOE's. 2D NOESY spectrum of CdSe NCs stabilized by tightly bound oleic acid ligands in toluene-d_8 (figure adapted with permission from [12])

can therefore expect that large molecules (i.e., ligands bound to the surface of a NP) will develop negative NOE's, whereas small molecule (i.e., free ligands) will have positive or even no NOE's.

The behavior of free and bound ligands in NOESY has been validated using a system in no-exchange, where indeed bound ligands at the NP surface exhibit very efficient cross-relaxation resulting in rapidly growing and strongly negative NOE cross-peaks between the resonances (diagonal peaks) of bound ligands. When a solution of the ligand is investigated in the absence of NPs, no or very weak NOE cross-peak intensities are observed [12]. In other words, we can use NOESY measurements to screen for true ligands (i.e., molecules that indeed interact with the NPs) in mixtures when working with NP samples.

10.4.2 Recognizing Ligands in Fast Exchange

What makes NOESY even more unique and almost irreplaceable for NP systems is that it can also recognize ligands that are in fast exchange with the NP surface and whose interaction is hard to pick up from linewidth or diffusion measurements, since the parameters are dominated by the free state. Indeed, in NOESY the rate at which the NOE cross-peak develops (σ) is in the range of $\approx 10\ s^{-1}$ for bound ligands and $\approx 0.1\ s^{-1}$ for free ligands. Therefore, when a particular ligand molecule spends part of the time bound to the surface, and the rest of the time free in solution, the negative NOE developed during cross-relaxation with rate σ_{bound} in the bound state is much stronger in intensity than the positive NOE developed with rate σ_{free} in the free state. The average cross-relaxation rate is population averaged and can be written as:

$$\sigma_{avg} = x_{bound}\sigma_{bound} + x_{free}\sigma_{free} \tag{10.9}$$

Here, x_{bound} and x_{free} denote the mole fraction of bound and free ligands, respectively. Even if $x_{free} \gg x_{bound}$, as in most of the cases where fast exchange occurs in NP solutions, for reasons of dispersion stability, the fact that $\sigma_{bound} \gg \sigma_{free}$ will lead to negative NOE cross-peaks. In summary, NOESY is able to screen for true ligands of the NPs in mixtures and also recognize ligand molecules that are in fast-exchange with the NP surface from completely free molecules.

10.5 The Solution NMR Toolbox in Action: Octylamine Stabilized CdSe NPs

In this section, we will discuss in more detail the case of colloidal CdSe NPs capped by Octylamine, as an illustrative example of the possibilities offered by the solution NMR toolbox when applied to organically capped colloidal NPs. The text was adapted with permission from ref [10].

10.5.1 Octylamine Stabilized CdSe NPs

Colloidal CdSe NPs were synthesized in a mixture of hexadecylamine (HDA), *tri*-octylphosphine (TOP), and *tri*-octylphosphine oxide (TOPO), using dimethylcadmium and TOP-Se as precursors [29]. Two samples were studied, with average diameters of 4.4 and 3.9 nm (samples A and B, respectively). A pyridine ligand exchange process [30] was used as an intermediate step to remove the native ligands (HDA and TOPO) and to produce octylamine (OctA) stabilized CdSe NPs.

The ^{1}H NMR spectrum of sample A in $CDCl_3$ after the ligand exchange demonstrates that the pyridine ligands are efficiently removed, since pyridine resonances [10] in the spectral window from 7 to 9 ppm are absent (Fig. 10.11). Note that, in the preparation of the samples, it was crucial to prevent the precipitate from drying out completely. Consequently, methanol, which was used as a non-solvent, is observed at 3.47 ppm (CH_3) and 2.34 ppm (OH). The OctA resonances appear at 2.69, 1.47, 1.30 and 0.89 ppm, respectively, and are slightly broadened in comparison to free OctA. The amine protons of the OctA most probably contribute to the pool of labile hydrogens at 2.34 ppm.

In the 2D NOESY spectrum (Fig. 10.12a) strong, negative NOE cross-peaks are observed between the different OctA resonances. These negative cross-peaks demonstrate that the OctA ligands spend time on the surface of the NPs. The labile hydrogens at 2.34 ppm also have negative NOE cross-peaks with the OctA resonances, probably because the OH-group of residual methanol and the NH_2-group of OctA both contribute to this resonance.

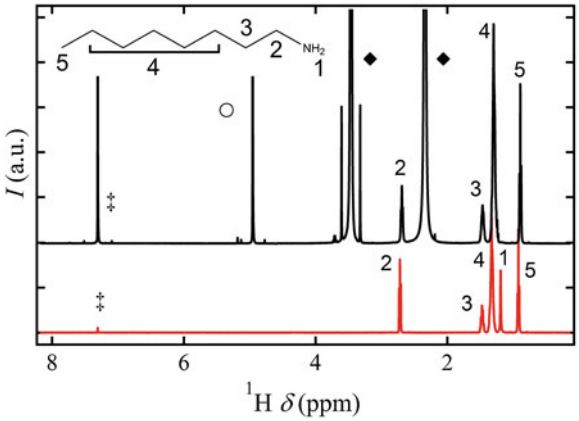

Fig. 10.11 ^{1}H NMR spectra of Octylamine(OctA) (*bottom trace*) and CdSe NPs capped with OctA in $CDCl_3$ (*top trace*). Resonances are assigned to residual $CDCl_3$ (*double dagger*), methanol (*diamond*), which was used during the ligand exchange, CH_2Br_2 (*circle*), added as a concentration standard, and OctA (numbered according to the inset). A comparison of both spectra shows that the OctA resonances in the OctA stabilized CdSe NP dispersion are only slightly broadened and shifted with respect to free OctA resonances. Reprinted with permission from reference [10]. Copyright (2010) American Chemical Society

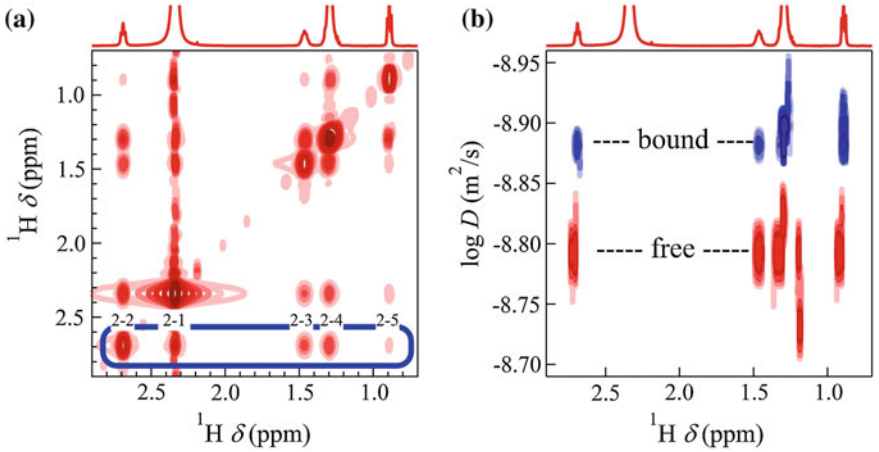

Fig. 10.12 **a** Typical NOESY spectrum of CdSe NPs capped with OctA in $CDCl_3$ using a 600 ms mixing time. Cross-peaks (NOEs) starting from diagonal α-CH_2 peak are indicated in the spectrum, where the numbers refer to the labeling introduced in Fig. 10.11. The observation of strong negative NOEs demonstrates that OctA interacts with the CdSe NPs. **b** DOSY spectrum of free OctA (*red*) and CdSe NPs capped with OctA (*blue*) in $CDCl_3$ using a diffusion delay of 50 ms. In the presence of CdSe NPs, OctA diffuses slower, yet the measured diffusion coefficient is larger than expected for tightly bound ligands. The combination of NOESY and DOSY points to a fast adsorption/desorption equilibrium between free and bound OctA. Reprinted with permission from reference [10]. Copyright (2010) American Chemical Society

From DOSY, we obtain a single diffusion coefficient for all OctA resonances. It amounts to 1.29×10^{-9} m^2 s^{-1} for sample A and 1.24×10^{-9} m^2 s^{-1} for sample B. This values are merely 18 % and 22 % slower than the diffusion coefficient of free OctA in $CDCl_3$ (1.59×10^{-9} m^2 s^{-1}, Fig. 10.12b), respectively, yet they considerably exceed the value expected for a NP with a hydrodynamic diameter of 4–5 nm. Similar to CdTe NPs stabilized by DDA [12], the 1D ^{1}H, NOESY, and DOSY results all indicate a fast exchange of OctA between a free and a bound state, with an excess of free OctA. This excess of free OctA is confirmed by a quantitative ^{1}H NMR spectrum. In the case of sample A, we calculate that on average 3,000 ligands are present for each CdSe NP. Using a typical ligand density of 4 nm^{-2} [7], this corresponds to a free/bound ligand ratio of about 12:1. Importantly, due to the fast chemical exchange the slightly broadened OctA ^{1}H resonances represent exchange averaged signals that are impossible to deconvolute to quantify the ratios of bound and free ligands [30].

10.5.2 NOE Buildup

To demonstrate that every OctA ligand in the dispersion is involved in the exchange process, the build-up of the NOE cross-peak intensity can be analyzed as a function of the NOE mixing time. These build-up curves are described by:

$$\frac{I_{AB}(t)}{I_{AA}(0)} = Ce^{-R_L t}\left(1 - e^{-R_C t}\right) \tag{10.10}$$

Here, $I_{AB}(t)$ is the intensity of the NOE cross-peak between resonance A and B at time t, and $I_{AA}(0)$ is the initial intensity of the diagonal peak of resonance A (associated with the α-CH_2 resonance). R_L is the overall T_1 longitudinal relaxation rate describing the return to equilibrium and R_C is the cross-relaxation rate giving rise to the NOE transfer. The pre-factor C is the relative intensity that the NOE cross-peak would attain if no longitudinal relaxation occurred. As such, it measures the fraction of the initial spin polarization of resonance A that is transferred to resonance B. By summing up this pre-factor over all possible final resonances, we can estimate what fraction of the ligands is involved in the exchange process. Indeed, if no exchange takes place, the NOESY cross-peak intensity will only be due to the fraction of bound ligands (f). Starting then from the excitation of the α-CH_2, the polarization from these 2 α-CH_2 protons is transferred to all 17 other protons. Hence, a fraction 17/19f of the initial spin polarization of the α-CH_2 will be transferred. Considering the 12:1 free/bound ligand ratio, estimated above from the quantitative NMR spectrum, we should observe a polarization transfer of 6.6 % in this case. On the other hand, under conditions of fast exchange, all molecules spend time on the NP surface during the NOESY mixing time. Thus, all ligands contribute to the NOESY cross-peaks and a polarization transfer of 89 % (i.e., 17/19) may be expected.

The parameters resulting from a fit of the NOESY build-up curves to Eq. (10.10) depend on the actual value of the T_1 relaxation time, which itself is hard to determine from the NOESY build-up. Therefore, we measured T_1 independently for all OctA resonances (2.69, 1.47, 1.30 and 0.89 ppm), yielding values that varied between 2.5 and 3.1 s. As a result, fixed values of T_1, 2.5 and 3.0 s, were used to fit the NOE build-up curves (Fig. 10.13). Apart from the transfer to the CH_3 group (I_{2-5}), this leads to well defined fitting parameters (Table 10.1), yielding an upper and a lower limit on the polarization transfer of about 90 % and 70 %, respectively. As outlined above, these high values confirm that essentially every OctA ligand in the CdSe NP dispersion contributes to the negative NOE cross-peak and thus spends time on the NP surface.

10.5.3 The Fast Exchange Rate of Octylamine

The disadvantage of a situation of rapid exchange in NMR is that it only yields a lower limit on the overall exchange rate $k_{on/off}$, which is defined for bimolecular exchange as [12]:

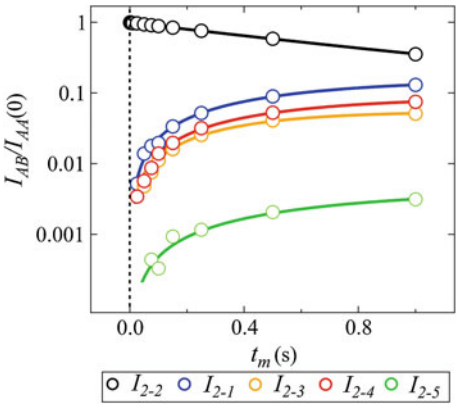

Fig. 10.13 Open circles: build-up of the intensity of the NOE cross-peaks as a function of the time span allowed for cross-relaxation (mixing time t_m). Full lines: best fits of the experimental data to Eq. (10.10), obtained using a fixed T_1 relaxation time of 2.5 s. The subscripts denoting the respective peak intensities refer to the labels introduced in Fig. 10.12a. Reprinted with permission from reference [10]. Copyright (2010) American Chemical Society

Table 10.1 Parameters obtained from a fit of the NOE build-up curves to Eq. (10.10) keeping the transversal relaxation time (T_1) fixed at the values indicated

	T_1 = 2.5 s		T_1 = 3.0 s	
	C	$1/R_c$ (s)	*C*	$1/R_c$ (s)
I_{2-1}	0.52(6)	2.2(3)	0.40(4)	1.6(2)
I_{2-3}	0.12(1)	0.91(8)	0.10(1)	0.78(7)
I_{2-4}	0.26(3)	1.8(2)	0.21(2)	1.4(2)
I_{2-5}	0.02(1)	3(1)	0.012(6)	2(1)

Pre-factor C gives the fraction of the initial spin polarization which is transferred from one resonance to other. R_C is the cross-relaxation rate giving rise to the NOE transfer. As the sum of the pre-factors is close to unity, we conclude that each OctA ligand in the CdSe/OctA dispersion is involved in the rapid exchange process

$$k_{on/off} = k_{off}\left(1 + \frac{x_{bound}}{x_{free}}\right) \tag{10.11}$$

Here, k_{off} is the first-order rate constant for desorption, while x_{bound} and x_{free} denote the molar fractions of bound and free ligands, respectively. Lower limits on $k_{on/off}$ are most easily obtained from the DOSY spectra, where the transition between rapid and slow exchange (characterized by the appearance of two diffusion coefficients) occurs when the exchange rate is comparable to the inverse of the diffusion delay Δ. We therefore performed DOSY measurements with a Δ of 100 ms, 50 ms and 20 ms, respectively. This always resulted in a single, constant diffusion coefficient, which demonstrates the occurrence of fast exchange in all cases (Table 10.2).

Given the excess of free ligands ($x_{bound}/x_{free} \approx 0.08$), we can conclude that the first-order rate constant k_{off} of OctA desorption strongly exceeds 50 s^{-1}. After

Table 10.2 Diffusion coefficients (D) obtained from the DOSY measurements using different diffusion delays (Δ)

Δ (ms)	100	50	20
D (m^2/s)	$1.292 \pm 0.015 \times 10^{-9}$	$1.315 \pm 0.024 \times 10^{-9}$	$1.315 \pm 0.029 \times 10^{-9}$

As a single, constant diffusion coefficient is obtained for delays down to 20 ms, we conclude that the exchange rate $k_{on/off}$ strongly exceeds 50 s^{-1}

reducing the temperature down to −40 °C, which is above the freezing point of $CDCl_3$ (−64 °C) but below the freezing point of neat OctA (−5 °C), still no component with a small diffusion coefficient appeared in the DOSY spectrum (Δ = 100 ms). The diffusion coefficient of OctA at low temperature can be calibrated by using the diffusion coefficient values of $CDCl_3$ and CH_2Br_2. After calibration the OctA diffusion coefficient amounts to 1.14×10^{-9} m^2 s^{-1}. Compared to the diffusion coefficient value measured under the same conditions at room temperature (1.29×10^{-9} m^2 s^{-1}), the low temperature diffusion coefficient is only ≈11 % slower. Hence, even at these low temperatures, the fast dynamics persists, with a k_{off} exceeding 10 s^{-1}.

10.6 Outlook

The power of the solution NMR toolbox has been only recently acknowledged in the study of NP systems leading to optimization of 1D ^{1}H NMR and a set of 1D and 2D NMR techniques. Although it may seem that the "low-hanging fruits" (*i.e.*, the easily accessible experimental studies) in the field of colloidal NPs have already been picked, the recent progress show that the surface chemistry of colloidal NPs can be very versatile, sensitive and still offers a lot to learn, even on systems that have been studied for years, such as CdSe and CdTe NPs [5, 6, 31, 32]. Moreover, the combination of the solution NMR toolbox with other experimental techniques, such as photoluminescence (PL) spectroscopy, has proven to be a powerful approach to probe the surface chemistry of colloidal NPs and to understand the impact of the surface dynamics on the properties of NPs [32, 33]. The solution NMR toolbox is ensuring its position in the routine characterization techniques of colloidal NP suspensions, where its potential and importance as an in situ method can hardly be overemphasized.

10.7 Exercises

The temperature is set to 25 °C unless mentioned otherwise. Toluene-d_8 is used as a solvent (η = 0.556 MPa s) and the NMR sample volume is 500 µl.

1. Ligands at the surface of a NP are observed to have a single diffusion coefficient of 1.49×10^{-10} m^2 s^{-1}. NP size is 5 nm and the length of the ligands is 1.8 nm.

Calculate the expected the diffusion coefficient value and evaluate in what exchange regime the ligands are.

2. Diffusion delay was decreased from 250 to 50 ms. If the ligand exchange regime would change from fast to slow exchange, what would you expect to see in the 2D DOSY spectrum and what is the estimated exchange rate?
3. You observe two diffusion coefficient values in DOSY measurements, 1.403×10^{-10} m^2 s^{-1} and 2.182×10^{-10} m^2 s^{-1}, respectively. The NP diameter is 2 nm and the length of the ligands is 1.8 nm. Based on the diffusion coefficient values, what are the two species that you have observed?
4. From quantitative ^{1}H NMR measurements you obtain the ligand concentration (1.9 mM) in the NMR sample under investigation. On the other hand, you know that the concentration of there NPs is 7 μM and the diameter of the NPs is 5.0 nm. What is the ligand density (ligands/nm^2) in the NPs?
5. What is the sign of NOE cross-peaks for NP/ligand complex with diameter of 2 nm if you are measuring on a 300 MHz spectrometer? If the single quantum transitions would not play a role and zero quantum transitions would become more dominant for the system at hand, to which direction (i.e., sign of NOE cross-peaks) the system would go?

References

1. Sachleben, J.R., Avenue, W., Colvin, V., Lyon, D., Wooten, E.W., Alivisatos, A.P.: Solution-state nmr studies of the surface structure and dynamics of semiconductor nanocrystals. J. Phys Chem. B. **102**, 10117–10128 (1998)
2. Majetich, S.A., Carter, A.C., Belot, J., Mccullough, R.D.: 1H NMR characterization of the CdSe nanocrystallite surface. J. Phys. Chem. **98**, 13705–13710 (1994)
3. Sachleben, J.R., Wooten, E.W., Emsley, L., Pines, A., Colvin, V.L., Alivisatos, A.P.: NMR studies of the surface structure and dynamics of semiconductor nanocrystals. Chem. Phys. Lett. **198**, 431–436 (1992)
4. Hens, Z., Moreels, I., Martins, J.C.: In situ 1H NMR study on the trioctylphosphine oxide capping of colloidal InP nanocrystals. Chem. Phys. Chem. **6**, 2578–2584 (2005)
5. Moreels, I., Justo, Y., Haustraete, K., Martins, J.C., Hens, Z.: Quantum dots : a surface chemistry study. ACS Nano **5**, 2004–2012 (2011)
6. Gomes, R., Hassinen, A., Szczygiel, A., Zhao, Q., Vantomme, A., Martins, J.C., Hens, Z.: Binding of phosphonic acids to CdSe quantum dots: a solution nmr study. J. Phys. Chem. Lett. **2**, 145–152 (2011)
7. Moreels, I., Fritzinger, B., Martins, J.C., Hens, Z.: Surface chemistry of colloidal PbSe nanocrystals. J. Am. Chem. Soc. **130**, 15081–15086 (2008)
8. Moreels, I., Martins, J., Hens, Z.: Solution NMR techniques for investigating colloidal nanocrystal ligands: a case study on trioctylphosphine oxide at InP quantum dots. Sens. Actuators, B **126**, 283–288 (2007)
9. Moreels, I., Martins, J.C., Hens, Z.: Ligand adsorption/desorption on sterically stabilized InP colloidal nanocrystals: observation and thermodynamic analysis. Chem. Phys. Chem. **7**, 1028–1031 (2006)
10. Hassinen, A., Moreels, I., de Mello Donegá, C., Martins, J.C., Hens, Z.: Nuclear magnetic resonance spectroscopy demonstrating dynamic stabilization of CdSe quantum dots by alkylamines. J. Phys. Chem. Lett. **1**, 2577–2581 (2010)

11. Fritzinger, B., Capek, R.K., Lambert, K., Martins, J.C., Hens, Z.: Utilizing self-exchange to address the binding of carboxylic acid ligands to CdSe quantum dots. J. Am. Chem. Soc. **132**, 10195–10201 (2010)
12. Fritzinger, B., Moreels, I., Lommens, P., Koole, R., Hens, Z.: In situ observation of rapid ligand exchange in colloidal nanocrystal suspensions using transfer NOE nuclear. J. Am. Chem. Soc. **131**, 3024–3032 (2009)
13. Liu, H., Owen, J.S., Alivisatos, A.P.: Mechanistic study of precursor evolution in colloidal group II–VI semiconductor nanocrystal synthesis. J. Am. Chem. Soc. **129**, 305–312 (2007)
14. Steckel, J.S., Yen, B.K.H., Oertel, D.C., Bawendi, M.G.: On the mechanism of lead chalcogenide nanocrystal formation. J. Am. Chem. Soc. **128**, 13032–13033 (2006)
15. Claridge, T.D.W.: High-Resolution NMR Techniques in Organic Chemistry, 2nd edn. Elsevier, Amsterdam (2008)
16. Silvestre, V., Goupry, S., Trierweiler, M., Robins, R., Akoka, S.: Determination of substrate and product concentrations in lactic acid bacterial fermentations by proton nmr using the ERETIC method. Anal. Chem. **73**, 1862–1868 (2001)
17. Akoka, S., Barantin, L., Trierweiler, M.: Concentration measurement by proton NMR using the ERETIC method. Anal. Chem. **71**, 2554–2557 (1999)
18. Barantin, L., Pape, A.L., Akoka, S.: A new method for absolute quantitation of MRS metabolites. Magn. Reson. Med. **38**, 179–182 (1997)
19. Wider, G., Dreier, L.: Measuring protein concentrations by NMR spectroscopy. J. Am. Chem. Soc. **128**, 2571–2576 (2006)
20. Hoult, D.I., Richards, R.E.: The signal-to-noise ratio of the nuclear magnetic resonance experiment. J. Magn. Reson. **24**, 71–85 (1976)
21. Farrant, R.D., Hollerton, J.C., Lynn, S.M., Provera, S., Sidebottom, P.J., Upton, R.J.: NMR quantification using an artificial signal. Magn. Reson. Chem. **48**, 753–762 (2010)
22. Sinnaeve, D.: The stejskal—tanner equation generalized for any gradient shape—an overview of most pulse sequences measuring free diffusion. Concepts Magn. Reson. **40A**, 39–65 (2012)
23. MatLab procedures are in-house written routines. For the in-house routine mentioned here acknowledgments are due to Dr. Davy Sinnaeve
24. NMR notebook software from NMRTEC. Uses Maximum Entropy method (Delsuc M.A.; Malliavin T.E.: Maximum Entropy Processing of DOSY NMR Spectra. Anal. Chem. **70**(10), 2146–2148 (1998)
25. Nilsson, M.: The DOSY Toolbox: A New Tool for Processing PFG NMR Diffusion Data. J. Magn. Reson. **200**, 296–302 (2009)
26. Bain, A.D.: Chemical exchange in NMR. Prog. Nucl. Magn. Reson. Spectrosc. **63**, 103 (2003)
27. Cabrita, E.J., Berger, S.: HR-DOSY as a new tool for the study of chemical exchange phenomena. Magn. Reson. Chem. **40**, S122–S127 (2002)
28. Ni, F.: Recent developments in transferred NOE methods. Prog. Nucl. Magn. Reson. Spectrosc. pp. 517–606 (1994)
29. Donega, C.D.M., Hickey, S.G., Wuister, S.F., Vanmaekelbergh, D., Meijerink, A.: Single-step synthesis to control the photoluminescence quantum yield and size dispersion of CdSe nanocrystals. J. Phys. Chem. B. **107**, 489–496 (2003)
30. Ji, X., Copenhaver, D., Sichmeller, C., Peng, X.: Ligand bonding and dynamics on colloidal nanocrystals at room temperature: the case of alkylamines on CdSe nanocrystals. J. Am. Chem. Soc. **130**, 5726–5735 (2008)
31. Owen, J.S., Park, J., Trudeau, P.-E., Alivisatos, A.P.: Reaction chemistry and ligand exchange at cadmium-selenide nanocrystal surfaces. J. Am. Chem. Soc. **130**, 12279–12281 (2008)
32. Hassinen, A., Moreels, I., De Nolf, K., Smet, P.F., Martins, J.C., Hens, Z.: Short-chain alcohols strip X-type ligands and quench the luminescence of PbSe and CdSe quantum dots, acetonitrile does not. J. Am. Chem. Soc. **134**, 20705–20712 (2012)
33. Rainò, G., Moreels, I., Hassinen, A., Stöferle, T., Hens, Z., Mahrt, R.: Exciton dynamics within the band-edge manifold states: the onset of an acoustic phonon bottleneck. Nano Lett. **12**(10), 5224–5229 (2012)

Index

C. de Mello Donegá (ed.), *Nanoparticles*,
DOI 10.1007/978-3-662-44823-6